PEDIATRIC RED MARROW AND ORGAN RADIATION DOSE ESTIMATES IN COMPUTED TOMOGRAPHY FROM MONTE CARLO SIMULATIONS

By

Diana Elizabeth Carver

Dissertation

Submitted to the Faculty of the

Graduate School of Vanderbilt University

in partial fulfillment of the requirements

for the degree of

DOCTOR OF PHILOSOPHY

in

Physics

August, 2015

Nashville, Tennessee

Approved:

Michael G. Stabin, Ph.D.

Aaron B. Brill, M.D., Ph.D.

J. Kelly Holley-Bockelmann, Ph.D.

David R. Pickens, Ph.D.

Ronald R. Price, Ph.D.

DEDICATION

For my family, blood related and not.

ACKNOWLEDGEMENTS

> "It doesn't happen all at once," said the Skin Horse. "You become. It takes a long time. That's why it doesn't happen often to people who break easily, or have sharp edges, or who have to be carefully kept. Generally, by the time you are Real, most of your hair has been loved off, and your eyes drop out and you get loose in the joints and very shabby. But these things don't matter at all, because once you are Real you can't be ugly, except to people who don't understand."
>
> — Margery Williams, The Velveteen Rabbit

I gratefully acknowledge the funding sources that made my Ph.D. work possible. I was supported by grant NIH/NCI 1 R01 CA155400-01A1 awarded by the National Institutes of Health, United States Department of Health and Human Services. The computational facilities used in this project were provided by the Vanderbilt Advanced Computing Center for Research and Education (ACCRE).

This thesis and research would not have been possible without my advisor, Dr. Michael Stabin, as well as the invaluable support from Dr. David Pickens and Dr. Ronald Price. I would also like to thank Dr. Kelly Holley-Bockelmann and Dr. Aaron Brill for their sound advice and scientific insights.

I thank Dr. W. Paul Segars of Duke University for an immeasurable amount of guidance and assistance in the development of the pediatric deformable phantom series. Dr. Segars developed the original phantoms that were used as a basis for this new series, and without them this work would not have been feasible.

Susan Kost, your continuous aid and support on all aspects of this project made the goals attainable. Together we have made tremendous achievements, and I know the future will only bring more. You have not only earned my highest respect as a scientist

and colleague, but also someone that I can now truly call a best friend.

Dr. Charles Coffey, I am eternally thankful for the door you opened when you accepted me into the Medical Physics program. You provided me the chance to become a medical physicist, and all future opportunities are ultimately because of you. Thank you.

Anandi Salinas, thank you for always being at my side through the joys and struggles of life as my best friend. I am so thankful we met fifteen years ago, when our academic journey began. You are always willing to lend a listening ear, celebrate the accomplishments, care for the wounds, and be there for me through everything.

Ken and Arden, I love you both deeply, and you mean the world to me. Thank you for being a source of constant support. Life would remain unfulfilled without your enduring love. You make my life complete, and I am excited for what our future may bring.

Mom and Dad, thank you for providing opportunities along the long, winding road that led to where I am today.

Finally, I thank all of my family, friends, and colleagues in my life on my never-ending journey to become Real.

Table of Contents

List of Tables

List of Figures

Chapter I

INTRODUCTION

1.1 Motivation

There are associated risks and benefits for any medical procedure, and diagnostic medical imaging examinations are no exception. Radiation-dose calculations are indispensable in the understanding of this delicate balance, including computed tomography (CT) examinations. For pediatric patients, this is of even greater importance as it is often true that this population has greater radiosensitivity (e.g., Donnelly et al., 2001; Donnelly, 2005; UNSCEAR, 2013). Additionally, there has been a huge increase in the contribution of medical imaging to our overall annual radiation exposure as a population. The 2009 NCRP report on human population exposure to radiation noted a dramatic increase in the contributions of medical sources to our overall annual radiation exposure (Schauer and Linton, 2009). There is a great need for more accurate dose prescription as well as systems for long-term dose-tracking of patients. Standard CT manufacturer software only provides generic dose estimates such as CT dose index (CTDI) or effective dose estimates (ED), but not individual organ dose values.

Currently, the CT vendor-supplied CT dose index (CTDI) and dose-length-product (DLP) values for pediatric subjects are based on dose estimates derived from a standard 16-cm acrylic cylinder (McCollough et al., 2008) and are assigned uniformly to all subjects (Dixon, 2003). A large amount of attention has been directed at radiation doses to pediatric patients, since they comprise a particularly sensitive popula-

tion (e.g., Brenner et al., 2001; Donnelly et al., 2001; Donnelly, 2005; Dixon, 2003; Linton and Mettler Jr, 2003). The Alliance for Radiation Safety in Pediatric Imaging (url-http://www.pedrad.org/associations/5364/ig/) notes the need for special care in prescribing pediatric CT studies, encouraging scanning only areas necessary for evaluation, and reducing dose-sensitive technique parameters (kVp and mAs) as much as possible (Donnelly, 2005; Goske et al., 2008). Medical professionals have noted the need for more accurate patient-specific dose values than are currently provided by the standardized manufacturer CT software (Strauss et al., 2009). There is also a great amount of effort to account for CT dose differences due to a patient's size (e.g., ICRP 102, 2007; McCollough et al., 2008; Goske et al., 2008).

Radiation-dose estimates from CT scans are commonly reported as CTDI values (mGy), which are derived from standard measurements made with one of two standard (16- or 32-cm diameter) acrylic phantoms for a given technique (kVp, mAs, collimation, and pitch). Values are assigned uniformly across pediatric and adult patients without regard to specific patient size and weight. These values are also assumed to apply equally to all subjects imaged for particular types of studies, e.g., body or head CT examinations.

To investigate how CTDI is related to patient-specific organ dose, a Monte Carlo radiation-transport code was developed to simulate pediatric patients undergoing CT exams on a Philips Brilliance 64 at Vanderbilt Children's Hospital, Nashville, TN. Two separate avenues were pursued to provide better estimates of pediatric dose.

First, several pediatric subjects that received CAP scans were selected for manual and semi-automatic organ identification and segmentation. These segmented patient images were converted into voxelized versions for importation into the Monte Carlo simulation.

Second, a series of deformable anatomical human body models (anthropomorphic phantoms) based on mathematical non-uniform rational b-splines (NURBS) has been developed. There are both models for standard average-population individuals as well as individuals with variations in size, weight, and age. Additionally, pediatric phantoms to represent a select number of obese patients were also developed.

Using these phantoms, patient-individualized dose calculations can now be investigated in a practical manner for numerous radiation sources. The phantom models and simulations provide individual organ doses from different CT exams, thus providing effective dose estimates that are more accurate than those from CTDI calculations in two reference models. Future changes in organ-weighting factors can also be taken into account.

A major goal of this research is to create a database of whole-body and organ doses from actual clinical CT scans in pediatric subjects to document patient-specific dose estimates. With the development of a large number of these phantoms, patient-specific dosimetry can be achieved through the use of patient-matched NURBS models. Dose estimates from CT exams for a pediatric subject can be assigned from the most similar phantom in the database. The quality of dose data to be assigned to pediatric patients receiving CT examinations can be significantly improved using the information obtained in this study.

Bone marrow is a very radiosensitive organ and tissue, so the implications of radiation exposure are greater for young pediatric patients than for adults. The Law of Bergonié and Tribondeau (Bergonié and Tribondeau, 1906) says that cells tend to be radiosensitive if they:

- Have a high division rate
- Have a long dividing future
- Are of an unspecialized type

Red marrow consists of progenitor and stem cells that are pluripotent, rapidly dividing, and have a long dividing future. Therefore, they are some of the most radiosensitive cells in the human body. They also generate red blood cells, platelets, leukocytes, and other important blood elements important in controlling infection. Radiation dose and potential radiation damage to these cells, especially in children, are of utmost concern.

One of the goals of this research is to develop patient-specific organ dose estimates using realistic anthropomorphic deformable phantoms prior to and after CT examinations. Another significant goal is to investigate how red marrow dose from CT imaging varies with patient age and body stature; new calculations and improved estimates of red-marrow dose should be of benefit to patients receiving diagnostic and therapeutic radiation doses.

1.2 Interactions of Radiation with Matter

Photons penetrate, scatter, or are absorbed when traveling through matter. The three major types of radiation interactions of X- and gamma-ray photons and associated electrons that are relevant to the energy range used in diagnostic imaging include: (a) Rayleigh scattering, (b) Compton Scattering, (c) Photoelectric absorption, and (d) Bremsstrahlung.

1.2.1 Coherent Scattering

Also known as "Rayleigh" or "classical" scattering, coherent scattering only occurs for very low diagnostic energies around 15 to 30 keV. Here, an incident photon excites the whole atom, and all of the electrons in the atom oscillate in phase (Figure 1.1). The atom immediately radiates this energy and emits a photon of the same incident energy, but in a different direction. Electrons are not ejected, thus ionization does not occur. Coherent scattering varies with the atomic number of absorber (Z) and incident photon energy (E) by Z^2/E. This interaction has a low probability for diagnostic energies in CT. Rayleigh scattering accounts for about 12% of interactions at approximately 30 keV in soft tissue (Bushberg and Boone, 2011).

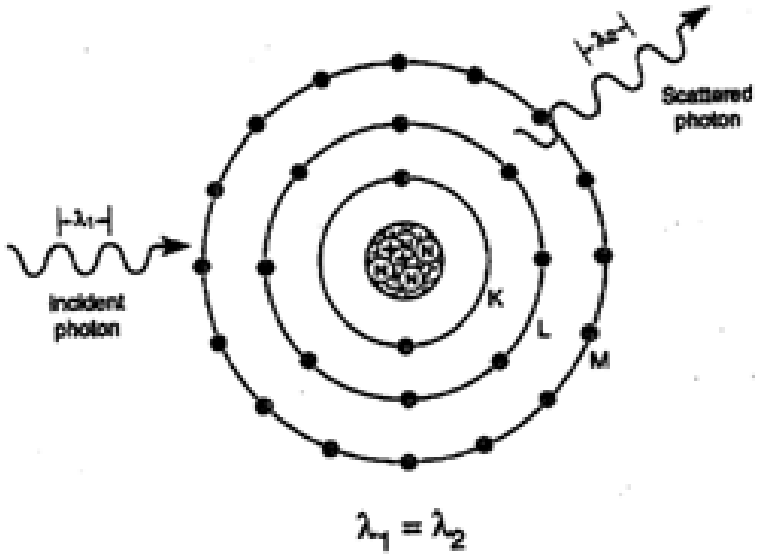

Figure 1.1: Rayleigh (elastic) scattering (Bushberg and Boone, 2011).

1.2.2 Compton Scattering

Compton scattering (also known as inelastic or non-classical scattering) is the chief interaction with soft tissue of X-ray and gamma-ray photons for diagnostic energies. It also dominates well beyond diagnostic energies to approximately 30 MeV. This interaction is most likely to occur between photons and outer shell electrons where the electron is ejected, and the photon is scattered with reduced energy (Figure 1.2). To conserve both energy and momentum, the energy of the incident photon is equal to the sum of the energy of the scattered photon and the kinetic energy of the ejected electron.

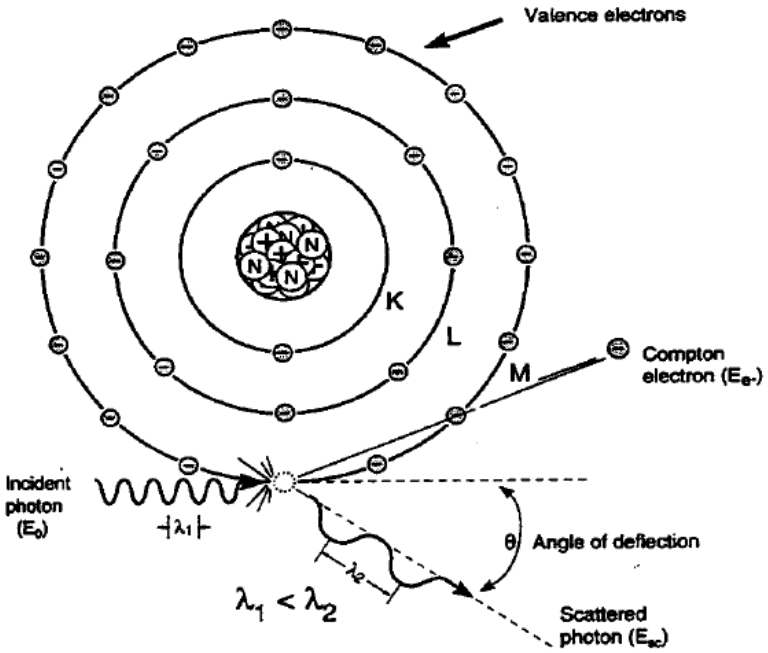

Figure 1.2: Compton (inelastic) scattering (Bushberg and Boone, 2011).

Compton scattering results in ionization of the atom, and the ejected electron will subsequently lose kinetic energy via excitation and ionization of atoms in the surrounding tissue. The scattered photon may cross through the medium without interaction or un-

dergo successive interactions (Compton scattering, photoelectric absorption, or Rayleigh scattering.)

The probability of a Compton interaction increases as the incident photon energy increases, since the incident photon must have substantially greater binding energy than the electron before the interaction is probable. The probability also depends on the electron density. The number of electrons per unit mass is roughly constant in tissue, so the probability of Compton scattering per unit mass is nearly independent of Z. The probability of Compton scattering per unit volume is roughly proportional to the density of the material (Bushberg and Boone, 2011).

1.2.3 Photoelectric Absorption

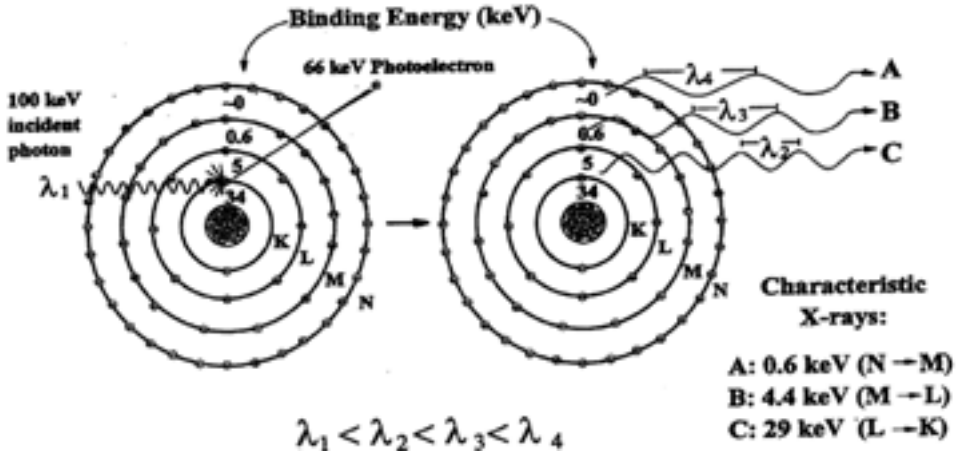

Figure 1.3: Photoelectric effect (Bushberg and Boone, 2011).

In the photoelectric effect, all of the incident photon energy is transferred to an electron, which is ejected from the atom. The kinetic energy of the ejected photo-electron

(E_e) is equal to the incident photon energy (E_o) minus the binding energy (E_b) of the orbital electron:

$$E_e = E_o - E_b. \tag{1.1}$$

For photoelectric absorption to occur, the incident photon must have energy greater than or equal to the binding energy of the electron to be ejected, and the atom is ionized, leaving an electron vacancy (Figure 1.3). If the ejected electron comes from an inner shell, its vacancy will be filled by an electron from a higher shell with a lower binding energy, which also creates a vacancy. Thus, an electron cascade from outer to inner shells occurs. Characteristic X-rays or Auger electrons are released with energy that is the difference in binding energies. For soft tissue and diagnostic energies, the probability of characteristic X-ray emission is relatively low, since the probability decreases as atomic number (Z) of the absorbing material decreases.

1.2.4 Bremsstrahlung

Electrons can undergo inelastic interactions with atomic nuclei in which the path of the electron is deflected by the positively charged nucleus, with a loss of kinetic energy (Figure 1.4). This energy is instantaneously emitted as ionizing electromagnetic radiation (X-rays). The energy of the X-ray is equal to the energy lost by the electron, as required by the conservation of energy.

The radiation emission accompanying electron deceleration is called bremsstrahlung, a German word meaning "braking radiation." The deceleration of the high-speed electrons

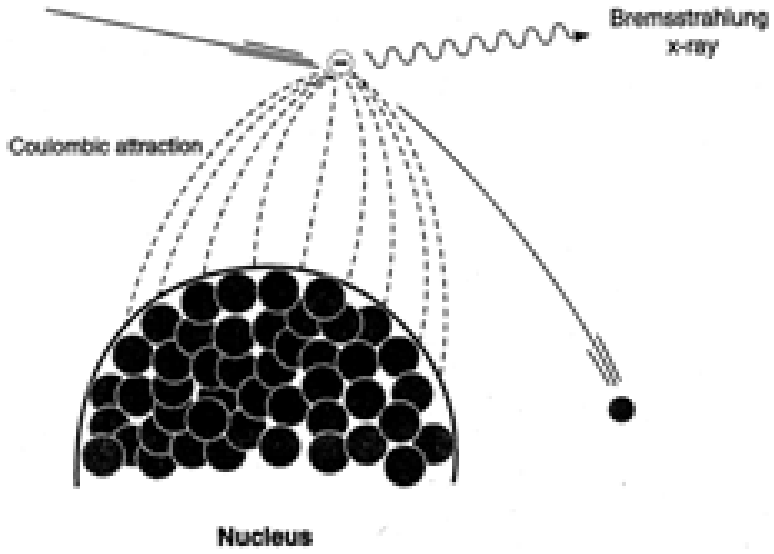

Figure 1.4: Bremsstrahlung (Bushberg and Boone, 2011).

in an X-ray tube produces the bremsstrahlung X-rays used for diagnostic imaging.

The energy of a bremsstrahlung X-ray photon can be any value up to and including the entire kinetic energy of the deflected electron. Thus, when multiple electrons undergo bremsstrahlung interactions, the result is a continuous spectrum of X-ray energies. The frequency and energy of bremsstrahlung emissions increases with Z of the interacting medium.

1.3 Basic Concepts in Dosimetry

1.3.1 Exposure

Exposure defines the ability of X-rays to ionize air and is measured in roentgens (R). One roentgen is the quantity of X-rays that produces 2.58×10^{-4} C of charge collected per kilogram of air at standard temperature and pressure. Exposure is typically measured with an ionization chamber and with an electrometer. It describes how much ionization

is present in a specific volume of air, but it does not tell how much energy is absorbed.

1.3.2 Kerma

As a beam of indirectly ionizing radiation passes through a medium, it deposits energy. First, energy carried by the photons (or other indirectly ionizing radiation) is transformed into kinetic energy of charged particles, such as electrons. Next, the directly ionizing charged particles deposit their energy in the medium by excitation and ionization.

Kerma (kinetic energy released in matter) is defined as the kinetic energy transferred to charged particles by indirectly ionizing radiation per unit mass expressed as J/kg or gray (Gy). For X- and gamma rays, kerma can be calculated from the mass-energy-transfer coefficient of the material and the energy fluence.

1.3.2.1 Mass-Energy-Transfer Coefficient

The mass-energy-transfer coefficient is given the symbol:

$$\left(\frac{\mu_{\mathrm{tr}}}{\rho_o}\right). \tag{1.2}$$

The mass-energy-transfer coefficient is the mass-attenuation coefficient multiplied by the fraction of the energy of the interacting photon that is transferred to charged particles as kinetic energy. As was mentioned above, energy deposition in matter by photons is largely delivered by the production of energetic charged particles. The energy in scattered photons that escape the interaction site is not transferred to charged particles in the volume of interest. Therefore, the mass-energy-transfer coefficient will always be less

than the mass attenuation coefficient (Bushberg and Boone, 2011).

For a mono-energetic photon beam with an energy fluence, Ψ, and energy, E, the kerma, K, is:

$$K = \Psi \left(\frac{\mu_{\text{tr}}}{\rho_o} \right)_E , \tag{1.3}$$

where ρ_o is the density of the media, and $(\mu_{\text{tr}}/\rho_o)_E$ is the mass-energy-transfer coefficient of the absorber (ρ_o) at energy E. The units of energy fluence are J/m^2, and the units of the mass-energy-transfer coefficient are m^2/kg. Therefore, kerma has units of J/kg.

1.3.3 Absorbed Dose

Absorbed dose (D) is defined as the energy (ΔE) deposited by ionizing radiation per unit mass of (Δm). Absorbed dose is defined for all types of ionizing radiation and is measured in gray (Gy). One gray is equal to 1 J/kg. If the energy imparted to charged particles is deposited locally and bremsstrahlung losses are negligible, the absorbed dose will be equal to the kerma. For X-rays and gamma rays, the absorbed dose can be calculated from the mass-energy-absorption coefficient and the energy fluence of the beam (Bushberg and Boone, 2011).

1.3.3.1 Mass-Energy-Absorption Coefficient

The mass-energy-transfer coefficient describes the portion of the mass-attenuation coefficient that gives rise to the initial kinetic energy of electrons in a small volume of absorber. These energetic electrons may subsequently produce bremsstrahlung radiation

that can escape the small volume of interest. Consequently, the mass-energy-absorption coefficient is somewhat smaller than the mass-energy-transfer coefficient. Relatively low energies are used in diagnostic imaging, and low-Z absorbers (air, water, tissue) have little radiative losses (bremsstrahlung). Therefore:

$$\left(\frac{\mu_{\text{en}}}{\rho_o}\right) \approx \left(\frac{\mu_{\text{tr}}}{\rho_o}\right). \tag{1.4}$$

The dose for any material can be calculated by:

$$D = \Psi \left(\frac{\mu_{\text{en}}}{\rho_o}\right)_E. \tag{1.5}$$

The difference between kerma and dose to air is that kerma is defined using the mass energy transfer coefficient, whereas dose is defined using the mass energy absorption coefficient. The mass energy transfer coefficient includes energy transferred to charged particles, but these energetic charged particles (mostly electrons) in the absorber will radiate bremsstrahlung radiation, which can exit the small volume of interest.

1.3.4 Effective Dose

Not all tissues are equally sensitive to the effects of ionizing radiation. Tissue weighting factors (w_T) were established in ICRP 60 (1991) and updated in ICRP 103 (2007) to assign a particular organ or tissue (T) the proportion of the detriment from stochastic effects resulting from irradiation of that tissue compared to uniform whole-body irradiation. The sum of the products of the equivalent dose to each organ or tissue irradiated (H_T) and the corresponding weighting factor (w_T) for that organ or tissue is called the effective dose

(ED):

$$\mathrm{ED} = \sum_{T} w_T \cdot H_T. \tag{1.6}$$

1.4 Dose Measurement in Computed Tomography

Compton scattering is the principal interaction mechanism in CT. Scattered radiation is not restricted to the collimated beam profile as primary X-rays are, so an acquired CT slice receives a significant dose from scatter to adjacent tissues. Furthermore, this is important in the acquisition of a series of near-contiguous CT slices over the tissue volume as it adds to tissue dose received during CT examinations.

1.4.1 Multiple Scan Average Dose (MSAD)

The multiple scan average dose (MSAD) is the standard for determining radiation dose in CT. The MSAD includes the dose attributable to scattered radiation coming from all neighboring slices. The MSAD could be measured directly by placing a small exposure meter at a point in a dose calibration phantom, taking a series of CT scans of the phantom with the meter in the middle of the slices, and adding the doses from all slices (Bushberg and Boone, 2011).

1.4.2 CT Dose Index (CTDI)

Measuring the CT dose index (CTDI) can assess the MSAD for just a single scan and offers a good estimate to the MSAD when the slices are contiguous. The CTDI measurement protocol seeks to measure the scattered radiation dose from adjacent CT slices in

a practical manner. The CTDI is defined by the U.S. Food and Drug Agency as "the radiation dose to any point in the patient including the scattered radiation contribution from 7 CT slices in both directions, for a total of 14 slices." This is also known as the $\mathrm{CTDI_{FDA}}$ (Bushberg and Boone, 2011).

CTDI is measured using a long, 100-mm, pencil ionization chamber. The chamber is long enough to span the width of 14 contiguous 7-mm CT scans to provide a decent estimate of the $\mathrm{CTDI_{FDA}}$ for 7- and 8-mm slices. All of the energy deposition along the length of the ion chamber is assigned to the thickness of the CT slice:

$$\mathrm{CTDI} = \frac{(f \times X \times L)}{nT}, \tag{1.7}$$

where X is the measured air kerma (mGy) or exposure (R) to the ion chamber, f is the air-kerma-to-dose (mGy/mGy) or exposure-to-dose (mGy/R) conversion factor, L is the length of the pencil ion chamber, and nT is the beam collimation (mm). In a multi-detector system, n is defined as the number of detector elements, and T is the width of each detector element. The 100-mm pencil ion chamber is commonly used for all slice thicknesses in addition to 7-mm slices, and this is referred to as the $\mathrm{CTDI_{100}}$. The $\mathrm{CTDI_{100}}$ provides a much better estimate of the MSAD for thin slices, since the $\mathrm{CTDI_{FDA}}$ underestimates the MSAD for small slice thicknesses. The $\mathrm{CTDI_{100}}$ is defined as:

$$\mathrm{CTDI_{100}} = \frac{1}{nT} \int_{z=-50\ \mathrm{mm}}^{z=+50\ \mathrm{mm}} D(z)dz, \tag{1.8}$$

where n is the number of slices acquired, T is the slice thickness, and $D(z)$ is the radiation dose as a function of position along the axis of the scanner.

The CTDI_{100} can be measured at the center of the phantom and at the periphery. The weighted CTDI is an approximate measure of the mean dose and is calculated as:

$$\mathrm{CTDI}_{\mathrm{w}} = \frac{1}{3}\mathrm{CTDI}_{100}^{\mathrm{center}} + \frac{2}{3}\mathrm{CTDI}_{100}^{\mathrm{periphery}}. \tag{1.9}$$

There are two commercially available standard phantoms used for measuring dose in CT. A 16-cm-diameter Poly(methyl methacrylate) (PMMA) cylinder is used to simulate adult heads and pediatric torsos, and a 32-cm-diameter cylinder is used to simulate the abdomen for adults. Holes are drilled to allow the placement of the pencil chamber at different positions within the phantom. PMMA rods are used to plug the holes not occupied by the pencil chamber. The ionization chamber reads out exposure (R) or air kerma (Gy) and dose is calculated through a conversion factor. For PMMA phantoms, this conversion factor is 0.893 mGy/mGy (for air kerma measurements) and 8.7 mGy/R (for exposure measurements). Dose to soft tissue is about 20% larger than the dose to PMMA. Radiation dose in CT is proportional to the mAs used per slice, so doubling of the mAs doubles the dose (Bushberg and Boone, 2011).

1.4.3 Helical CT and $\mathrm{CTDI}_{\mathrm{vol}}$

Pitch is defined as the ratio of the table feed (mm) per 360° gantry rotation to the collimated beam width. Helical CT scanning with a pitch of 1.0 is comparable to a conventional axial scan with contiguous slices. For CT scanners with multiple detector arrays, the pitch should be used for dose calculations. The dose is calculated in the same way as axial CT, but a correction factor is needed:

$$\text{Dose}_{\text{helical}} = \frac{\text{Dose}_{\text{axial}}}{\text{pitch}}. \tag{1.10}$$

The CTDI_{vol} is the dose measurement parameter displayed on most CT scanner consoles. It was developed to provide a standardized method to compare radiation output levels between different CT scanners using reference phantoms (International Electrotechnical Commission et al., 2002). CTDI_{vol} is defined as:

$$\text{CTDI}_{\text{vol}} = \frac{\text{CTDI}_{\text{w}}}{\text{pitch}}. \tag{1.11}$$

The dose length product (DLP) is sometimes used in addition to the CTDI_{vol}. It is simply the product of CTDI_{vol} and scan-length and is related to the overall ionizing energy imparted.

1.4.4 Size-Specific Dose Estimates (SSDE)

The CTDI_{vol} is known to underestimate absorbed dose for pediatric patients and smaller adults. AAPM Task Group 204 (American Association of Physicists in Medicine et al., 2011) was chartered to develop conversion factors, which when multiplied by the CTDI_{vol} value displayed on the CT console, result in more accurate dose estimates for patients of a specific size.

In addition to scanner radiation output, patient size also has a large effect on the dose a patient receives. CTDI_{vol} only provides information based on scanner output. Therefore, it does not accurately estimate dose, since it does not take into account size (McCollough et al., 2011). This is concerning for smaller pediatric patients, since interpretation of the

machine's displayed $CTDI_{vol}$ as patient dose could underestimate the real dose level by a factor of 2-3 if the larger 32-cm reference phantom was used (American Association of Physicists in Medicine et al., 2011).

The SSDE attempts to modify $CTDI_{vol}$ through the use of size-specific conversion factors that are based on lateral dimension (LAT) and anterior-posterior dimension (AP). LAT is defined as the side-to-side or left-to-right measurement of the body part being scanned. It can be determined on a standard PA CT radiograph prior to the actual CT scan. Likewise, AP is the measurement of the body part being scanned in the anterior-posterior or front-to-back direction. This can also be determined from a CT radiograph, but a lateral projection is necessary. In the absence of these radiographs, both measurements could be assessed by physically measuring the patient with calipers (American Association of Physicists in Medicine et al., 2011).

The SSDE method does not provide estimates of organ doses, however, so it is not possible to determine effective dose from the SSDE. It can improve accuracy of the average dose estimate by somewhat taking into account patient size, but it is not a very precise estimation method. Its use is an attempt to improve the estimate provided by the $CTDI_{vol}$ parameter.

1.5 Summary

The results of this research provide improved estimates of radiation dose to pediatric subjects undergoing CT scans. Current estimates are based only on simple dose estimate methods (i.e., CTDI values) that are assigned uniformly to all subjects for a given scan type without regard to patient size or weight. This work provides high quality dosimetry

tools and information for use in tracking and cumulating patients' doses over time. Physicians should be able to use this body of knowledge when prescribing exposure parameters for a given subject and study type with the goal of minimizing radiation dose while still achieving high quality images.

Chapter II

PHYSICAL AND COMPUTATIONAL PHANTOM MODELS

Calculations of radiation dose in external dosimetry serve as an important goal in gauging the biological response of healthy tissues. Measuring dose to these tissues directly with *in vivo* detectors is unfeasible. This limitation means that the use of realistic phantoms is an important tool for modeling human anatomy for dose assessment. This chapter provides a summary of dose estimation methods employing both physical and computational phantoms and their subsequent applications in pediatric CT dosimetry.

2.1 Physical Phantoms

In general, there have been very few studies that estimate organ and effective doses for pediatric patients in CT. In published studies, simple, cylindrical, or anthropomorphic physical phantoms of varying size have been utilized in order to estimate radiation dose as function of patient age.

2.1.1 Cylindrical Physical Phantoms

Shrimpton and Wall (Shrimpton and Wall, 2000) used 16-cm diameter Poly(methyl methacrylate) (PMMA) physical phantoms to produce reference dose indices such as weighted-CTDI values for single-slice scans and dose-length-product (DLP) for multiple-slice scans. Unfortunately, these metrics are insufficient to determine individual patient dose. These authors made an even greater effort to calculate effective dose (ED) using

the DLP. They did this by deriving normalization factors as a function of age, generated from simulation data of adult anthropomorphic-stylized phantoms.

Other authors have investigated size-dependent effects for radiation dose to children. Boone et al. (2003) analyzed size-dependent technique factors like varying tube current and voltages. They used phantoms ranging from 10 to 32 cm in diameter to report CT techniques (kVp and mAs) that maintained constant image quality while also reducing dose for pediatric patients.

Nickoloff et al. (2003) also investigated how phantom size, tube voltage, tube current, and scanner type affected CTDI values. They found that CTDI is an exponential function of phantom diameter, the value of which increases in phantoms with smaller diameters. Siegel et al. (2004) did a similar study using a wider array of physical phantoms (8, 16, 24, and 32 cm) for abdominal CT exams.

2.1.2 Anthropomorphic Physical Phantoms

Anthropomorphic physical phantoms have also been used to make experimental measurements of organ doses. Axelsson et al. (1999) used an anthropomorphic physical phantom of a 1-year-old with many implanted thermoluminescent dosimeters (TLDs) for axial head CT exams as well as spiral-CT studies of the lower trunk on a GE HiSpeed Advantage CT scanner with a nominal tube voltage of 120 kVp. Chapple et al. (2002) performed studies on a whole series of pediatric physical phantoms. Internally placed TLDs were used to estimate organ and effective doses using a Siemens Somatom Plus 4 CT scanner for head, chest, abdomen, and pelvic exams. They also derived conversion coefficients to estimate effective dose from DLP for different phantom sizes.

2.2 Computational Phantoms

Computational phantom models allow one to include detailed descriptions of organ geometries, volumes, and properties such as specific tissue chemical composition and physical density. There are three main categories of computational phantoms used in radiation dosimetry: stylized phantoms, voxel phantoms, and boundary-representation (BREP) phantoms. The following sections describe these phantom classes and their utilization in CT dosimetry. For more extensive summaries, Stabin and Xu (2014) and Xu and Eckerman (2009) have composed thorough reviews of the anatomical models employed in radiation dosimetry.

2.2.1 First-Generation Stylized Computational Phantoms

The first class of anatomical models constructed were mathematical in nature and used geometric shapes to define body surfaces and internal organ structures. These models were created from the concept of a standard or "reference" man to represent the average sizes and weights of the Western adult population. The main purpose of these computational phantoms at the time was to assess organ dose for internal emitters in patients and radiation workers. One advantage of using simple mathematical equations for organ and body definitions was that computational simulations of radiation interactions required less computation time.

2.2.1.1 Snyder-Fisher Stylized Phantoms

The first stylized computational phantoms were developed at Oak Ridge National Laboratory (ORNL) by Fisher and Snyder in the 1960s (i.e., Fisher and Snyder, 1966;

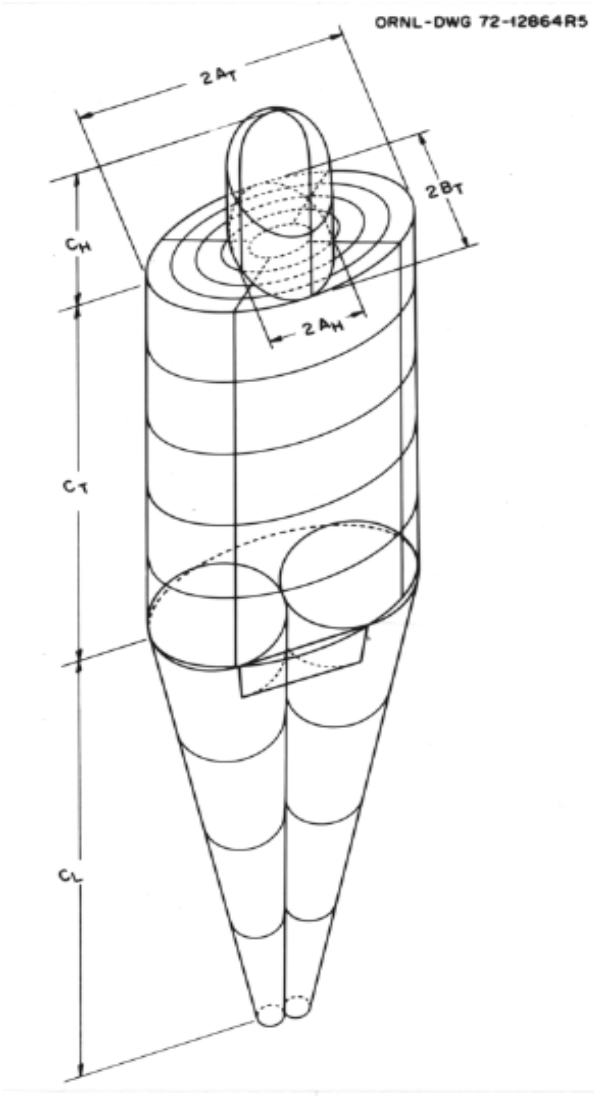

Figure 2.1: Stylized adult phantom (Cristy, 1980).

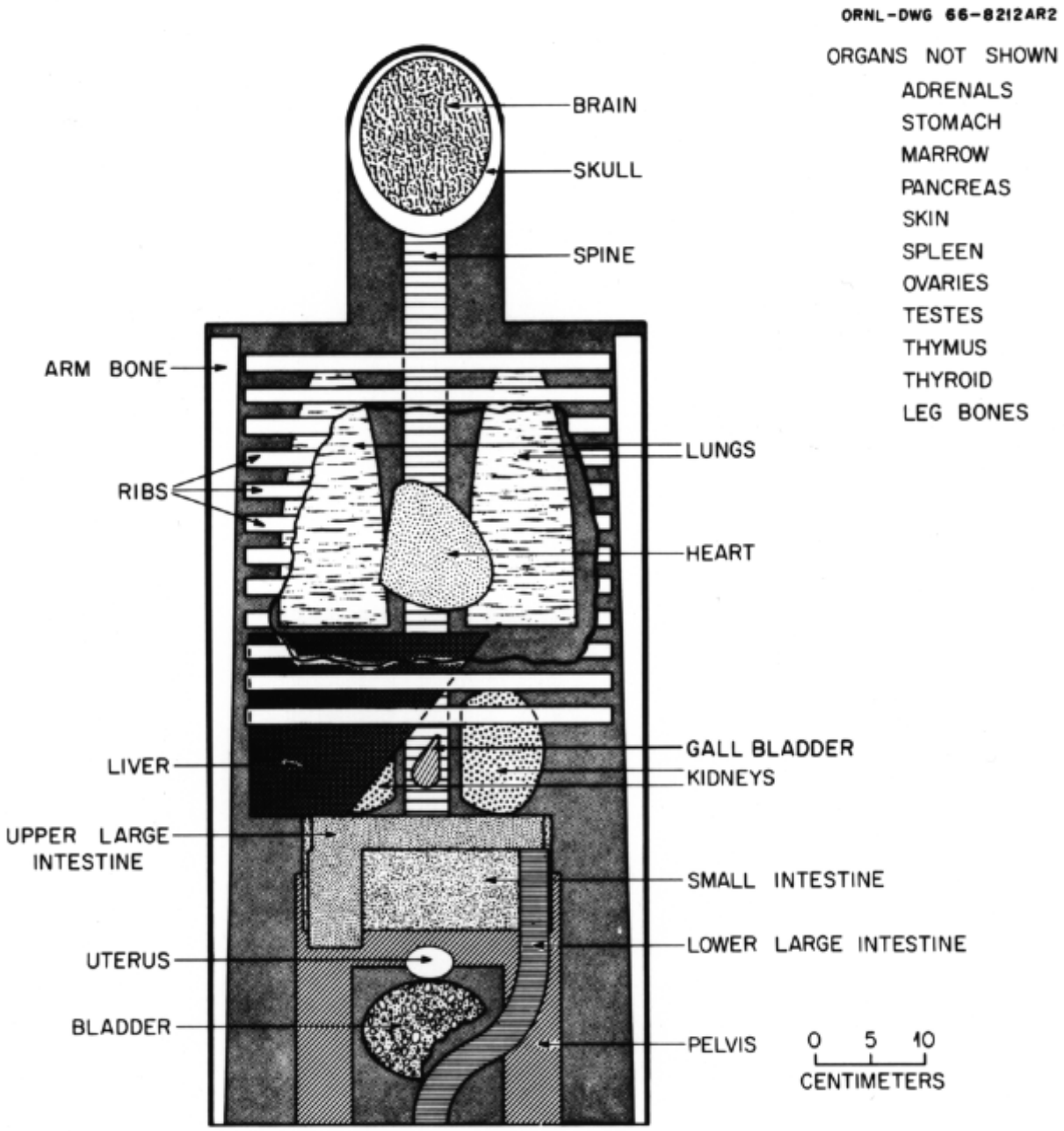

Figure 2.2: Snyder-Fisher adult phantom (Snyder et al., 1969).

Fisher Jr and Snyder, 1967; Snyder et al., 1969). The first phantom was hermaphroditic and consisted of a cylindrical base to represent the torso, abdomen, and arms. The head and neck were modeled as an elliptical cylinder, and truncated elliptical cones were used to describe the legs (Figure 2.1). Models of the skeleton, lungs, and remainder soft tissue were also included in later versions ("MIRD-5") (Figure 2.2). The original model was designed to represent an average adult male, known as "The Reference Man" as defined by Snyder et al. (1975). Results for more than 20 organs were released later by Snyder et al. (1978).

Kramer et al. (1982) used the hermaphroditic MIRD-5 phantom to make adult phantoms known as ADAM and EVA for external dosimetry. The adult female, EVA, was modeled by down-scaling volumes by a whole-body mass ratio of 0.83. Sex-related organs including testes, ovaries, uterus, and breasts were subsequently added to relevant phantoms. Female breasts were modeled as two ellipsoids attached to EVA's thoracic region.

Further efforts at ORNL were made in the 1970s to create pediatric phantoms, but all of these were based on the adult models. Hwang et al. (1976a) and Hwang et al. (1976b) designed a newborn, 1-year-old, and 5-year-old, and Jones et al. (1976) created a 15-year-old. Deus and Poston (1976) simulated a 10-year-old, which was quite different than the other four ages as it was intended to be more realistic. Applying scaling factors to adult phantoms to create age-dependent phantoms had obvious limitations.

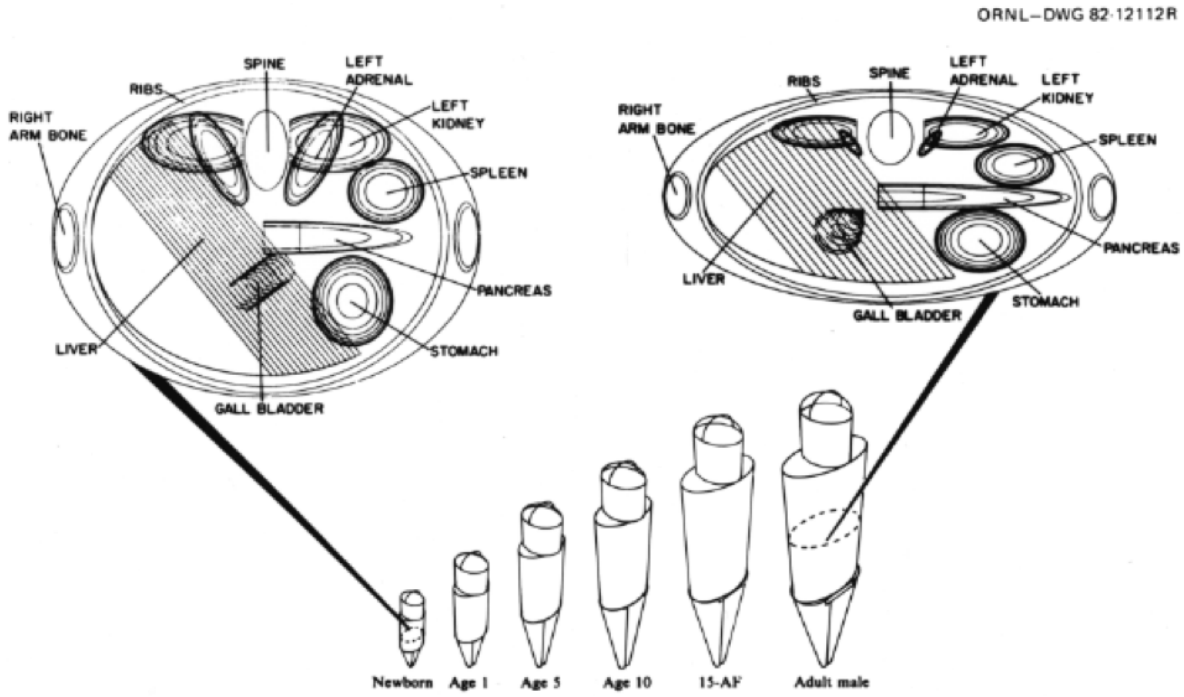

Figure 2.3: Cristy-Eckerman pediatric series showing views of the phantoms of different ages as well as the middle-trunk cross-sections of the newborn and adult phantoms. The head is relatively larger, the legs are relatively smaller, and the trunk is relatively thicker in the younger phantoms when compared to the adults. Organ placement also changed dramatically from birth to adulthood.

2.2.1.2 Cristy-Eckerman Pediatric Series

These limitations motivated the development of more tailored pediatric phantoms. In 1980 Cristy created a new pediatric series of stylized phantoms (Cristy, 1980) and worked with Eckerman in 1987 (Cristy and Eckerman, 1987). This series of pediatric ages included newborn, 1, 5, 10, and 15 years in addition to the adult male as well as an adult female with more anatomical features (Figure 2.3). The phantoms were composed of bone, soft tissue, and lung in the same manner as those by Snyder-Fisher. In comparison to the adults, the pediatric group had relatively larger heads, thicker trunks, and smaller legs. Since organ positioning also varies from birth to adulthood, this was also modeled based on age-dependent anatomical data. Total mass and individual organ masses were based on Reference Man data (Snyder et al., 1975).

Other updates were also made in the Cristy-Eckerman series. The chemical composition and physical density for soft tissue, lung tissue, and skeleton were improved in the newborn. Models for the heart and lungs were improved, including representation of the different sizes of the right and left lung. Female breast tissue was also added to the adult and 15-year-old female phantoms.

2.2.1.3 MCAT Phantom

The Mathematical Cardiac-Torso (MCAT) phantom was developed using the stylized method for use in nuclear medicine image research applications (e.g., Pretorius et al., 1997; Tsui et al., 1993, 1994). The MCAT phantom contained the major organs and structures of the torso (Figure 2.4). Later on, Segars extended the MCAT concept into a NURBS-

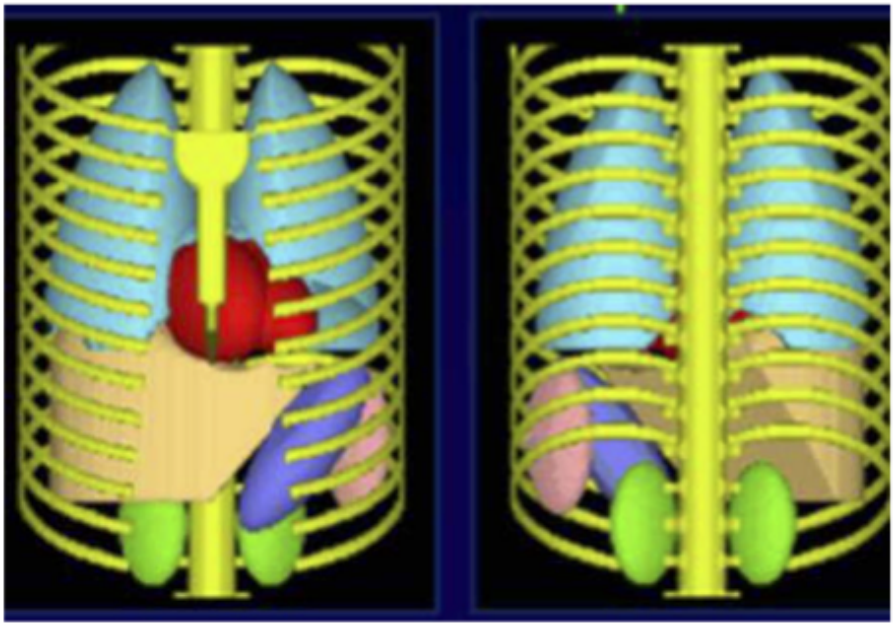

Figure 2.4: Anterior (left) and posterior (right) views of the Mathematical Cardiac-Torso (MCAT) phantom (Segars and Tsui, 2009).

based motion-simulating phantom that will be discussed in Section 2.2.3.1 (Segars, 2001).

2.2.1.4 Stylized Phantom CT Applications

Monte Carlo radiation transport methods using computational phantoms for different age groups provide a more accurate and versatile method of describing radiation absorption by the body, and some authors have used this method for CT dosimetry estimates. In Monte Carlo simulations using computational phantoms, the user has the ability to assign elemental compositions to each organ and calculate absorbed dose to any areas of interest.

Khursheed et al. (2002) used pediatric-stylized phantoms of various ages including newborn, 1-, 5-, 10-, and 15-year olds from the Oak Ridge National Laboratory (ORNL) series to estimate effective doses for three different CT scanners at one tube voltage.

However, the use of stylized phantoms in simulations can lead to discrepancies between actual and estimated dose due to unrealistically modeled torso shapes and organ locations. For example, the geometry of the esophagus resulted in an estimated dose 12 times higher than reported elsewhere. Also, only axial scanning was modeled, and phantom arms were not removed to simulate the normal clinical practice, the arms raised above the head during the course of the scan.

2.2.2 Second-Generation Voxel Computational Phantoms

More powerful computer and tomographic imaging technologies made it possible in the 1980s to develop more complex, anatomically realistic models. While stylized phantoms were simple and useful, they used ideal geometric shapes that lacked the detail of real anatomical structures. However, CT and MRI allowed 3D digital visualization of the internal structures of the body. This led to the creation of "voxel" or "tomographic" phantoms. Since a voxel is just a 3D representation of a pixel, 2D slice image data can be used to create detailed 3D representations of the body and its internal organ structures; voxel volume is equal to the pixel size multiplied by the slice thickness. These models are referred to as "voxel computational phantoms."

CT and MR images from live subjects and cadavers can be used to construct many phantoms, and many research groups have undertaken these efforts (e.g., Williams et al., 1986; Zankl et al., 1988; Zubal et al., 1994; Xu et al., 2000; Zhang et al., 2008). Voxel-based models are made up of identification numbers for each voxel that correspond to an individual organ or tissue. Each identification number specifies physical properties like density and chemical composition. Voxel phantoms may be either whole-body models or

only partial-body models such as torso-only or head-torso region models.

There are four main steps to generate a voxel phantom: (1) Tomographic image sets (from CT or MR) must be obtained, (2) organs and tissues must be segmented and assigned identification numbers to each pixel for each image slice, (3) physical densities and chemical compositions for the organs and tissues must be defined, and (4) the segmented image slices must be registered to generate the entire 3D idealized patient volume (Figure 2.5).

The generation of complete voxel phantoms presents some challenges, however. First, whole-body scans are needed to acquire images for all organs and tissues of interest. These are generally not routine scans. Second, segmenting out all organs and tissues of interest requires a large amount of time and effort. Third, data size for these types of images, especially when at high resolution, can be enormous, since a voxel phantom is made up of a very large amount of cubes grouped together to represent various organ structures. This is in high contrast to the simple quadric surface equations used to described stylized phantoms.

Two of the most well-known voxel phantom models will be discussed here: (1) the VIP-Man and (2) the GSF family.

2.2.2.1 VIP-Man

Xu et al. (2000) developed the VIP-Man (or Visible Photographic Man) as one of the first high-resolution, whole-body models. The creation of this phantom involved the use of high-resolution images ($0.33 \times 0.33 \times 1.0$ mm voxels) from the Visible Human Project. This project involved CT, MR, and color photographic images of normal male

and female human bodies. Manual segmentation of organs from these images allowed the creation of 3D representations of the entire body. The first Monte Carlo simulations of charged particles used the VIP-Man voxel phantom to perform internal dosimetry calculations (Chao and Xu, 2001).

2.2.2.2 GSF Family

A whole series of voxel phantoms was created due to the long-term research efforts of the National Research Center for Environment and Health (GSF) in Germany. High-resolution CT images of healthy volunteers were used to create phantoms of various ages and sizes including adult males and females, a 7-year-old child, and an infant. Eventually, a whole family of 12 voxel phantoms was generated and given the names: BABY, CHILD, DONNA, FRANK, HELGA, IRENE, GOLEM, GODWIN, VISIBLE HUMAN, LAURA, KLARA, and KATJA (Petoussi-Henss et al., 2002; Veit et al., 1989; Zankl et al., 1988; Zankl and Wittmann, 2001).

Voxel representations were created through both manual and semi-automatic segmentation of organs and tissues of interest. For organs such as the lung and skeleton, which are high-contrast, ranges of Hounsfield Units (HU) were used to define these regions. For many organs, additional image processing software was used to sharpen edges, get rid of artifacts, and perform morphological changes to the organ volumes.

2.2.2.3 Voxel Phantom CT Applications

Monte Carlo simulations to estimate organ doses in adults for axial and helical CT have been performed by Jarry et al. (2003), employing an adult-stylized ORNL phantom

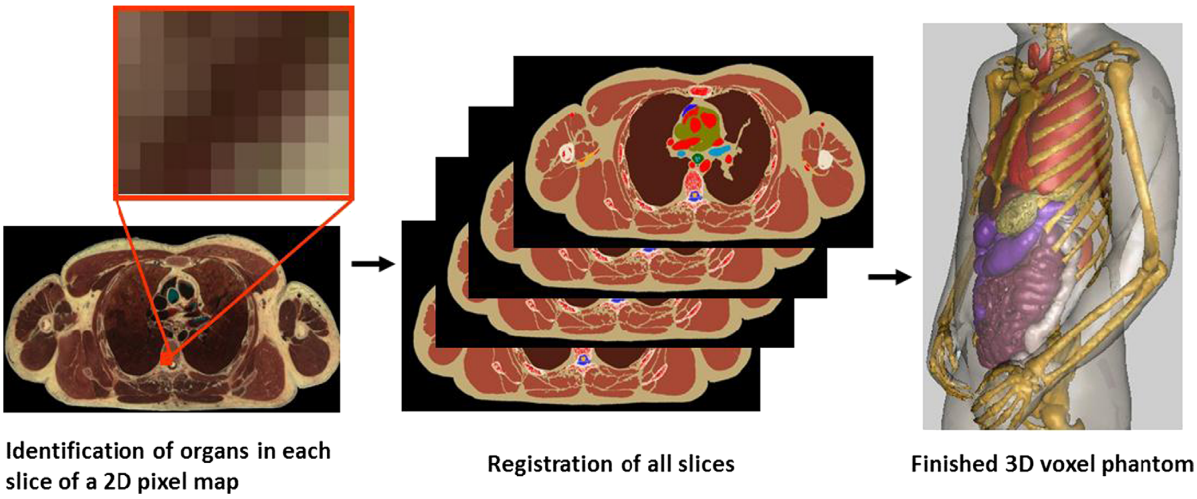

Figure 2.5: Voxel phantom creation process (Stabin and Xu, 2014).

and simple partial-body voxel phantom. This was the first work where helical movement of the X-ray CT source was explicitly modeled along with detailed beam attenuation profiles through the bowtie filter. Staton et al. (2006) used both stylized and voxel phantoms of a newborn to calculate organ and effective doses for multi-slice helical CT based on the Jarry et al. (2003) techniques.

Lee et al. (2005) has also used voxel phantoms, employing the techniques of Jarry et al. (2003) to simulate a Siemens SOMATOM Sensation 16 helical multi-slice CT scanner using manufacturer-provided information on X-ray spectral and beam shaping filtration. The University of Florida (UF) Series B voxel phantoms includes a 9-month male, a 4-year female, an 8-year female, an 11-year male, and a 14-year male phantom (Lee et al., 2006b). The UF Series B was developed from the UF Series A, which was constructed from image segmentation of head and chest-abdomen-pelvis (CAP) scans of patients. The UF Series A has patient-specific organ masses and body dimensions, and it encompasses only the head and torso regions. The UF Series B was made to include arms and legs,

taken as scaled segmented images from an adult CT-based phantom. The organs were morphed to align them with age-interpolated values from ICRP 89 reference masses.

2.2.3 Boundary Representation Computational Phantoms

Although voxel computational phantoms are realistic, there are several limitations (e.g., the need for whole-body scans, the large efforts to segment organs, and large data size). Another significant limitation of voxel phantoms is that they represent a specific individual and not a population, since they are created from patient images. These issues led to efforts to create "deformable" human models from boundary representation (BREP) methods in the early 2000s. BREP techniques allow models to be deformed to fit a particular organ shape or changes in time in order to represent organ motion.

Most BREP modeling uses non-uniform rational B-splines (NURBS) surfaces to represent solid volumes for defining the organs and body. NURBS are essentially boundary surface representations that are defined by a set of control points that can be scaled, translated, and rotated by means of affine transformations. This makes NURBS phantoms simple to manipulate to represent a specific individual. Hence, BREP phantoms garner significant advantages over previous methods: (1) NURBS-based phantoms can be developed much quicker than by manually segmenting patient data, (2) phantoms have a high level of internal consistency, and (3) phantoms are complete with no missing organs.

The first anthropomorphic phantom based on NURBS surfaces was created by Dr. Paul Segars (Segars 2001). Several other NURBS phantoms have been subsequently produced including adult and pediatric phantoms of various ages, sizes, and statures (e.g., Johnson et al., 2009; Marine et al., 2010), obese adults (Clark et al., 2010), and a series

of adult and pediatric models at reference ages (Stabin et al., 2012).

2.2.3.1 NCAT and XCAT Phantoms

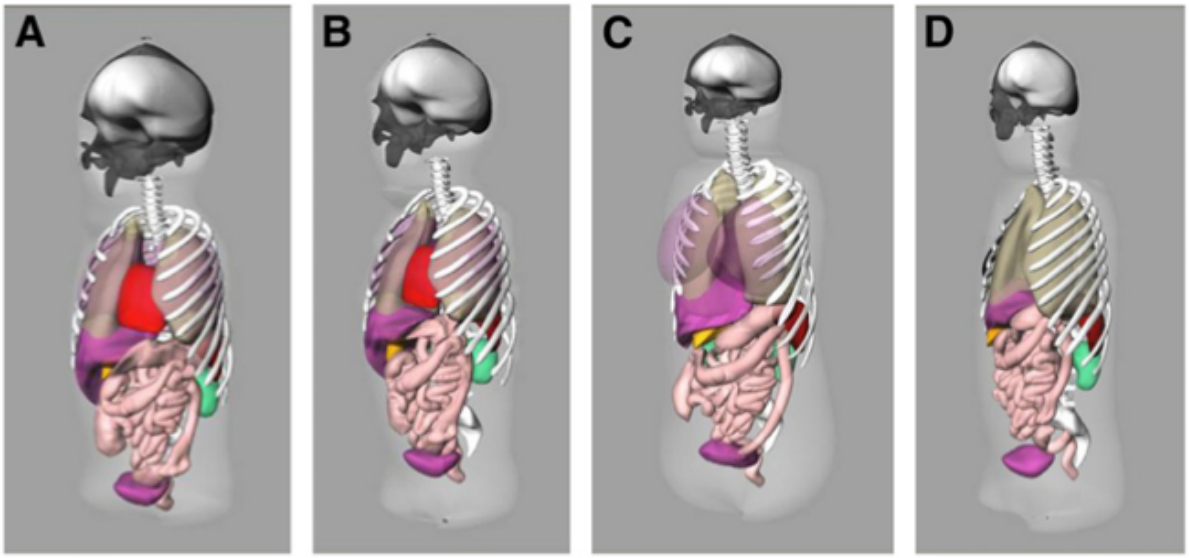

Figure 2.6: NCAT NURBS phantoms: newborn female model (A), 5-year-old male model (B), 10-year-old female model (C), and 15-year-old male model (D) (Stabin et al., 2012).

The first BREP phantom, the NURBS-based Cardiac-Torso phantom (NCAT) was developed using Visible Human CT image data sets. Manually-segmented structures were converted to smooth polygon contours that were fit to cubic NURBS surfaces. The 3D anatomy was later extended into 4D time-dependent models (4D NCAT) to simulate cardiac and respiratory motions. The beating heart model was produced from 4D tagged MRI data from a real patient (4D NCAT). Respiratory models were created from respiratory-gated CT data (Segars and Tsui, 2002; Segars et al., 2003, 2007).

Stabin et al. (2012) developed a family of adult and pediatric reference phantoms using

ICRP 89 values for body and organ masses. The NURBS-based original NCAT adult male and female phantoms (Segars, 2001) were adapted to create a series of reference pediatric ages (the same ages as the Cristy-Eckerman series) for both genders. (Figure 2.6).

Segars later updated the NCAT phantom to produce an extended version of the NCAT known as the XCAT phantom (Segars et al., 2008). While the original NCAT phantom contained hundreds of organs and structures (mainly within the torso region of the body), the updated XCAT phantom which contains thousands of organs and structures including detailed brain, nervous, and vascular models (Segars et al., 2010). Body and organ mass values for a 50th-percentile male and female were defined according to ICRP Publication 89 (Valentin, 2002).The XCAT phantoms are the most detailed and anatomically and physiologically realistic anthropomorphic phantom models to date, and these have been used by many researchers to simulate and predict radiation dose.

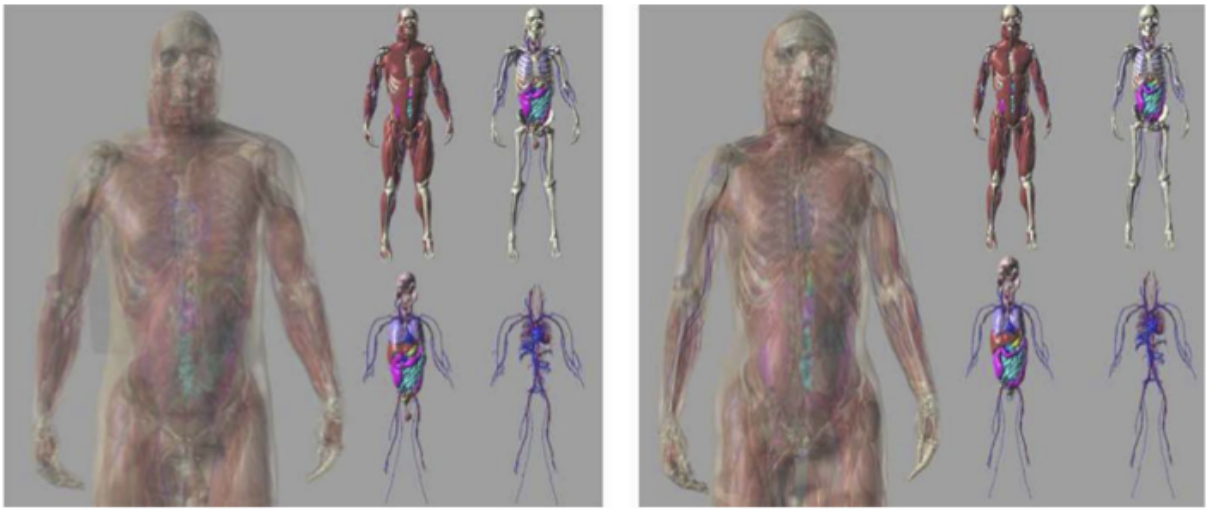

Figure 2.7: The muscles, skeleton, organs, and circulatory system are shown for both male (left) and female (right) anatomies of the extended NCAT or "XCAT" phantom. The whole body models are built from different levels of detail are shown with transparency (Segars and Tsui, 2009).

2.2.3.2 BREP Phantom CT Applications

Li et al. (2008) calculated organ and effective dose values by simulating a 64-slice GE LightSpeed VCT scanner for chest scan protocols. They developed full-body models of seven pediatric patients using multi-detector CT data, in which organs and structures in the scan range were manually segmented. Other organs were created by scaling existing ICRP 89 adult models. Three-dimensional polygon models were then generated for each structure, and three-dimensional NURBS surfaces were fit to the polygon models. Organ volumes for each pediatric model were made to match age-interpolated organ data in ICRP Publication 89. Using the same process, additional patient-specific models for a 5-week-old female patient and a 12-year-old male patient were subsequently added in Li et al. (2011c) (see also, Li et al., 2011a,b).

The University of Florida group has created a series of hybrid phantoms for use in CT applications. Hybrid 15-year-old male and female phantoms were developed from the UF 14-year-old male voxel phantom along with CT data of 15-year-old female subjects. The 50th weight-percentile hybrid 15-year-old male and females were named $UFH15M_{50}$ and $UFH15F_{50}$, respectively. These were built to represent ICRP 89 reference anatomy, and a total of eight anthropometric parameters were matched to standard values within an error of 4%. The UF group has also generated a range of weight-percentile phantoms from 10th to 90th percentile by using the 50th weight-percentile phantoms as a template. These phantoms have been used to simulate chest and abdomen CT exams to estimate doses using three male and female 15-year-olds for 120 kVp (Lee et al., 2008).

Chapter III

MONTE CARLO RADIATION TRANSPORT CODE

Using the GEANT4 Monte Carlo toolkit (Agostinelli et al., 2003; Allison et al., 2006), a radiation transport code to simulate patients undergoing exams on a CT scanner similar to that at Monroe Carrell, Jr. Children's Hospital at Vanderbilt has been created. Measured values of dose from both ionization chamber measurements as well as optically-stimulated-luminescent (OSL) technology in physical phantoms were used to calibrate and validate the simulated output from the GEANT4 CT code. The focus of this chapter is on the validation of this simulation with real-world physical dosimetry measurements, using two independent techniques. Exposure measurements were made with a standard 100-mm CT pencil ionization chamber, and absorbed doses were also measured using optically-stimulated-luminescent (OSL) dosimeters. Measurements were made in air, in a standard 16-cm acrylic head phantom, and in a standard 32-cm acrylic body phantom. Physical dose measurements determined from the ionization chamber in air for 100 and 120 kVp beam energies were used to derive photon-fluence calibration factors. Both ion chamber and OSL measurement results provide useful comparisons in the validation of the Monte Carlo simulations.

3.1 Introduction to GEANT4

GEANT4 (Agostinelli et al., 2003; Allison et al., 2006) is an open source, integrated software package that allows simulation of radiation transport for many particle types

and many irradiation geometries. The toolkit provides a complete set of tools for all areas of detector simulation including geometry, tracking, physics models, and run and event management. The code includes all relevant physical processes governing particle interactions, stores and tracks event data, and permits the scoring of deposited energy and dose in selected target regions. The user must specify the specific characteristics of their simulation such as the detector geometry, materials, particles, physics processes, and primary events generation. A summary of all aspects of the simulation process included in the toolkit are listed below:

- Geometry of the system
- Materials of interest
- Fundamental particles of interest
- Generation of primary events
- Particle tracking through materials and fields
- Physics processes governing particle interactions
- Detector response
- Event data and storage
- Detector and particle trajectory visualization.

At the heart of GEANT4 is an abundant set of physics models to handle the interactions of particles with matter across a very wide energy range (Agostinelli et al., 2003).

Multifaceted detector geometries can also be user-defined, making it straight-forward to execute dose calculations using voxelized phantoms. A comprehensive description of the physics employed can be found in the Physics Reference Manual (Geant4 Collaboration et al., 2007).

3.1.1 Particle Tracking and Step Size

In Monte Carlo simulation, there is a balance between optimizing performance and preserving tracking precision for particle transport. The chief limiting factor is the amount of CPU time spent moving the particle in one step. For the GEANT4 code, particles are transported, and tracking is independent of particle type or physics process. There is a defined step for each physics process, and the maximum step is set as the smaller of two quantities: the maximum allowed step stipulated by the user or the step-size defined by the actions of all physical processes modeled.

During a step, each physical process may take one or more actions, categorized by where the action occurs, including:

- At rest—for particles at rest (particle decay)
- Along step—for actions that occur continuously along a step (energy loss or secondary particle production)
- Post step—invoked at the end of the step (secondary particle production by decay or interaction).

A particle in passage experiences many competing processes that limit the step-size invoked. The distance the particle travels to the point of interaction or decay limits

the step-size, or continuous energy loss may limit the step to preserve precision. In a real detector, a particle will regularly travel through many regions of different materials, shapes, and sizes before interacting or decaying, without crossing a detector boundary during a step. An efficient way of determining which process limits the step-size must be determined by the simulation, and parameters must be updated for the next step (if the particle continues).

The mean-free path (λ) determines the distance to interaction for a given process and is a function of the particle energy. It is expressed in terms of the total cross section:

$$\lambda(E) = \left(\sum_i n_i \cdot \sigma(Z_i, E) \right)^{-1}. \tag{3.1}$$

where n_i is the number density of the i^{th} element of the material, $\sigma(Z, E)$ is the total cross-section per atom of the process, and the sum is over all elements in the interaction material.

The mean-free path is material-dependent; therefore, it cannot be used to sample the probability of interaction in a heterogeneous medium. The number of mean-free paths the particle travels is, however, independent of the material. This is given by:

$$n_\lambda = \int_{x_1}^{x_2} \frac{dx}{\lambda(x)}. \tag{3.2}$$

If one assumes that a random variable (n_r) represents the number of mean-free paths the particle travels before interacting, then the distribution function of n_r would be:

$$P(n_r < n_\lambda) = 1 - e^{-n_\lambda}. \tag{3.3}$$

The distance to the point of interaction, $s(x) = n_\eta \cdot \lambda(x)$, is sampled by using a random number (η) uniformly distributed in the range (0,1) to determine n_λ:

$$n_\lambda = -\log(\eta). \tag{3.4}$$

The process that returns the smallest distance is chosen, and its post-step action is performed. If the post-step action is an interaction or decay, the particle is terminated; secondary particles are then generated and tracked. Otherwise, the particle has another opportunity to decay or interact. The amount of mean-free paths for each process is shrunk by an amount corresponding to the step length. The whole procedure is then repeated for the next step.

The aforementioned algorithm operates under the assumption that the cross-sections remain constant over the step, but charged-particle cross-sections vary due to continuous energy loss. Consequently, GEANT4 has adopted an integral approach to charged-particle processes including ionization and bremsstrahlung. The reaction probability (p) is sampled from:

$$p = 1 - \exp\left(-\int_{E_i}^{E_f} n\ \sigma(E) ds\right). \tag{3.5}$$

where E_i is the particle energy at the beginning of the step, and E_f is the energy at the end of the step.

The simulation tracks charged particles to the end of their range, but in order to optimize computation time and performance, there is a range cut for tracking secondary particles. Particles that have a range less than a user-defined value are suppressed, and

the energy of the particle is added to the energy deposited during or at the end of the step.

The use of a cut is an absolute necessity for bremsstrahlung in order to suppress a large amount of soft electrons and photons. Charged particles can be completely stopped in matter, so the use of a range cut is natural. The range cut for photons is approximated from the absorption cross-section, which is the sum of the cross-sections for the "destructive" processes for photons such as gamma conversion, Compton scattering, and photoelectric effect. The range cut is defined for each material as the absorption length for the minimum absorption cross-section, specified by:

$$L_{\text{abs}} = \frac{5}{\sigma_{\text{abs}}}. \tag{3.6}$$

A factor of 5 means that very few ($e^{-5} = 0.7\%$) of the suppressed photons generated at the cut energy should survive the absorption length.

3.1.2 Dose Calculations

The GEANT4 Monte Carlo radiation transport toolkit allows investigation of radiation doses for many different types of individuals that could undergo CT examinations. Using this tool, a plethora of individuals of various ages, body weights, and statures may be modeled. Specific organ doses for these models will be calculated, and effective doses will be assessed using recommended tissue weighting factors from ICRP 103 (2007).

3.2 Development and Validation

In order to accurately estimate the risks from CT scans, one must be able to know the absorbed dose to each individual radiosensitive organ to determine effective dose (ICRP 60, 1991; ICRP 103, 2007). While there are methods to estimate effective dose from DLP (AAPM Report 96 2008), estimating individual organ doses relies on Monte Carlo simulations. There have been many endeavors to calculate organ and effective dose from CT exams using computational methods, (e.g., Jarry, 2002; Jarry et al., 2003; DeMarco et al., 2005, 2007; Lee et al., 2007, 2008; Li et al., 2011a,b,c). These groups have validated their Monte Carlo methods against ionization chamber measurements in both cylindrical as well as anthropomorphic phantoms. The work here applies similar validation methods using ionization chamber measurements to compare against OSL dosimeters (Landauer, Inc., 2006).

3.2.1 Simulation of the CT Scanner

The detector geometry in the simulation consists of a nested parameterized 3D volume. One significant advantage of nested parameterization is the ability to assign each voxel unique material properties and chemical compositions. Energy deposition due to each primary event, including any secondary particles generated, is tallied for each voxel in the parameterized volume. Once all events are tracked, the simulation produces a map of total energy deposited that is used to create a 3D dose map to quantify the dose distribution within a particular region.

The parameterized 3D volume containing the voxels is positioned flush to an exam

table. The physical exam table at Monroe Carrell, Jr. Children's Hospital at Vanderbilt was measured for size and thickness and modeled in the simulation geometry as a trapezoid with a thickness of 3 mm and height of 9 cm. The long and short sides measure 42 and 22 cm, respectively.

GEANT4 requires the user to define the particle type, position and direction vectors, and initial energy for each primary event. Primary photons must be generated to represent accurately the X-ray energy spectrum, bowtie filtration, and source-to-isocenter geometry of the CT scanner. Source energy spectra were obtained for nominal beam energies typically used in pediatric protocols (100 and 120 kVp) and implemented in the simulation as look-up tables. A detailed description of the CT source model follows.

To model accurately the CT scanner under consideration, comprehensive descriptions of the scanner properties including its photon energy spectrum, inherent and bowtie filtration, and geometry are necessary. However, scanner-specific descriptions are normally proprietary and difficult to obtain without non-disclosure agreements. To overcome this limitation, numerous physical measurements were taken, and the methods of Turner et al. (2009) were employed to generate an equivalent energy-fluence source model for the specific CT scanner in the simulation. The fluence model also includes the effects of the body bowtie filter that provides X-ray filtration across the transverse direction of the patient to account for variations in body thickness.

All X-rays originate at the focal spot with energies determined by sampling the equivalent spectra across the bowtie filter. These photons are given initial direction vectors to populate each angle in the fan beam with relative weights determined by the measured bowtie filter attenuation profile (Figure 3.3. It was assumed that the particle fluence was

uniform in the scan direction, and photons are assigned uniformly random axial direction components. The full-width-half-max (FWHM) beam width measured at isocenter was used to define the beam collimation. The CT head moves in one-degree increments with 100,000 primary photons generated at each angle. The x-ray source rotates and translates helically based on a user-defined pitch until the entire range of the scan is complete. A detailed description of the measurements required to generate equivalent spectra for this specific CT scanner is provided in the following section.

3.2.2 Equivalent CT Source Modeling

A third generation multi-detector array CT scanner (Philips Brilliance 64, Philips Healthcare, Andover, MA) with 64 rows of detectors of 0.625 mm each was modeled. X-ray beam collimations available for this particular scanner include 2×0.625 mm, 12×0.625 mm, 16×0.625 mm, and 64×0.625 mm. These beam collimations are reported as nT, where n is the number of detector elements, and T is the width of each detector element. The Philips Brilliance 64 has a source-to-isocenter distance of 57 cm and a source-to-detector distance of 104 cm.

3.2.2.1 HVL Measurements

To quantify the photon beam hardness and energy spectrum, it was necessary to perform half-value-layer (HVL) measurements of the photons coming out of the face of the collimators. These measurements are essential to determine the inherent and bowtie filtration properties for the scanner. The gantry was parked so that the X-ray tube remained stationary at the 6 oclock position. The ion chamber remained stationary and

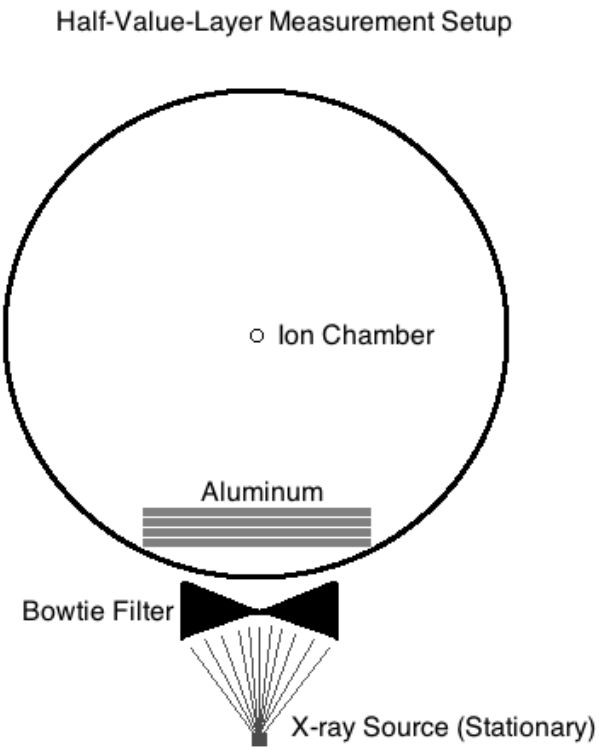

Figure 3.1: Setup for the half-value-layer (HVL) measurements. The scanner gantry was parked with the X-ray tube at the 6 oclock position. Thin sheets of aluminum were stacked vertically as exposure readings were made.

fixed at isocenter along the central axis directly above the X-ray tube. The table was not in the beam path. As for any HVL measurements, an initial exposure without filtration was obtained first. Thin sheets (1.0 mm) of type-1100 high-purity aluminum were added as repeated exposure measurements were taken until the reading was less than half of the initial value. Then all sheets were removed, and another measurement without filtration was taken as a check. Figure 3.1 shows the HVL measurement setup.

3.2.2.2 Equivalent Spectrum Generation

Using Boone and Seiberts tungsten anode spectral model of interpolated polynomials (TASMIPs) (Boone and Seibert, 1997), an initial soft tungsten spectrum was obtained for 100 kVp and 120 kVp without added filtration and with zero percent voltage ripple. A detailed explanation of the method to obtain an equivalent spectrum is provided in Turner et al. (2009). Briefly, (1) the initial soft tungsten spectrum is transmitted through a very thin and uniform sheet of hardening material. Aluminum was chosen for these purposes. Assuming exponential attenuation, this produces a candidate spectrum. (2) The candidate spectrum is transmitted through the central ray of the bowtie filter, and the air KERMA is calculated. (3) The resulting transmitted spectrum is next transmitted through a very thin and uniform sheet of aluminum, and the air KERMA is calculated again. (4) The third step is repeated iteratively while increasing the thickness of aluminum by 1 micron until the air KERMA is one-half of the initial air KERMA value in the second step. Photon mass-attenuation coefficients (μ/ρ) and mass energy-absorption coefficients (μ_{en}/ρ) (Hubbell and Seltzer, 2004) were used to perform exponential attenuation and KERMA was calculated as

$$\text{KERMA} = \Psi \left(\frac{\mu_{\text{en}}}{\rho} \right), \tag{3.7}$$

where Ψ (J m^{-2}) is the energy fluence of photons passing through the area of the absorbing material, and (μ_{en}/ρ) is the mass energy-absorption coefficient for mono-energetic photons. The total air KERMA of a spectrum was calculated by summing over all energies as

$$\text{KERMA}_{\text{total}} = \sum_i n_i \Psi_i \left(\frac{\mu_{\text{en}}}{\rho} \right)_i , \tag{3.8}$$

where n_i is the number of photons in each bin, Ψ_i is the corresponding energy fluence, and $(\mu_{\text{en}})/\rho)_i$ is the mass energy-absorption coefficient for each energy, i.

3.2.2.3 Bowtie Filter Profile Measurements

The Philips Brilliance 64 has a single bowtie filter that was modeled by following the procedure in Turner et al. (2009). Measurements of the bowtie filter profile were used to determine the real spectrum's attenuation across the photon beam due to the bowtie geometry and filtration. The gantry was parked with the tube in the 3 o'clock position in order to eliminate attenuation due to the exam table. The ion chamber was clamped to a ring stand, and exposure measurements were taken every 1 cm, starting at isocenter, by incrementally moving the table up in order to determine the attenuation in exposure from bowtie filter center to edge. Measurements were taken for the upper half of the bowtie filter, and it was assumed symmetric about the central axis (Figure 3.2).

Using this attenuation profile (Figure 3.3), the bowtie-filter path length as a function of distance across the bowtie filter (transverse direction) was determined iteratively (Turner et al., 2009). All routines were coded in MATLAB R2012b (MathWorks, Inc., 2012). This was done for each equivalent spectra determined in the previous section.

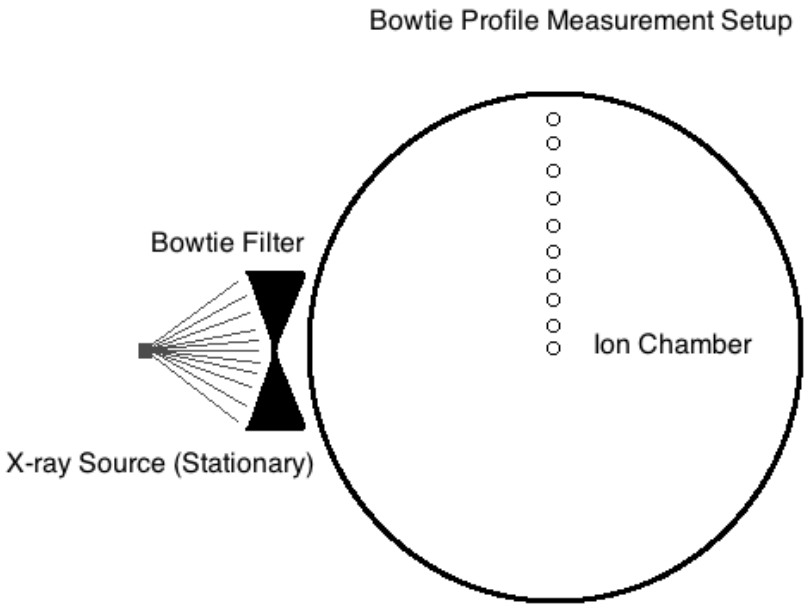

Figure 3.2: Experimental setup for measurements of the bowtie filter attenuation profile. The CT scanner gantry was parked with the X-ray tube at the 3 oclock position. Exposure readings were made every 1 cm across the filter starting at isocenter moving toward the edge of the filter.

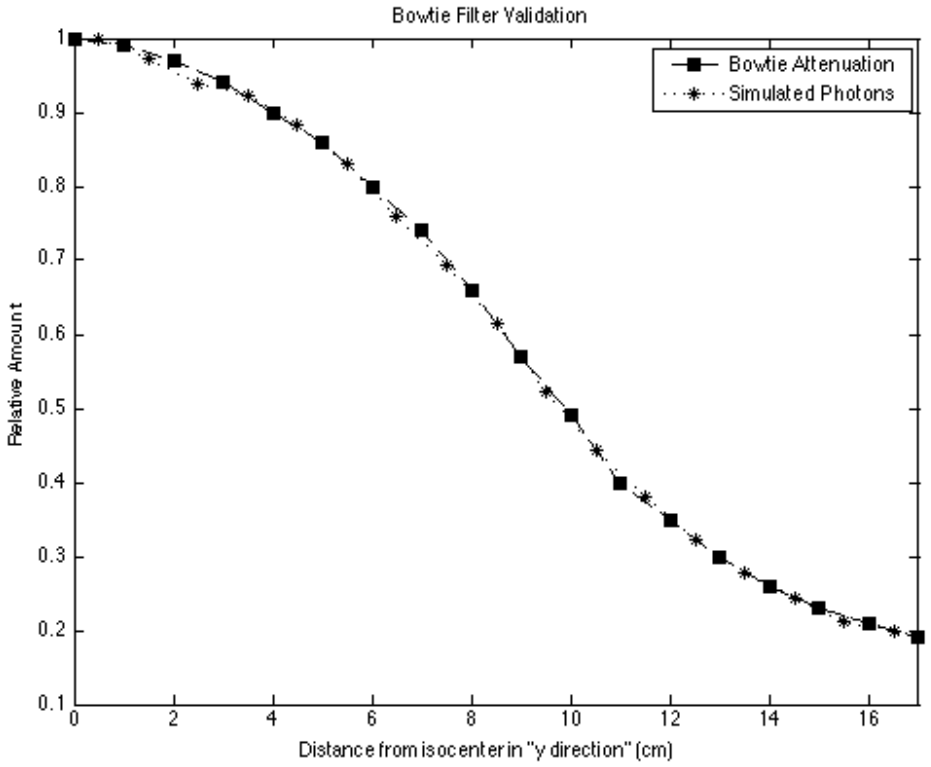

Figure 3.3: The measured bowtie filter attenuation profile as a result of ionization chamber measurements made every 1 cm moving away from the central ray is plotted with photons generated by the simulation. Simulated photon positions are binned according to their path lengths as a function of their distances relative to the central ray at isocenter. Attenuation measurements are plotted according to bin edges, whereas simulated photons are plotted at bin center.

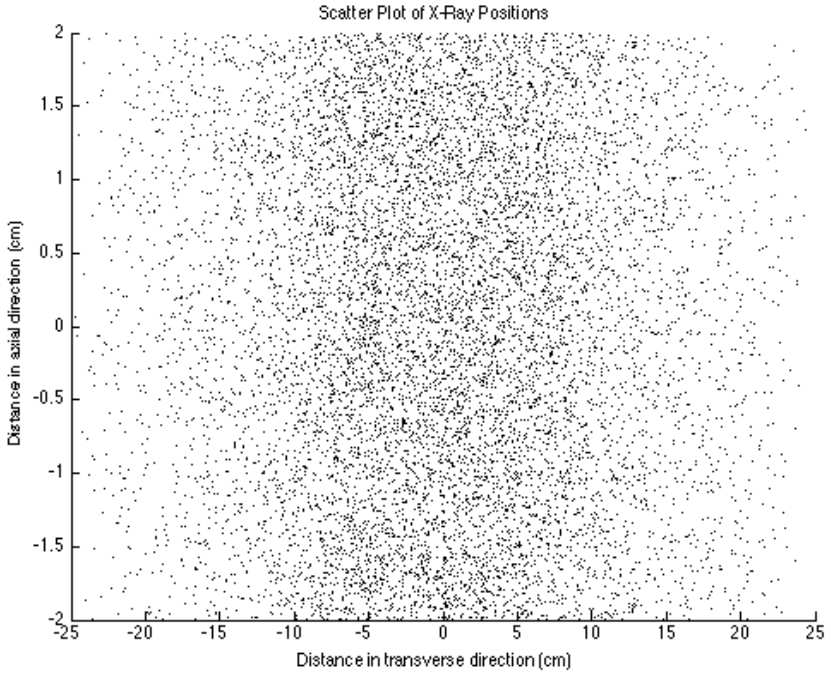

Figure 3.4: The spatial distribution dependence of source photons at system isocenter is shown. The transverse direction demonstrates the bowtie filter dependence in the spatial distribution. The axial direction is across the the face of the collimators. The direction toward the simulated phantom or patient would be into the page.

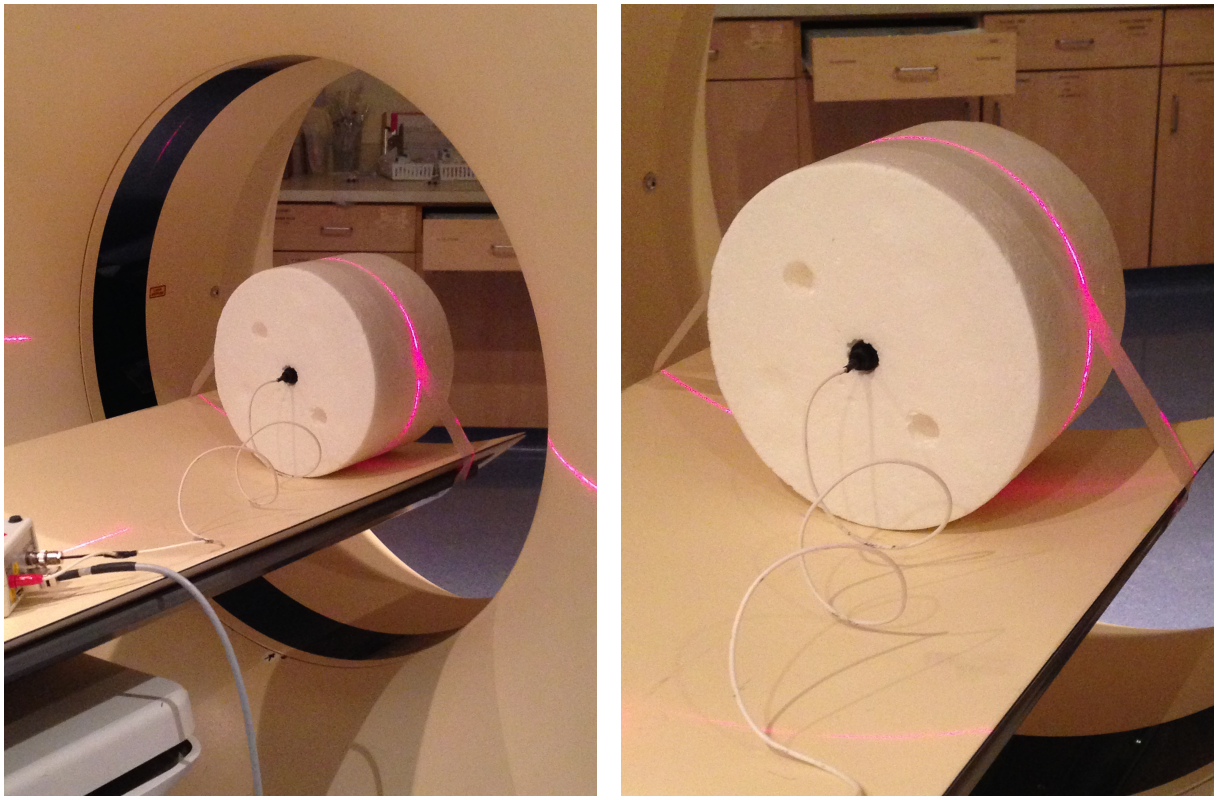

Figure 3.5: Experimental setup for measuring CTDI in air.

3.2.3 Experimental Measurements

3.2.3.1 CT Pencil Ionization Chamber Measurements

A standard 100-mm long CT pencil ionization chamber (Fluke Biomedical Model 8000 chamber with NERO Max, Fluke Biomedical, Everett, WA) was used to take exposure measurements in air (Figure 3.5), as well as in 16-cm and 32-cm acrylic CTDI dose phantoms at isocenter for center and peripheral (12 o'clock) positions. Measurements were collected for 100 and 120 kVp at 300 mAs. At least three unique measurements were made for each energy, mAs, and collimation combination. The average of these exposure readings was used for purposes of calculating the dose to the chamber. These were converted to standard computed-tomography dose indices ($CTDI_{100}$) following AAPM

Report 96 (McCollough et al., 2008). These were calculated as:

$$\mathrm{CTDI}_{100} = \frac{f \times C \times L \times X}{nT}, \tag{3.9}$$

where f is the exposure-to-dose conversion factor for air (8.7 mGy R^{-1}), C is the chamber calibration factor (0.31 for the chamber used here), L is the active length of the pencil ionization chamber (100 mm), X is exposure in R, n is the number of detector elements, and T is the size of a detector element.

3.2.3.2 Simulations in Air, 16-cm, and 32-cm Dose Phantoms

Next, CTDI measurements were modeled in the Monte Carlo simulation. A thin-walled ionization chamber was constructed from manufacturer specifications. For this particular model of ion chamber, the wall is made of Poly(methyl methacrylate) (PMMA, $(\mathrm{C_5O_2H_8})_n$). The chamber's active volume is 10.1 cm^3 with a sensitive length of 10.0 cm. The chamber outside diameter measures 12.7 mm $\pm$ 0.4 mm, and the chamber inside diameter is 11.44 mm. To model the chamber in the simulations, an inner diameter of 11.5 mm and outer diameter of 12.5 mm were used. Each voxel measured $0.5 \times 0.5 \times 2.5\mathrm{mm}^3$. The PMMA dose phantom itself and the air in the active chamber volume were identified as separate regions. Energy deposited into the air chamber was scored in the simulation and used to calculate simulated dose.

All physical densities and elemental compositions of the materials modeled in this system geometry were taken from NIST database definitions (Coursey et al., 2010) (Table IV.1). PMMA was used to model the CTDI acrylic dose phantoms in the simulations.

Table III.1: Summary of materials used in the Monte Carlo simulation model. Material compositions are reported from the NIST database (Coursey et al., 2010).

Material	Density (g cm^{-3})	Chemical Composition (% by mass)				
		H	C	N	O	Elements Z >8
Air	1.20×10^{-3}		0.012	75.53	23.18	Ar (1.28)
Exam Table	2.27		100			
PMMA	1.19	8.05	59.99		31.96	

The exam table was modeled as pure carbon composition, as the exact chemical composition was considered proprietary information. The composition of air was used for both surrounding outside air in the simulation as well as the air in the modeled ionization chamber.

3.2.4 Monte Carlo Normalization Factor

The real $CTDI_{100}$ measurements in air were compared to the simulated $CTDI_{100}$ values in air to derive normalization factors for 100 and 120 kVp at a nominal beam collimation of 64×0.625 mm (40 mm). The Monte Carlo normalization factor, K, as a function of energy is described by:

$$K_E = \frac{D_{\text{air,measured}_E}}{D_{\text{air,simulated}_E}}. \tag{3.10}$$

3.2.5 Measurements Reported by OSL Dosimeters

Several linear arrays of optically-stimulated-luminescence (OSL) dosimeters manufactured by Landauer, Inc. (Landauer, Inc., 2006) were exposed. The dosimeter material is housed in a black polycarbonate case, and the length of the OSL strip inside is 150 mm long and 0.4 mm thick. The dosimeter material is a polymer substrate of aluminum oxide

doped with carbon (Al_2O_3:C). According to the manufacturer, these OSL dosimeters can measure radiation doses of 0.01 mGy or less, and less than 0.2% of the signal is erased when a dosimeter is read (Landauer, Inc., 2006).

3.3 Results

The measured HVL on the Philips 64-slice Brilliance scanner was 7.6 ± 0.2 mm of Al for 100 kVp and 9.0 ± 0.2 mm of Al for 120 kVp. The measured bowtie filter attenuation profile at system isocenter is shown in Figure 3.3, and a sample of the spatial distribution dependence of photons is shown in Figure 3.4.

3.3.1 CTDI Measurements

The measured and simulated $CTDI_{100}$ in air at isocenter for a single axial scan taken at 100 and 120 kVp and 300 mAs are presented in Table III.2. $CTDI_{100}$ center values were calculated using Equation 3.9. Normalization factors were derived by taking the ratio of the measured dose to the simulated dose in air for each nominal kVp. In the present study, only one nominal beam collimation of 64×0.625 mm (40 mm) was considered. The normalization factors were used to convert the dose simulated to absolute absorbed dose for 100 and 120 kVp for this particular beam collimation.

As mentioned in the previous section, the simulated CT X-ray source moves in one-degree increments with 100,000 primary photons per step. Multiple simulations were performed and achieved overall relative errors of 0.5% or less in the specified detector regions in the simulation. To obtain the total error in the normalization factors and CTDI values, error from the simulation was propagated with the manufacturer-specified

Table III.2: Measured and simulated $CTDI_{100}$ in air at isocenter and derived Monte Carlo normalization factors are reported for 100 and 120 kVp for a nominal beam collimation of 40 mm.

Energy (kVp)	Measured $CTDI_{100}$ in air (10^{-2} mGy mAs^{-1})	Simulated $CTDI_{100}$ in air (10^{-2} mGy mAs^{-1})	Normalization factor (10^{10} particle mAs^{-1})
100	8.47 ± 0.42	2.17 ± 0.0067	3.91 ± 0.20
120	13.7 ± 0.68	2.32 ± 0.0074	5.91 ± 0.30

5% error in the ion chamber measurements.

The results of the $CTDI_{100}$ measurements and simulations are presented in Table III.3 for 100 kVp and Table III.4 for 120 kVp. Differences on the order of < 10 μGy mAs^{-1} are observed. The uncertainties in the ionization chamber measurements are reported at the level of 5%, according to the manufacturer. Errors on the simulated values are reported as the Monte Carlo associated relative error of each particular detector region in the simulation.

Table III.3: Comparison of $CTDI_{100}$ measurements from the ion chamber to simulated CTDI values in GEANT4 at a nominal tube voltage of 100 kVp for a nominal beam collimation of 40 mm.

Phantom	Center Position		
	Ion chamber $CTDI_{100}$ (10^{-2} mGy mAs^{-1})	Simulated $CTDI_{100}$ (10^{-2} mGy mAs^{-1})	Difference (10^{-2} mGy mAs^{-1})
16-cm head	6.3 ± 0.32	6.2 ± 0.31	-0.1
32-cm body	2.0 ± 0.10	2.4 ± 0.12	0.4

Results for $CTDI_{100}$ measurements from the OSL dosimeters and the ionization chamber are reported in Table III.5 for 100 kVp and Table III.6 for 120 kVp. The observed differences were also compared to previous differences observed by other authors. For 120 kVp, the percent differences observed are on par with those observed by Vrieze et al. (2012) and observed to be approximately less than 10% in the majority of cases. The OSLs appear to show some under response in the air-only and peripheral measurement cases, but tend to overestimate dose when compared to the ion chamber in the center regions. However, for 100 kVp, there was a tendency for over response in all cases, but unfortunately, there were not other previous results to compare to for 100 kVp. It should be noted that these measurements were not intended as an exhaustive comparison study of OSL versus ionization chamber measurements. The values reported by other authors are intended as a descriptive tool to compare to observed results.

3.3.2 Dose Profiles

The OSL dose profile reported by the manufacturer in air at 120 kVp and 300 mAs allowed direct measurement of the realistic beam width including effects of geometric

Table III.4: Comparison of $CTDI_{100}$ measurements from the ion chamber to simulated CTDI values in GEANT4 at a nominal tube voltage of 120 kVp for a nominal beam collimation of 40 mm.

	Center Position		
Phantom	Ion chamber $CTDI_{100}$	Simulated $CTDI_{100}$	Difference
	(10^{-2} mGy mAs^{-1})	(10^{-2} mGy mAs^{-1})	(10^{-2} mGy mAs^{-1})
16-cm head	10.4 ± 0.52	9.7 ± 0.49	-0.7
32-cm body	3.6 ± 0.18	4.1 ± 0.21	0.5

Table III.5: Results of CT OSL and ion chamber $CTDI_{100}$ measurements for a tube potential of 100 kVp at 300 mAs. Percent differences are reported as $(CTDI_{OSL} - CTDI_{\text{ion chamber}})/CTDI_{\text{ion chamber}} \times 100$.

Phantom	Center Position		
	Ion chamber $CTDI_{100}$ (mGy)	OSL $CTDI_{100}$ (mGy)	Percent difference mean $CTDI_{100}$ values (%)
16-cm head	18.9	21.3	12.7
32-cm body	6.1	6.7	9.8
	12 o'clock Position		
16-cm head	22.0	24.8	12.7
32-cm body	11.5	11.0	-4.3

unsharpness. The actual beam width was found to be 42.1 mm, slightly larger than the nominal beam width of 40 mm. The actual beam width in the simulations was modeled using this knowledge.

Figure 3.6a shows the dose profile in air modeled for the 100 kVp spectra, and Figure 3.6b illustrates the comparison between the 120 kVp OSL profile in air and the simulated profile in air, allowing confirmation that the beam widths indeed match. The discrepancy of the dose magnitude between the OSL and GEANT4 profile is due to the difference in the reported dose in air, with the OSL underreporting dose compared to the ion chamber. The ionization chamber-measured values were used as the standard in the derivation of the normalization factors. The discussion section also assesses the observed discrepancies between OSL and ion chamber values.

Figures 3.7 and 3.8 illustrate the results for the 16-cm head and 32-cm body phantoms for dose profiles at the center position in the phantoms. The dose profiles from the OSL dosimeter measurements taken in those regions, as reported by the manufacturer, are

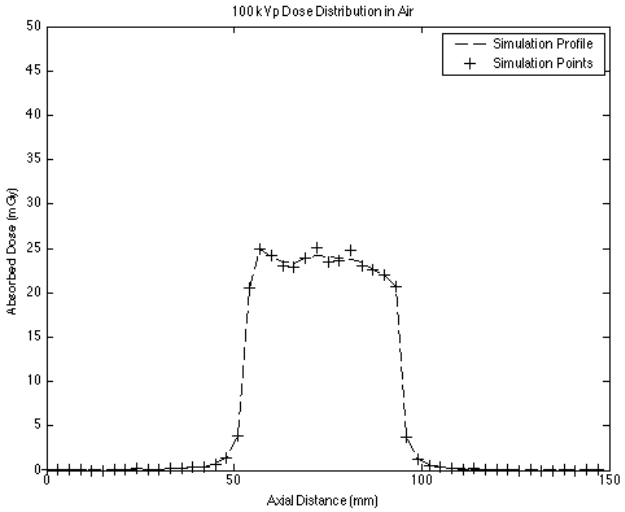

(a) 100 kVp

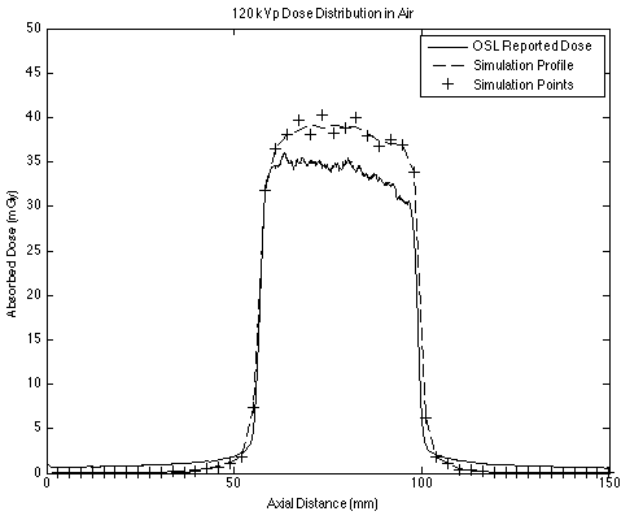

(b) 120 kVp

Figure 3.6: Simulated dose distributions in air for (a) 100 kVp and (b) 120 kVp, at 300 mAs. The distribution for 120 kVp also shows the dose profile obtained from an OSL dosimeter exposed in air at 120 kVp. The comparison between the two methods provides confirmation of the match between the observed beam width (42.1 mm) and the beam width generated from simulation.

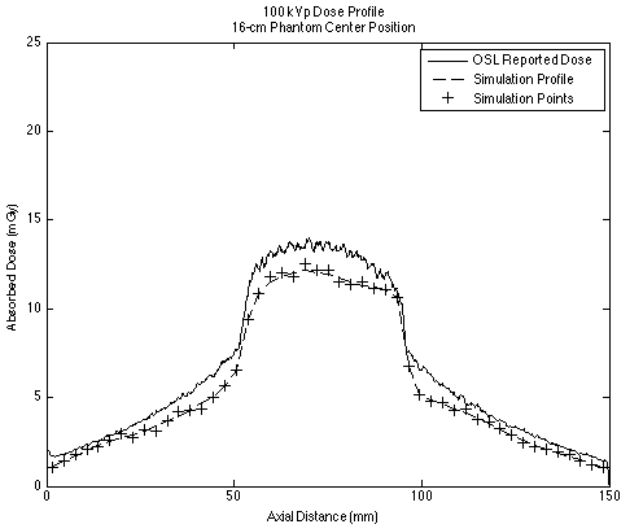

(a)

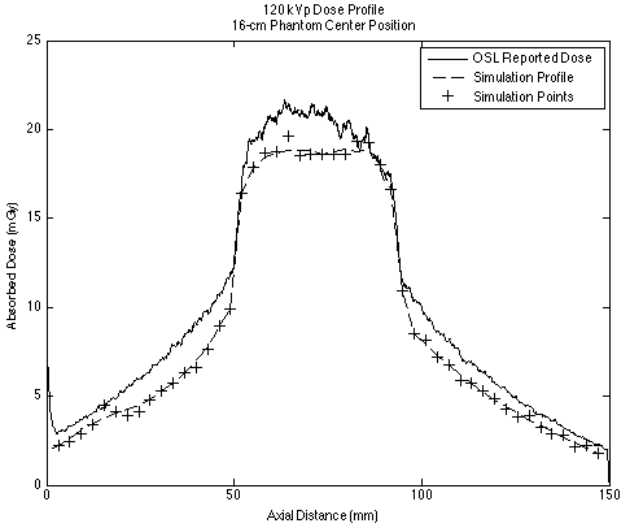

(b)

Figure 3.7: (a) The dose profile for the 16-cm CTDI phantom results for 100 kVp at the center position, and (b) shows the dose profile for the 16-cm CTDI phantom results at 120 kVp. The dose profile obtained from the OSL dosimeter reported by Landauer is shown as a solid black line, the simulation data points from GEANT4 are shown as plus signs, and the smoothed GEANT4 profile is shown as a dashed black line.

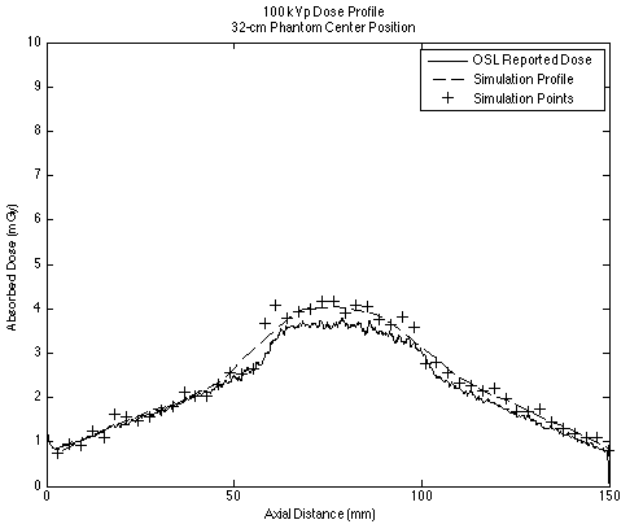

(a)

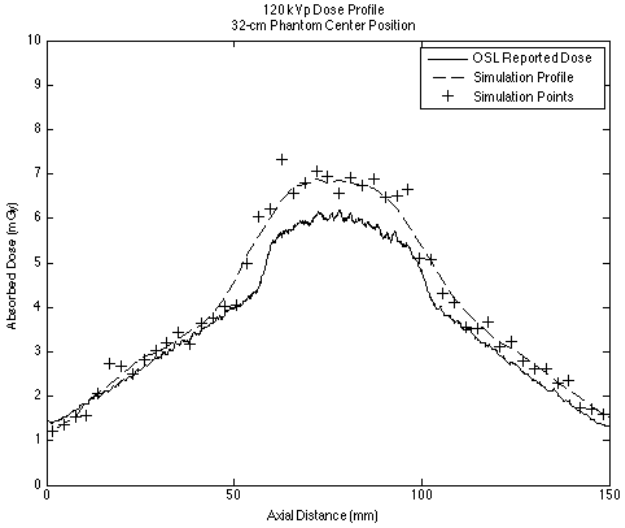

(b)

Figure 3.8: (a) The dose profile for the 32-cm CTDI phantoms at the center position for 100 kVp, and (b) shows the dose profile in the 32-cm phantom center case for 120 kVp. The dose profile obtained from the OSL dosimeter reported by Landauer is shown as a solid black line, the simulation data points from GEANT4 are shown as plus signs, and the smoothed GEANT4 profile is shown as a dashed black line.

Table III.6: Results of CT OSL and ion chamber $CTDI_{100}$ measurements for a tube potential of 120 kVp at 300 mAs. Percent differences are reported as $(CTDI_{OSL} - CTDI_{\text{ion chamber}})/CTDI_{\text{ion chamber}} \times 100$. Vrieze *et al.* (2012) percent differences are reported for a beam width of 28.8 mm.

Phantom	Center Position			
	Ion chamber $CTDI_{100}$ (mGy)	OSL $CTDI_{100}$ (mGy)	Percent diff mean $CTDI_{100}$ values (%)	Vrieze *et al.* (2012) percent diff (%)
None (in air)	41.0	37.8	-7.8	-9.9
16-cm head	31.2	33.0	5.8	3.6
32-cm body	10.7	11.1	3.7	10.4
	12 o'clock Position			
16-cm head	34.5	35.2	2.0	-5.5
32-cm body	18.7	17.3	-7.5	-5.0

plotted on top of the dose profiles obtained from the model simulation.

3.4 Discussion

The GEANT4 simulation environment is very flexible and has been extensively verified. It has been used previously to simulate internal sources of radiation (Stabin et al., 2012); its use for external radiation sources, particularly to simulate a CT scanner, has been demonstrated by others as well as other medical physics applications (e.g., Archambault et al., 2003; Carrier et al., 2004; Jiang and Paganetti, 2004). Shown here is a simulated CT source modeled after a Philips Brilliance 64, with a bowtie filter. The actual spectral data from the manufacturer was not able to be obtained, so a reasonable X-ray spectrum was modeled based on methods from the literature and experimental data. The simulated X-ray spectrum showed excellent agreement (differences of < 10 μGy mAs^{-1}) with the independently measured ionization chamber results.

Simulations were calibrated against ion chamber measurements in acrylic phantoms. The ion chamber measurements and simulation results show reasonable agreement with an overall average percent difference of 6% in the CTDI values. For both nominal kVp values, the simulated CTDI values tend to overestimate the measured CTDI values in the 32-cm body phantom. However, for the 16-cm head phantom, the simulated CTDI values tend to under-predict the measured values slightly. Some differences between the simulation and real-world measurements could be due to inaccuracies in the X-ray spectra, filtration, and geometry modeled. Also, beam hardening in the simulated spectra may be responsible for these observed results. Uncertainties in the geometry and modeling of the table material could be contributing factors, as there is non-negligible attenuation through the table. There may be differences between the simulated and measured results due to the ideal assumption of using point-source geometry in the Monte Carlo simulation. Focal-spot size was not taken into account when modeling the CT source. Despite these sources of error, there is acceptable agreement between the measured and simulated results in order to validate the model.

Random errors in the simulated dose may have contributed to the differences observed as well as uncertainty in the normalization factors used to calculate dose. The normalization factors derived from in-air measurements are used to convert all of the simulated results. There is a 5% uncertainty in all of the ionization chamber measurements, and, when coupled with the uncertainty in the simulation (Monte Carlo associated relative error of 0.5% or less), there is a greater than 5% error in the absolute dose results reported. Although 50-150 runs per geometry with 100,000 primary photons per one-degree increment were performed, some of the plots indicate the data still contain noise. The

amount of noise present is due to scoring in air, which is very low density. Nonetheless, the results agree well with the measured values, and a smoothed profile can express the true nature of the results (e.g., Figures 3.6, 3.7, and 3.8).

Other researchers have observed similar discrepancies between these particular manufactured OSL dosimeters and ionization chamber measurements. Lavoie et al. (2011) found that OSL dosimeter energy response decreased with increased tube voltage. For 135 kVp, they report a -15.5% difference when compared to a NIST-traceable calibrated ionization chamber, whereas for 80 kVp the percent difference was only -2.0%. Vrieze et al. (2012) revealed, for 120 kVp measurements taken at the center position, that deviations of 10.4% were observed in the 32-cm acrylic phantom and 3.6% in the 16-cm phantom. Similar to the in-air results, they found a deviation of -9.9% at 120 kVp (where a difference of -7.8% was seen here). Therefore, the percent differences observed in these experiments are comparable to results observed by other authors.

The aluminum-oxide-based OSL material has an energy-dependent response, and a correction factor is necessary to achieve high accuracy in the dose results. Variables such as tube voltage, phantom size and material, and position within the phantom could influence the interaction of the beam with the dosimeters (Vrieze et al., 2012). While it is assumed that the manufacturer-reported results from the OSL dosimeters take into account a suitable energy-dependent correction factor, this is not known with absolute certainty. Hence, this could account for some discrepancies observed between the OSL and ion chamber results in the present work and those of other authors.

These results demonstrate that Monte Carlo models for multi-detector CT can be used to determine accurately patient dose at a voxel level. The calibrated Monte Carlo

simulation will be used to determine organ doses and effective dose values for patients who previously received CT examinations at Vanderbilt Medical Center. The application of this calibrated GEANT4 radiation transport code for CT dosimetry to pediatric patient data and to a series of deformable phantoms will be the subject of future publications.

3.5 Conclusion

A new Monte Carlo code using the GEANT4 toolkit to simulate patients receiving a CT examination has been developed and tested. In order to model accurately the complexity of the X-ray beam and CT geometry, measurements of the beam half-value layer, bowtie filter attenuation, and physical characteristics of the CT scanner model are required. Calibrations to physical dose measurements were made in air with a pencil ionization chamber by deriving photon fluence normalization factors for 100 and 120 kVp. Absorbed dose values and profiles determined from simulation were in overall agreement to within 6% of measured values.

Chapter IV

REALISTIC PEDIATRIC DEFORMABLE PHANTOMS

4.1 Development of the Pediatric Phantom Series

4.1.1 Patient-Specific Voxel Phantoms

To create a set of patient-specific voxel phantoms, pediatric patients were studied who had received chest-abdomen-pelvis (CAP) CT exams at Monroe Carrell, Jr. Children's Hospital at Vanderbilt. The retrospectively studied CT datasets from previously imaged patients were selected from image archives by pediatric radiologists. In accordance with the Health Insurance Portability and Accountability Act (HIPAA), all images were anonymized. A total of 40 patients were selected. They varied in age (7 months to 17 years, mean 7.8 years) and weight (7 to 100 kg, mean 34 kg, median 25 kg). Out of the total 40 datasets, 19 were female patients (0-17 years, 9-84 kg), and 21 were male patients (0-16 years, 7-100 kg) (Kost et al., 2015).

The ITK-SNAP program (Yushkevich et al., 2006) was used to segment organs manually and semi-automatically within the image field of view and torso region. A voxelized phantom (Figure 4.1) was generated for each patient, and each voxel was assigned a unique integer to identify each organ. These identifiers were used to define materials and track energy deposition during simulation.

Absorbed doses were calculated for the segmented organs in all of the subjects, and other standard dose metrics such as dose-length-product (DLP), CT dose index ($CTDI_{vol}$), and effective dose (ED) were also determined for each subject. For a comprehensive report

and thorough discussion of the results and analysis from the patient-specific studies, see Kost et al. (2015).

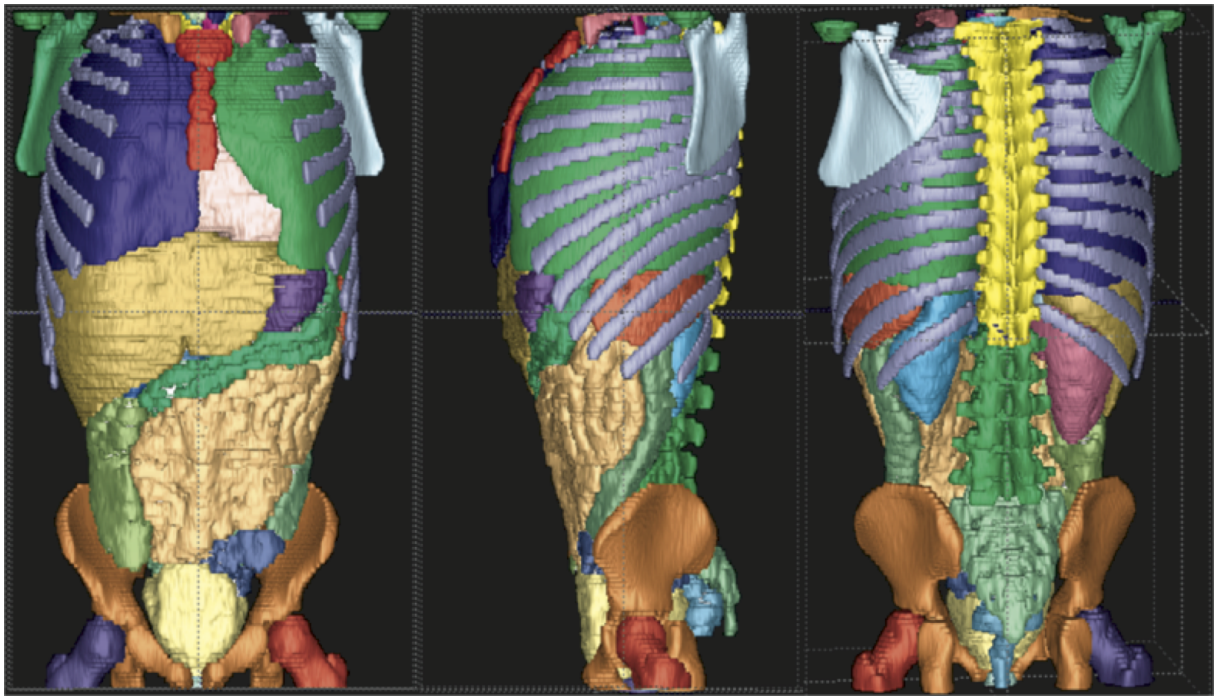

Figure 4.1: Segmented pediatric CT data set (7-year-old male), colored-coded based on the organ identification numbers used in the computer model (Kost et al., 2015).

4.1.2 XCAT NURBS Phantoms

The XCAT phantom is capable of modeling patient-specific variations in anatomy by modification of the control points that define the overall NURBS surface. Using affine transformations, these surfaces can be scaled and translated, allowing customization of each phantom to represent different patients properly. The shape of the organ surface can be morphed to imitate individual patient anatomy. The affine transformation is represented mathematically by:

$$P_{i,j}^{\text{transformed}} = \mathbf{M} P_{i,j}, \tag{4.1}$$

where $P_{i,j}$ are the control points being altered, and $\mathbf{M}$ is the 4×4 transformation matrix (Segars et al., 2000).

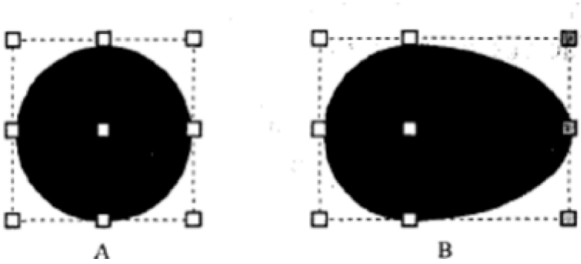

Figure 4.2: Illustration of modification of a NURBS surface through manipulation of its control points. (A) Spherical NURBS surface. (B) Modified surface with one of the control points translated to the right (Segars et al., 2000).

Anthropomorphic phantoms represent substantial improvement in accurate anatomical depiction. Anatomical organs are modeled specifically and modeling of organ juxtaposition is improved. Deforming the NURBS phantoms allows the representation of adults and children of different ages, shapes, and sizes.

4.1.2.1 Percentiles

Female and male versions of 10th, 25th, 50th, 75th, and 90th height percentiles were developed to model a range of sizes and weights for children of normal stature (e.g., Figure 4.6). The 50th percentile phantoms with ICRP 89 reference organ mass values (Valentin, 2002) were used as starting points for building the other height percentiles.

50th-percentile reference phantoms, both male and female, were built for all standard ICRP reference ages: newborn (Figure 4.3), 1-year (Figure 4.4), 5-year (Figure 4.5), 10-year (Figure 4.7), and 15-year (Figure 4.8). Since the original 50th-percentile reference children already had correct placement of organs relative to one another, corresponding to realistic variations of human anatomy with age, these were not changed when creating the other percentiles.

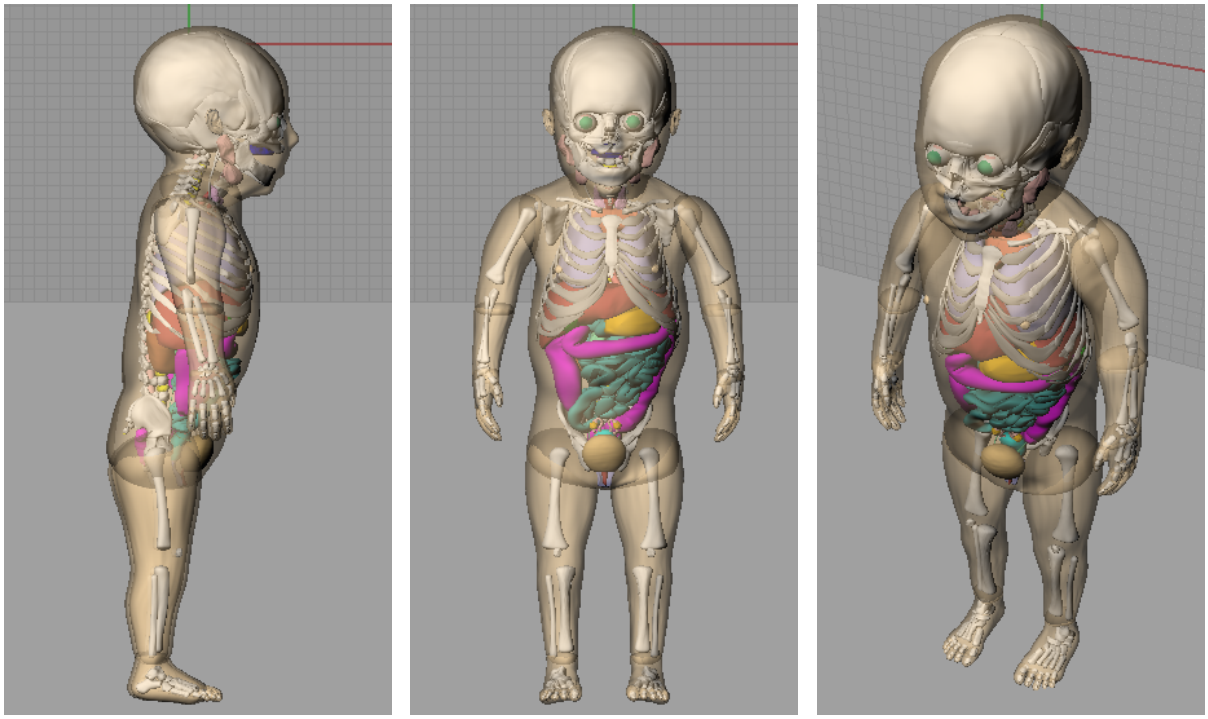

Figure 4.3: XCAT newborn female 50th-percentile phantom.

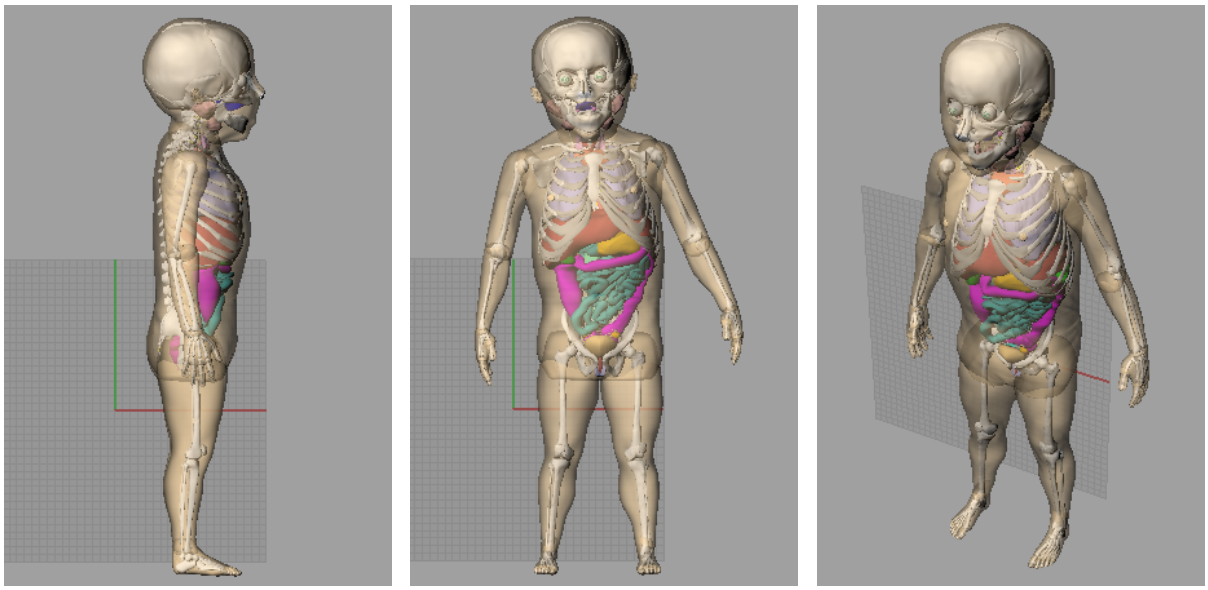

Figure 4.4: XCAT 1-year-old female 50th-percentile phantom.

To build other height percentiles, growth chart data from the CDC (National Center for Health Statistics (US) et al., 2000) and data from the National Health and Nutrition Examination Survey (NHANES) (National Center for Health Statistics (US) et al., 2002) were first used to scale uniformly each 50th percentile to obtain the desired height. This was done to keep all of the normal-stature phantoms proportional to each other due to limited data on the body sizes of children of only normal stature. For example, waist-measurement-percentile data are available across a broad spectrum of children, but these also include children that are overweight or obese. Hence, a 90th-percentile-waist measurement does not in practice correspond to the appropriate waist measurement of the 90th-height-percentile child of normal stature; rather it would correspond to an overweight child. Therefore, the phantoms were scaled proportionally with height as a first-order approximation.

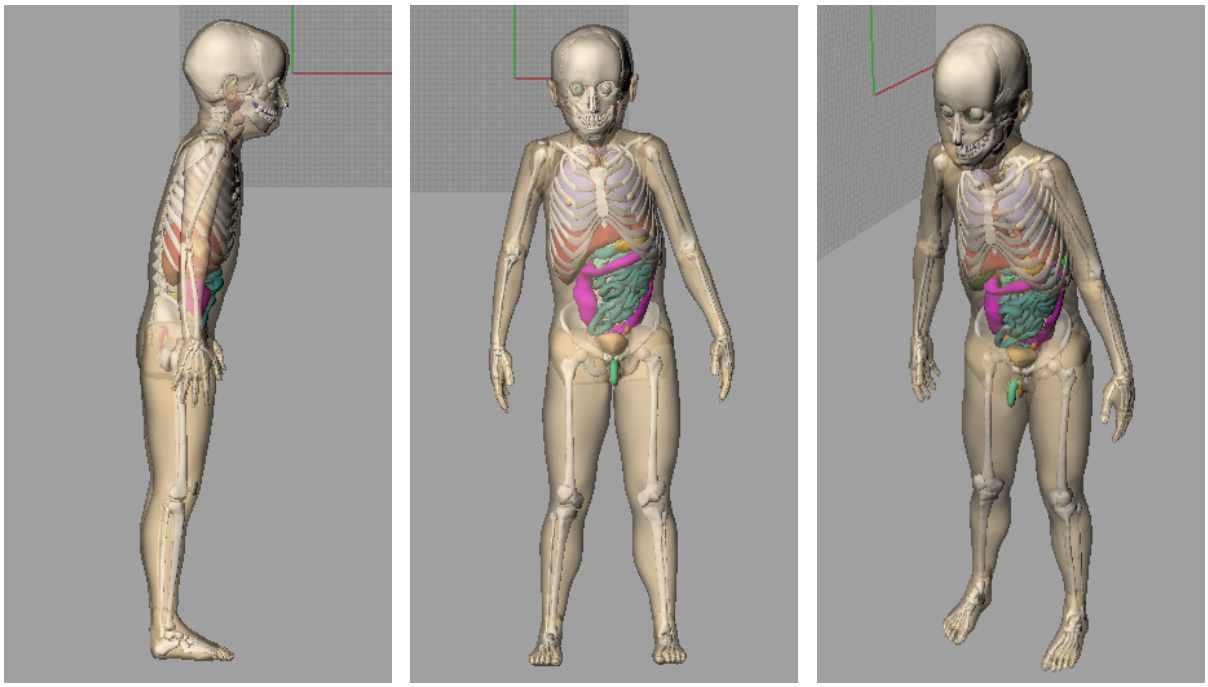

Figure 4.5: XCAT 5-year-old male 50th-percentile phantom.

After reference phantoms for all of the reference ages were created, they were subsequently used to create another series of non-reference ages, including: 3-year-olds, 8-year-olds, and 13-year-olds. These phantoms were developed to fill in the gaps between the reference-age data. Since growth rates of children can change rapidly at different stages of development, likewise body morphometry can change.

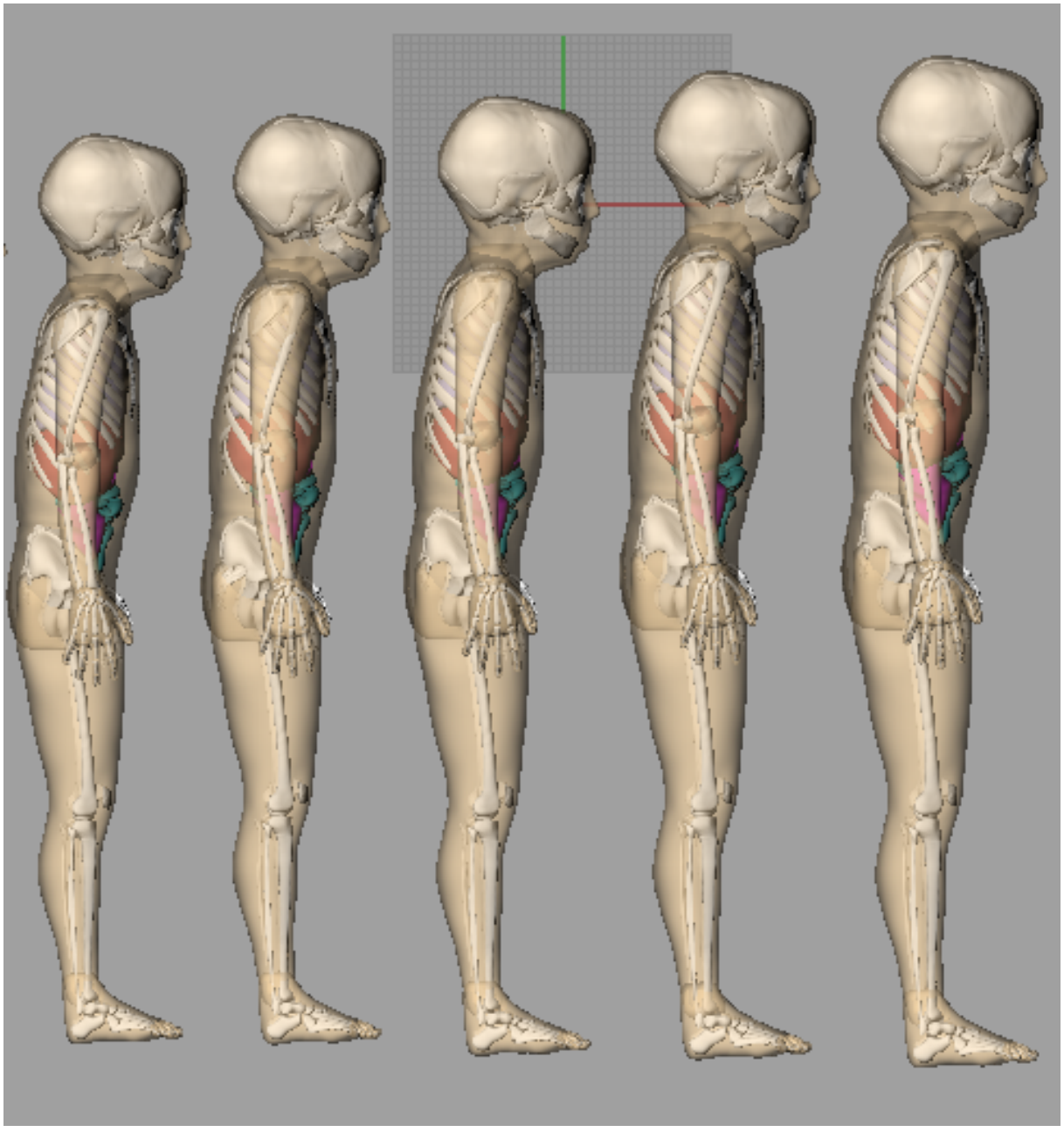

Figure 4.6: XCAT 5-year-old male series from 10th to 90th height percentiles.

Creation of the realistic non-reference age phantoms proved a bit more challenging than using simple scalings. When scaling down a 50th-percentile 3-year-old from the 50th-percentile 5-year-old, for example, a 3-year-old is produced that would be too small in the axial dimensions. It was necessary to rescale the axial dimensions to match anthropometric parameters in the literature. This effort was focused on developing realistic non-reference 50th-percentile phantoms first, using the 50th-percentile values from literature (e.g., National Center for Health Statistics (US) et al., 2000; Kuczmarski et al., 2002; Open Ergonomics, 2008). Then the additional percentiles were created from the 50th percentile using the previous method of scaling proportionally by height.

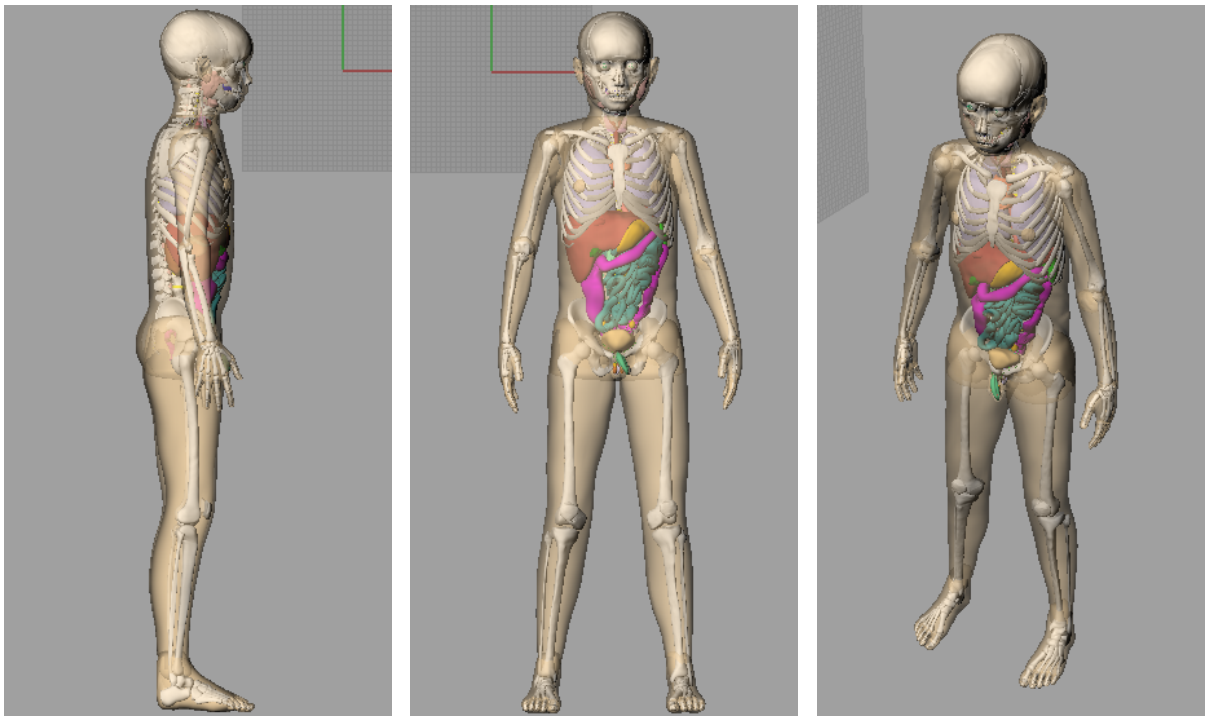

Figure 4.7: XCAT 10-year-old male 50th-percentile phantom.

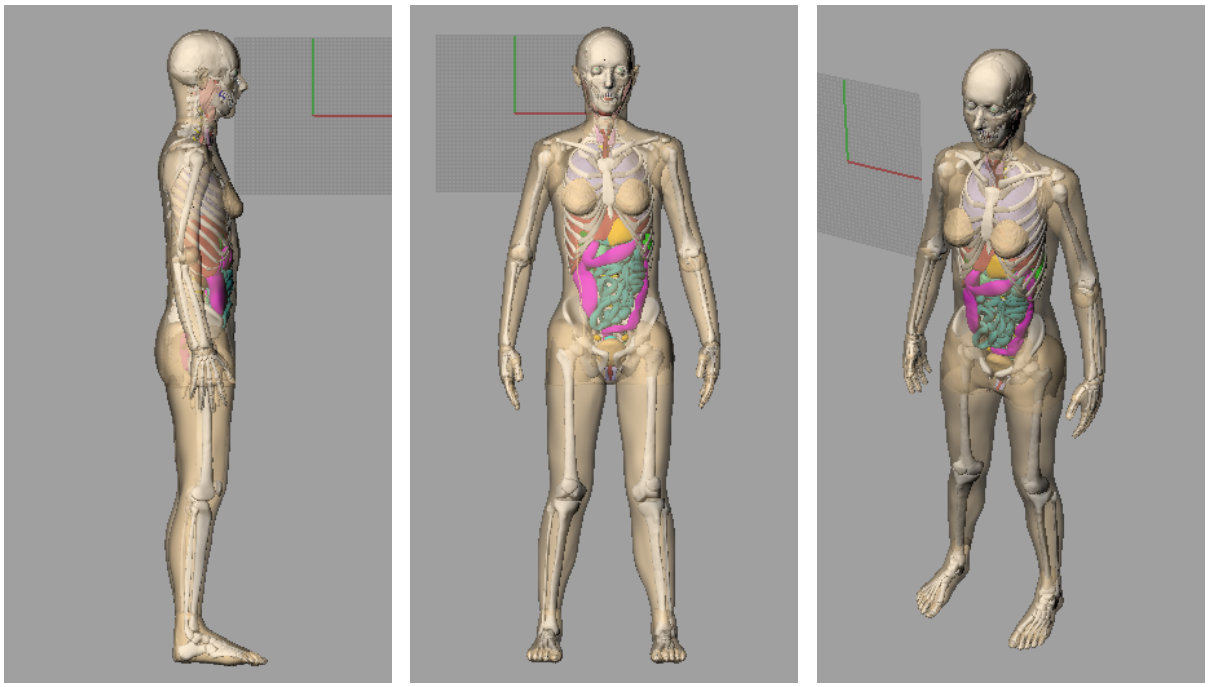

Figure 4.8: XCAT 15-year-old female 50th-percentile phantom.

A total of 40 female and 40 male pediatric phantoms of normal stature (5 percentile categories) were created. This new series of phantoms spans an age range of newborn up to 15 years old (total of 8 ages) and corresponding distributions of heights and weights (Figure 4.9).

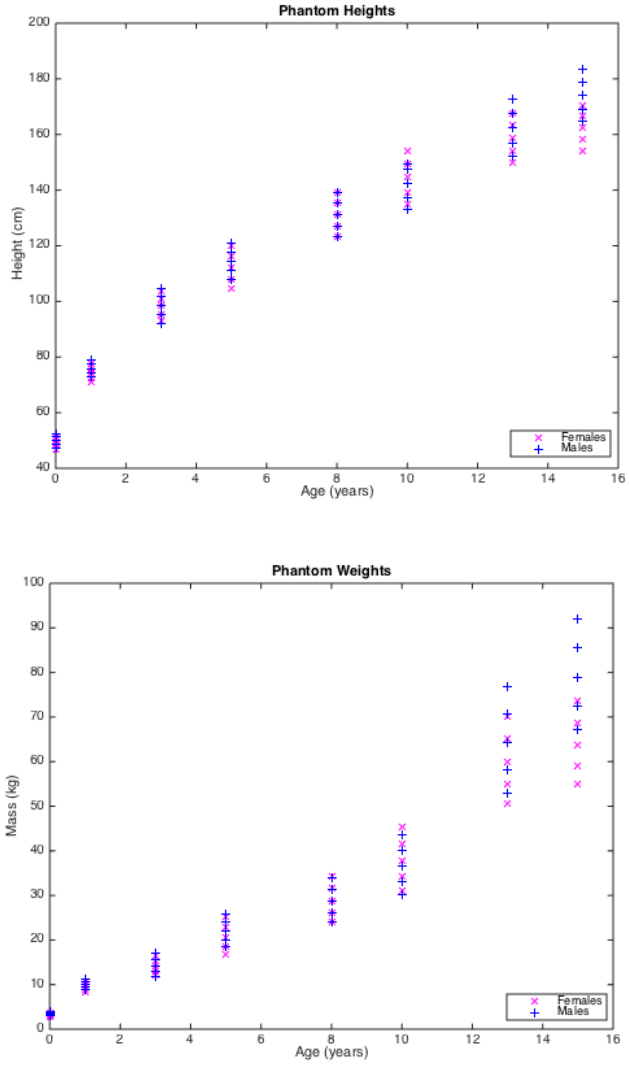

Figure 4.9: Height and weight distributions for constructed phantom series.

4.2 Organ Dose Results

4.2.1 Dose Calculations

A technique of 120 kVp nominal tube voltage, 100 mAs, and a pitch of 1.0 was used for all simulated CT scans. The CT source moved in one-degree increments for each tube rotation and tracked 3.6×10^6 total photon histories every 360 degrees. The scan length ranged from 2 cm below the bottom of the ischium to 2 cm above the apex of the lungs; to include overscan (required for reconstruction of images in helical scanning), half of the total beam collimation (2 cm) was added to each end. Table IV.1 lists the material definitions for tissues used in all simulations. Compositions for soft tissue, cortical bone, and marrow from ICRU Publication 46 (White and Wilson, 1992) were used to model the pediatric anatomy. Age-dependent cortical bone compositions and densities were selected based on phantom age.

Table IV.1: Summary of materials used in the Monte Carlo simulation model.

Material	Density (g/cm^3)	Chemical Composition (% by mass)									
		H	C	N	O	Na	P	S	Cl	K	Other
Air[a]	1.205×10^{-3}	–	0.01	75.5	23.2	–	–	–	–	–	1.3 (Ar)
Soft Tissue[b]	1.03	10.5	25.6	2.7	60.2	0.1	0.2	0.3	0.2	0.2	
Brain[c]	1.04	10.7	14.5	2.2	71.2	0.2	0.4	0.2	0.3	0.3	
GI Tract/Intestines[d]	1.03	10.6	11.5	2.2	75.1	0.1	0.1	0.1	0.2	0.1	
Heart[e]	1.06	10.3	12.1	3.2	73.4	0.1	0.1	0.2	0.3	0.2	0.1 (Fe)
Kidney[f]	1.04	10.6	9.4	2.1	77	0.2	0.2	0.1	0.2	0.2	
Liver[g]	1.06	10.2	13.9	3.0	71.6	0.2	0.3	0.3	0.2	0.3	
Lung Tissue[h]	0.26	10.3	10.5	3.1	74.9	0.2	0.2	0.3	0.3	0.2	
Mammary Gland[i]	1.06	10.2	15.8	3.7	69.8	0.1	0.1	0.2	0.1	0.1	
Ovary[c]	1.05	10.5	9.3	2.4	76.8	0.2	0.2	0.2	0.2	0.2	
Pancreas[c]	1.04	10.6	16.9	2.2	69.4	0.2	0.2	0.1	0.2	0.2	
Skin[c]	1.09	10	20.4	4.2	64.5	0.2	0.1	0.2	0.3	0.1	
Spleen[c]	1.06	10.3	11.3	3.2	74.1	0.1	0.3	0.2	0.2	0.3	
Testes[c]	1.04	10.6	9.9	2.0	76.6	0.2	0.1	0.2	0.2	0.2	
Thyroid[c]	1.05	10.4	11.9	2.4	74.5	0.2	0.1	0.1	0.2	0.1	0.1 (I)
Urinary Bladder[j]	1.04	10.5	9.6	2.6	76.1	0.2	0.2	0.2	0.3	0.3	
Cortical Bone[k] (0 y)	1.68	4.7	15.4	4.2	48.5	0.1	8.2	0.2	0.1	–	0.2 (Mg), 18.4 (Ca)
Cortical Bone[l] (1 y)	1.71	4.5	15.9	4.4	46.7	0.1	8.7	0.3	0.1	–	0.2 (Mg), 19.1 (Ca)
Cortical Bone[m] (5 y)	1.75	4.3	15.8	4.4	45.7	0.1	9.3	0.3	0.1	–	0.2 (Mg), 19.8 (Ca)
Cortical Bone[n] (10 y)	1.79	4.0	15.9	4.4	45.0	0.1	9.6	0.3	0.1	–	0.2 (Mg), 20.4 (Ca)
Cortical Bone[o] (15 y)	1.83	3.8	16.0	4.4	44.3	0.1	9.9	0.3	–	–	0.2 (Mg), 21.0 (Ca)
Spongiosa[p]	1.18	8.5	40.4	2.8	36.7	0.1	3.4	0.2	0.2	0.1	0.1 (Mg), 7.4 (Ca), 0.1 (Fe)
Red Marrow[q]	1.03	10.5	41.4	3.4	43.9	–	0.1	0.2	0.2	0.2	0.1 (Fe)
Yellow Marrow[r]	0.98	11.5	64.4	0.7	23.1	0.1	–	0.1	0.1	–	

[a]NIST	Composition of air, dry (near sea level)
[b]ICRU 46	Appendix A Adult, ICRU-44 male
[c]ICRU 46	Appendix A Adult
[d]ICRU 46	Appendix A Adult, GI tract
[e]ICRU 46	Appendix A Adult, blood-filled
[f]ICRU 46	Appendix A Child, 2 years
[g]ICRU 46	Appendix A Adult, healthy
[h]ICRU 46	Appendix A Adult, healthy, inflated
[i]ICRU 46	Appendix A Breast - mammary gland, adult #3
[j]ICRU 46	Appendix A Adult, empty
[k]ICRU 46	Appendix A Skeleton - cortical bone, infant (3 months)
[l]ICRU 46	Appendix A Skeleton - cortical bone, child (1 year)
[m]ICRU 46	Appendix A Skeleton - cortical bone, child 5 year)
[n]ICRU 46	Appendix A Skeleton - cortical bone, child (10 year)
[o]ICRU 46	Appendix A Skeleton - cortical bone, child (15 year)
[p]ICRU 46	Appendix A Skeleton - spongiosa
[q]ICRU 46	Appendix A Skeleton - red marrow
[r]ICRU 46	Appendix A Skeleton - yellow marrow

The computational facilities used in this project were provided by the Vanderbilt Advanced Computing Center for Research and Education (ACCRE). Typical simulation times ranged from approximately 2 to 15 hours depending on the size of the phantom and the scan length, with the younger, smaller newborn phantoms taking the least amount of time versus the older, larger phantoms that took much longer. The Monte Carlo simulation tallied the energy deposited in each voxel, which was output as a 3D map. These energy maps were later used to convert to absorbed dose using the corresponding 3D phantom and assigned tissue densities (Table IV.1). Relative statistical uncertainties were less than 1% in each organ (defined as the 1σ standard deviation of the energy deposited divided by the average energy deposited). The normalization factor determined during code calibration (1.4×10^6 mGy/100 mAs) was applied to simulated absorbed dose values to convert to absolute dose. Absorbed doses to radiosensitive organs were calculated, and effective doses (ED) were determined using tissue-weighting factors from ICRP 103 (2007). These tissue-weighting factors, which have been averaged over both genders and all ages, have been applied to these pediatric models due to the lack of tissue-weighting factors derived specifically for pediatric populations.

The relationship between organ doses and phantom body size was investigated for several anthropometric measurements. Phantom diameter was determined to best correlate with doses to organs in the scanned region. Average phantom diameters were determined for the torso regions, assuming a cylindrical volume, i.e.,

$$d = 2\sqrt{\frac{V}{\pi h}}, \tag{4.2}$$

where V is the volume of the total defined torso region, and h is the determined torso height. Average torso diameter was calculated using an axial range of 2 cm above the apex of the lungs to 2 cm below the ischium. To eliminate variability due to scan length differences, which can affect the amount of scatter dose individual organs receive, all organ doses were normalized by the scanner-specific dose-length-product (DLP). Previous studies (e.g., Li et al., 2011a; Turner et al., 2011; Lee et al., 2012; Tian et al., 2014) also suggest that normalized organ dose ($\mathrm{nD}_{\mathrm{organ}}$) decreases exponentially with body diameter, d, so an exponential function was chosen to obtain fit coefficient parameters from nonlinear regression:

$$\mathrm{nD}_{\mathrm{organ}}(d) = \exp(\alpha_{\mathrm{organ}} d + \beta_{\mathrm{organ}}). \tag{4.3}$$

The coefficient parameters (α_{organ} and β_{organ}) are specific to each organ scanned within the field-of-view. These fit results may be used to estimate organ dose, using the diameter of a patient and the scanner-specific DLP prior to the CT scan. Nonlinear regression was also performed to determine the fit coefficients for effective dose (ED) normalized by DLP (nED) to diameter using:

$$\mathrm{nED}(d) = \exp(\alpha_{\mathrm{ED}} d + \beta_{\mathrm{ED}}). \tag{4.4}$$

4.2.2 Dose Results

Table IV.2 provides a summary of all fit parameters from the nonlinear regression of DLP-normalized absorbed and effective doses for all organs within the scan range.

A strong correlation between dose and torso diameter is indicated by the reported R^2 correlation coefficients and root-mean-squared errors (RMSE) reported.

The relationship between DLP-normalized effective dose and average torso diameter is shown in Figure 4.10. Similarly, Figures 4.11 through 4.23 show plots of DLP-normalized organ doses as a function of average torso diameter for selected major organs.

Table IV.2: Nonlinear regression coefficients for DLP-normalized organ and effective doses for simulated CAP CT scans.

	α	β	R^2	RMSE
Adrenals	-0.0800	-2.30	0.991	8.95×10^{-4}
Bladder	-0.0771	-2.34	0.974	1.52×10^{-3}
Brain	-0.1718	-4.88	0.934	9.50×10^{-5}
Breasts	-0.0703	-2.51	0.920	2.37×10^{-3}
Colon	-0.0644	-2.57	0.996	4.52×10^{-4}
Cortical Bone	-0.0653	-2.24	0.985	1.28×10^{-3}
Esophagus	-0.0777	-2.42	0.993	6.91×10^{-4}
Eye Lenses	-0.2222	-3.80	0.901	2.07×10^{-4}
Gall Bladder	-0.0601	-2.66	0.957	1.44×10^{-3}
Heart	-0.0700	-2.39	0.991	8.60×10^{-4}
Kidneys	-0.0724	-2.37	0.992	8.23×10^{-4}
Liver	-0.0671	-2.52	0.989	8.31×10^{-4}
Lungs	-0.0751	-2.38	0.994	6.71×10^{-4}
Ovaries	-0.0768	-2.34	0.966	1.77×10^{-3}
Pancreas	-0.0707	-2.46	0.997	4.66×10^{-4}
Prostate	-0.0930	-2.19	0.984	1.24×10^{-3}
Red Marrow	-0.0864	-2.50	0.966	1.36×10^{-3}
Salivary Glands	-0.1966	-2.40	0.940	8.43×10^{-4}
Small Intestines	-0.0654	-2.51	0.991	7.36×10^{-4}
Spinal Cord	-0.0945	-2.24	0.974	1.53×10^{-3}
Spleen	-0.0723	-2.46	0.946	1.96×10^{-3}
Stomach	-0.0658	-2.57	0.994	5.97×10^{-4}
Testes	-0.0520	-2.87	0.837	2.50×10^{-3}
Thymus	-0.0710	-2.46	0.992	7.51×10^{-4}
Thyroid	-0.0807	-2.38	0.945	2.06×10^{-3}
Uterus	-0.0797	-2.34	0.964	1.82×10^{-3}
Effective Dose - Females	-0.0751	-2.51	0.994	6.25×10^{-4}
Effective Dose - Males	-0.0738	-2.67	0.995	4.76×10^{-4}

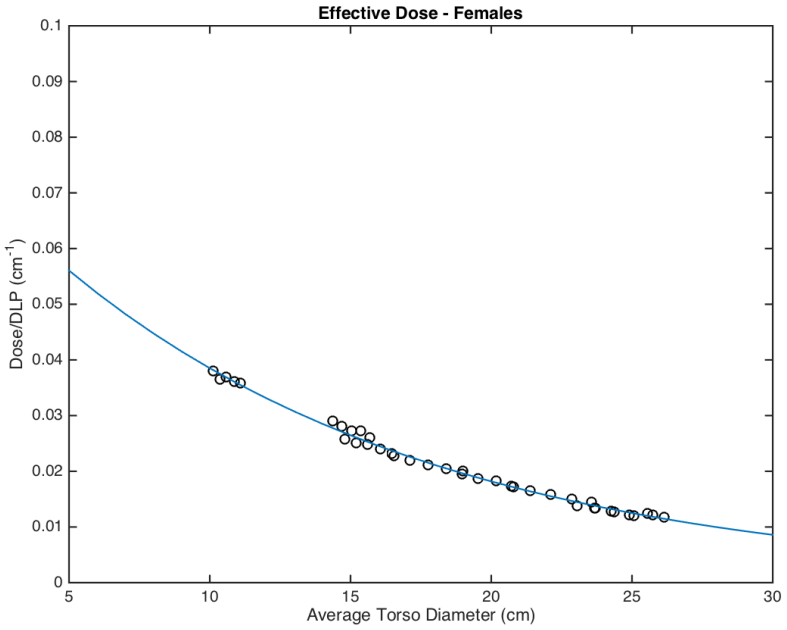

(a)

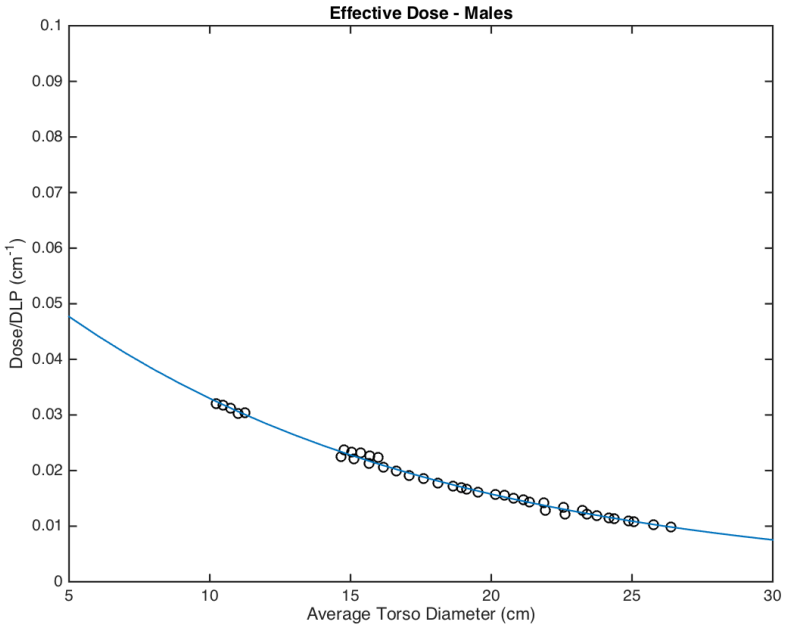

(b)

Figure 4.10: Plots of DLP-normalized effective dose for (a) females, and (b) males, with the corresponding exponential fits demonstrating the dependence of dose on torso diameter.

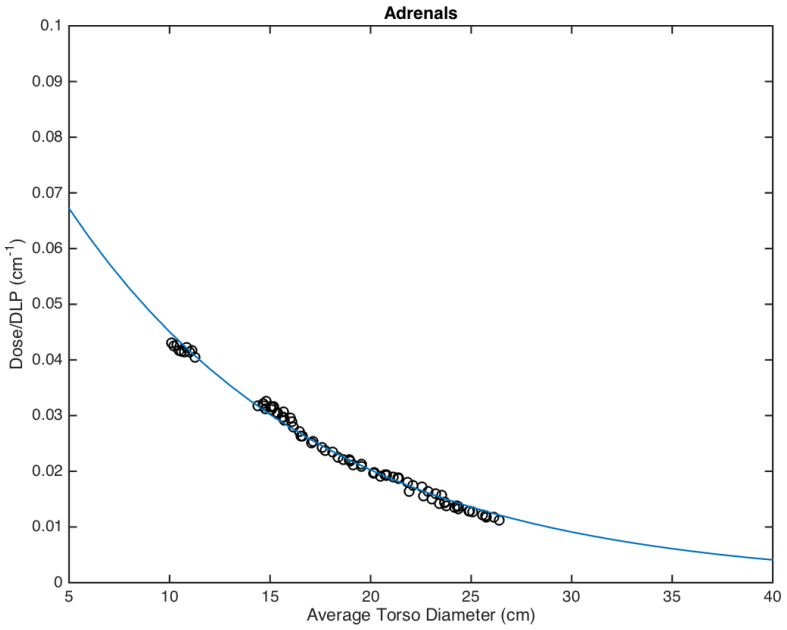

(a)

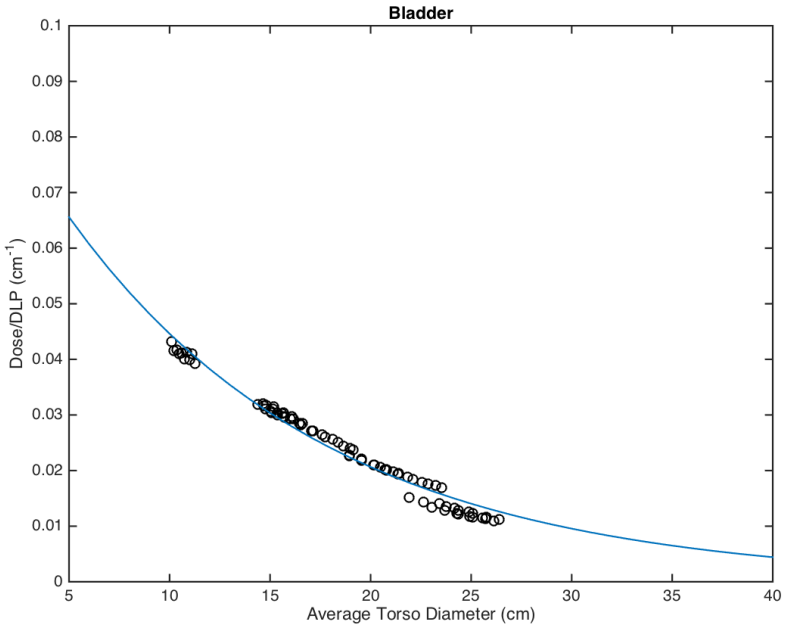

(b)

Figure 4.11: Plots of DLP-normalized organ dose for (a) adrenals, and (b) bladder, with the corresponding exponential fits demonstrating the dependence of dose on torso diameter.

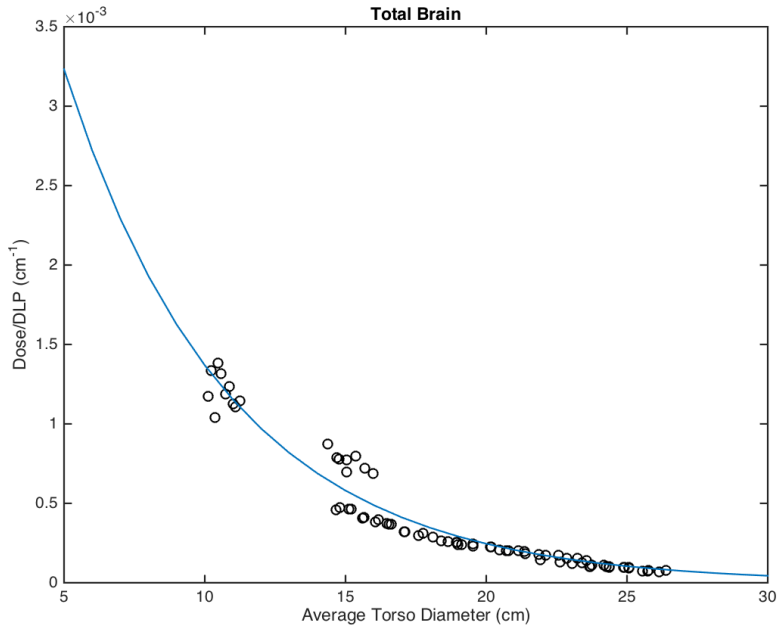

(a)

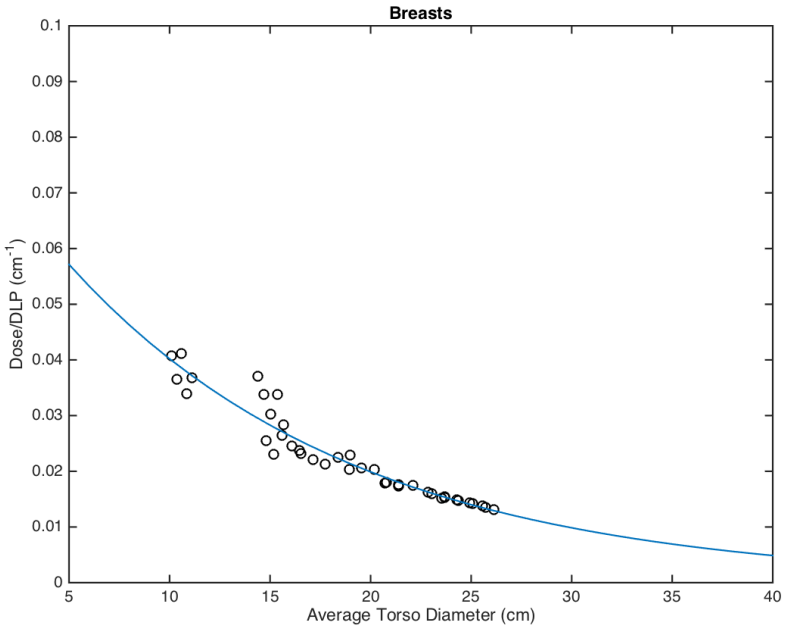

(b)

Figure 4.12: Plots of DLP-normalized organ dose for (a) brain, and (b) breasts, with the corresponding exponential fits demonstrating the dependence of dose on torso diameter.

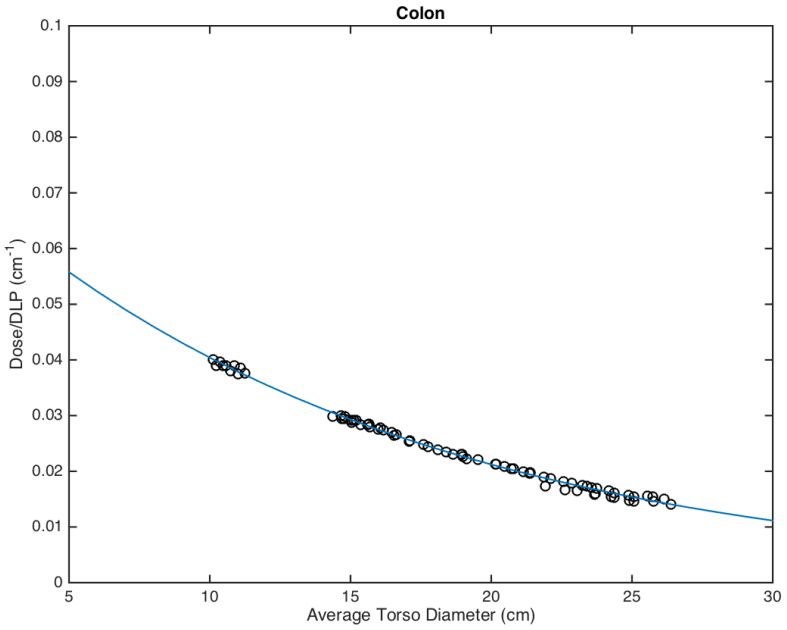

(a)

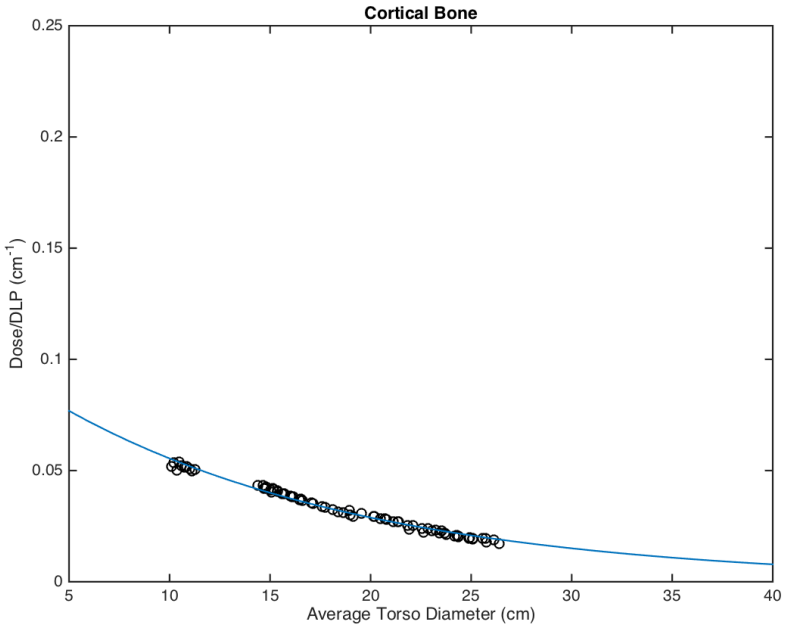

(b)

Figure 4.13: Plots of DLP-normalized organ dose for (a) colon, and (b) cortical bone, with the corresponding exponential fits demonstrating the dependence of dose on torso diameter.

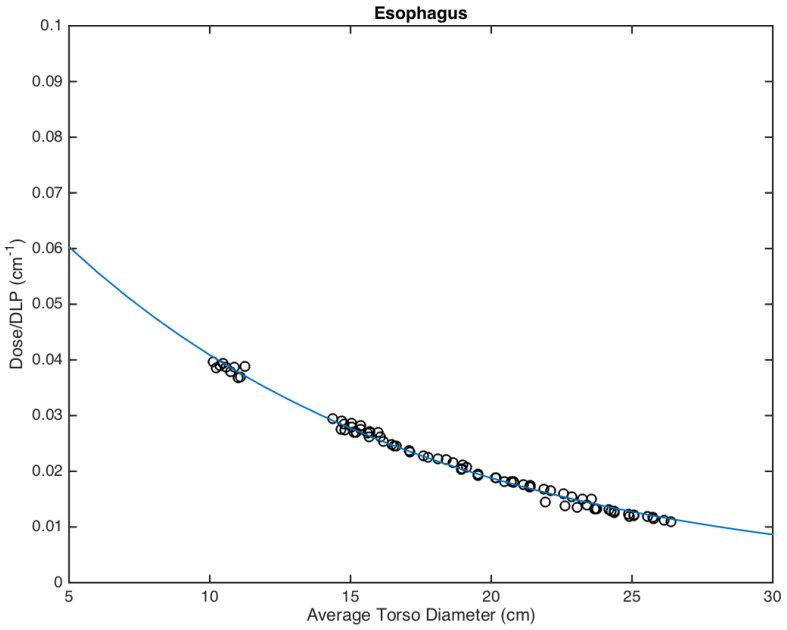

(a)

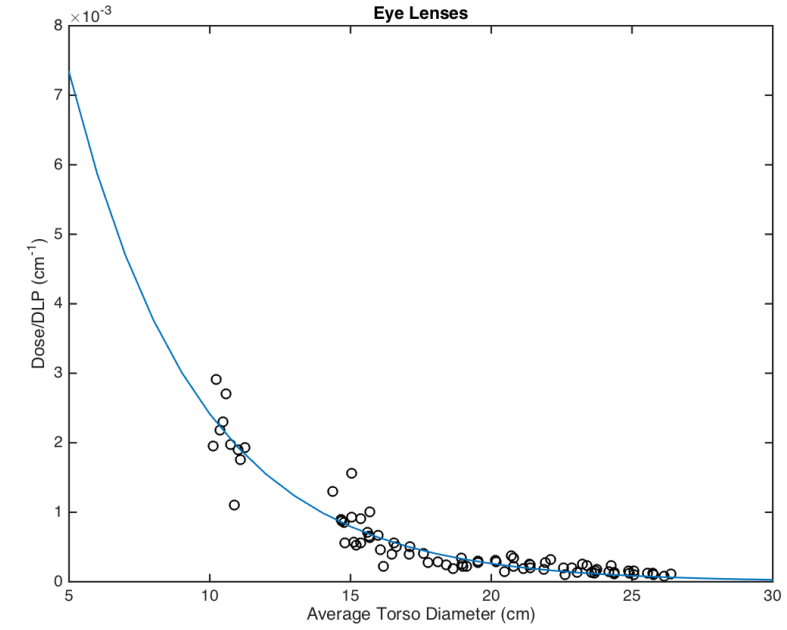

(b)

Figure 4.14: Plots of DLP-normalized organ dose for (a) esophagus, and (b) eye lenses, with the corresponding exponential fits demonstrating the dependence of dose on torso diameter.

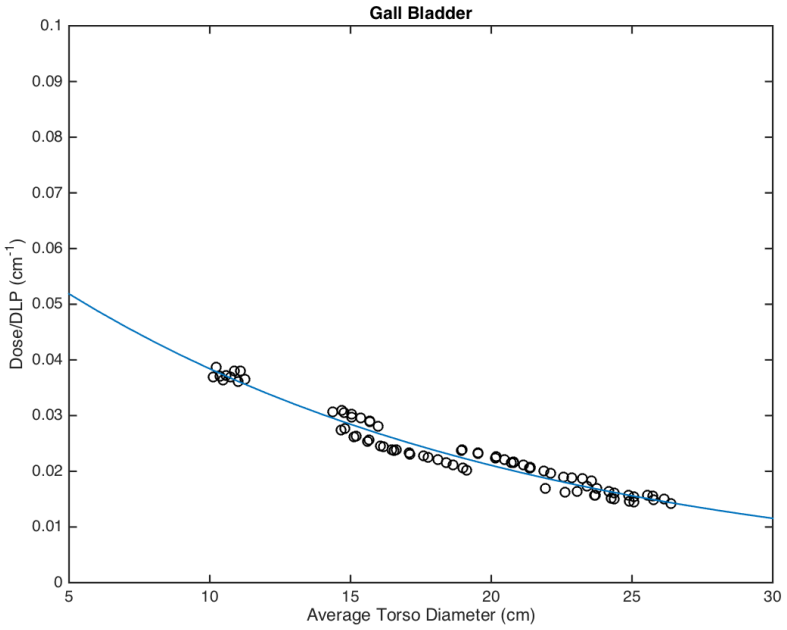

(a)

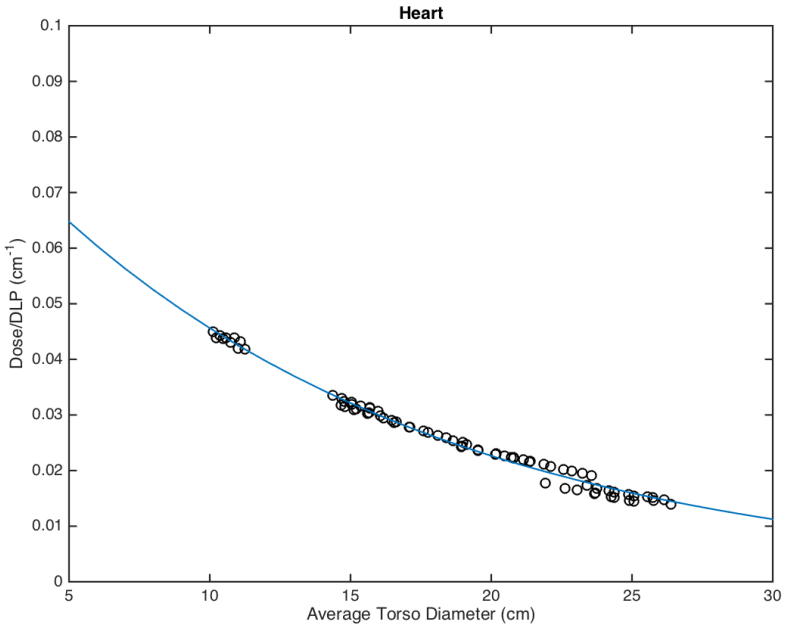

(b)

Figure 4.15: Plots of DLP-normalized organ dose for (a) gall bladder, and (b) heart, with the corresponding exponential fits demonstrating the dependence of dose on torso diameter.

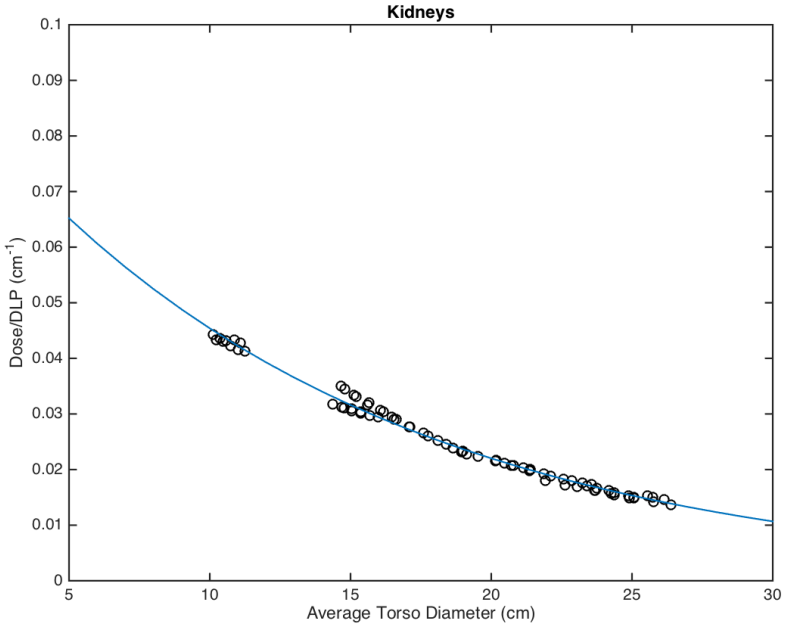

(a)

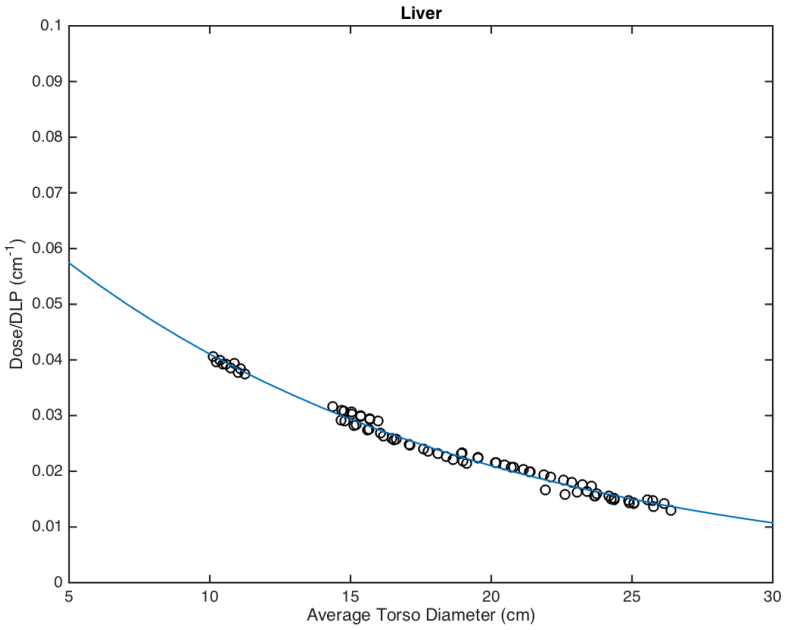

(b)

Figure 4.16: Plots of DLP-normalized organ dose for (a) kidneys, and (b) liver, with the corresponding exponential fits demonstrating the dependence of dose on torso diameter.

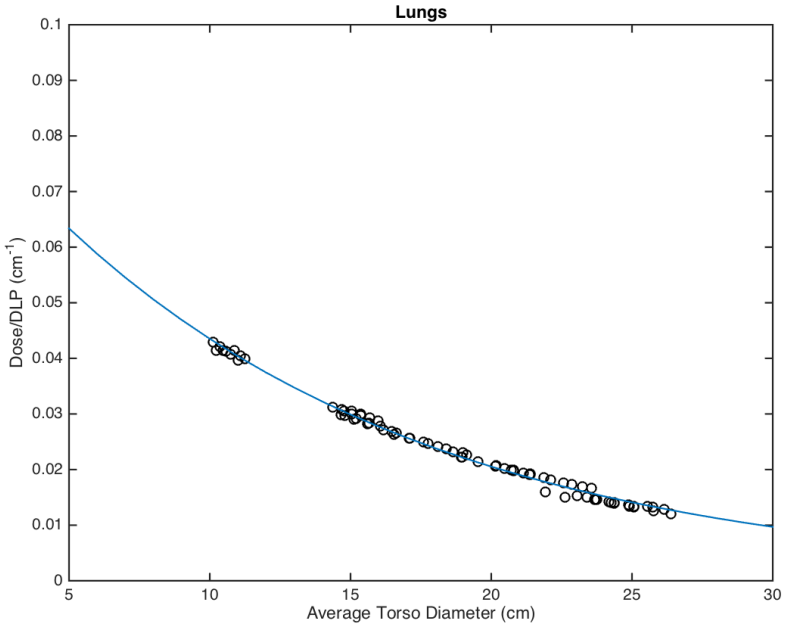

(a)

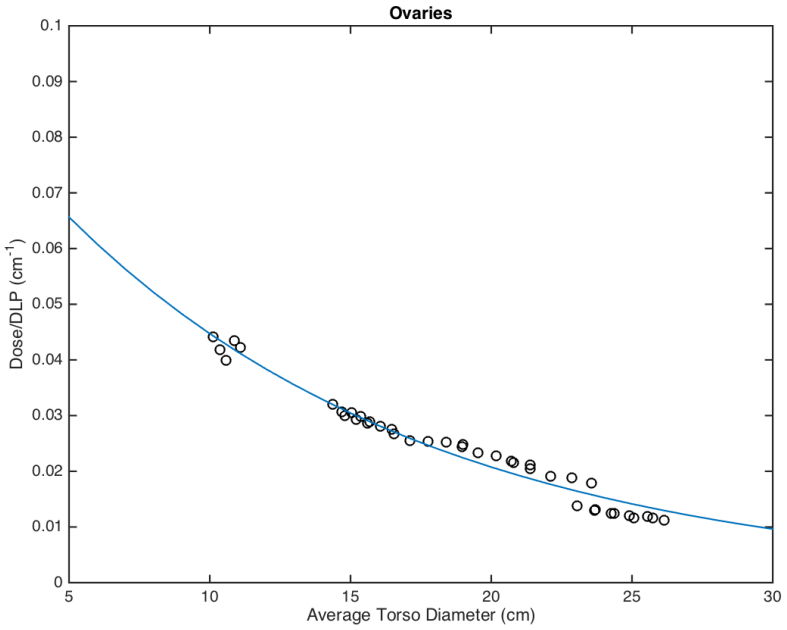

(b)

Figure 4.17: Plots of DLP-normalized organ dose for (a) lungs, and (b) ovaries, with the corresponding exponential fits demonstrating the dependence of dose on torso diameter.

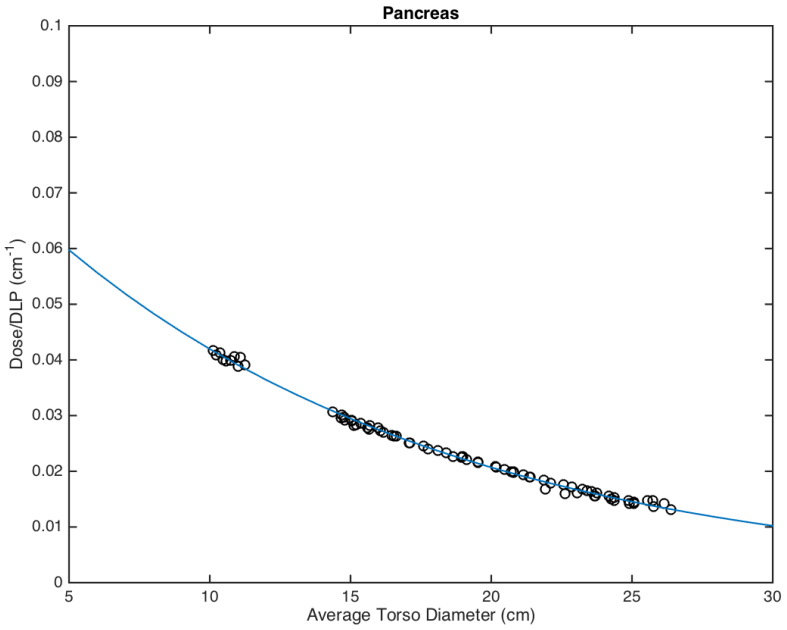

(a)

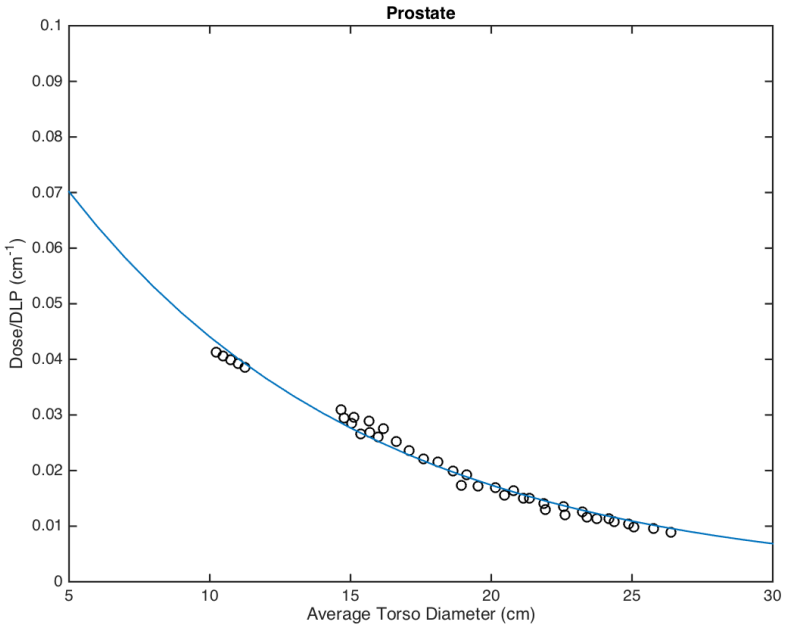

(b)

Figure 4.18: Plots of DLP-normalized organ dose for (a) pancreas, and (b) prostate, with the corresponding exponential fits demonstrating the dependence of dose on torso diameter.

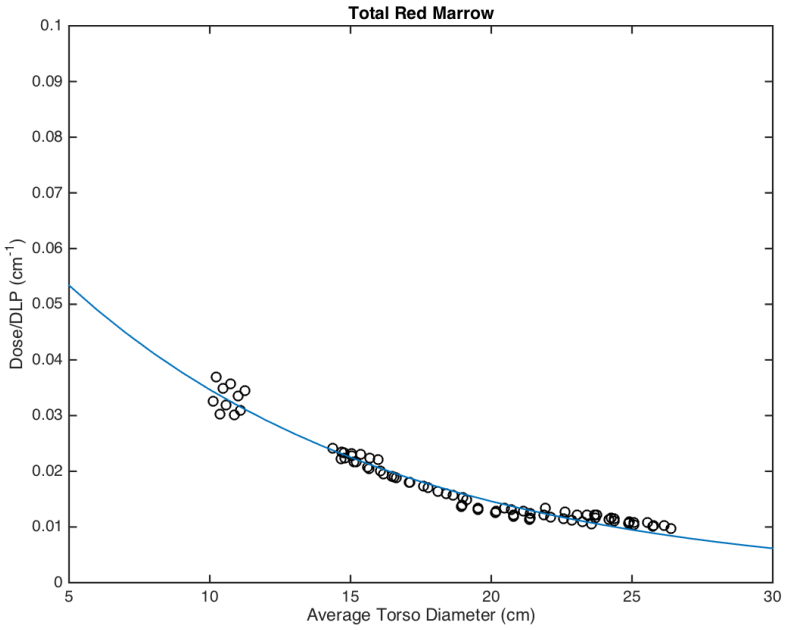

(a)

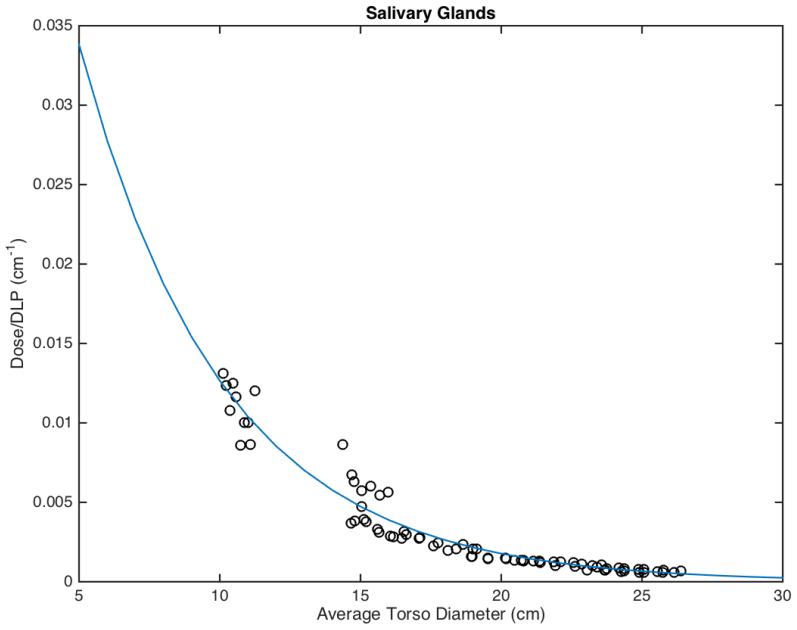

(b)

Figure 4.19: Plots of DLP-normalized organ dose for (a) total red marrow, and (b) salivary glands, with the corresponding exponential fits demonstrating the dependence of dose on torso diameter.

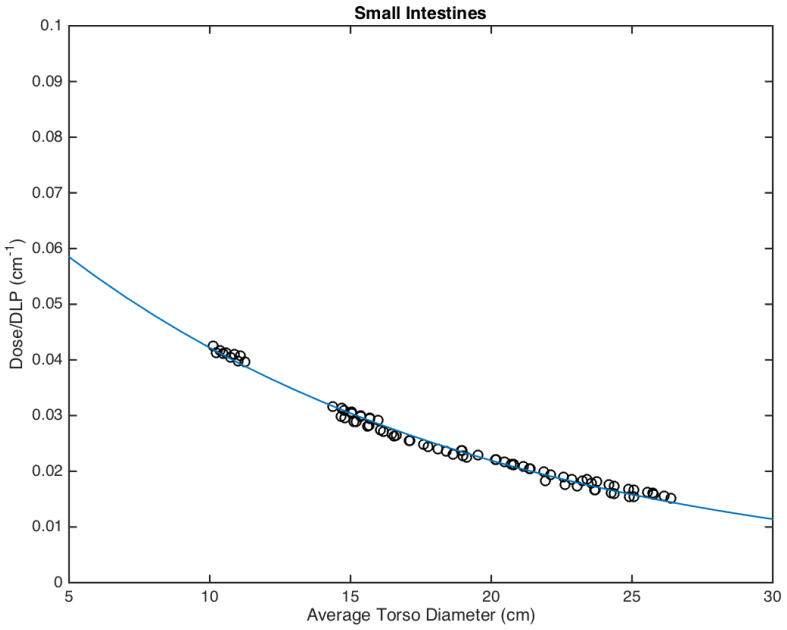

(a)

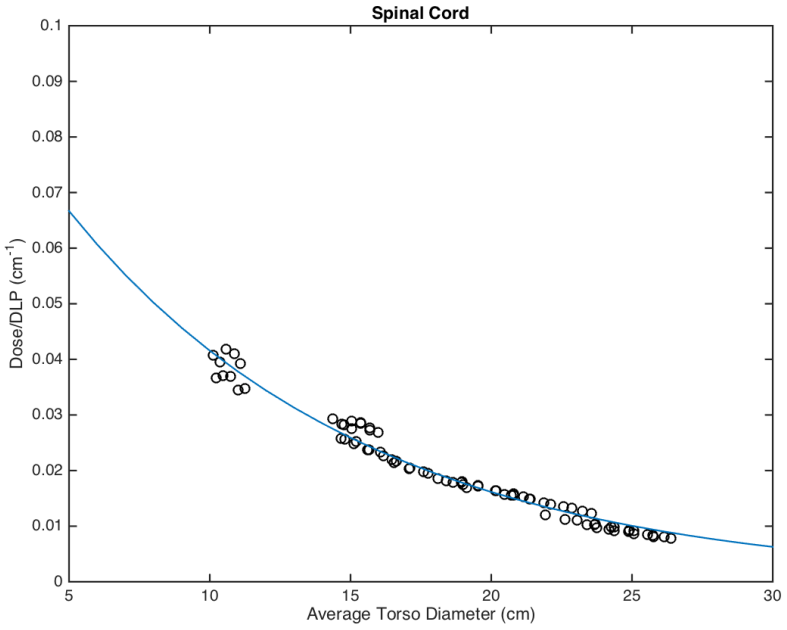

(b)

Figure 4.20: Plots of DLP-normalized organ dose for (a) small intestines, and (b) spinal cord, with the corresponding exponential fits demonstrating the dependence of dose on torso diameter.

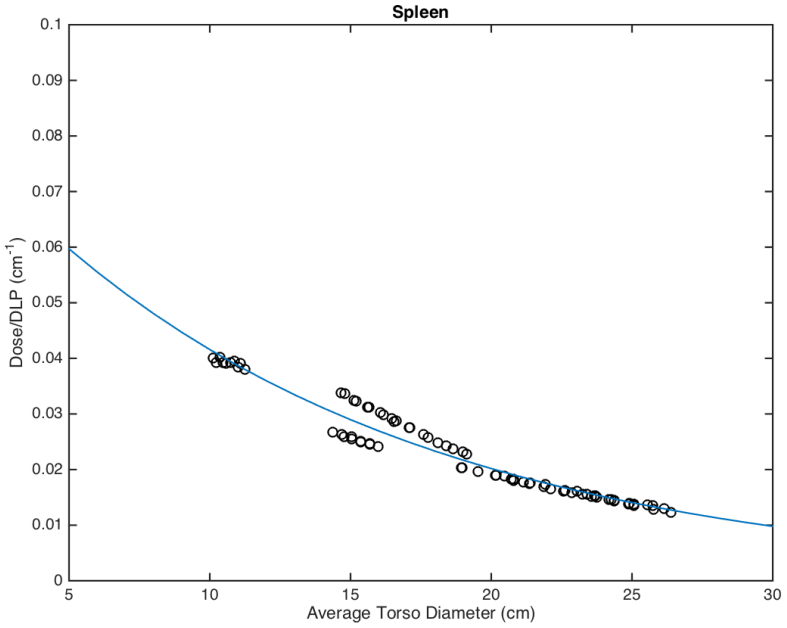

(a)

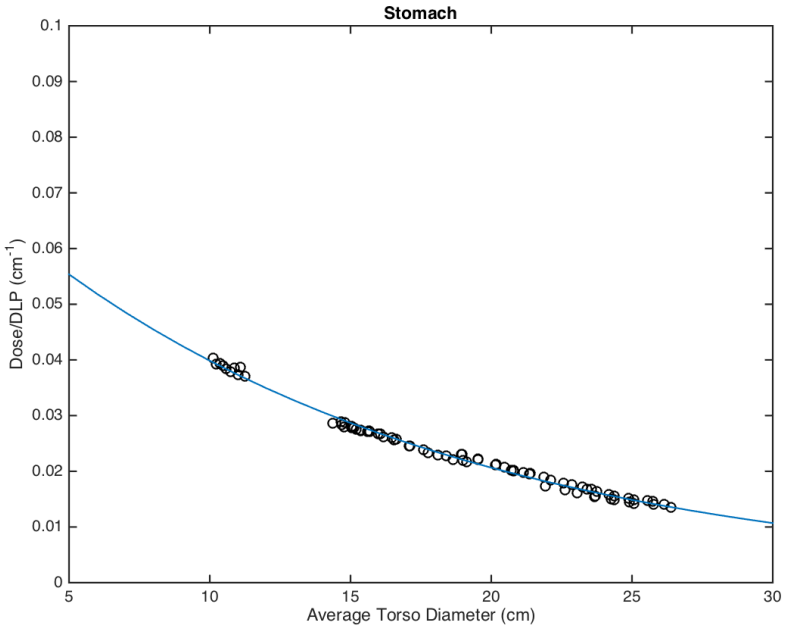

(b)

Figure 4.21: Plots of DLP-normalized organ dose for (a) stomach, and (b) spleen, with the corresponding exponential fits demonstrating the dependence of dose on torso diameter.

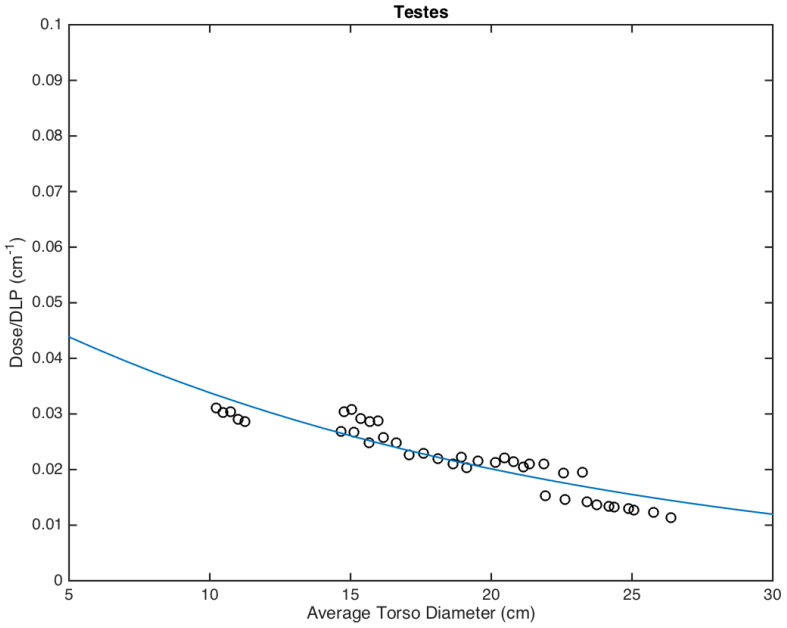

(a)

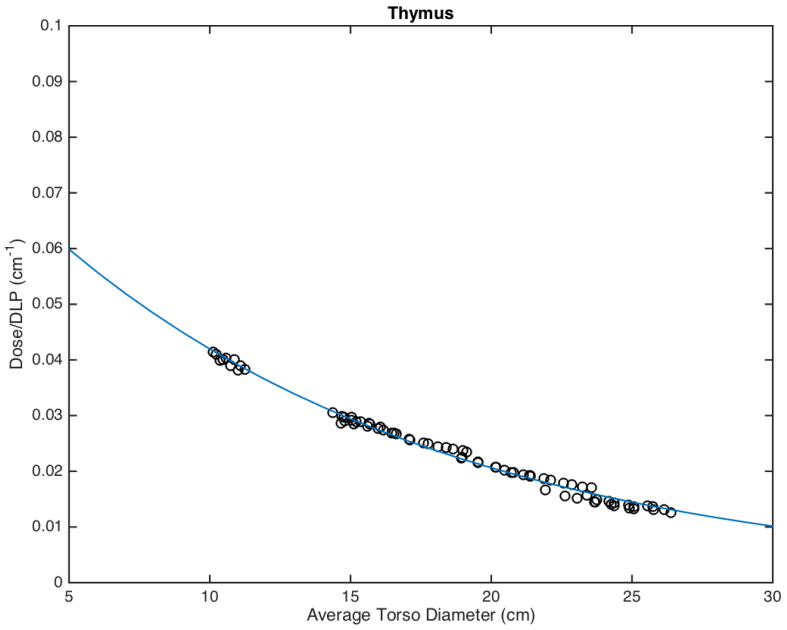

(b)

Figure 4.22: Plots of DLP-normalized organ dose for (a) testes, and (b) thymus, with the corresponding exponential fits demonstrating the dependence of dose on torso diameter.

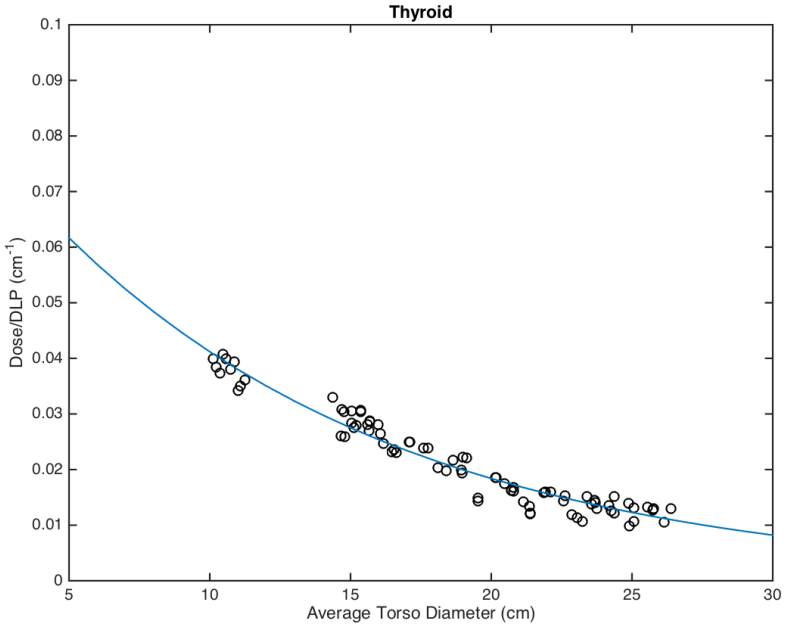

(a)

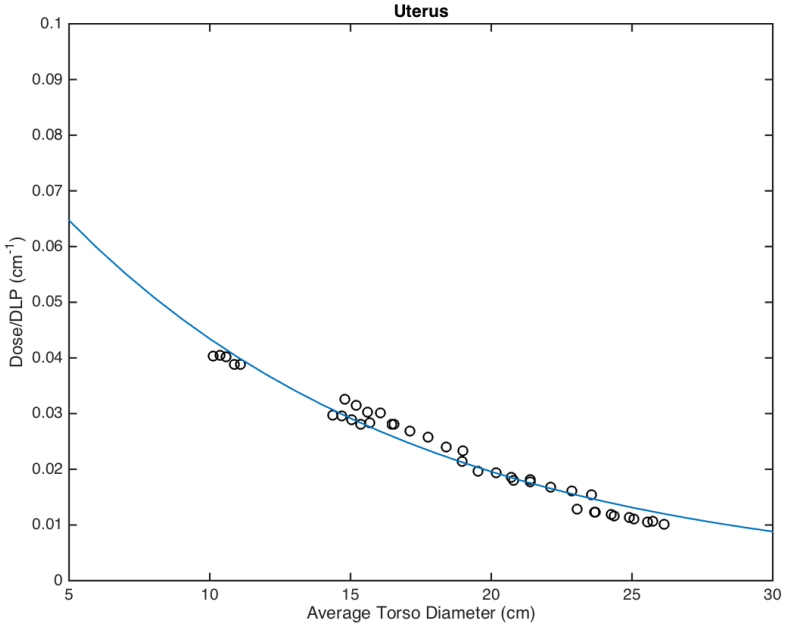

(b)

Figure 4.23: Plots of DLP-normalized organ dose for (a) thyroid, and (b) uterus, with the corresponding exponential fits demonstrating the dependence of dose on torso diameter.

4.3 Patient-Phantom Dose Comparisons

Monte Carlo organ-dose estimates derived from actual pediatric CT scans were compared with organ dose estimates from simulated CT scans of anthropomorphic NURBS phantoms. In general, there is good agreement between the organ doses for comparison of the NURBS models to real patients of similar stature. It should be noted that in this case the NURBS model was not deformed to be a close match to the patient, but that a real patient who was fairly close in stature to one of the defined NURBS models was selected for comparison. Matching real subjects with a large library of NURBS models of different ages and body types allows assignment of more patient-specific organ absorbed doses for pediatric subjects who receive CT scans. The quality of dose data to be assigned to pediatric patients receiving CT examinations thus will be significantly improved using the information obtained in this study.

4.3.1 Patient-Phantom Match Criteria

Since red marrow distribution in children is a function of age (to be discussed in more detail in Chapter 5), this is the first variable that must be considered when matching a patient to a phantom. Therefore, each patient was matched to only a subset of phantom percentiles that was close in age. For example, if a patient was a 5-year-old, the candidate phantoms would be the 10th- through 90th-percentile 5-year-old phantoms. In the case of a 4-year-old patient, however, all of the 3-year-old and 5-year-old percentile phantoms would be considered as match candidates due to variances in red marrow distribution.

In conjunction with age, the gender of the patient and phantom was also used as a

factor in matching, i.e., female and male patients were only matched to female and male phantoms, respectively. This was necessary due to the presence of gender-specific organs, e.g., the ovaries and uterus in the females and the prostate and testes in the males.

As previously demonstrated, organ dose is strongly correlated with patient diameter. Therefore, average torso diameter was used as the next match criterion. The patient's measured average torso diameter was compared to the subset of candidate phantoms. The closest one in diameter in the appropriate age-gender category was then determined to be the "best match".

4.3.2 Patient-Phantom Match Results

Absorbed dose results for organs within the thoracic region were used to match between patients and phantoms due to the fact that only chest-abdomen-pelvis CT scans were simulated. Organs outside of this field of view were not used in the match comparisons. On an organ-by-organ basis, dose results between the patients and phantoms were compared. Absolute dose differences and percent differences between each patient-phantom pair were calculated for each organ. Then an overall average of dose differences was calculated for each patient-phantom pair, and these results are summarized in Table IV.3 for all 40 patients. Figures 4.24 through 4.33 provide a visualization of all patient-phantom organ dose comparisons.

It should be noted that in some cases dose to thyroid, ovaries, or prostate drastically differed from the corresponding dose results for the matched phantom. This was caused by these particular organs in the original patient CT images not being visible enough to segment manually, by being on the edge of the scan range, or not being in the scan

area at all. Only major torso organs that fall within the scan range and field-of-view of a typical chest-abdomen-pelvis CT scan were used in the matches. Average matched dose differences ranged from 0.44 to 2.48 mGy, and average matched percent differences ranged from 3.6 to 23.1%. For the entire patient-phantom dataset, the average overall dose difference was 1.08 mGy, and the average overall percent difference was 8.9% (see Table IV.3).

Table IV.3: Results of matching each patient-specific dataset to closest phantom matched by gender, age, and average torso diameter.

Patient ID	Phantom ID	Patient Age (years)	Phantom Age (years)	Patient Diameter (cm)	Phantom Diameter (cm)	Avg Dose Difference (mGy)	Avg Percent Difference (%)
1	6	0.7	1	13.1	14.4	1.88	14.1
2	7	1.4	1	14.6	14.7	1.04	8.2
3	14	2.6	3	15.9	16.1	0.87	6.3
4	15	3.4	3	16.4	16.5	0.63	4.7
5	18	4.4	5	17.7	17.7	1.04	7.9
6	16	4.6	5	16.3	16.5	0.92	6.7
7	16	4.8	5	15.8	16.5	1.03	7.4
8	19	5.9	5	18.5	18.4	1.00	7.4
9	16	6.0	5	16.6	16.5	0.97	7.2
10	21	7.4	8	18.3	19.0	0.95	7.4
11	21	8.5	8	18.8	19.0	0.75	5.7
12	30	9.3	10	23.3	23.5	0.59	4.9
13	26	9.7	10	19.3	20.7	0.85	6.8
14	26	10.3	10	20.9	20.7	0.84	6.5
15	29	10.9	10	22.6	22.9	1.26	11.6
16	35	12.6	13	31.2	28.3	1.69	16.2
17	37	14.4	15	26.6	26.7	0.78	7.7
18	36	14.8	15	25.1	26.1	0.70	6.7
19	36	16.8	15	25.3	26.1	0.94	8.8
20	46	0.6	1	13.1	14.8	1.17	9.2
21	46	1.1	1	13.8	14.8	0.80	6.1
22	50	1.6	1	15.9	16.0	1.02	8.0
23	52	2.6	3	14.9	15.1	1.76	12.7
24	52	2.7	3	15.1	15.1	1.81	13.0
25	55	3.0	3	16.4	16.6	0.93	7.0
26	56	4.3	5	16.7	17.1	1.00	7.4
27	56	4.7	5	15.8	17.1	0.79	5.8
28	56	5.7	5	16.9	17.1	1.55	11.6
29	61	6.7	8	18.3	19.0	0.48	3.6
30	62	7.1	8	19.6	19.5	0.88	7.6
31	61	8.5	8	18.8	19.0	0.79	6.3
32	64	9.0	8	20.7	20.8	0.44	3.6
33	70	9.3	10	24.9	23.2	1.28	11.1
34	70	10.7	10	27.6	23.2	1.86	15.5
35	75	12.3	13	29.0	29.0	0.98	9.7
36	71	13.2	13	20.2	25.6	2.48	23.1
37	72	13.6	13	26.2	26.4	0.99	10.1
38	76	14.6	15	23.4	27.7	1.38	13.2
39	76	15.4	15	27.0	27.7	0.72	7.1
40	80	15.9	15	33.8	30.7	1.15	12.3
					Average:	1.08	8.9

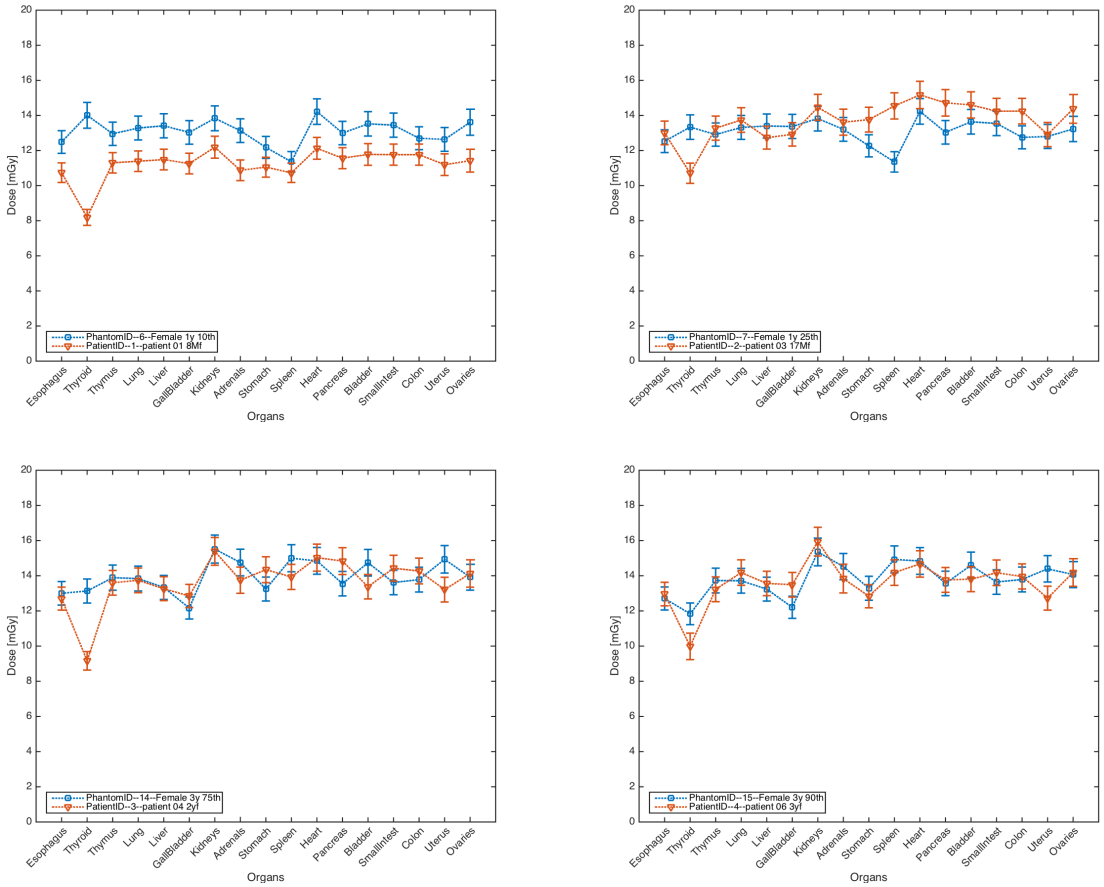

Figure 4.24: Plots of patient-phantom matched organ dose results for patients numbers 1 through 4. Phantom dose data are shown in blue, and patient dose data are shown in orange (all in units of mGy). Error bars correspond to the overall uncertainty calculated for each organ as result of propagating the relative Monte Carlo error with the error in the normalization factor used to convert all simulated doses to absolute dose values.

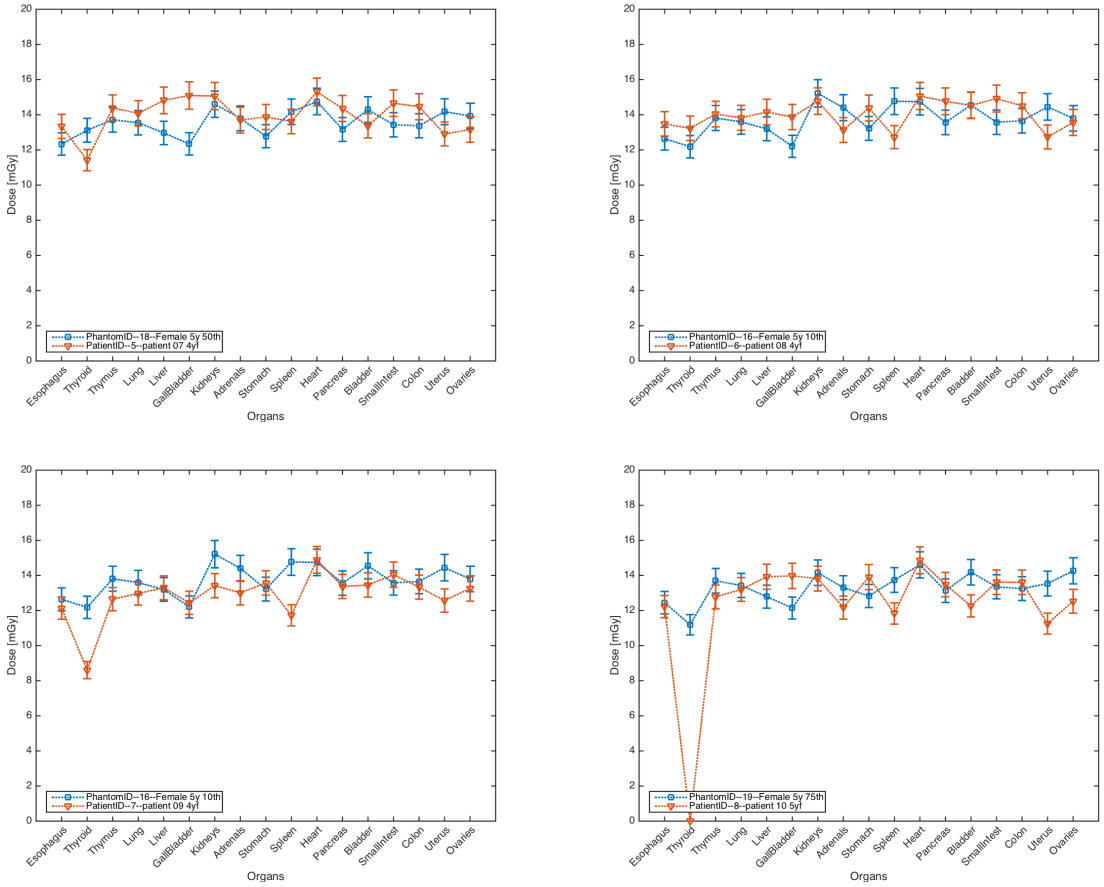

Figure 4.25: Plots of patient-phantom matched dose results for patients numbers 5 through 8. Phantom dose data are shown in blue, and patient dose data are shown in orange (all in units of mGy). Error bars correspond to the overall uncertainty calculated for each organ as result of propagating the relative Monte Carlo error with the error in the normalization factor used to convert all simulated doses to absolute dose values.

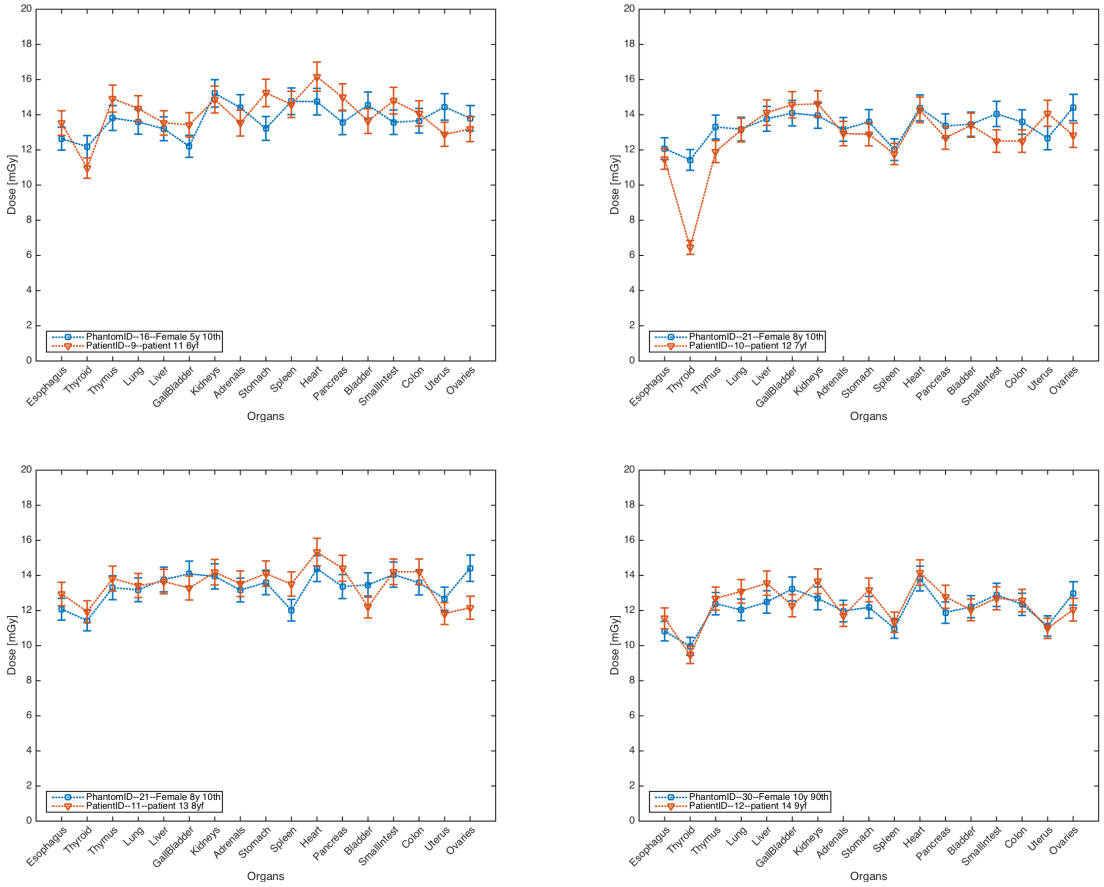

Figure 4.26: Plots of patient-phantom matched dose results for patients numbers 9 through 12. Phantom dose data are shown in blue, and patient dose data are shown in orange (all in units of mGy). Error bars correspond to the overall uncertainty calculated for each organ as result of propagating the relative Monte Carlo error with the error in the normalization factor used to convert all simulated doses to absolute dose values.

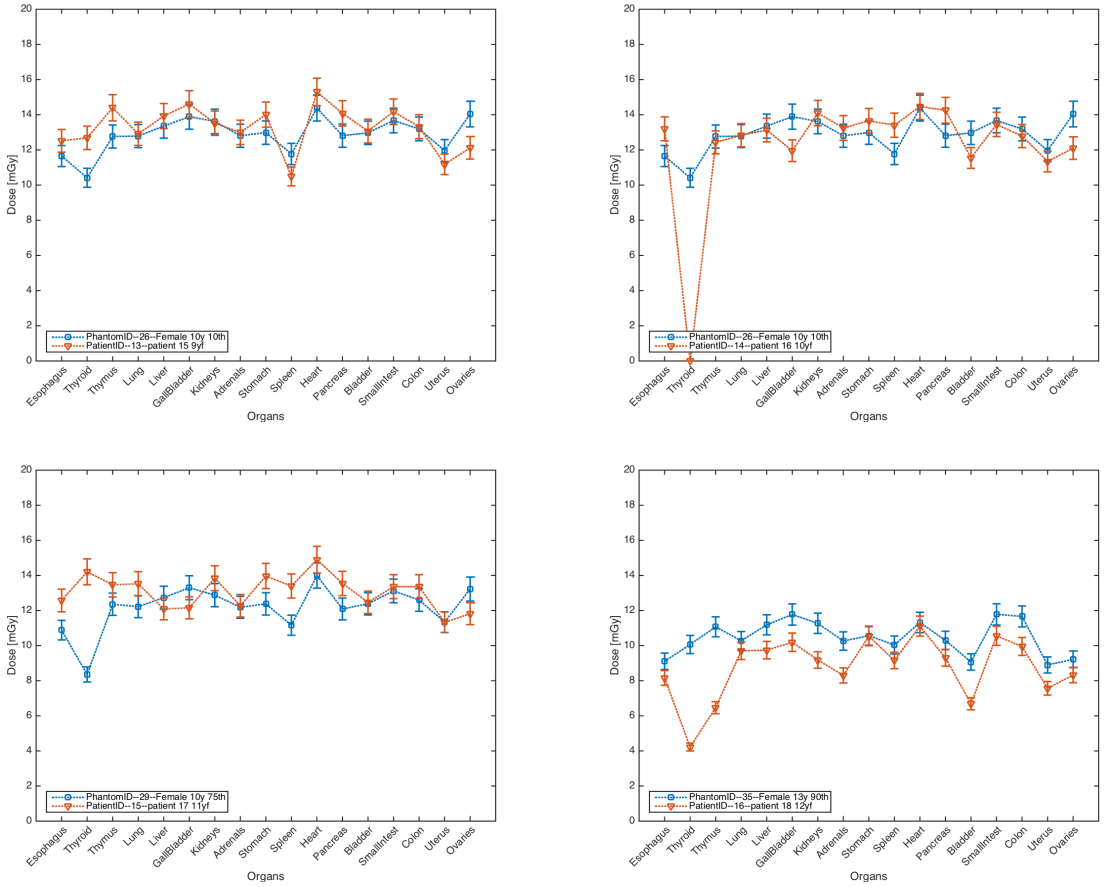

Figure 4.27: Plots of patient-phantom matched dose results for patients numbers 13 through 16. Phantom dose data are shown in blue, and patient dose data are shown in orange (all in units of mGy). Error bars correspond to the overall uncertainty calculated for each organ as result of propagating the relative Monte Carlo error with the error in the normalization factor used to convert all simulated doses to absolute dose values.

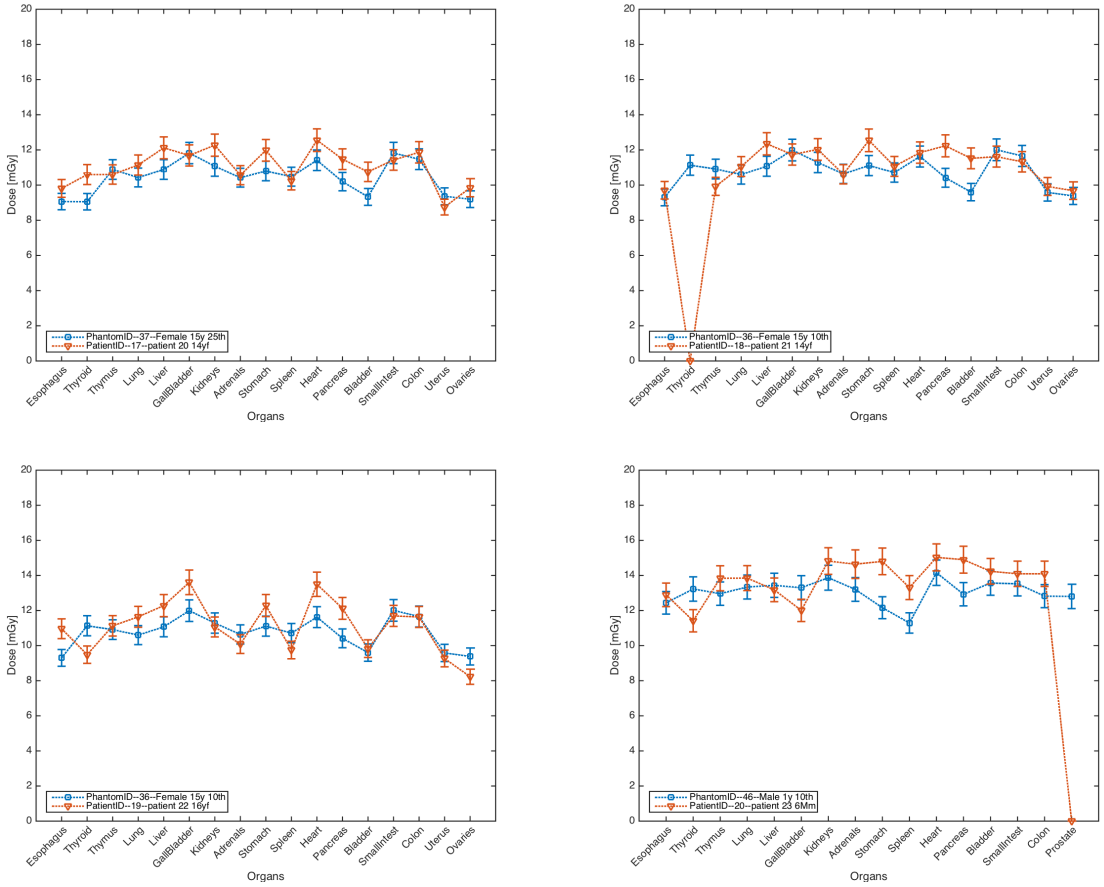

Figure 4.28: Plots of patient-phantom matched dose results for patients numbers 17 through 20. Phantom dose data are shown in blue, and patient dose data are shown in orange (all in units of mGy). Error bars correspond to the overall uncertainty calculated for each organ as result of propagating the relative Monte Carlo error with the error in the normalization factor used to convert all simulated doses to absolute dose values.

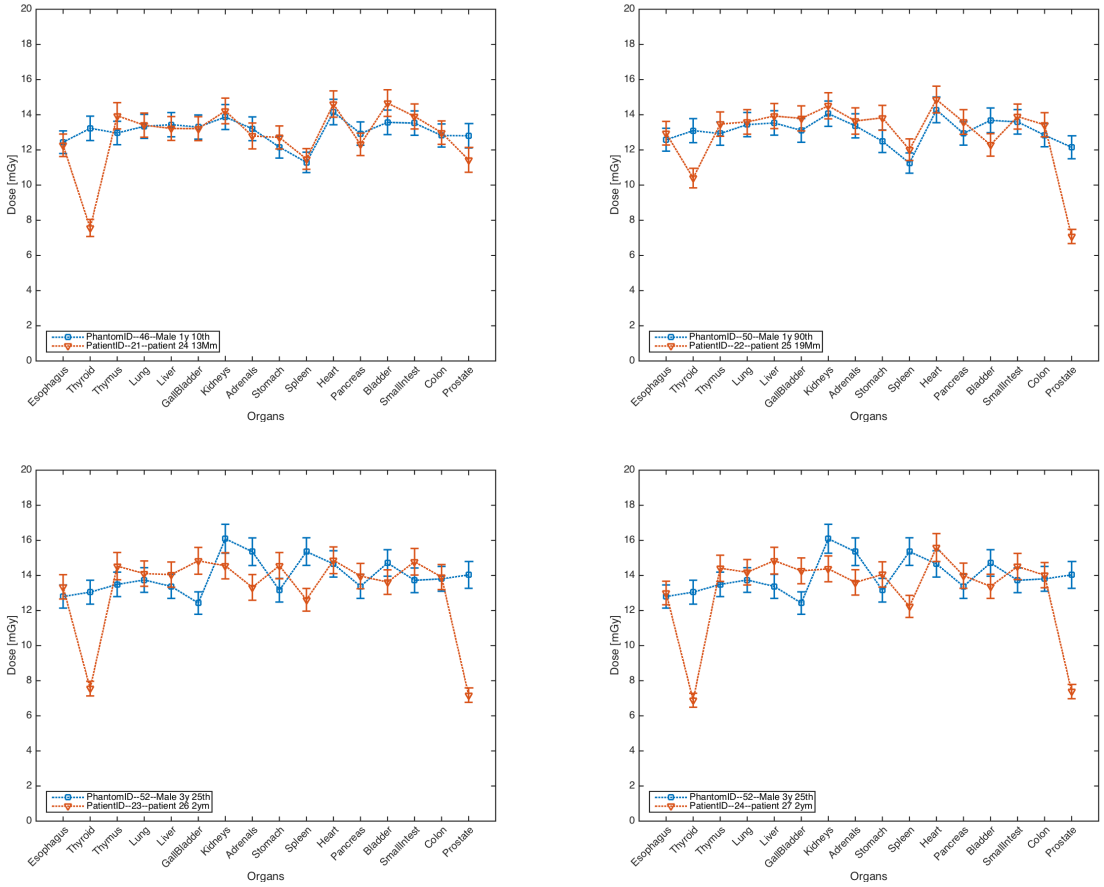

Figure 4.29: Plots of patient-phantom matched dose results for patients numbers 21 through 24. Phantom dose data are shown in blue, and patient dose data are shown in orange (all in units of mGy). Error bars correspond to the overall uncertainty calculated for each organ as result of propagating the relative Monte Carlo error with the error in the normalization factor used to convert all simulated doses to absolute dose values.

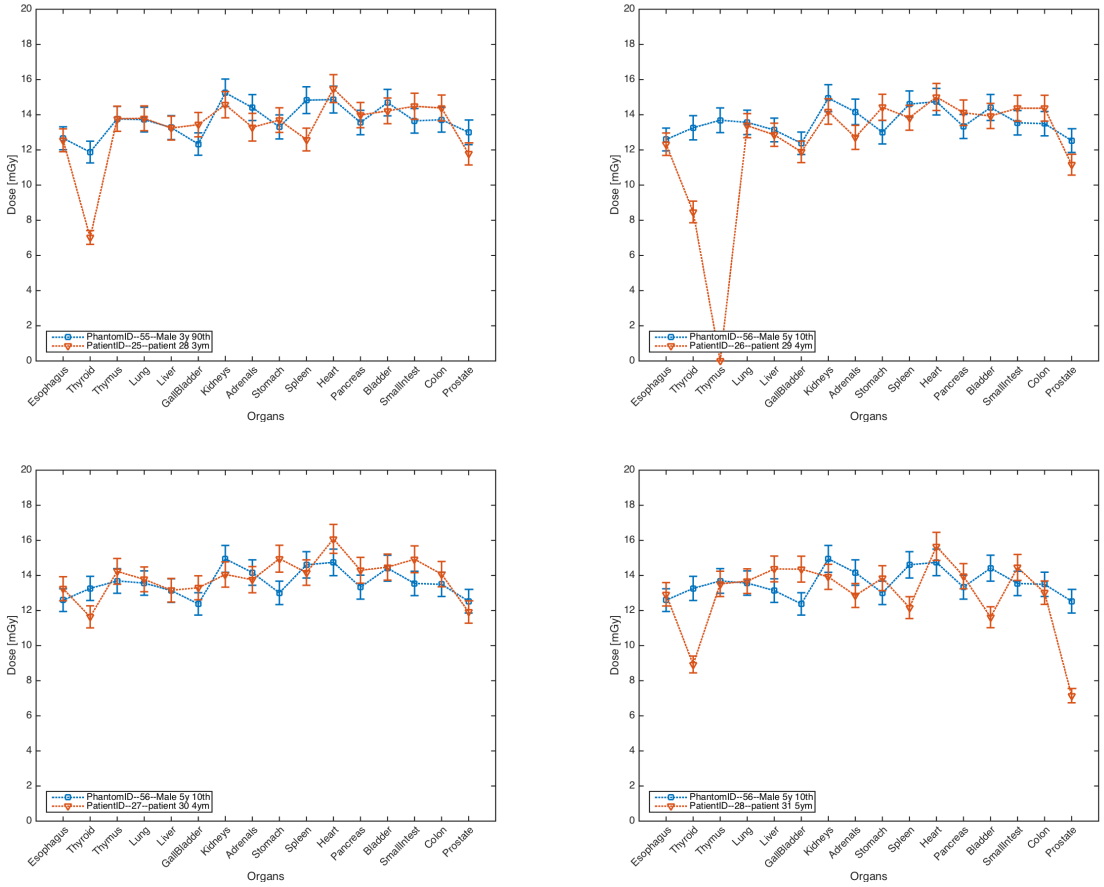

Figure 4.30: Plots of patient-phantom matched dose results for patients numbers 25 through 28. Phantom dose data are shown in blue, and patient dose data are shown in orange (all in units of mGy). Error bars correspond to the overall uncertainty calculated for each organ as result of propagating the relative Monte Carlo error with the error in the normalization factor used to convert all simulated doses to absolute dose values.

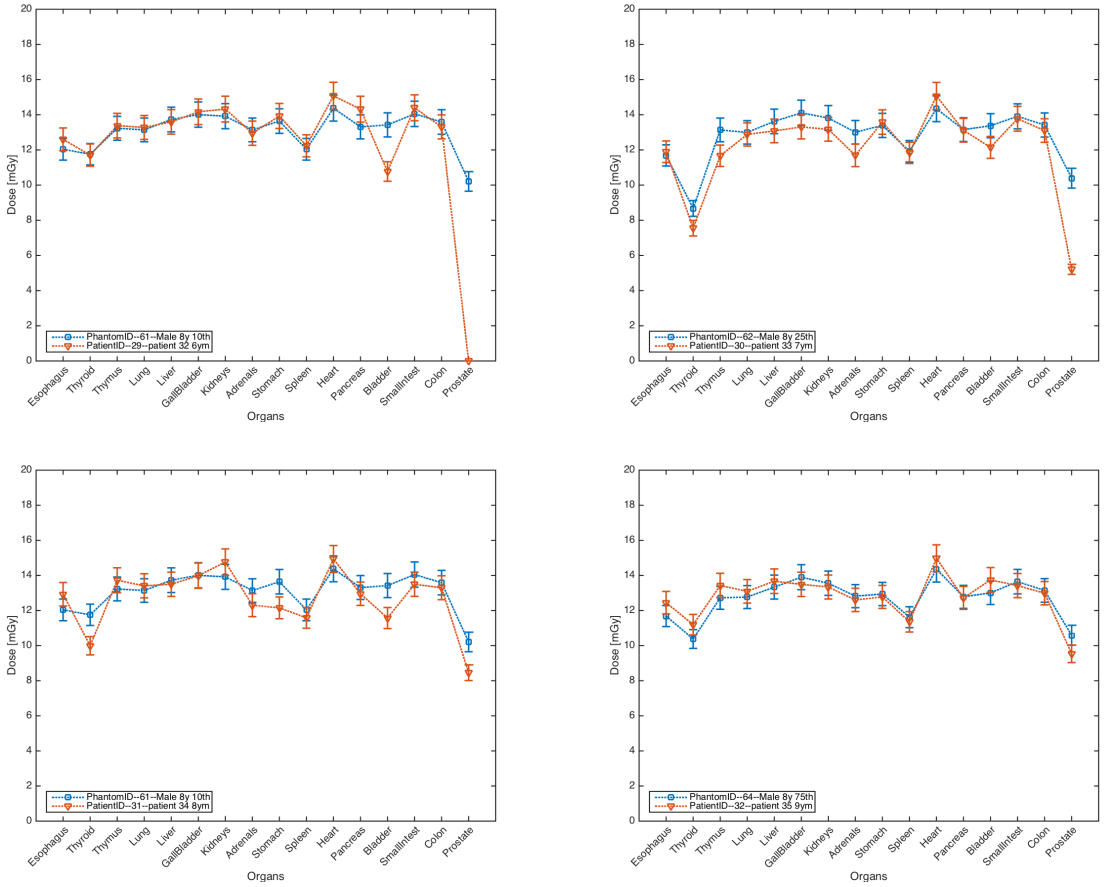

Figure 4.31: Plots of patient-phantom matched dose results for patients numbers 29 through 32. Phantom dose data are shown in blue, and patient dose data are shown in orange (all in units of mGy). Error bars correspond to the overall uncertainty calculated for each organ as result of propagating the relative Monte Carlo error with the error in the normalization factor used to convert all simulated doses to absolute dose values.

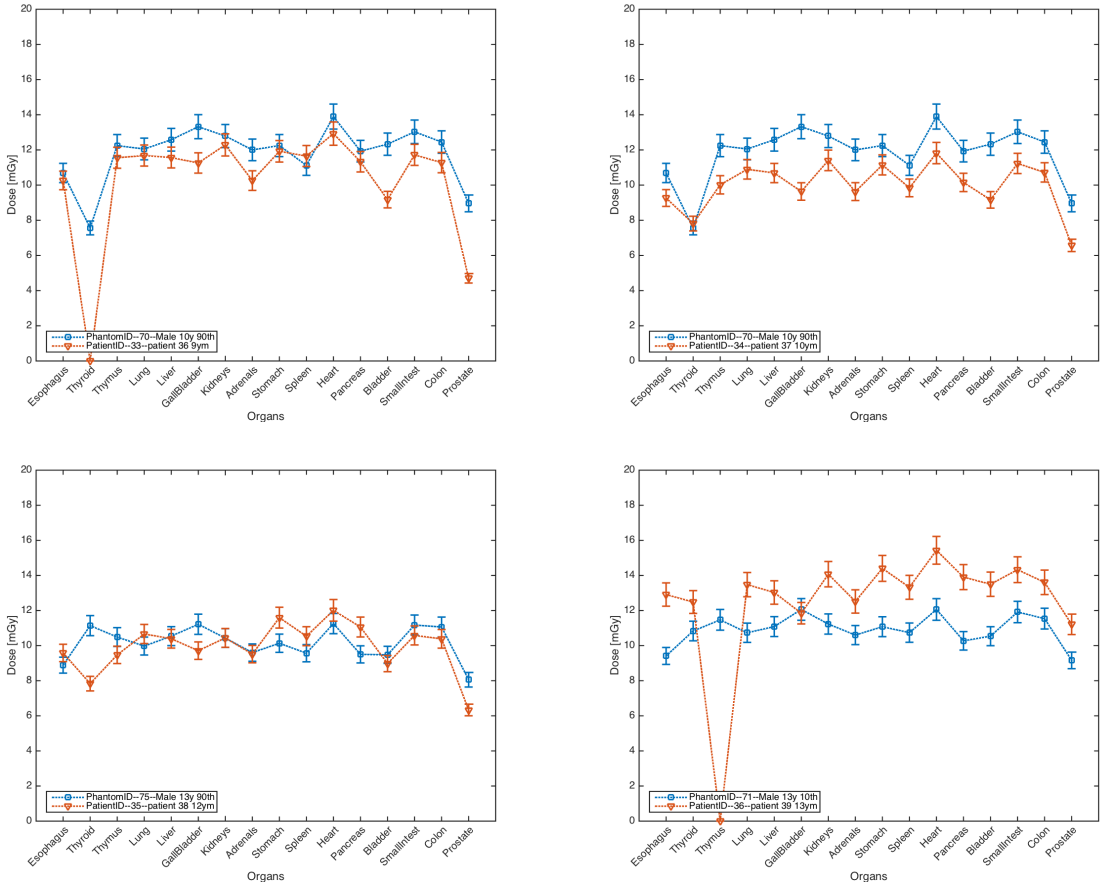

Figure 4.32: Plots of patient-phantom matched dose results for patients numbers 33 through 36. Phantom dose data are shown in blue, and patient dose data are shown in orange. Error bars correspond to the overall uncertainty calculated for each organ as result of propagating the relative Monte Carlo error with the error in the normalization factor used to convert all simulated doses to absolute dose values.

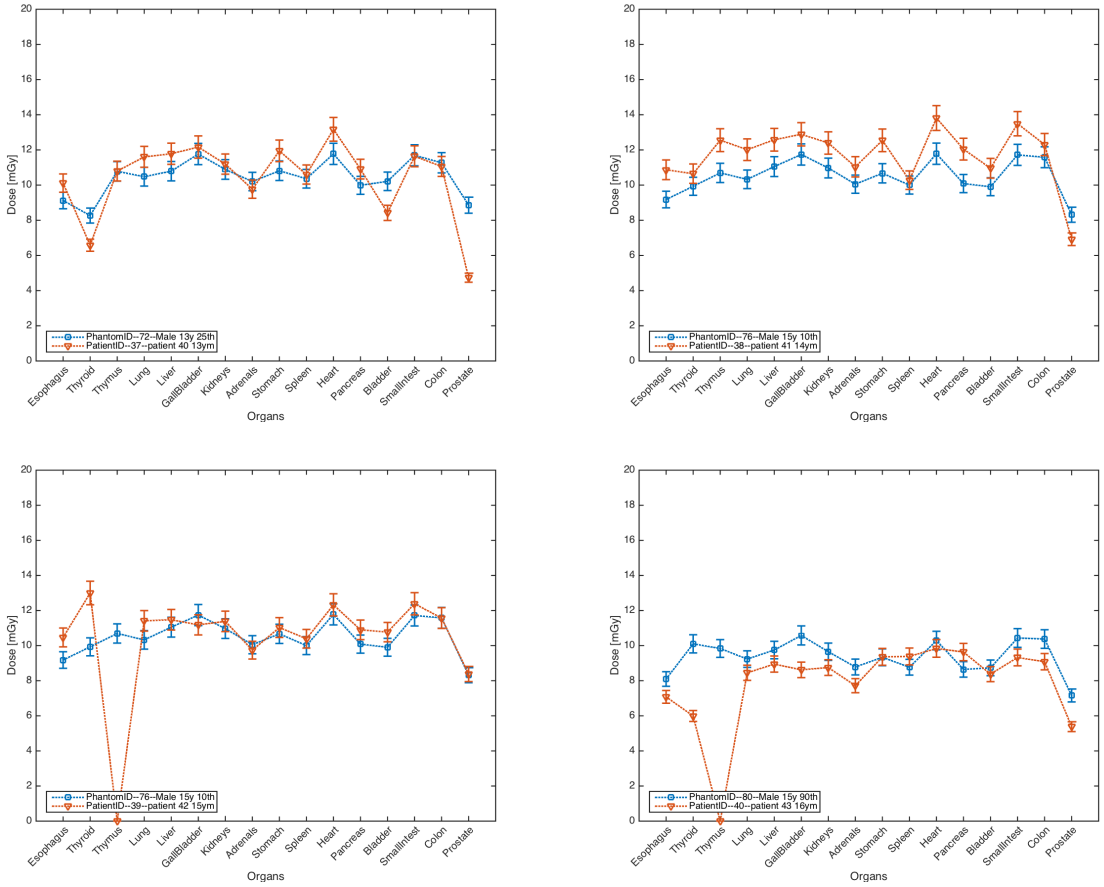

Figure 4.33: Plots of patient-phantom matched dose results for patients numbers 37 through 40. Phantom dose data are shown in blue, and patient dose data are shown in orange (all in units of mGy). Error bars correspond to the overall uncertainty calculated for each organ as result of propagating the relative Monte Carlo error with the error in the normalization factor used to convert all simulated doses to absolute dose values.

4.4 Discussion

Most published studies of patient-specific organ doses have focused on pediatric protocols for chest and abdominopelvic CT scans (e.g., Tian et al., 2014; Li et al., 2011a). Chest-abdomen-pelvis (CAP) studies have also been performed for pediatric reference phantoms, but reported organ doses were limited to a Siemens commercial CT scanner (Lee et al., 2012).

Here, a Philips Brilliance 64 CT scanner was modeled to perform simulations of patients receiving helical CT scans. Patient-specific results came from manually segmented patient images, which were input as voxelized organ maps into the Monte Carlo code. Simulations were also subsequently performed for a large library of NURBS-based anthropomorphic reference phantoms. A variety of specific organ and effective doses were calculated for a diverse range of pediatric anatomies.

Strong correlations were determined between both DLP-normalized organ dose and effective dose and average torso diameter ($R^2 > 0.9$). An exponential function was found to best describe the relationship between dose and the amount of X-ray beam path attenuation through the traversed tissue. The dose deposited from the attenuated X-ray beam decreases as the depth of the organ increases, and this is also observed in patients that have large amounts of subcutaneous fat and moreover, larger torso diameters.

Exponential fits of DLP-normalized organ dose to patient diameter (Figures 4.11 through 4.19) may allow patient-specific organ doses from chest-abdomen-pelvis CT examinations to be predicted. It may also be possible to use these fit parameters to predict organ doses for patients imaged on other CT scanners (of similar beam collimation and

bowtie filter), since the parameters could be adapted using scanner-specific DLP values and measurements of the average patient torso diameter. These results are a great improvement over current estimation methods (i.e., $CTDI_{vol}$, DLP, and SSDE) of patient organ doses for diagnostic imaging studies of children.

DLP-normalized effective dose similarly showed a strong correlation with average patient torso diameter (Figure 4.10). This method of estimation of effective dose is an improvement over the single vendor-supplied value assigned for all patients regardless of age or patient size. However, effective dose values are intended only to be applied to populations averaged over gender and all ages, so the assignment of effective dose to an individual patient is inconsistent with the intended use. Therefore, this value should only be viewed as the estimated aggregated health detriment in a population of patients with similar anatomy and size; caution is needed if one were to apply effective dose estimates that were calculated here.

Each patient's dose results was matched to the closest reference phantom in the database by gender, age, and size. For these CAP data sets, only dose values for the major organs in the torso and field of view were used in evaluating the effectiveness of the match. Absolute dose differences and percent differences between the patient's and phantom's organ dose results were calculated, and overall averages for each patient-phantom match were calculated (Table IV.3). Average percent differences ranged from 3.6 to 23.1%, and average dose differences were on the order of 0.44 to 2.48 mGy. For all 40 patient data sets, for all of the matches performed, there was an average dose difference of 1.08 mGy and an overall average percent difference of 8.9%. Figures 4.24 through 4.33 show each patient's dose results plotted with the matched phantom's dose results. As one

can see, not all organs that would normally be within the scan range for the patient are present (e.g., thyroid, ovaries, and prostate). In these cases, the average differences in the match were naturally higher. However, the differences most often ranged at the level of approximately 1 mGy and percent differences $< 10\%$, so these differences were found to be reasonable and acceptable clinical dose estimates.

4.5 Conclusion

Organ and effective doses were calculated for pediatric patients receiving chest-abdomen-pelvis (CAP) CT exams. A strong relationship was observed between dose and average patient torso diameter, and the results were best fit by linear regression to an exponential function. Additionally, by measuring patient diameter and scanner output ($CTDI_{vol}$, DLP), estimates of dose from other similar CT scanners may also be made. However, other scanner-specific parameters such as bowtie filtration and beam collimation may also affect the specific relationship, thus attention must be given to these other parameters when extrapolating these dose coefficients to other scanners.

A large set of pediatric reference phantoms have been developed at Vanderbilt that include both genders, a wide range of ages (newborn to 15 years), and varying body sizes for normal stature children. This database provides a large amount of data that can be used to compare to individual patient-specific voxel phantoms developed from CT images. The doses calculated using this phantom database provide improved, more accurate, and realistic estimate of pediatric patient dose.

The ability to match an individual patient to a phantom in the database has been demonstrated with a high degree of confidence. Overall, this method of dose estimation

provides great improvements over current CT vendor-supplied values. Perhaps most significantly, this method offers a way to predict patient dose prior to CT examination as well as for use in retrospective risk-analysis studies, which were not previously possible.

Chapter V

BONE AND MARROW DOSE RESULTS

5.1 Bone Tissue

Bones are organs that consist of cortical and trabecular bone and associated structures, including: cartilage, periosteum, red and yellow marrow, and blood. Bone tissue is made up of a mostly organic matrix of various components, including several different proteins, carbohydrates, and lipids, along with inorganic salts. The bone tissue material largely consists of collagen, a major protein (Triffitt, 1980). Microscopic deposits of calcium phosphate comprises the bulk of the inorganic matter (Neuman, 1980; Fawcett and Bloom, 1986).

Cortical and trabecular bones differ in their hardness, porosity, and soft-tissue content. The outer walls of all bones are made of compact bone, which is very hard and dense. Most of the compact bone material in the body is found in the shafts of the long bones. Trabecular bone, also called "cancellous" or "spongy" bone, is located in the ends of the long bones as well as in the interior of flat bones. This soft, spongy bone has a lattice-like structural appearance and a much higher porosity and soft-tissue content (bone marrow) than compact bone. However, bone tissues may not always be easily classified as compact or trabecular since there is often a transition zone of bone tissue that is the intermediate of both types (Parfitt, 1988). In this work, "trabecular bone" will refer only to the osseous tissue, and trabecular bone tissue plus its soft tissue components will be referred to as "spongiosa".

5.1.1 Compact and Trabecular Bone

On average, 75-85% of bone mass in the body is compact bone, with the rest generally as trabecular bone (Parfitt, 1988; Johnson, 1964; Frost and Straatsma, 1964). The greatest percentage of trabecular bone is found in the axial skeleton (Parfitt, 1988). Studies by Johnson (1964) and Spiers and Beddoe (1983) have provided estimates of the percentages of compact and trabecular bone tissues within individual bones. These values are provided in Table V.1.

Table V.1: Cortical and tabecular portions of different bones as a percentage of mass of bone tissue (ICRP 70, 1995).

	Johnson (1964)		Spiers and Beddoe (1983)	
Bone	Cortical	Trabecular	Cortical	Trabecular
Femur	67	33	77	23
Tibia	74	26	83	17
Humerus	80	20	90	10
Radius	84	16	87	13
Ulna	87	13	87	13
Fibula	76	24	89	11
Cervical Vertebrae	25	75		
Thoracic Vertebrae	25	75		
Lumbar Vertebrae	34	66		
Sacrum	75	25		
Innominate	90	10		
Skull	95	5		
Hands	95	5		
Feet	65	5		
Chest cage (clavicle, sternum, scapula, ribs)	94	6		

For long bones, the amount of trabecular bone is higher in the metaphyses than the relatively low amounts in the diaphyses. Bohr and Schaadt (1985) studied the femora of adult females and males (aged 37 to 95 years) and found that the percentage of cortical ash in the neck of the femur to be an average of 57%, whereas the average percentage in the shaft was 95%. Bohr and Lund (1987) and Bohr and Schaadt (1987) found that the proximal tibia plateau contained 55-75% trabecular bone versus the midshaft where they saw less than 1%. A large percentage (80-90%) of trabecular bone was found by Schlenker and VonSeggen (1976) within the first 3 centimeters of the styloid tips of the radii and ulnae, but they found a low amount (0.5-10%) at 3-12 centimeters from the styloid tips.

5.2 Bone Marrow

Bone marrow is a soft, highly cellular tissue that is found in the cylindrical cavities of long bones and the cavities within the trabecular bone of the vertebrae, ribs, sternum, and the flat bones of the cranium and pelvis. Total bone marrow consists of a spongy, reticular, connective tissue framework called stroma, blood-cell-forming tissue, fat cells, small accumulations of lymphatic tissue, and numerous blood vessels (ICRP 70, 1995). Bone marrow is made up of many different components in the trabecular spaces, with more primitive cell types closest to the trabeculae (Figure 5.1). There are two main types of marrow cells with very different functions: red marrow (hematopoietic cells) and yellow marrow (fat cells).

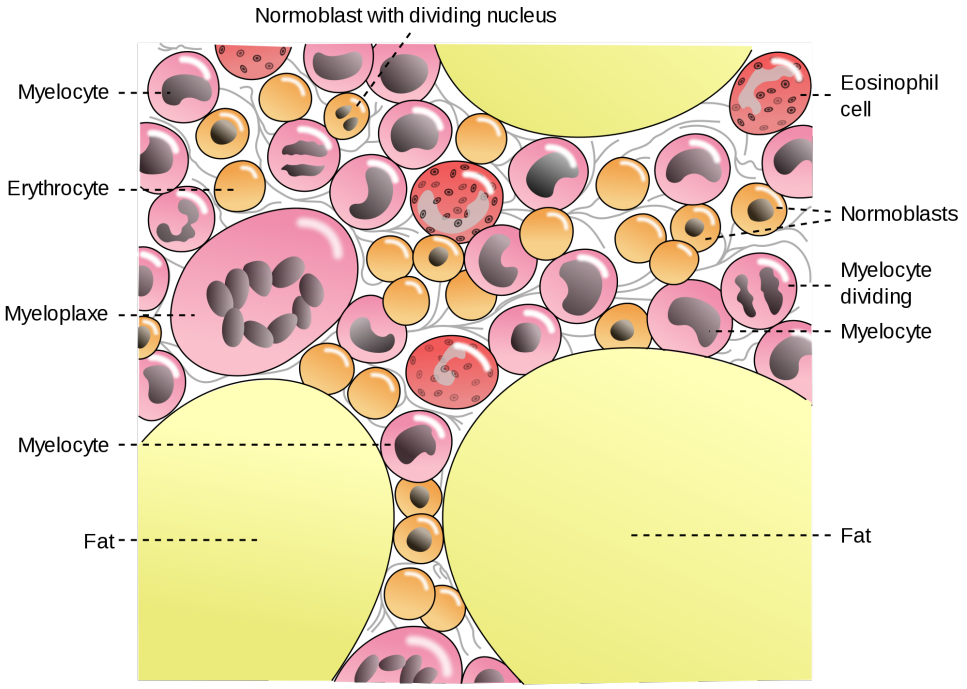

Figure 5.1: Marrow cells (Wikipedia, 2010).

5.2.1 Red Marrow

Red marrow is found in many of the large, flat bones of the body, such as hips, ribs, and skull. Within it are immature blood cells, macrophages, fat cells, and reticular cells (secretion of fibers). Red bone marrow is responsible for blood cell formation (hematopoiesis) and contains cells at all developmental stages. The three main types of blood cells produced here are:

- Red blood cells—transport oxygen from the lungs to the rest of the body,
- White blood cells—defend the body from outside intruders, infections, and diseases, and
- Platelets—involved in healing wounds, stop bleeding, and repair the blood vessels when the vessels are broken.

Each type of blood cell is produced in different numbers in response to changing body needs and different regulatory factors.

Although the various formed elements have different functions, there are similarities in their life histories. All arise from the same type of stem cell, the pleuripotent hematopoietic stem cell, or hemocytoblast, which resides in the red bone marrow. However, their maturation pathways differ, and, once a cell is committed to a specific blood cell pathway, it cannot change (ICRP 70, 1995; Marieb and Hoehn, 2007).

5.2.2 Yellow Marrow

Yellow marrow is found in the central cavities of many of the long bones of the body (such as the femur). It is yellow because it is composed almost entirely of fat cells. As humans grow older, the amount of yellow marrow in their bones increases as their need to store fat increases. In times of famine this supply of fat cells can be consumed. Additionally, when the red marrow is not capable of producing enough new blood cells, yellow marrow can be converted back into red marrow (Marieb and Hoehn, 2007).

5.2.3 Temporal and Spatial Distribution

All bones contain haemopoietically red, active marrow at birth, but over the course of childhood, bone marrow increases in its fractions of yellow, inactive marrow. This happens gradually over decades in some bones, but much more rapidly in others. For example, by adulthood almost all of the marrow in the long-bone shafts has been replaced by yellow marrow. In contrast, fatty yellow marrow begins replacing the active red marrow in the toes and feet in the infant by the age of 1 year (Emery and Follett, 1964).

Red marrow is typically located within the trabecular cavities of spongy bone of long bones and in the diploë of flat bones (i.e., skull, sternum, scapulae, ribs, and pelvis). In newborn infants, the medullary cavity of the diaphysis and all areas of spongy bone contain red bone marrow. In adults, red marrow is found chiefly in the bones of the axial skeleton, pelvic girdles, and in the proximal epiphyses of the humerus and femur. In most adult long bones, the fat-containing medullary cavity extends well into the epiphysis, and little red marrow is present in the spongy bone cavities. Hence, blood cell production in adult long bones routinely occurs only in the heads of the femur and humerus. The red marrow found in the diploe of flat bones (such as the sternum) and in some irregular bones (such as the hip bone) is much more active in hematopoiesis. However, yellow marrow in the medullary cavity can revert to red marrow when a person becomes very anemic and needs enhanced red blood cell production (ICRP 70, 1995).

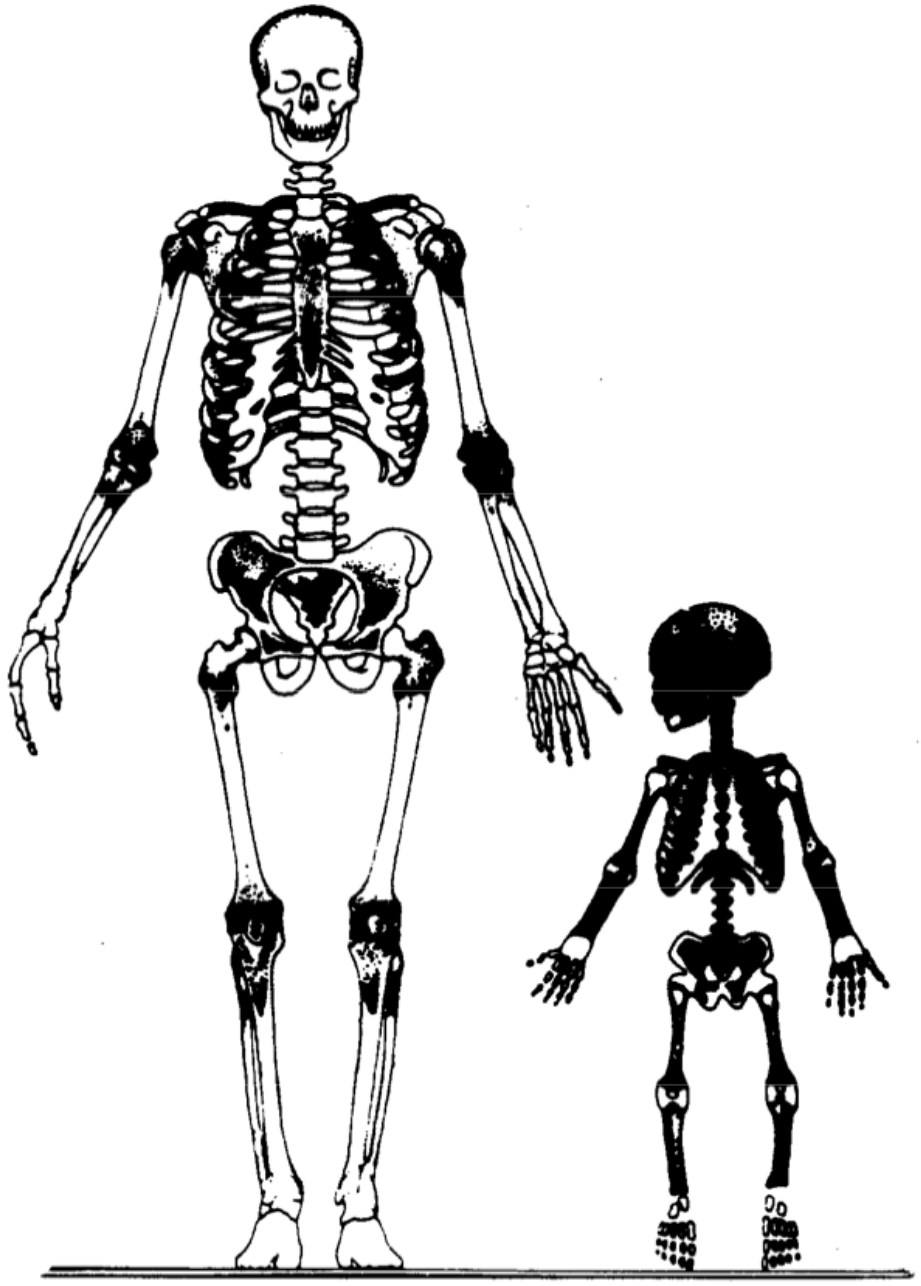

Figure 5.2: Sites of red marrow in the body for adults and children (Bierman, 1961; ICRP 70, 1995).

Hartsock et al. (1965) examined bone marrow from the iliac crests of haematologically normal subjects and found that fatty marrow increased from around 20% to 50% from the age of 5 to 35 years. They also found that the amount of marrow fat stayed stable around 50% until approximately 65 years of age but then increased to about 67% by 75 years of age. Meunier et al. (1971) investigated the volume of marrow fat in the ilium and found that this increased from 15% at the age of 20 years to 60% by the age of 65 years. Additionally, trabecular bone volume was found to decline from 26% to 16% from 20 to 65 years of age.

Table V.2: Bone marrow cellularity data (Cristy, 1981).

	Cellularity factor at various ages (years)						
Bone	0	1	5	10	15	25	40
Vertebrae, sternum, ribs	1.00	0.95	0.85	0.80	0.75	0.72	0.70
Skull, scapulae	1.00	0.95	0.80	0.65	0.55	0.42	0.38
Clavicles	1.00	0.95	0.79	0.63	0.52	0.37	0.33
Upper half of femora and humeri	1.00	0.95	0.77	0.60	0.45	0.30	0.25
Lower half of femora and humeri	1.00	0.89	0.71	0.39	0.10	0	0
Tibiae, fibulae, patellae, ulnae, radii	1.00	0.89	0.57	0.23	0	0	0
Ankle, foot, wrist, and hand bones	1.00	0.50	0.20	0	0	0	0
Os coxae	1.00	0.95	0.79	0.72	0.64	0.58	0.48

The majority of active red marrow is in the ribs, vertebrae, and os coxae by early adulthood, and, of the total active marrow in the body, only about 8% is located within the skull and about 10% in the limbs (ICRP 70, 1995). Quantitative and qualitative age-specific data for marrow cellularity for each individual bone type are provided by Cristy (1981) (Table V.2). Figure 5.3 provides an illustration of the decline of active red marrow in each specific bone as a function of age.

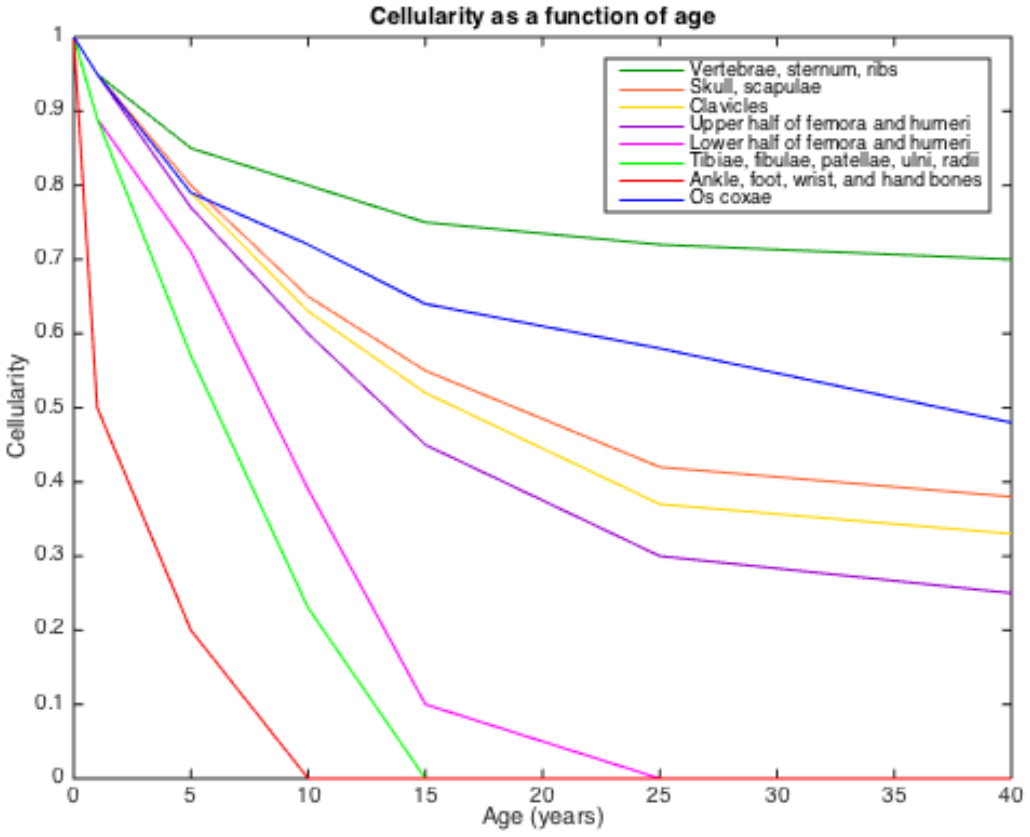

Figure 5.3: Bone marrow cellularity data plotted as a function of age. Data from Cristy (1981).

5.3 Modeling of Bones and Marrow

5.3.1 Marrow Cavity Creation

Models for all of the bones and skeletal surfaces are defined in the XCAT phantoms but not for marrow spaces and cavities, and these must be inserted into the phantoms after all scalings and deformations take place. This happens during the voxelization step in the phantom creation process. A specialized voxelization program was developed to handle the creation of marrow cavities in the NURBS surfaces and is part of the work done for this research project.

To produce appropriate marrow cavities in the bones, the program renders each specific bone at high resolution. A user-defined cortical bone thickness (in units of mm) is defined for each bone type, and each is given to the voxelization program at the time of input. The program then uses these values to erode each bone by the desired thickness to form the inner chamber. A NURBS surface is then fit to the inner chamber. The NURBS surface is initialized, and then control points are inserted to fit the inner chamber. These inner portions of the bones are then defined as marrow cavities.

The pediatric series of phantoms developed here have an age-dependent cortical bone thickness defined. Data from Virtama and Helelä (1969) were used to determine appropriate cortical bone thicknesses as a function of age and gender. Values are listed in Table V.3.

Table V.3: Cortical bone thickness (units of mm) as a function of age and gender (Virtama and Helelä, 1969).

	Females							
Bone	Newborn	1 year	3 year	5 year	8 year	10 year	13 year	15 year
Humerus	1.9	1.9	2.3	2.6	2.9	3.1	3.3	3.3
Radius	1.1	1.1	1.5	1.6	1.9	2.0	2.3	2.4
Ulna	2.5	2.5	2.8	3.0	–	–	3.3	3.3
Hand	0.8	0.8	1.0	1.2	1.4	1.6	1.7	1.7
Femur	2.4	2.4	3.7	4.1	5.5	5.5	5.7	5.9
Tibia	2.2	2.2	3.1	3.4	3.8	4.0	4.7	4.8
Fibula	1.0	1.0	1.5	1.7	2.0	2.1	2.8	2.8
Foot	0.7	0.7	1.1	1.3	1.5	1.6	2.0	2.1
Average	**1.6**	**1.6**	**2.1**	**2.3**	**2.7**	**2.9**	**3.2**	**3.3**
	Males							
Bone	Newborn	1 year	3 year	5 year	8 year	10 year	13 year	15 year
Humerus	2.2	2.2	2.4	2.7	3.6	3.6	3.8	4.6
Radius	1.2	1.2	1.6	1.7	2.2	2.1	2.4	2.8
Ulna	2.5	2.5	2.8	2.6	2.3	2.3	3.0	3.5
Hand	0.8	0.8	1.1	1.2	1.5	1.6	1.7	2.0
Femur	2.8	2.8	3.5	4.5	5.2	6.0	7.2	8.4
Tibia	2.3	2.3	3.2	3.5	4.3	4.6	4.9	5.2
Fibula	1.2	1.2	1.6	2.0	2.4	2.4	3.0	3.0
Foot	0.8	0.8	1.1	1.2	1.5	1.8	2.1	2.2
Average	**1.7**	**1.7**	**2.1**	**2.4**	**2.9**	**3.0**	**3.5**	**4.0**

5.3.2 Marrow Distribution Method

Since cellularity changes as a function of age, phantom age was taken into account in the marrow distribution process. For each marrow cavity of each individual bone type, red and yellow marrow voxels were distributed according to their age-dependent cellularity factors (Table V.2). This resulted in a spatially varying distribution within the phantoms as well as a temporal distribution with age.

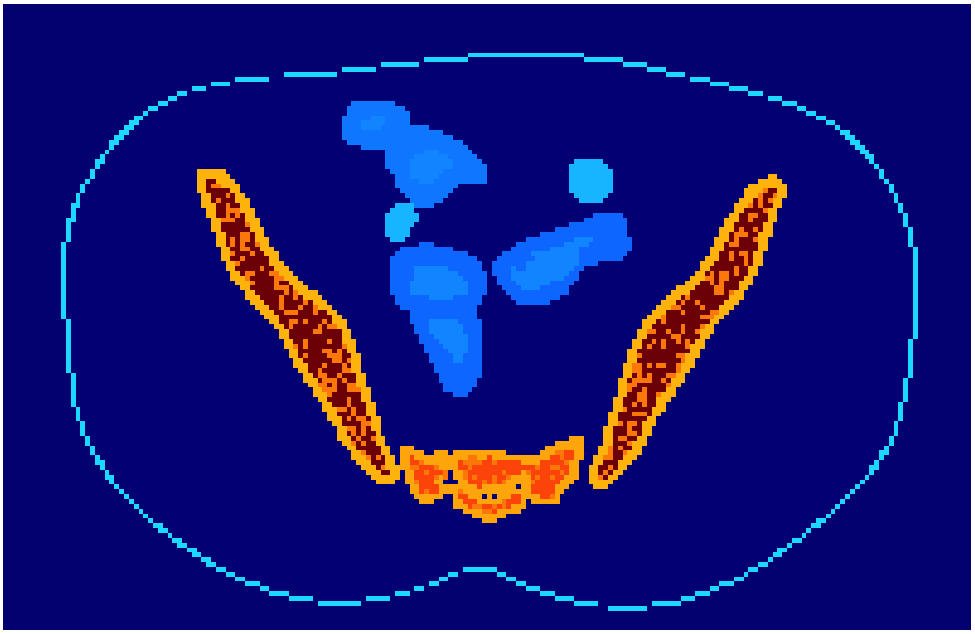

Figure 5.4: Axial slice through the pelvis of the 10-year-old female 50th-percentile phantom showing the distribution of red and yellow marrow voxels.

Cellularities for the reference ages (i.e., newborn, 1-year, 5-year, 10-year, and 15-year) for individual bones are known; however, cellularity factors for non-reference ages are not reported. Therefore, a spline interpolation of the reference values (Table V.2) was calculated in order to determine marrow cellularity values for non-reference ages (i.e., 3-year, 8-year, and 13-year). This was found to achieve a more realistic fit to the cellularity curves than a simple linear interpolation between the reference age values, based on the trends in the data (Figure 5.3).

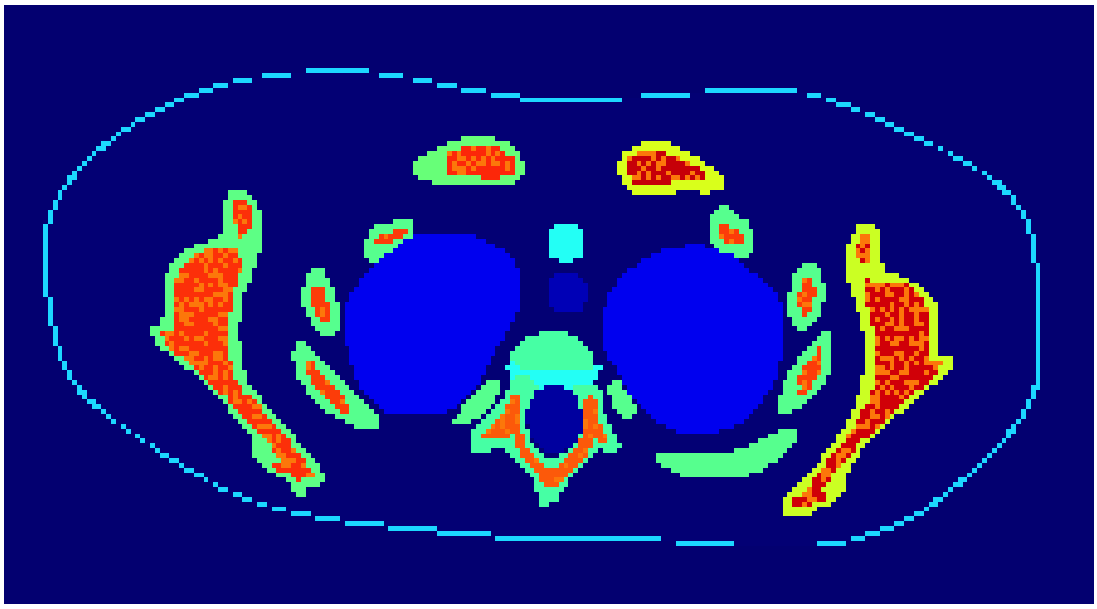

Figure 5.5: Axial slice through the scapulae, vertebrae, and ribs of the 10-year-old female 50th-percentile phantom showing the distribution of red and yellow marrow voxels. Red marrow voxels are shown as a dark red-orange whereas yellow marrow voxels are shown as lighter speckles.

The cellularity factor (fraction of red marrow) was next used to determine the fraction of voxels out of the total number of marrow voxels within the cavity that needed to be defined as red and yellow marrow. For most bones, yellow marrow was seeded according to its correct percentage within the marrow cavity, using a random sampling algorithm. An example of this can be seen in the pelvis, and Figure 5.4 demonstrates this for the 10-year-old female 50th-percentile phantom. Figure 5.5 shows an example slice through the scapulae, ribs, and vertebrae of this same phantom. Another view through the ribs and vertebrae is seen in Figure 5.6. A slice showing the marrow in the cranium of a 5-year-old male phantom is shown in Figure 5.7.

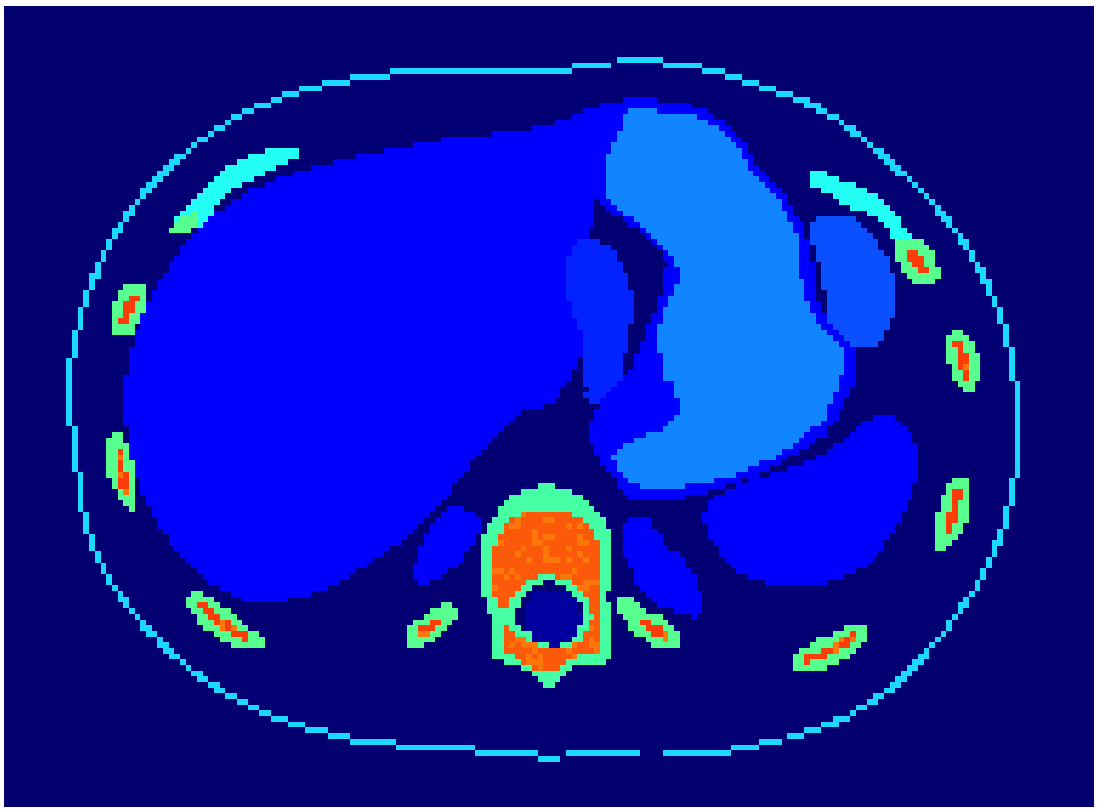

Figure 5.6: Axial slice through the vertebrae and ribs of the 10-year-old female 50th-percentile phantom showing the distribution of red and yellow marrow voxels. Red marrow voxels are shown as a dark red-orange whereas yellow marrow voxels are shown as lighter speckles.

The marrow distribution process differed slightly for some bone types including all of the long bones as well as the bones of the hands, wrists, feet, and ankles. In these bones, marrow was not distributed as a random sampling; rather, a spatial-dependent seeding algorithm was necessary. As previously discussed, the conversion to yellow marrow happens rapidly in these bones. Additionally, the amount of red marrow is seen to recede in a directional fashion away from the fingers and toes, and this is also true for the radii, ulnae, tibiae, and fibulae. Therefore, marrow distribution in these cases mimicked this behavior. Other bones including the femora and humeri were also treated in the same manner except that the upper and lower halves were treated separately with the red marrow receding away from the diaphysis (middle of the shaft) in both cases. Additionally, the upper and lower halves of these bones are reported to have different cellularity values (Table V.2) according to Cristy (1981). An example in the femora of the 10-year-old female can be seen in Figure 5.8.

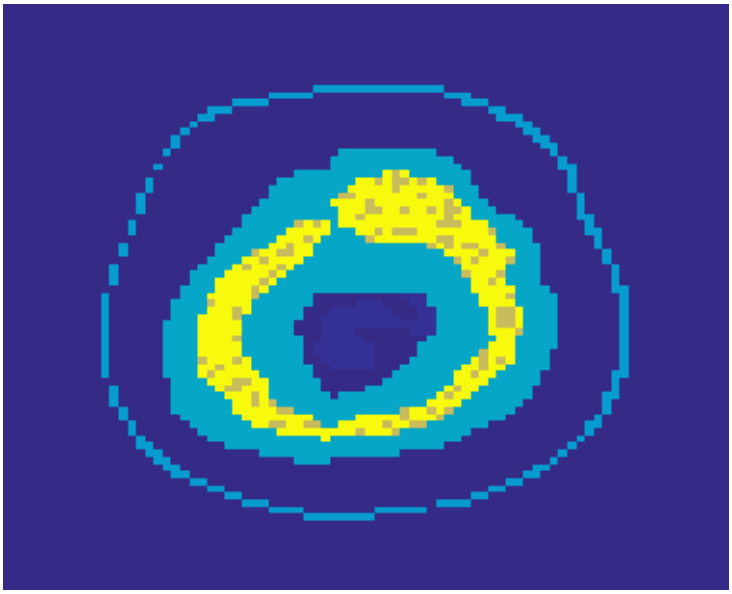

Figure 5.7: Axial slice through the cranium of the 5-year-old male 50th-percentile phantom showing the distribution of red and yellow marrow voxels. Red marrow voxels are shown as yellow whereas yellow marrow voxels are shown as brown speckles.

Once red and yellow marrow voxels were distributed in the phantoms, they were assigned as different materials with different physical properties in the GEANT4 simulations. As described in Chapter IV, age-dependent bone properties were also defined according to White and Wilson (1992) (Table IV.1). For vertebrae, where there is a higher percentage of trabecular bone, a spongiosa mixture was defined to model the mixture of trabecular bone tissue and red marrow. Since we were limited by voxel size ($1.5 \times 1.5 \times 3.0$ mm), it was not possible to model the fine sub-microstructure of the bone tissue itself.

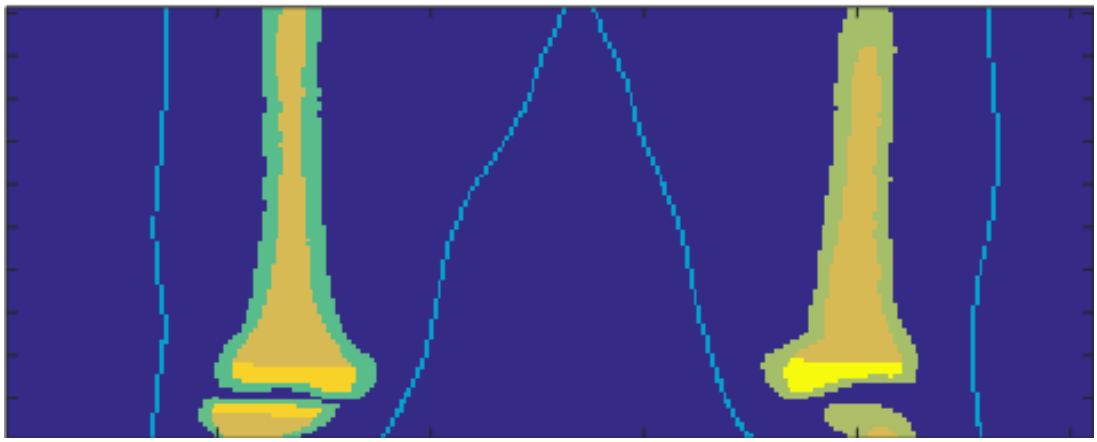

Figure 5.8: Coronal (frontal) slice through the 15-year-old female 50th-percentile phantom showing the spatial distribution of red and yellow marrow in the femora. By adolescence, most of the marrow in the long bones is in the form of yellow marrow. Yellow marrow is shown as light brown within both femur bone cavities, and red marrow is shown as yellow on the right and gold on the left.

5.4 Results

5.4.1 Bone Dose Results

Similar to the organ dose results, an exponential function was chosen to obtain fit coefficient parameters from nonlinear regression:

$$\mathrm{nD}_{\mathrm{bone}}(d) = \exp(\alpha_{\mathrm{bone}} d + \beta_{\mathrm{bone}}). \tag{5.1}$$

Table V.4 provides a summary of all fit parameters from the nonlinear regression of DLP-normalized cortical bone doses within the scan range. As seen with the other organ doses, a strong correlation between dose and torso diameter is indicated by the reported R^2 correlation coefficients and root-mean-squared errors (RMSE). The relationship between DLP-normalized doses and average torso diameter is shown in Figures 5.9 through 5.13 for bones within the field of view or on the edge of the scan range.

Table V.4: Nonlinear regression coefficients for DLP-normalized individual cortical bone doses for simulated CAP CT scans.

	α	β	R^2	RMSE
Cervical Vertebrae	-0.1606	-0.95	0.919	5.95×10^{-3}
Clavicles	-0.0735	-1.38	0.965	4.57×10^{-3}
Femora	-0.1450	-1.15	0.980	2.68×10^{-3}
Lumbar Vertebrae	-0.0835	-0.99	0.991	3.33×10^{-3}
Pelvis	-0.0865	-0.98	0.994	2.61×10^{-3}
Ribs	-0.0679	-1.38	0.991	2.39×10^{-3}
Sacrum	-0.0899	-0.88	0.978	5.55×10^{-3}
Scapulae	-0.0833	-1.31	0.921	7.24×10^{-3}
Sternum	-0.0607	-1.29	0.974	4.41×10^{-3}
Thoracic Vertebrae	-0.0803	-1.12	0.978	4.60×10^{-3}
Total Cortical Bone	-0.0653	-2.24	0.985	1.28×10^{-3}

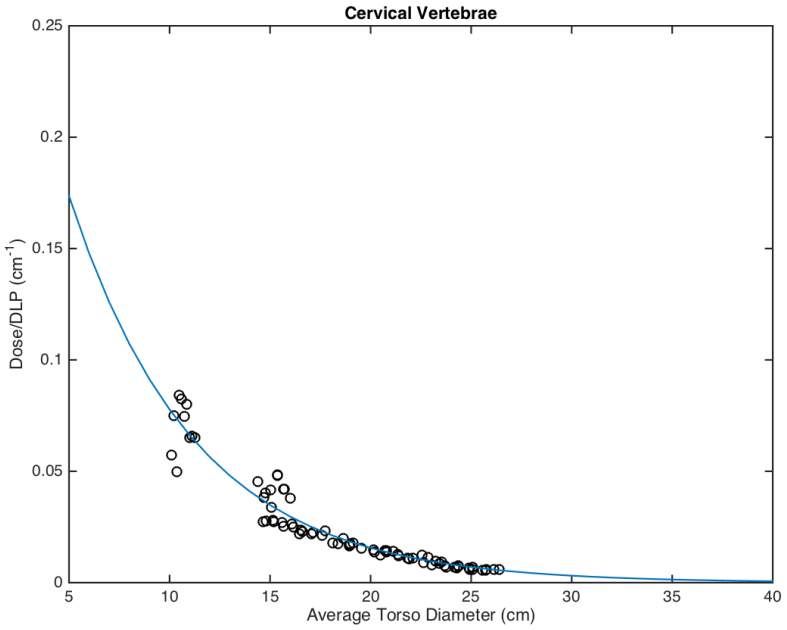

(a)

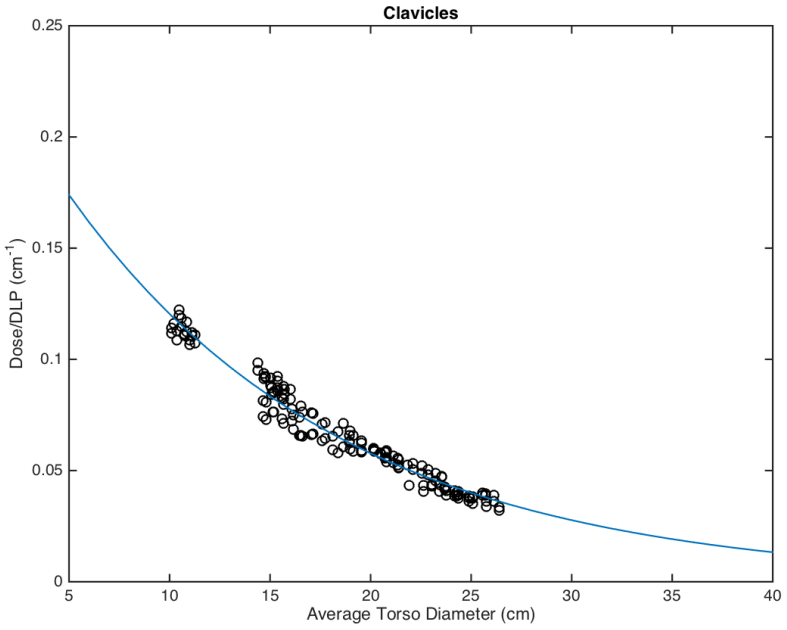

(b)

Figure 5.9: Plots of DLP-normalized bone dose for (a) cervical vertebrae and (b) clavicles, with the corresponding exponential fits demonstrating the dependence of dose on torso diameter.

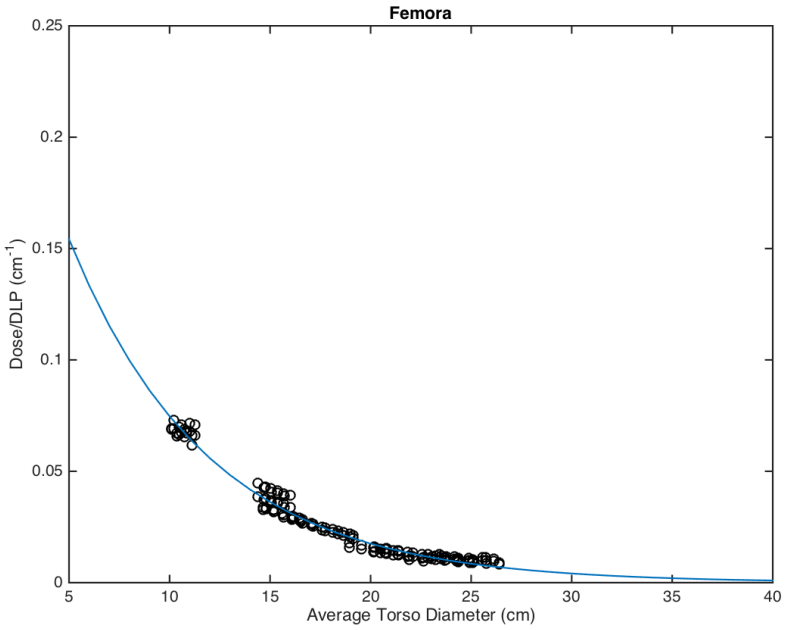

(a)

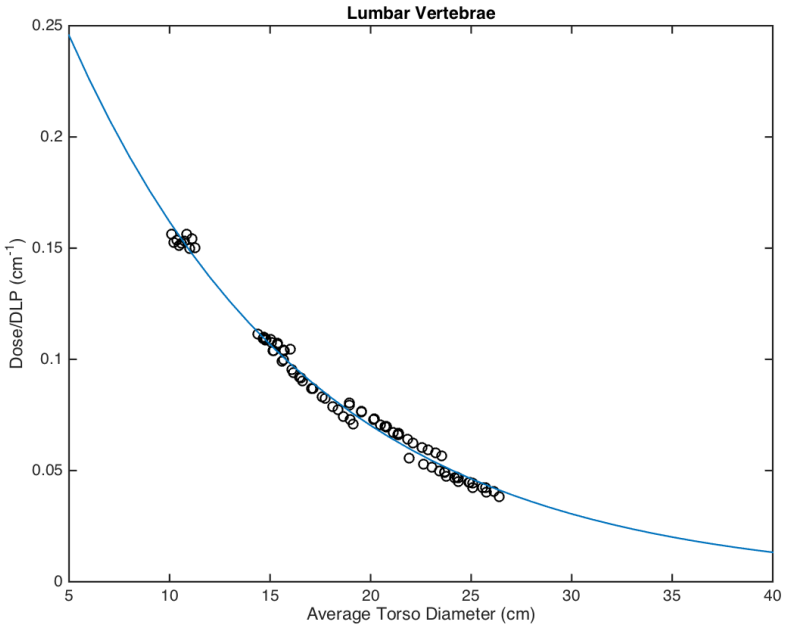

(b)

Figure 5.10: Plots of DLP-normalized bone dose for (a) femora and (b) lumbar vertebrae, with the corresponding exponential fits demonstrating the dependence of dose on torso diameter.

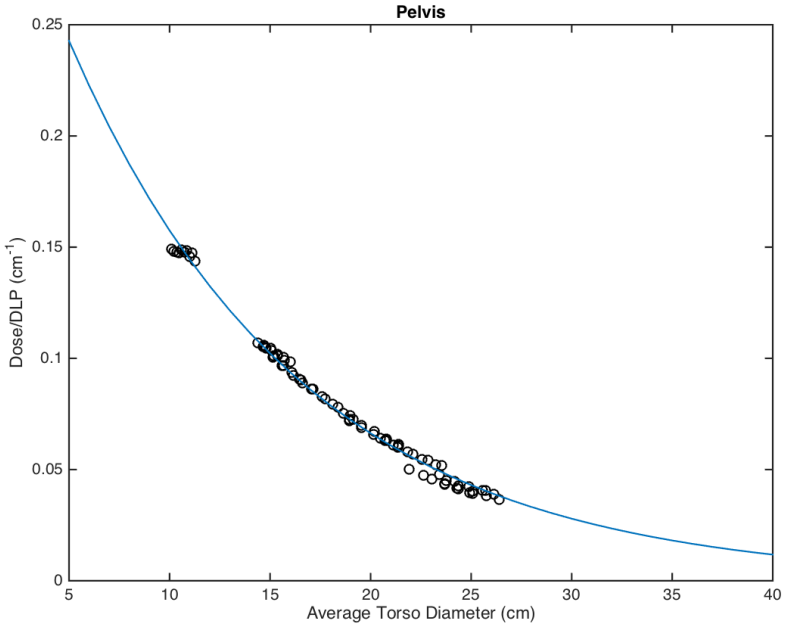

(a)

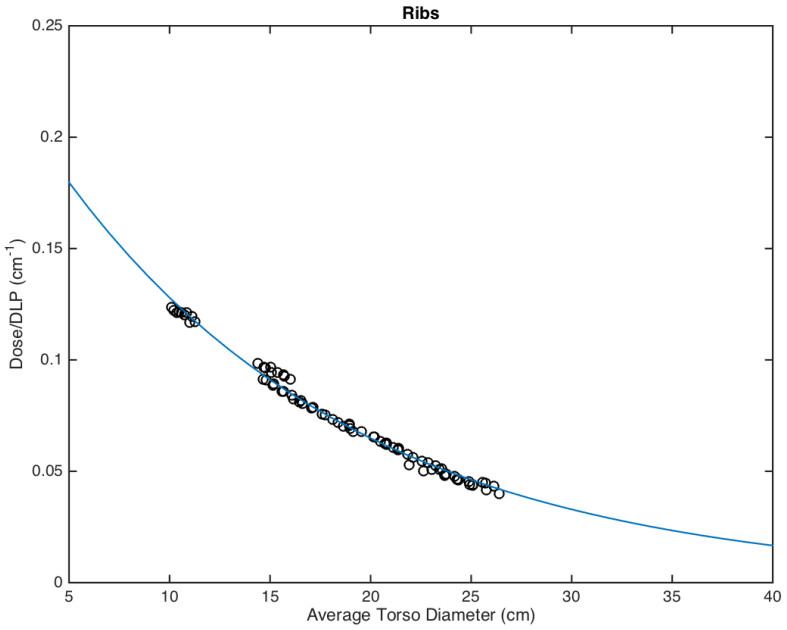

(b)

Figure 5.11: Plots of DLP-normalized bone dose for (a) pelvis and (b) ribs, with the corresponding exponential fits demonstrating the dependence of dose on torso diameter.

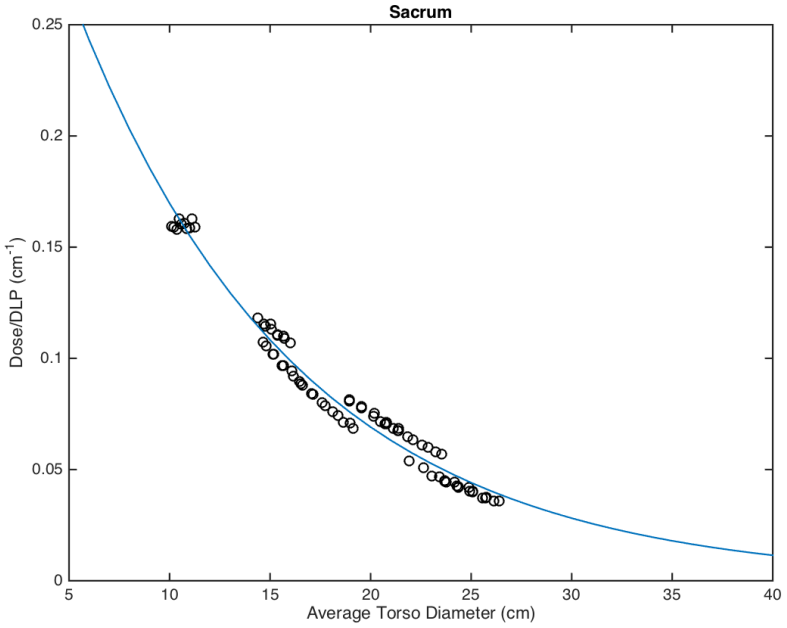

(a)

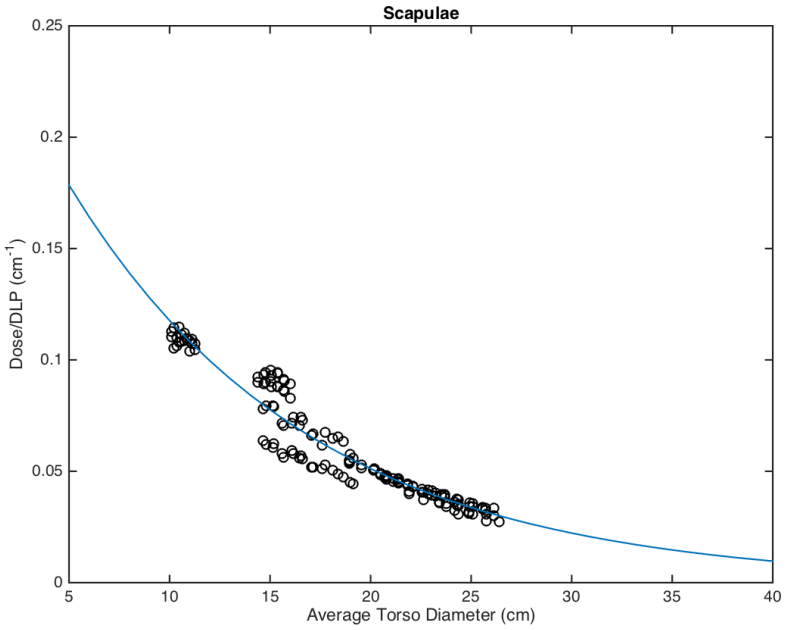

(b)

Figure 5.12: Plots of DLP-normalized bone dose for (a) sacrum and (b) scapulae, with the corresponding exponential fits demonstrating the dependence of dose on torso diameter.

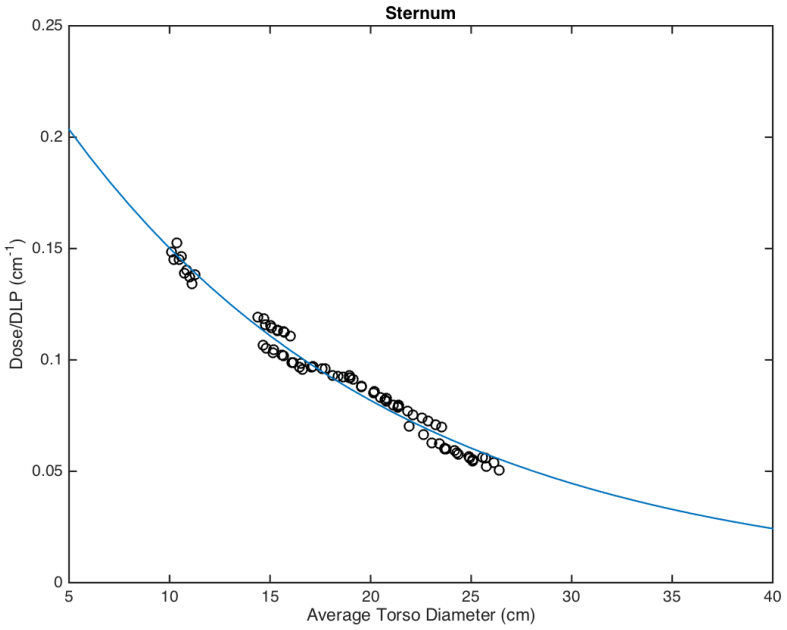

(a)

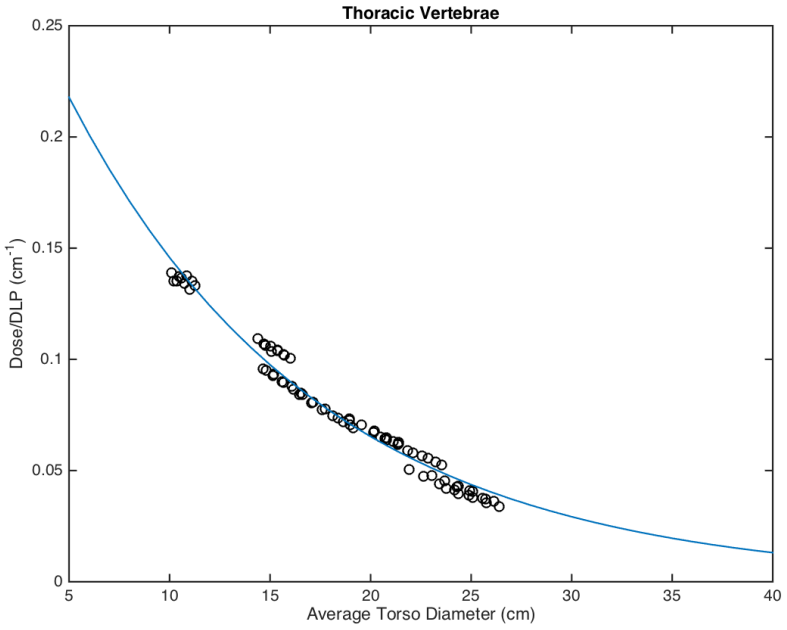

(b)

Figure 5.13: Plots of DLP-normalized bone dose for (a) sternum and (b) thoracic vertebrae, with the corresponding exponential fits demonstrating the dependence of dose on torso diameter.

5.4.2 Marrow Dose Results

For the red marrow results, an exponential function was again chosen to obtain fit coefficient parameters from nonlinear regression:

$$\mathrm{nD}_{\mathrm{marrow}}(d) = \exp(\alpha_{\mathrm{marrow}} d + \beta_{\mathrm{marrow}}). \tag{5.2}$$

A summary of red marrow fit parameters is provided in Table V.5 for the nonlinear regression of DLP-normalized marrow doses within the scan range. Again, a strong correlation between dose and torso diameter is indicated by the reported R^2 correlation coefficients and root-mean-squared errors (RMSE). Figures 5.14 through 5.18 demonstrate the results for all marrow within the field of view.

Table V.5: Nonlinear regression coefficients for DLP-normalized marrow doses for simulated CAP CT scans.

	α	β	R^2	RMSE
Cervical Vertebrae Marrow	-0.2068	-0.69	0.916	4.97×10^{-3}
Clavicles Marrow	-0.1972	-0.47	0.738	1.26×10^{-2}
Femora Marrow	-0.3091	0.50	0.920	5.33×10^{-3}
Lumbar Vertebrae Marrow	-0.1202	-1.03	0.977	3.82×10^{-3}
Pelvis Marrow	-0.1389	-1.42	0.968	2.65×10^{-3}
Ribs Marrow	-0.1726	-0.83	0.923	5.42×10^{-3}
Sacrum Marrow	-0.1932	-0.45	0.918	6.75×10^{-3}
Scapulae Marrow	-0.1277	-1.81	0.955	2.36×10^{-3}
Sternum Marrow	-0.1553	-0.92	0.874	7.54×10^{-3}
Thoracic Vertebrae Marrow	-0.1138	-1.19	0.981	3.16×10^{-3}
Total Red Marrow	-0.0864	-2.50	0.966	1.36×10^{-3}

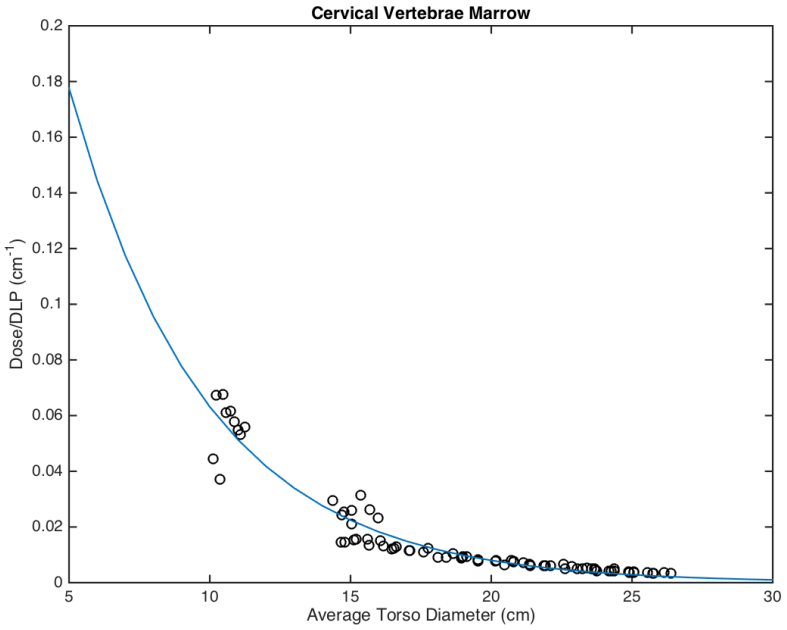

(a)

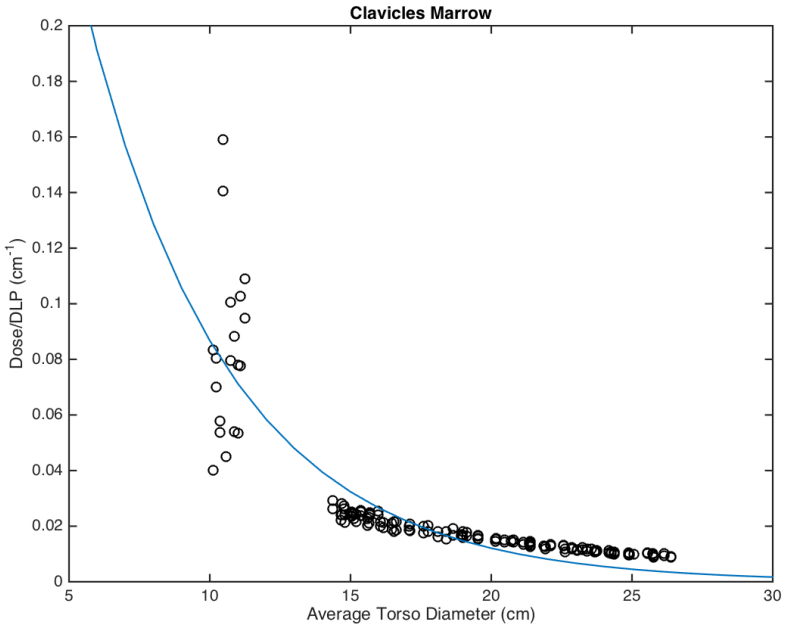

(b)

Figure 5.14: Plots of DLP-normalized marrow dose for (a) cervical vertebrae marrow and (b) clavicles marrow, with the corresponding exponential fits demonstrating the dependence of dose on torso diameter.

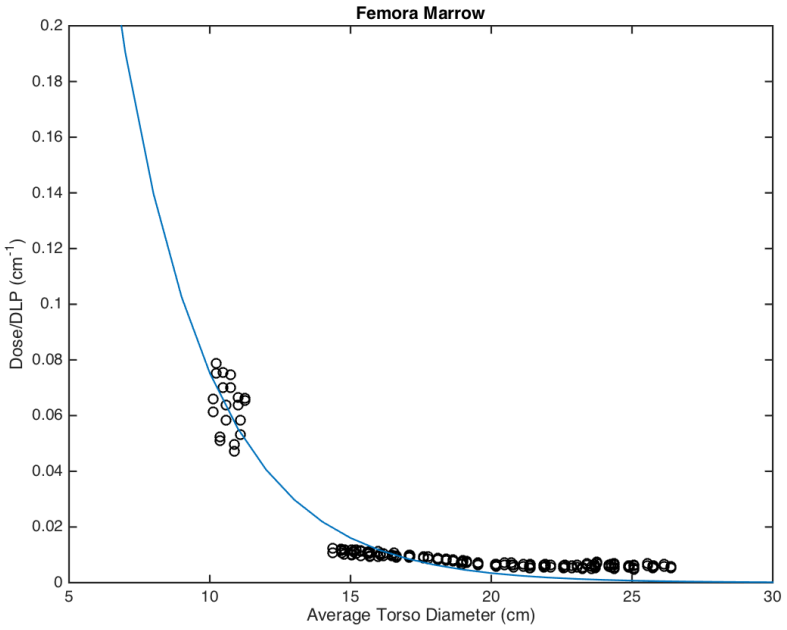

(a)

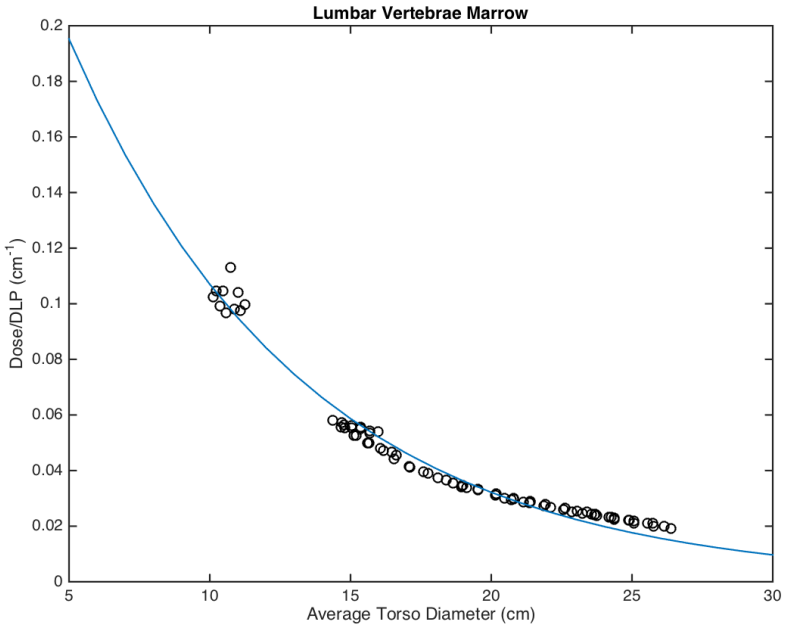

(b)

Figure 5.15: Plots of DLP-normalized marrow dose for (a) femora marrow and (b) lumbar vertebrae marrow, with the corresponding exponential fits demonstrating the dependence of dose on torso diameter.

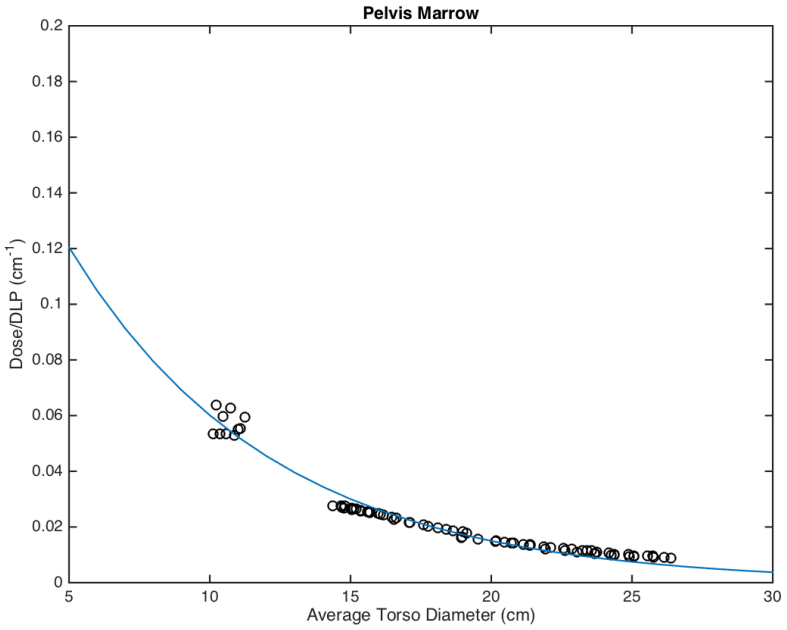

(a)

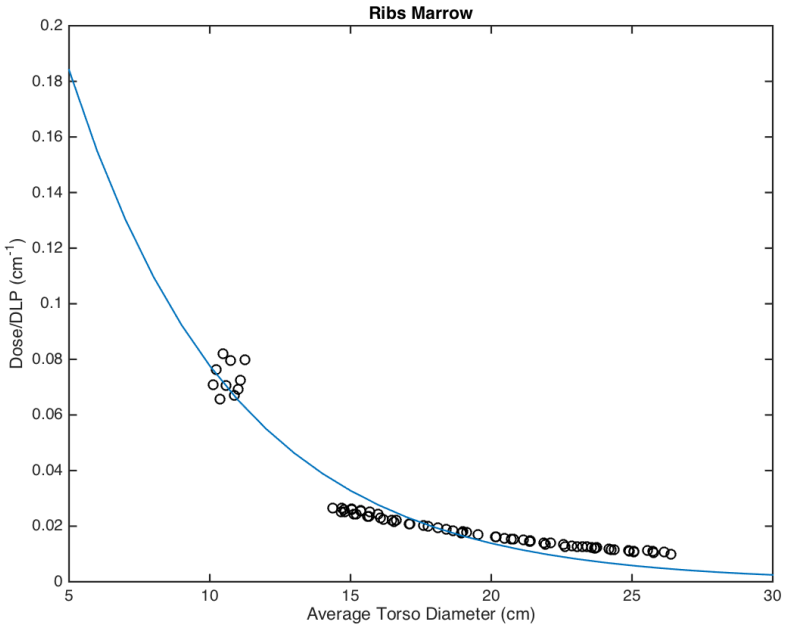

(b)

Figure 5.16: Plots of DLP-normalized marrow dose for (a) pelvis marrow and (b) ribs marrow, with the corresponding exponential fits demonstrating the dependence of dose on torso diameter.

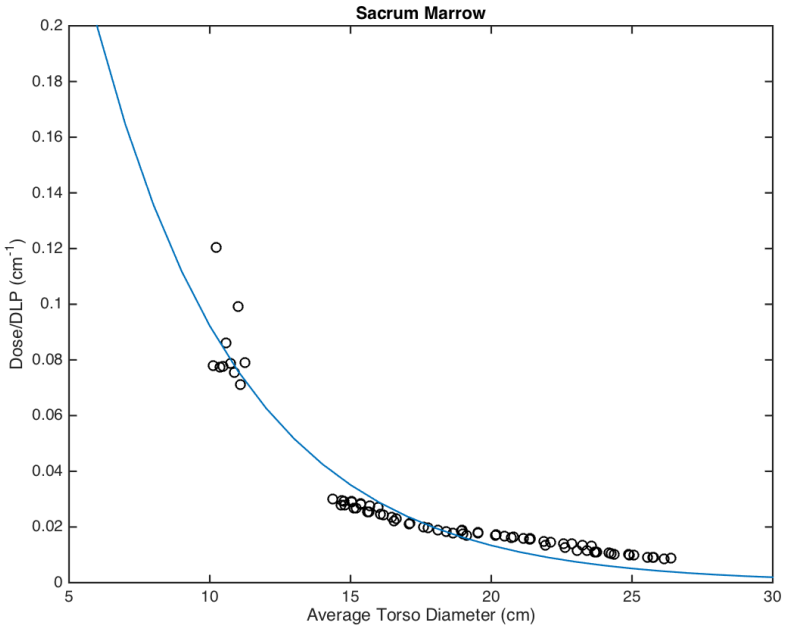

(a)

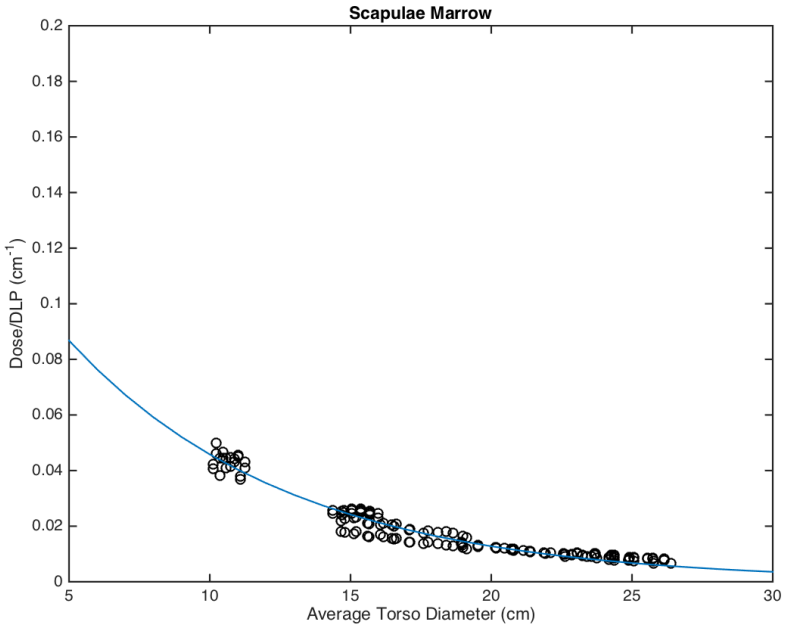

(b)

Figure 5.17: Plots of DLP-normalized marrow dose for (a) sacrum marrow and (b) scapulae marrow, with the corresponding exponential fits demonstrating the dependence of dose on torso diameter.

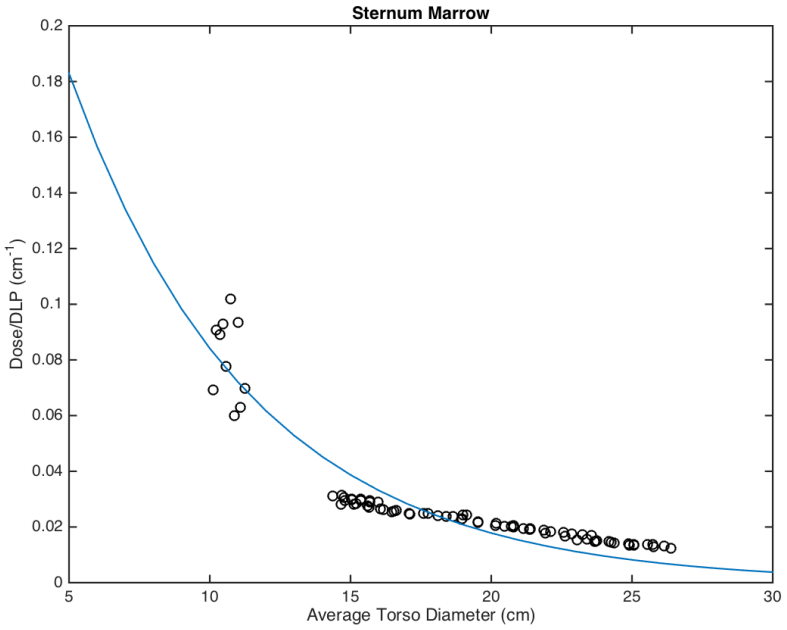

(a)

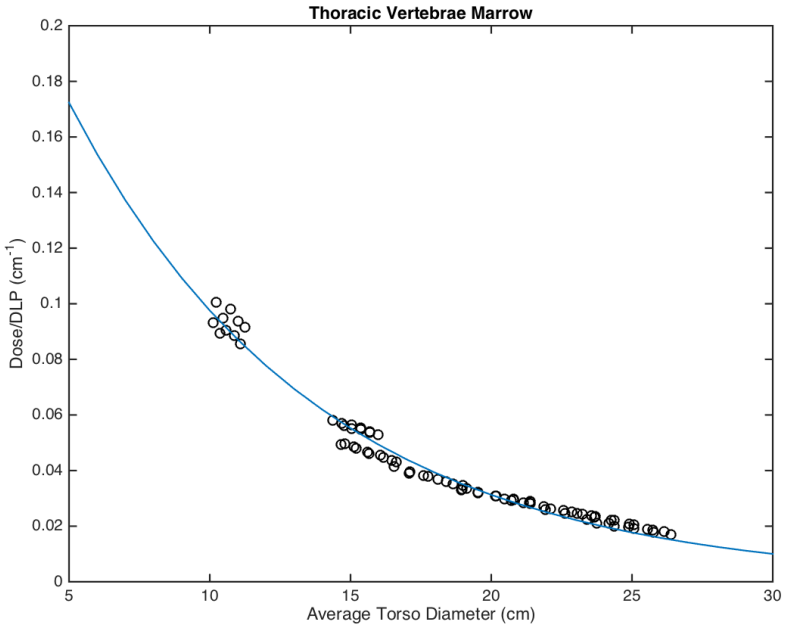

(b)

Figure 5.18: Plots of DLP-normalized marrow dose for (a) sternum marrow and (b) thoracic vertebrae marrow, with the corresponding exponential fits demonstrating the dependence of dose on torso diameter.

5.5 Discussion

As seen previously with other organs in the simulated scan range and field of view (Chapter IV), a strong relationship was observed between DLP-normalized bone and marrow dose as a function of average torso diameter ($R^2 > 0.9$ for most bones and their respective marrow). Again, an exponential function was found to best describe the relationship between dose and the amount of X-ray beam path attenuation through the traversed tissue so the dose deposited decreased as the depth of the bone or marrow increased.

The biggest discrepancies between the exponential fits and the calculated dose values are seen for bones or marrow that are on the edge of the scan range. For example, the cervical vertebrae are only partially irradiated on the edge (since the scan end is at the apex of the lung), so much of this dose is due to scattered radiation in those areas. This effect is seen similarly in the results for the femur bone and femur marrow as well as in the results for the scapulae and partially in the clavicles. In all of these cases, the differences are more pronounced in the smaller (younger) phantoms. This is due to the shorter overall scan length of the simulated examinations for those patients. The amount of scatter is decreased for these phantoms and as a result, there are fewer hits in the Monte Carlo simulation, which leads to more statistical noise in these data values. For the larger (older) phantoms, the amount of noise in the data is seen to be decreased in comparison. Another contributing factor to the statistical uncertainty in these organs is the smaller available mass for energy deposition for the smaller, younger phantoms compared to the larger, older phantoms.

Here, the bones and marrow of the skeleton were modeled using age-dependent bone compositions and densities as well as age-dependent marrow distributions. These individual age-dependent skeletal dose results, specifically for red marrow, are novel for external CT dosimetry applications in deformable reference phantoms. While much work has been done in the field of nuclear medicine and internal dosimetry for estimations of marrow dose (e.g., Stabin et al., 2002; Bolch et al., 2002; Wessels et al., 2004; Lee et al., 2006a), dose only to red marrow in CT applications has not been treated extensively. One of the major reasons for this is the high level of difficulty in segmenting marrow directly from medical images.

Broad techniques to model the skeleton have previously been applied using stylized or voxel-based computational whole body phantoms. With these techniques, the skeleton is defined as a homogeneous tissue with elemental composition and density defined as a whole skeleton mixture. These methods have then been applied equally to skeletal dose estimation for both external and internal photon sources.

Another technique employed to estimate red marrow dose was developed by Snyder et al. (1969). Snyder *et al* assumed for the MIRD-5 and MIRD-5-Revised adult stylized phantoms that the photon energy per gram absorbed for the mineral bone and the bone marrow is the same. Therefore, the fractional mass of the red marrow within the homogeneous skeletal tissue was applied as a single scaling factor. However, this technique potentially overestimates the marrow dose for photon energies less than 100-200 keV.

Kramer and Drexler (1982) and Rosenstein (1976) tried to account for the additional energy absorption in mineral bone for low energy photons and introduced a second scaling factor, the ratio of the mass-energy absorption coefficient of red marrow to the homogenous

skeletal tissue. This approach still presented drawbacks in that it assumes charged particle equilibrium within trabecular spongiosa, when, in actuality, electrons generated from photoelectric absorption in the trabecular bone provide supplemental electron dose to the marrow tissues in the marrow cavities.

A third scaling factor was then developed, the "dose enhancement factor", based on experimental studies by Spiers (1969). This has been applied to both stylized and voxel (tomographic) computational phantoms for skeletal regions considered to be homogeneous in composition and density. However, errors can result for skeletal areas with large cortical bone thicknesses due to decreased fluence of low energy photons before entering the trabecular spongiosa (Lee et al., 2006a).

Zankl and Wittmann (2001) proposed a CT number approach, where the fractional mass of red marrow was allowed to vary on a voxel-by-voxel basis corresponding to the Hounsfield unit (HU) in the original CT image. This was done to tackle the problem of compositional heterogeneities. Kramer et al. (2003) and Kramer et al. (2004) applied this to the GSF family of voxel phantoms. This method uses two threshold CT numbers (Hounsfield units) to divide the cortical bone and bone marrow into separate regions. These two values of threshold numbers are set such that the whole-body bone marrow masses correspond to those given in Snyder et al. (1975) and Valentin (2002). This approach was a major improvement over previous methods but could only be applied to voxel computational phantoms where CT images and constant reconstruction algorithms are defined.

A few other approaches have been taken (e.g., Cristy and Eckerman, 1987), but these techniques have been applied to stylized or tomographic computational phantoms. Stud-

ies have primarily focused within the field of nuclear medicine, using internal photon sources. Hence, this work is one of the first, if not only, attempt to characterize the dose delivered to red and yellow bone marrow distributions as a function of temporal and spatial distribution for external diagnostic-energy photon sources.

5.6 Conclusion

Bone and red marrow absorbed doses were calculated for pediatric patients receiving chest-abdomen-pelvis (CAP) CT exams. As seen with the major organs within the torso (and field of view and scan range), a strong correlation was observed between the average phantom torso diameter and the dose delivered to bones and bone marrow. The method developed here provides the potential to predict the cortical, trabecular, and red and yellow marrow absorbed doses delivered to patients prior to or after CT examination.

The red and yellow bone marrow distribution was modeled as a function of age and varying spatial distribution within a large set of pediatric reference phantoms of both genders, various ages (newborn to 15 years), and varying sizes. Additionally, individual bones were modeled with age-dependent elemental compositions and densities and cortical bone thickness was also taken into account. This is a novel approach in that no other published studies to date have addressed this topic in a large series of pediatric reference phantoms.

Chapter VI

DISCUSSION

6.1 Exposure and Cancer Risk in Children

The second largest source of ionizing radiation exposure of adults and children in the world is medical radiation exposure. There is limited data on the amount of diagnostic medical procedures performed on children, but it is estimated to be around 3-10% (see Table VI.1) (UNSCEAR, 2013).

Table VI.1: Percentages of various types of medical examinations performed on infants and children (0-15 years old) in well-developed countries. Adapted from UNSCEAR (2013).

Examination	Percentage performed on children (%)
CT Head	8
CT Abdomen	4
CT Thorax	5
CT Spine	3

Children are potentially at higher risk of tumor induction than adults. Cancers and other late effects may occur after radiation exposure at a young age, and such effects may occur within a few years or decades afterward. According to UNSCEAR (2013), radiogenic tumor incidence in children depends on the type of tumor, age, and gender, and also varies more than for adults. For about 25% of cancer types, children are more radiosensitive than adults. Leukemia, thyroid, skin, breast, and brain cancer are among the types of tumors that are greatly relevant for evaluation in radiological medical exams.

The induction of leukemia by radiation is well established, so bone marrow dose is of particular concern.

Conversely, roughly 15% of cancer types (e.g., colon) demonstrate that children experience about the same level of radiosensitivity as adults. For some (e.g., lung cancer), it seems that children are less radiosensitive than adults (approximately 10% of cancers). However, for many cancers (about 20%) conclusions cannot be drawn as the data are too weak (UNSCEAR, 2013).

Predictions of lifetime risk for specific cancers and other effects due to radiation exposure at young ages are currently not well established. More studies, both in children and adults, are needed. Therefore, one should avoid generalizations surrounding the magnitude of the radiosensitivity of children (UNSCEAR, 2013).

Table VI.2: Comparison of carcinogenesis risks at age-at-exposure for children versus adults. The excess absolute risk (EAR) is defined as the cancer rate in the irradiated group minus the rate in the corresponding unexposed group. The excess relative risk (ERR) is defined as the ratio of risk in the exposed group to that in the unexposed group. Both are presented when data is available. Adapted from UNSCEAR (2013).

Cancer site	More	No difference	Less	Insufficient data	Evidence
Esophagus				X	
Stomach (mortality)	ERR	EAR			Moderate
Small intestine				X	
Colon					
- (incidence)	EAR	ERR			Weak
- (mortality)	EAR & ERR				
Rectum				X	
Pancreas				X	
Liver		X			Weak
Lung			X		Moderate
Skin non-melanoma	X				Moderate
Breast	X				Strong
Uterus				X	
Cervix				X	
Ovary				X	
Prostate				X	
Kidney				X	
Bladder		X			Moderate
Brain	X				Strong
Thyroid	X				Strong
Parathyroid				X	
Hodgkins lymphoma				X	
Non-Hodgkins lymphoma				X	
Myeloma				X	
Leukaemia non-CLL	X				Strong
Myelodysplasia	X				Weak

6.2 Effective Dose Applied to Medical Exposures

The concept of "effective dose" was conceived in 1975 (Jacobi, 1975; ICRP 26, 1977) in an attempt to relate a specific quantity to the risk of health detriment as a result of a series of exposures to low dose ionizing radiation. Its intended use was to link a uniform whole-body equivalent dose to the radiation-induced risk of health detriment for an exposed reference person. This overall aggregated health detriment is considered for a population averaged over all ages and both genders. The effective dose attempts to account for the probabilities of radiation-induced effects, including cancers (fatal and non-fatal) and the associated latency periods for the development of those cancers and other non-malignant and potential hereditary disorders.

Equivalent doses to radiosensitive organs and tissues in the body are weighted according to individual factors and summed up to result in the overall effective dose. The individual weighting factors used are based chiefly on data from the life-span study (LSS) of the Japanese atomic bomb survivors, and these factors were derived from statistical analyses of the long-term incidence of cancer and mortality rates of this population (see, e.g., Pierce and Preston, 2000; Pierce, 2003; Preston et al., 2003a,b, 2004, 2007; Pierce et al., 2012; Preston et al., 2012).

Often, the effective dose has been applied to specific individuals of known gender and age for medical exposures, even though the effective dose should not be applied to an individual and certainly should not be used to assign a numerical value of risk to an individual; it was never intended to be used in a such a manner. It is often, however, used in informed consent documents as a comparison to other known risks.

Conversion coefficients that allow effective dose to be calculated from quantifiable dose metrics have been derived for medical exposures (Jones and Wall, 1985; Hart and Wall, 1994). These are typically reported to two or three significant figures without mention of their inherent uncertainties. Similarly, the uncertainties in the ICRP tissue-weighting factors are not explicitly defined. Without considering individual variations in size, age, gender, physiology, and genetic susceptibility to cancer induction, risk projections will have greater uncertainties (Martin, 2014).

It is important that caution be used when applying effective dose to medical exposures even when the associated uncertainties are included. Martin (2014) reports the need for caution in the use of ED due to the uncertainty in the calculation of effective dose to a reference patient for a medical exposure being approximately 40% with an 80-90% confidence limit.

The ED risk data came mainly from studies of Japanese Life Span Study (LSS). The Japanese LSS contains many uncertainties, including: cancer diagnosis uncertainty, variations in dose reconstruction, genetic makeup of the population, size of individuals, the type of risk model used, and the method of extrapolation of high-dose level incidence rates to low-dose levels.

Much debate has been centered around the extrapolation of epidemiological results from high-dose levels to low-dose levels. Some groups have found no compelling evidence for higher cancer incidence for less than 100-150 mSv (UNSCEAR, 2000; ICRP 99, 2004). Occupational and diagnostic doses are also much less than this range. Others have debated whether or not adaptive cellular repair-responses for DNA damage provide protection at low doses (e.g., Clarke, 2004; Feinendegen et al., 2007; Wall et al., 2014). Chronic

exposures of radiation workers and populations with higher levels of background radiation have not shown evidence of higher cancer rates, but some studies have shown borderline significance of solid tumor and leukemia incidence (UNSCEAR, 2000; Gilbert, 2001). Some recent assessments of LSS data have shown some attestation of increased incidence and mortality for acute doses of X-rays down to 10-50 mSv for solid tumors (Pierce and Preston, 2000; Preston et al., 2003b; Brenner et al., 2003). Siegel and Stabin (2012) assert that the LNT model is inconsistent with the LSS data, and at radiation doses below 100 mSv, effects have been unobservable, implying that they are very low or non-existent. Siegel and Welsh (2015) also provide a review of the contended inadequacies of the LNT model.

Therefore, the use of effective dose in applications for medical radiation exposures should be exercised with caution and not treated with a great amount of reliance in predicting specific risk to an individual. An uncertainty of approximately 40% corresponds to the effective dose of a reference patient, and the associated risk may be much more variable for an individual (Martin, 2014).

6.3 Uncertainties in Dose Estimates

No scientific results are completely free of uncertainty and, accordingly, there are several factors of uncertainty contributing to the estimated dose values. A detailed, albeit not completely exhaustive, discussion of contributions to errors and uncertainty in these dose estimates follows:

As discussed in Chapter III, there is uncertainty in the exact value of the normalization factor used to convert all simulated dose results to real-world actual doses. Simulated dose

values are inherently subject to random statistical errors. Additionally, the 5% uncertainty in all of the ionization chamber measurements also contributes greatly to the value of the derived normalization factor. When propagated with the relative Monte Carlo error, there is a $> 5\%$ error in all computed dose results reported.

One of the most notable uncertainties in the estimation of patient dose arises due to the inherent patient anatomic variability. Each person has slightly different organ shapes and placement. This will directly affect the amount of attenuation the photon beam experiences traversing through tissue before reaching the organ of interest as well as the amount of energy deposited in the organ. The population-averaged reference phantoms utilized here are a good source of generalized dose results, but ultimately, each patient's specific anatomy will likely deviate, and will lead to errors in the absolute dose values estimated.

A similar uncertainty emerges in organ masses. Organ masses are adjusted to specified standard reference masses at the stage of NURBS fitting prior to voxelization. The NURBS surfaces themselves contain a high level of detail and resolution, but once these NURBS surfaces are voxelized according to a new user-defined resolution, some dispersion will result. This is dependent on the chosen resolution of the voxelized phantom and discrepancies diminish with increased resolution (smaller voxel sizes). However, using a very high resolution is not always computationally feasible nor necessary to arrive at reasonable dose estimates within the desired levels of accuracy.

The axial variability of organ placement within the phantoms can also lead to uncertainties in dose results. Absorbed dose is a strong function of the amount of tissue material traversed before deposition of energy into underlying organs. This was demonstrated in

the strong exponential relationship observed between absorbed dose and patient diameter. Not only can this lead to variability in results for a specific patient's anatomy, but this is also relevant for the phantom calculations. The phantoms were built to represent reference anatomy as closely as possible, but errors may still occur in the development stage. A change in axial distance of just a few millimeters may lead to noticeable differences, with movement toward the periphery of the phantom leading to slightly higher dose values and conversely an inward movement leading to slightly depressed values.

The particular location of chosen anatomical landmarks to determine scan length is another source of variability and introduced uncertainty. A CT technologist typically predetermines these landmarks, which determine the start and stop of the scan, when planning the examination using a "scout" scan. While there are generally accepted prescribed landmarks used to decide where the scan begins and ends (e.g., the location of the pubic symphysis, superior extant of the liver, apex of the lungs, etc.), differences may be introduced by the user. Other circumstances may lead to the edge of the scan being different enough that dose results are greatly affected for organs near the edge of the scan. One example can be seen for testes in the male. Testes are typically and purposefully not selected to be covered in the scan range if possible. However, for some patients imaged, testes have been included in the scan area, sometimes unavoidably due to the close proximity of other regions in need of necessary imaging (e.g., trauma cases).

Uncertainties in elemental compositions and physical densities could also contribute to uncertainty in dose estimates. Compositional differences may occur due to the materials modeled in the phantoms as well as actual compositional differences within patients. Bone tissue, especially for children, can vary greatly in its calcium content and physical

density. This can influence the energy imparted to the bone tissue and the underlying marrow tissues within the bone. It is well known that the photoelectric mass-attenuation coefficient varies with Z^3, where Z is the effective atomic number. This means that bone, a high-Z material, absorbs much more low energy photons than would have been absorbed for the same energies in an equal amount of lower density tissue. Therefore, even small variations between the patient and modeled phantom materials could lead to differences in estimated bone and marrow doses. Uncertainties in specific tissues for major organs would not likely differ as much due to this effect, but these differences are more likely to be seen in the skeleton.

Other errors could crop up during the patient-phantom matching process. The torso diameter was deemed to be the best metric for matching individual subjects to phantoms. While the method employed here determined the overall average diameter over all slices of interest, in practicality in a clinical environment, a patient's diameter would likely be measured from a scout scan. It is unlikely that the torso diameter would be determined for each slice; rather a location would likely be selected to measure the effective diameter in accordance with the guidelines in AAPM Report 204 (American Association of Physicists in Medicine et al., 2011). Therefore, uncertainty in the patient diameter is introduced as this measurement location may vary, and the measurement may not be the best representation of the average diameter. Since this diameter is used to match a patient to a phantom, this difference could cause a patient to be matched to a slightly different percentile phantom. This amount of mismatch is unlikely to change the results drastically with typical errors in matching (around 10%, but sometimes as great as 20%), but it is an important potential source of uncertainty.

6.4 Future Directions

This project presents many additional explorable ideas and future directions. This work could naturally be expanded to include an even larger number of non-reference age phantoms. This would lead to an even greater number of phantom diameters for use in matching of patient doses as well as more age-dependent bone and marrow distributions.

Similarly, the patient-specific data set was limited to phantoms constructed from 40 image sets of patients previously imaged at the Monroe Carell Jr. Children's Hospital at Vanderbilt. While the utility of matching patient data sets to the phantom database was demonstrated, further studies could be done to expand the patient data set to include more ages, sizes, and body types.

Current efforts have already been underway to expand the phantom database to include additional body types such as overweight and obese pediatric phantoms. There is also the possibility to develop and include underweight phantoms, though this effort would be particularly challenging. While it is relatively simple to add varying degrees of body tissue to normal-stature phantoms in order to generate overweight or obese phantoms, taking away material without changing or compromising the underlying organ structures already present has proved extremely challenging. It is possible that underweight children also experience decreased organ mass, but little quantitative data was found on this subject. Nonetheless, this is a potential avenue that could be explored.

Additionally, this work could obviously be expanded to model other commercial CT scanner types. The methodology has already been laid out, but an entirely new set of calibration and validation measures would need to be undertaken. Moreover, for each scanner

type, varying techniques and scanning protocols could be modeled. This study has focused on the chest-abdomen-pelvis (CAP) exam protocol, but it would be straightforward to simulate chest, abdominopelvis (AP), or head examinations as well.

Finally, one of the ultimate goals for this project was the implementation of its results in the clinical environment. Plans are already underway to implement the results for direct use for patient scans on the Philips Brilliance 64-slice scanner at Monroe Carell Jr. Children's Hospital at Vanderbilt. This could be done (1) through the use of look-up tables to access calculated dose values generated from a database of phantom dose values, or (2) the individual exponential dose fits could be used to predict values prior to examination. For these methods, the only additional parameters needed are the patient's measured diameter and potentially the estimated scanner DLP value.

Chapter VII

CONCLUSIONS

Diagnostic CT imaging examinations offer benefits and associated risks just like any other medical procedure; radiation dose calculations are essential to understanding this delicate balance. The long-term dose tracking of patients is a current goal and more accurate dose prescriptions are becoming more important.

Estimates of radiation dose from CT scans are generally reported as CTDI values and are assigned to pediatric and adult patients without regard to specific patient size and weight. Additionally, these values are applied equally to all subjects imaged for different types of imaging protocols.

Red marrow is a highly radiosensitive organ as it consists of progenitor and stem cells that are extensively unspecialized, rapidly dividing, and have a long dividing future. These hematopoietic cells are some of the most radiosensitive cells in the body, and radiation dose and radiation damage to these marrow cells is of great interest especially for pediatric patients.

A new Monte Carlo code built with the GEANT4 tool kit was developed and validated in order to simulate patients undergoing a CT examination. The specific CT scanner modeled was a Philips Brilliance 64, which is currently used to image pediatric patients at Monroe Carell Jr. Children's Hospital at Vanderbilt. The CT scanner simulation model takes into account the complexities of the X-ray beam properties, bowtie filter attenuation profile, and CT geometry. This code was extensively calibrated and validated

using real-world physical dose measurements and photon-fluence normalization factors.

Patient-specific voxel computational phantoms were created from images of pediatric patients who had prior chest-abdomen-pelvis (CAP) CT exams at Monroe Carrell, Jr. Children's Hospital at Vanderbilt. Organs within the image field of view and torso region were segmented manually and semi-automatically. Voxelized computational phantoms were generated for all patient data sets (40 total).

A total of 80 deformable pediatric reference NURBS phantoms were developed for ages ranging from newborns to 15-year-olds for both genders and varying percentiles of normal stature children. These phantoms were built according to reference anatomies and organ masses. Additionally, the skeletons of these phantoms were modeled in much more detail than in any previous studies. Individual bones were modeled accurately using age-dependent elemental compositions, physical densities, and cortical bone thicknesses. The red and yellow bone marrow distributions were modeled as a varying function of temporal and spatial distribution within the phantoms. This modeling approach had not been published previously for external dosimetry CT studies.

Absorbed doses for organs and effective doses for pediatric patients receiving chest-abdomen-pelvis (CAP) CT exams were calculated, and a strong relationship was observed between organ dose and average patient torso diameter. This was found to be best fit by linear regression to an exponential function. Bone and red marrow absorbed doses were calculated, and again, a strong correlation with phantom diameter was observed. The methods utilized here provide the power to predict doses delivered to patients prior to and after CT examinations.

The dose estimation methods demonstrated here are vast improvements over the cur-

rent CT vendor-supplied values. The high quality information generated here may be used to track patients' cumulative doses over time. The ability to predict patient dose prior to CT examination and to match an individual patient to a phantom in the database is a significant achievement. Vanderbilt physicians and scientists will be able to use this information in their analysis of dose, of exposure parameters, and dose prescriptions for particular subjects and study types. In the end, the goal of minimizing radiation dose while still acquiring high quality images and, ultimately, improved patient care may better be achieved.

Appendix A

RADIATION DOSE AND RISK

The primary interaction of radiation with matter is between photons and electrons. The result is either the removal of electrons (ionization) or a change in the electrons' energy state. Tissue damage occurs when there is a change in the chemical properties of molecules following ionization, and DNA is the most critical molecule where this occurs. Direct ionization of DNA can cause strand breaks, but this is of low probability. Indirect interactions of radiation are the biggest contributors to DNA damage because of the formation of free radicals. A free radical molecule carries an unpaired electron in its outer shell, which makes the molecule very reactive. The body is made of mainly water, and hydroxyl radical formation from the water ionization is the primary cause of radiation damage. The reaction of hydroxyl radicals with DNA causes single- and double-strand breaks. Double-strand breaks are not easily repaired, and they result in cell death or in a mutation of the DNA-encoding, which can lead to hereditary changes or induction of cancer (Hall and Giaccia, 2006).

1.1 Deterministic Effects

Deterministic effects are effects in which the outcome can be pre-determined. These will occur when the energy absorbed in a tissue is great enough to cause the tissues function to be changed due to cell death. The threshold dose is defined as the amount of absorbed energy for these deterministic effects to occur (tissue-specific), and these have

been determined from experimental cell cultures and animal studies as well as human epidemiology studies. Reviews have shown that below 0.1 Gy no deterministic effects from radiation exposure have been observed. Typically, deterministic effects are not seen in patients due to diagnostic imaging; however, when multiple radiographic examinations are performed on the same patient, the cumulative dose can exceed the 0.1 Gy level (Stabin, 2007).

1.2 Stochastic Effects

Stochastic effects are random or probabilistic in nature; therefore the occurrence of individual events cannot be predicted. Measuring the distribution of all observations, however, may allow an expected pattern to be determined using statistical methods. Stochastic effects can be divided into two groups: genetic and carcinogenic effects. The production of genetic changes or the induction of cancer in an individual cannot be determined regardless of the amount of energy absorbed as there is not a threshold dose where these effects will always occur. As energy absorption increases, the probability of seeing an effect also increases, but the severity does not increase proportional to dose (Stabin, 2007).

1.2.1 Genetic Effects

The radiation exposure of a population may cause cellular damage that eventually results in mutations in the descendants of that population. These mutations are specific to the cell line exposed, so the radiation damage only produces DNA-sequencing errors that could have occurred naturally. Instead of producing unique mutations, the radiation

damage results in a higher frequency of spontaneous mutations. A large number of studies have shown that the deleterious effects for subsequent generations are negligible.

1.2.2 Carcinogenic Effects

Cancer induction is the most vital stochastic radiation effect. There is a countless amount of evidence of radiation-induced cancer in both humans and animals. Recent analysis of the long-term studies of the Japanese survivors of the atomic bomb attacks on Hiroshima and Nagasaki (e.g., Little, 1996; Little and Muirhead, 1998; Little et al., 1999; Pierce and Preston, 2000; Little and Muirhead, 2004; Little et al., 2010) have shown increased cancer incidence in these populations at lower dose levels.

Stochastic effects have a latency period between the time of exposure and cancer inception. This period is on the order of years for all cancers but varies with individual type. For example, leukemia has the shortest latency period—around 5 to 15 years. Many solid tumors on the other hand have a latency period of 20 to 60 years.

1.3 Risk Estimation

If the deposition of energy in tissue is large enough, cellular changes or death will occur. For deterministic effects, there is a threshold dose in certain tissues where radiation effects are not seen below this level. Nevertheless, there is a small probability that damage to even a single cell may result in a change that causes the cell to become malignant. However, we also know that cells routinely (every day) repair radiation damage, so the possibility that there is no risk at all at "low doses" is a possibility. The probability that stochastic effects will occur cannot be ruled out, however, even at low radiation doses. The National

Academy of Sciences, in their Biological Effects of Ionizing Radiation Reports (BEIR VII, 2006), as well as other scientific organizations that study the effects of radiation, use a definition of "low dose" to be between 0.1 and 0.15 Sieverts.

1.3.1 Low Dose Extrapolation

Cell culture and animal studies have provided information demonstrating generation of tumors from high levels of radiation exposure, yet at lower dose levels both deterministic and stochastic effects are not observed or the studies have not been comprehensive enough to demonstrate these changes conclusively. These studies exhibit data only for high radiation dose levels, so the determination of risk for cancer induction at low dose must be extrapolated from the high dose data.

Using the high dose data, three extrapolation models for low-dose effects have been proposed. These are the:

- linear-quadratic model,
- linear-threshold model, and
- linear-no-threshold model.

1.3.2 Linear-quadratic Model

It is assumed that the incidence of induced cancer at low dose levels increases linearly with radiation dose up to a certain dose level. Then at high dose levels, the incidence increases much more rapidly and changes from linear at low-dose levels to quadratic at high-dose levels. The linear-quadratic model is derived from a large number of animal

studies that demonstrate this fit in specific cancers such as leukemia and non-melanoma skin cancer. The shape of the linear-quadratic fit to other cancers suggests that there is a large variation in the curve fitting parameters, making the extrapolation to low-dose levels variable depending on the cancer and/or cell type. Therefore, utilizing these fits to predict cancer would require different models for each specific cancer type, but there is not enough data in humans.

1.3.3 Linear-threshold and Linear-no-threshold Models

Here it assumed that the incidence of induced cancer is linearly proportional to the dose at all dose levels. The difference between the two linear models is whether or not there is a threshold below which too few cells are affected or cellular repair mechanisms compensate for any damage that occurs. If a threshold level for stochastic effects exists, it has been proposed that this would be near 0.01 to 0.5 Sieverts. This value is based on studies that suggest stochastic effects have not been demonstrated at or below this dose range (e.g., Little, 1996; Little and Muirhead, 1998; Little et al., 1999; Pierce and Preston, 2000; Little and Muirhead, 2004). There are also studies that have investigated the application of a linear-quadratic threshold model to low dose situations. These studies suggest that if there is a threshold it is also at a very low value, e.g., 0.07 to 0.11 Sieverts (Little and Muirhead, 2004). It should be noted that these "very low dose" thresholds are at the level where exposures from diagnostic radiology studies occur.

The most conservative approach is to use the linear no-threshold model, which is used by all advisory and regulatory agencies when setting limits for radiation exposure.

Appendix B

DATA TABLES

Table B.1: Newborn phantom organ dose data in units of mGy for simulated Philips Brilliance 64 helical CT chest-abdomen-pelvis scans for 120 kVp, 100 mAs, pitch = 1, and 64 × 0.625 mm beam collimation.

	Females					Males				
Organ	NB 10th	NB 25th	NB 50th	NB 75th	NB 90th	NB 10th	NB 25th	NB 50th	NB 75th	NB 90th
body remainder	7.93	7.81	8.30	8.30	8.30	8.35	8.38	8.42	8.44	8.45
cerebrum	0.28	0.26	0.32	0.31	0.29	0.33	0.34	0.31	0.30	0.31
cerebellum	0.72	0.67	0.95	0.90	0.81	0.99	1.06	0.87	0.83	0.89
brain stem	0.58	0.53	0.75	0.75	0.63	0.75	0.82	0.70	0.67	0.66
spinal cord	11.43	11.42	12.37	12.28	12.06	10.71	10.96	11.22	10.75	10.95
salivary glands	3.68	3.11	3.44	3.01	2.66	3.61	3.70	2.61	3.12	3.78
esophagus	11.15	11.25	11.47	11.62	11.34	11.29	11.65	11.51	11.45	12.24
thyroid	11.20	10.76	11.81	11.80	10.78	11.22	12.06	11.54	10.66	11.38
thymus	11.64	11.54	11.94	12.00	12.00	11.97	11.88	11.85	11.89	12.06
eyes	0.57	0.55	0.61	0.57	0.59	0.66	0.64	0.54	0.59	0.67
eye lens	0.55	0.63	0.80	0.33	0.54	0.85	0.68	0.60	0.59	0.61
lungs	12.05	12.14	12.22	12.41	12.45	12.09	12.27	12.37	12.35	12.56
liver	11.40	11.52	11.64	11.81	11.83	11.60	11.64	11.71	11.75	11.81
gall bladder	10.38	10.70	11.00	11.40	11.67	11.30	10.78	11.21	11.26	11.51
kidneys	12.45	12.57	12.78	13.01	13.15	12.67	12.73	12.83	12.92	13.01
adrenals	12.11	12.32	12.30	12.66	12.82	12.43	12.33	12.57	12.91	12.76
stomach	11.35	11.37	11.38	11.56	11.88	11.48	11.54	11.49	11.63	11.67
spleen	11.26	11.60	11.57	11.86	12.03	11.46	11.61	11.93	11.98	11.97
heart	12.64	12.79	12.99	13.16	13.28	12.81	12.97	13.06	13.06	13.19
pancreas	11.71	11.91	11.77	12.17	12.43	11.96	11.88	12.14	12.08	12.33
bladder	12.15	12.02	12.20	12.38	12.59	12.14	12.16	12.18	12.41	12.38
bladder contents	0.00	0.00	0.00	0.00	0.00	0.00	0.00	0.00	0.00	0.00
ascending large intestine	10.83	11.00	11.09	11.22	11.28	11.00	11.09	11.11	11.19	11.28
transcending large intestine	11.44	11.64	11.63	11.84	11.89	11.58	11.68	11.56	11.66	11.85
descending large intestine	10.67	10.88	11.08	11.22	11.50	10.97	11.04	11.03	11.39	11.55
sigmoid	12.05	12.22	12.26	12.40	12.69	11.99	12.53	12.33	12.46	12.65
rectum	14.17	14.19	14.75	15.24	15.40	14.22	14.43	14.76	15.14	15.90
small intestine	11.93	12.03	12.24	12.30	12.53	12.08	12.17	12.27	12.40	12.48
GI contents	11.09	11.16	11.29	11.42	11.58	11.22	11.27	11.36	11.37	11.51
prostate	0.00	0.00	0.00	0.00	0.00	12.07	12.02	12.13	12.21	12.16
testes	0.00	0.00	0.00	0.00	0.00	9.08	8.95	9.23	9.04	9.02
uterus	11.32	11.68	11.91	11.64	11.93	0.00	0.00	0.00	0.00	0.00
ovaries	12.41	12.08	11.83	13.03	12.99	0.00	0.00	0.00	0.00	0.00
skin	6.10	6.01	6.35	6.32	6.30	6.44	6.40	6.42	6.41	6.41
total brain	0.33	0.30	0.39	0.37	0.34	0.39	0.41	0.36	0.35	0.36
total colon	11.25	11.44	11.54	11.70	11.84	11.40	11.56	11.53	11.67	11.85
total breasts	11.44	10.54	12.18	10.19	11.33	0.00	0.00	0.00	0.00	0.00
total remainder tissues	8.30	8.20	8.66	8.67	8.69	8.69	8.73	8.77	8.80	8.82
Total ED (ICRP 103) in mSv	10.70	10.52	10.94	10.83	11.03	9.37	9.41	9.47	9.42	9.59
Average Torso Diameter (cm)	10.11	10.35	10.59	10.87	11.10	10.23	10.48	10.74	11.00	11.25
CAP Scan Length (cm)	22.30	22.90	23.50	23.80	24.40	23.20	23.50	24.10	24.70	25.00

Table B.2: 1-year-old phantom organ dose data in units of mGy for simulated Philips Brilliance 64 helical CT chest-abdomen-pelvis scans for 120 kVp, 100 mAs, pitch = 1, and 64 × 0.625 mm beam collimation.

	Females					Males				
Organ	1y 10th	1y 25th	1y 50th	1y 75th	1y 90th	1y 10th	1y 25th	1y 50th	1y 75th	1y 90th
body remainder	8.85	8.78	8.77	8.81	8.73	8.80	8.66	8.80	8.71	8.76
cerebrum	0.32	0.29	0.29	0.31	0.29	0.30	0.27	0.31	0.29	0.28
cerebellum	0.87	0.76	0.82	0.87	0.78	0.81	0.69	0.89	0.81	0.76
brain stem	0.76	0.66	0.67	0.72	0.66	0.67	0.61	0.71	0.66	0.62
spinal cord	12.44	12.24	12.70	12.89	12.68	12.31	12.22	12.87	12.53	12.52
salivary glands	3.67	2.92	2.53	2.71	2.49	2.74	2.09	2.71	2.49	2.64
esophagus	12.49	12.53	12.62	12.43	12.37	12.44	12.42	12.75	12.47	12.58
thyroid	14.01	13.33	13.45	13.84	13.21	13.23	12.55	13.72	13.14	13.10
thymus	12.95	12.91	13.07	13.05	13.05	12.96	12.96	13.05	13.08	12.93
eyes	0.46	0.43	0.36	0.41	0.42	0.42	0.37	0.40	0.40	0.37
eye lens	0.55	0.38	0.41	0.41	0.29	0.37	0.69	0.25	0.46	0.31
lungs	13.28	13.32	13.44	13.51	13.44	13.34	13.30	13.43	13.47	13.44
liver	13.41	13.40	13.46	13.50	13.52	13.44	13.40	13.46	13.45	13.53
gall bladder	13.03	13.37	13.29	13.32	13.30	13.30	13.20	13.33	13.25	13.11
kidneys	13.50	13.51	13.58	13.71	13.60	13.56	13.56	13.62	13.65	13.73
adrenals	13.47	13.70	13.90	13.76	13.60	13.58	13.76	13.68	13.37	13.82
stomach	12.18	12.27	12.38	12.38	12.47	12.16	12.32	12.29	12.45	12.49
spleen	11.36	11.35	11.38	11.28	11.27	11.29	11.33	11.34	11.32	11.25
heart	14.22	14.23	14.23	14.28	14.36	14.15	14.15	14.25	14.30	14.28
pancreas	13.00	13.04	12.85	12.89	12.94	12.93	12.85	12.89	12.93	12.94
bladder	13.52	13.64	13.50	13.69	13.63	13.57	13.50	13.51	13.56	13.68
bladder contents	0.00	0.00	0.00	0.00	0.00	0.00	0.00	0.00	0.00	0.00
ascending large intestine	13.59	13.58	13.61	13.72	13.79	13.69	13.64	13.71	13.83	13.83
transcending large intestine	12.72	12.87	12.94	12.89	12.88	12.90	12.79	12.88	12.99	13.04
descending large intestine	10.55	10.68	10.64	10.51	10.60	10.67	10.55	10.55	10.58	10.49
sigmoid	12.97	13.03	13.09	12.93	12.89	12.91	13.02	12.98	12.88	13.00
rectum	13.43	13.36	13.59	13.59	13.79	13.74	13.53	13.58	13.42	13.54
small intestine	13.45	13.55	13.50	13.49	13.56	13.52	13.48	13.54	13.50	13.60
GI contents	12.31	12.44	12.36	12.49	12.51	12.39	12.40	12.39	12.51	12.58
prostate	0.00	0.00	0.00	0.00	0.00	12.81	12.61	12.02	12.29	12.15
testes	0.00	0.00	0.00	0.00	0.00	13.25	13.65	13.18	13.13	13.41
uterus	12.63	12.80	12.71	12.70	13.03	0.00	0.00	0.00	0.00	0.00
ovaries	13.61	13.23	13.40	13.45	13.24	0.00	0.00	0.00	0.00	0.00
skin	6.75	6.65	6.60	6.65	6.59	6.68	6.53	6.65	6.59	6.60
total brain	0.37	0.34	0.34	0.36	0.33	0.34	0.31	0.36	0.33	0.32
total colon	12.70	12.75	12.81	12.78	12.82	12.82	12.75	12.79	12.82	12.84
total breasts	15.72	14.58	13.30	15.22	13.00	0.00	0.00	0.00	0.00	0.00
total remainder tissues	9.19	9.13	9.12	9.16	9.09	9.15	9.02	9.15	9.07	9.11
Total ED (ICRP 103) in mSv	12.32	12.11	12.02	12.31	11.97	10.37	10.33	10.44	10.40	10.45
Average Torso Diameter (cm)	14.38	14.69	15.04	15.37	15.68	14.77	15.05	15.37	15.69	15.99
CAP Scan Length (cm)	33.70	34.30	34.90	35.80	36.40	34.60	35.20	35.80	36.40	37.00

Table B.3: 3-year-old phantom organ dose data in units of mGy for simulated Philips Brilliance 64 helical CT chest-abdomen-pelvis scans for 120 kVp, 100 mAs, pitch = 1, and 64 × 0.625 mm beam collimation.

	Females					Males				
Organ	3y 10th	3y 25th	3y 50th	3y 75th	3y 90th	3y 10th	3y 25th	3y 50th	3y 75th	3y 90th
body remainder	6.91	6.86	6.79	6.64	6.61	6.89	6.90	6.68	6.70	6.57
cerebrum	0.19	0.19	0.18	0.17	0.16	0.19	0.19	0.18	0.17	0.17
cerebellum	0.44	0.44	0.42	0.41	0.39	0.42	0.45	0.40	0.41	0.40
brain stem	0.37	0.38	0.36	0.32	0.30	0.38	0.35	0.32	0.32	0.32
spinal cord	11.86	11.95	11.63	11.57	11.27	11.79	11.78	11.50	11.44	11.18
salivary glands	1.77	1.80	1.62	1.43	1.41	1.70	1.87	1.51	1.43	1.54
esophagus	12.69	12.76	13.13	13.00	12.71	12.61	12.80	12.72	12.81	12.66
thyroid	12.00	13.25	13.72	13.13	11.84	11.93	13.05	13.12	12.47	11.88
thymus	13.42	13.68	13.73	13.89	13.73	13.16	13.49	13.86	13.80	13.77
eyes	0.28	0.27	0.24	0.24	0.23	0.30	0.30	0.27	0.26	0.22
eye lens	0.26	0.25	0.35	0.23	0.20	0.41	0.27	0.32	0.11	0.26
lungs	13.77	13.82	13.79	13.84	13.72	13.70	13.74	13.77	13.71	13.72
liver	13.46	13.44	13.39	13.34	13.24	13.36	13.38	13.36	13.28	13.27
gall bladder	12.82	12.46	12.40	12.16	12.21	12.54	12.43	12.44	12.31	12.33
kidneys	15.95	15.71	15.43	15.25	15.08	16.06	15.82	15.53	15.29	14.98
adrenals	15.08	15.01	14.55	14.32	13.85	14.76	14.93	14.90	14.07	13.55
stomach	13.29	13.05	13.28	13.24	13.29	13.25	13.16	13.22	13.17	13.31
spleen	15.58	15.32	15.29	15.00	14.93	15.53	15.36	15.14	15.04	14.83
heart	14.59	14.74	14.79	14.85	14.84	14.55	14.66	14.74	14.85	14.86
pancreas	13.49	13.43	13.58	13.55	13.56	13.54	13.38	13.39	13.61	13.56
bladder	14.70	14.90	14.78	14.74	14.60	14.68	14.71	14.72	14.74	14.69
bladder contents	0.00	0.00	0.00	0.00	0.00	0.00	0.00	0.00	0.00	0.00
ascending large intestine	14.01	14.10	14.05	14.03	14.10	13.99	14.00	14.13	14.07	14.09
transcending large intestine	13.27	13.21	13.39	13.22	13.28	13.24	13.36	13.34	13.26	13.16
descending large intestine	13.29	13.31	13.34	13.34	13.49	13.17	13.10	13.23	13.35	13.41
sigmoid	15.18	15.18	14.93	14.91	14.61	15.21	15.13	15.09	14.96	14.53
rectum	14.65	14.37	14.28	13.95	13.56	14.78	14.61	13.93	13.77	13.43
small intestine	13.69	13.69	13.75	13.62	13.64	13.72	13.72	13.69	13.67	13.65
GI contents	13.18	13.17	13.15	13.06	13.06	13.13	13.13	13.14	13.04	13.07
prostate	0.00	0.00	0.00	0.00	0.00	14.21	14.03	14.05	13.86	13.00
testes	0.00	0.00	0.00	0.00	0.00	12.34	12.64	12.06	13.02	12.77
uterus	15.09	14.94	14.81	14.94	14.40	0.00	0.00	0.00	0.00	0.00
ovaries	13.88	13.89	14.02	13.92	14.07	0.00	0.00	0.00	0.00	0.00
skin	5.24	5.23	5.16	5.04	5.04	5.25	5.28	5.13	5.10	5.04
total brain	0.22	0.22	0.20	0.19	0.19	0.21	0.22	0.20	0.20	0.19
total colon	13.81	13.84	13.85	13.78	13.79	13.78	13.81	13.84	13.81	13.72
total breasts	11.80	10.93	12.90	12.17	12.17	0.00	0.00	0.00	0.00	0.00
total remainder tissues	7.34	7.29	7.23	7.08	7.05	7.33	7.33	7.13	7.14	7.01
Total ED (ICRP 103) in mSv	11.93	11.86	12.13	11.95	11.85	10.35	10.44	10.33	10.35	10.28
Average Torso Diameter (cm)	14.79	15.19	15.61	16.07	16.47	14.67	15.13	15.66	16.16	16.62
CAP Scan Length (cm)	36.70	37.60	38.80	39.40	40.60	36.40	37.60	38.50	40.00	40.90

Table B.4: 5-year-old phantom organ dose data in units of mGy for simulated Philips Brilliance 64 helical CT chest-abdomen-pelvis scans for 120 kVp, 100 mAs, pitch = 1, and 64 × 0.625 mm beam collimation.

	Females					Males				
Organ	5y 10th	5y 25th	5y 50th	5y 75th	5y 90th	5y 10th	5y 25th	5y 50th	5y 75th	5y 90th
body remainder	6.56	6.42	6.33	6.16	6.04	6.45	6.33	6.21	6.18	6.04
cerebrum	0.17	0.15	0.15	0.13	0.12	0.15	0.14	0.14	0.13	0.12
cerebellum	0.39	0.37	0.38	0.33	0.32	0.36	0.35	0.34	0.34	0.30
brain stem	0.31	0.29	0.28	0.26	0.25	0.29	0.25	0.26	0.28	0.24
spinal cord	11.04	10.83	10.73	10.24	10.12	10.75	10.69	10.37	10.28	9.97
salivary glands	1.64	1.47	1.35	1.18	1.20	1.46	1.23	1.11	1.35	1.22
esophagus	12.64	12.46	12.34	12.45	12.24	12.59	12.35	12.40	12.38	12.15
thyroid	12.18	13.24	13.12	11.19	12.89	13.26	12.92	11.35	12.52	12.96
thymus	13.81	13.63	13.72	13.70	13.79	13.69	13.62	13.63	13.84	13.76
eyes	0.22	0.21	0.19	0.18	0.16	0.19	0.18	0.18	0.18	0.16
eye lens	0.29	0.27	0.15	0.14	0.13	0.21	0.22	0.16	0.11	0.13
lungs	13.59	13.57	13.55	13.43	13.33	13.57	13.51	13.47	13.39	13.26
liver	13.20	13.08	12.96	12.79	12.66	13.14	13.00	12.89	12.72	12.61
gall bladder	12.21	12.22	12.34	12.14	11.91	12.38	12.34	12.27	12.21	11.83
kidneys	14.96	14.67	14.34	13.88	13.53	14.69	14.37	14.08	13.72	13.37
adrenals	13.54	13.46	13.03	12.71	12.64	13.33	13.12	13.08	12.73	12.41
stomach	13.22	13.04	12.78	12.83	12.76	13.01	12.92	12.77	12.70	12.72
spleen	14.77	14.61	14.17	13.74	13.41	14.60	14.27	13.83	13.67	13.35
heart	14.74	14.78	14.75	14.60	14.54	14.74	14.68	14.64	14.63	14.48
pancreas	13.56	13.33	13.16	13.13	13.10	13.33	13.29	13.23	13.03	12.96
bladder	14.55	14.41	14.30	14.18	13.95	14.41	14.30	14.25	14.09	13.95
bladder contents	0.00	0.00	0.00	0.00	0.00	0.00	0.00	0.00	0.00	0.00
ascending large intestine	13.96	13.98	13.90	13.77	13.68	13.91	13.97	13.83	13.86	13.64
transcending large intestine	13.16	13.03	12.88	12.81	12.83	12.94	12.92	12.86	12.81	12.71
descending large intestine	13.45	13.34	13.07	13.16	12.93	13.31	13.20	13.10	13.09	12.83
sigmoid	14.34	14.16	13.98	13.53	13.29	14.09	13.91	13.74	13.48	13.23
rectum	13.44	13.05	12.40	11.92	11.93	13.09	12.61	12.19	11.83	11.63
small intestine	13.57	13.51	13.43	13.35	13.20	13.54	13.44	13.34	13.25	13.19
GI contents	13.05	12.95	12.89	12.79	12.71	13.03	12.93	12.83	12.75	12.66
prostate	0.00	0.00	0.00	0.00	0.00	12.53	12.01	12.04	11.44	11.29
testes	0.00	0.00	0.00	0.00	0.00	12.04	12.40	12.24	12.13	11.97
uterus	14.45	14.26	14.17	13.54	13.53	0.00	0.00	0.00	0.00	0.00
ovaries	13.80	13.50	13.93	14.27	14.36	0.00	0.00	0.00	0.00	0.00
skin	5.02	4.94	4.86	4.75	4.67	4.97	4.88	4.81	4.78	4.70
total brain	0.19	0.17	0.17	0.15	0.14	0.17	0.16	0.16	0.15	0.14
total colon	13.66	13.56	13.38	13.25	13.14	13.49	13.43	13.31	13.24	13.04
total breasts	11.93	11.75	11.66	12.73	13.29	0.00	0.00	0.00	0.00	0.00
total remainder tissues	7.00	6.86	6.77	6.60	6.48	6.90	6.77	6.65	6.61	6.47
Total ED (ICRP 103) in mSv	11.77	11.66	11.58	11.55	11.59	10.13	10.06	9.90	9.88	9.77
Average Torso Diameter (cm)	16.54	17.12	17.75	18.39	18.99	17.08	17.59	18.11	18.64	19.12
CAP Scan Length (cm)	40.90	42.10	43.60	44.80	46.00	42.10	43.00	44.20	45.70	46.60

Table B.5: 8-year-old phantom organ dose data in units of mGy for simulated Philips Brilliance 64 helical CT chest-abdomen-pelvis scans for 120 kVp, 100 mAs, pitch = 1, and 64 × 0.625 mm beam collimation.

	Females					Males				
Organ	8y 10th	8y 25th	8y 50th	8y 75th	8y 90th	8y 10th	8y 25th	8y 50th	8y 75th	8y 90th
body remainder	6.56	6.47	6.34	6.20	6.07	6.56	6.43	6.33	6.22	6.13
cerebrum	0.14	0.13	0.12	0.12	0.11	0.14	0.13	0.13	0.12	0.11
cerebellum	0.32	0.30	0.28	0.29	0.26	0.31	0.29	0.29	0.26	0.26
brain stem	0.25	0.25	0.23	0.22	0.20	0.24	0.23	0.23	0.21	0.21
spinal cord	10.68	10.56	10.26	10.16	9.85	10.60	10.43	10.23	9.99	9.83
salivary glands	0.95	0.91	0.90	0.88	0.79	0.94	0.88	0.94	0.84	0.86
esophagus	12.07	11.90	11.75	11.62	11.47	12.04	11.69	11.81	11.69	11.36
thyroid	11.43	9.07	11.59	10.85	7.97	11.76	8.67	11.60	10.38	8.91
thymus	13.30	13.11	12.93	12.72	12.70	13.23	13.14	12.98	12.73	12.72
eyes	0.21	0.21	0.19	0.17	0.15	0.20	0.21	0.20	0.19	0.18
eye lens	0.15	0.17	0.18	0.14	0.16	0.20	0.18	0.19	0.22	0.17
lungs	13.18	13.03	12.94	12.81	12.66	13.14	13.00	12.90	12.77	12.63
liver	13.77	13.63	13.51	13.34	13.17	13.73	13.62	13.50	13.34	13.18
gall bladder	14.09	14.15	14.13	13.97	13.62	14.01	14.11	14.02	13.90	13.65
kidneys	13.70	13.61	13.52	13.31	13.18	13.67	13.57	13.49	13.34	13.14
adrenals	13.03	13.01	12.38	12.39	12.42	13.00	12.67	12.27	12.49	12.46
stomach	13.60	13.52	13.28	13.02	12.98	13.64	13.39	13.19	12.94	12.89
spleen	12.02	11.98	11.89	11.74	11.59	12.04	11.92	11.85	11.62	11.59
heart	14.39	14.44	14.39	14.41	14.32	14.37	14.34	14.35	14.36	14.30
pancreas	13.37	13.17	12.95	12.80	12.52	13.31	13.15	13.02	12.78	12.57
bladder	13.46	13.34	13.15	12.95	12.85	13.42	13.38	13.17	13.01	12.86
bladder contents	0.00	0.00	0.00	0.00	0.00	0.00	0.00	0.00	0.00	0.00
ascending large intestine	14.34	14.18	14.09	13.97	13.82	14.36	14.18	14.07	13.98	13.87
transcending large intestine	14.84	14.80	14.70	14.59	14.29	14.84	14.82	14.78	14.45	14.40
descending large intestine	12.36	12.27	12.07	11.88	11.68	12.31	12.14	12.08	11.82	11.71
sigmoid	12.56	12.41	12.27	12.15	11.99	12.58	12.31	12.18	12.08	11.88
rectum	12.62	12.81	12.53	12.31	12.08	12.64	12.36	12.05	12.20	12.01
small intestine	14.05	13.96	13.80	13.66	13.50	14.05	13.91	13.80	13.65	13.55
GI contents	13.39	13.30	13.14	12.99	12.86	13.36	13.27	13.12	12.98	12.86
prostate	0.00	0.00	0.00	0.00	0.00	10.21	10.39	10.54	10.59	9.95
testes	0.00	0.00	0.00	0.00	0.00	13.14	13.05	13.34	13.76	13.94
uterus	12.67	11.96	12.09	11.60	11.67	0.00	0.00	0.00	0.00	0.00
ovaries	14.41	14.23	14.23	13.87	13.90	0.00	0.00	0.00	0.00	0.00
skin	4.96	4.90	4.77	4.68	4.60	4.97	4.88	4.79	4.71	4.64
total brain	0.15	0.15	0.14	0.13	0.12	0.15	0.14	0.14	0.13	0.13
total colon	13.59	13.48	13.34	13.21	13.00	13.59	13.42	13.32	13.15	13.02
total breasts	12.02	12.58	12.74	11.61	11.63	0.00	0.00	0.00	0.00	0.00
total remainder tissues	6.94	6.85	6.73	6.59	6.46	6.94	6.82	6.71	6.61	6.51
Total ED (ICRP 103) in mSv	11.54	11.42	11.43	11.11	10.89	9.99	9.74	9.79	9.65	9.52
Average Torso Diameter (cm)	18.96	19.54	20.18	20.80	21.38	18.95	19.54	20.15	20.80	21.36
CAP Scan Length (cm)	46.90	48.40	49.60	51.10	52.30	46.90	48.10	49.60	51.10	52.60

Table B.6: 10-year-old phantom organ dose data in units of mGy for simulated Philips Brilliance 64 helical CT chest-abdomen-pelvis scans for 120 kVp, 100 mAs, pitch = 1, and 64 × 0.625 mm beam collimation.

	Females					Males				
Organ	10y 10th	10y 25th	10y 50th	10y 75th	10y 90th	10y 10th	10y 25th	10y 50th	10y 75th	10y 90th
body remainder	6.25	6.05	5.98	5.85	5.73	6.24	6.13	6.03	5.90	5.76
cerebrum	0.12	0.11	0.10	0.10	0.09	0.12	0.12	0.11	0.10	0.09
cerebellum	0.29	0.26	0.25	0.24	0.22	0.26	0.28	0.25	0.25	0.23
brain stem	0.21	0.21	0.18	0.18	0.18	0.20	0.20	0.19	0.19	0.18
spinal cord	10.06	9.77	9.51	9.38	8.93	9.92	9.99	9.57	9.43	9.03
salivary glands	0.87	0.79	0.86	0.78	0.78	0.87	0.86	0.85	0.84	0.74
esophagus	11.65	11.31	11.30	10.88	10.83	11.52	11.45	11.34	11.13	10.69
thyroid	10.42	8.02	10.98	8.36	9.96	11.08	9.22	10.67	10.03	7.56
thymus	12.76	12.58	12.59	12.36	12.39	12.79	12.62	12.63	12.46	12.25
eyes	0.18	0.17	0.15	0.14	0.14	0.19	0.16	0.15	0.15	0.14
eye lens	0.24	0.13	0.22	0.14	0.10	0.09	0.12	0.12	0.14	0.18
lungs	12.79	12.60	12.43	12.22	12.04	12.77	12.66	12.48	12.31	12.05
liver	13.35	13.17	12.99	12.73	12.49	13.38	13.26	13.07	12.84	12.58
gall bladder	13.89	13.66	13.47	13.30	13.23	13.94	13.74	13.52	13.26	13.32
kidneys	13.37	13.15	12.92	12.69	12.49	13.39	13.21	12.96	12.76	12.57
adrenals	12.48	12.36	12.01	11.51	11.34	12.06	12.40	12.14	11.96	11.41
stomach	12.99	12.99	12.64	12.38	12.18	13.13	12.91	12.76	12.47	12.25
spleen	11.77	11.59	11.35	11.17	10.98	11.89	11.56	11.43	11.22	11.12
heart	14.38	14.28	14.20	13.99	13.82	14.33	14.32	14.27	14.08	13.90
pancreas	12.81	12.53	12.30	12.09	11.88	12.89	12.63	12.45	12.24	11.93
bladder	12.97	12.76	12.64	12.38	12.22	13.04	12.86	12.69	12.50	12.33
bladder contents	0.00	0.00	0.00	0.00	0.00	0.00	0.00	0.00	0.00	0.00
ascending large intestine	14.03	13.87	13.66	13.46	13.28	13.95	13.82	13.68	13.47	13.32
transcending large intestine	14.52	14.35	14.19	14.07	13.80	14.62	14.39	14.25	14.16	13.94
descending large intestine	11.87	11.70	11.47	11.27	11.01	11.97	11.74	11.49	11.34	11.10
sigmoid	12.07	11.77	11.61	11.41	11.10	12.12	11.93	11.65	11.37	11.19
rectum	12.30	12.03	11.71	11.49	11.16	12.32	11.91	11.93	11.50	11.36
small intestine	13.67	13.46	13.31	13.12	12.89	13.68	13.56	13.39	13.19	13.03
GI contents	13.01	12.83	12.65	12.43	12.20	13.04	12.90	12.71	12.49	12.31
prostate	0.00	0.00	0.00	0.00	0.00	9.84	9.81	9.48	9.40	8.96
testes	0.00	0.00	0.00	0.00	0.00	13.97	13.34	14.20	13.49	13.89
uterus	11.97	11.99	11.54	11.34	11.12	0.00	0.00	0.00	0.00	0.00
ovaries	14.04	13.50	13.06	13.23	12.97	0.00	0.00	0.00	0.00	0.00
skin	4.73	4.59	4.54	4.40	4.34	4.72	4.65	4.57	4.47	4.39
total brain	0.13	0.12	0.12	0.11	0.10	0.13	0.13	0.12	0.12	0.11
total colon	13.19	12.99	12.79	12.60	12.35	13.23	13.02	12.83	12.63	12.45
total breasts	11.55	11.44	11.94	11.43	10.95	0.00	0.00	0.00	0.00	0.00
total remainder tissues	6.64	6.44	6.37	6.22	6.10	6.63	6.52	6.41	6.28	6.13
Total ED (ICRP 103) in mSv	11.17	10.89	10.89	10.58	10.43	9.82	9.59	9.59	9.37	9.14
Average Torso Diameter (cm)	20.70	21.39	22.11	22.86	23.55	20.47	21.13	21.86	22.56	23.23
CAP Scan Length (cm)	51.10	52.30	54.40	55.90	57.40	50.20	51.70	53.50	55.30	56.50

Table B.7: 13-year-old phantom organ dose data in units of mGy for simulated Philips Brilliance 64 helical CT chest-abdomen-pelvis scans for 120 kVp, 100 mAs, pitch = 1, and 64 × 0.625 mm beam collimation.

	Females					Males				
Organ	13y 10th	13y 25th	13y 50th	13y 75th	13y 90th	13y 10th	13y 25th	13y 50th	13y 75th	13y 90th
body remainder	6.27	6.14	6.00	5.84	6.12	6.50	6.34	6.67	6.44	6.26
cerebrum	0.08	0.07	0.08	0.08	0.06	0.10	0.09	0.09	0.08	0.07
cerebellum	0.17	0.15	0.15	0.14	0.11	0.22	0.20	0.19	0.17	0.16
brain stem	0.12	0.11	0.10	0.09	0.08	0.14	0.15	0.14	0.13	0.11
spinal cord	8.35	8.09	7.89	7.47	6.99	8.99	8.68	8.19	7.74	7.59
salivary glands	0.57	0.56	0.53	0.50	0.51	0.75	0.76	0.73	0.71	0.66
esophagus	10.23	10.28	10.08	9.82	9.85	10.90	10.64	11.13	10.77	10.39
thyroid	8.58	10.93	9.74	8.67	10.59	11.94	11.82	12.11	11.13	11.78
thymus	11.43	11.20	11.04	10.87	11.43	12.48	12.01	12.54	12.05	11.78
eyes	0.14	0.13	0.12	0.11	0.10	0.14	0.15	0.15	0.12	0.11
eye lens	0.10	0.12	0.11	0.08	0.10	0.21	0.08	0.19	0.12	0.13
lungs	11.57	11.38	11.19	10.93	11.05	11.94	11.65	12.02	11.72	11.48
liver	12.30	12.08	11.84	11.58	12.30	12.45	12.23	13.14	12.77	12.46
gall bladder	12.38	12.19	11.95	11.80	13.01	12.64	12.58	13.90	13.51	13.27
kidneys	12.84	12.61	12.37	12.14	12.62	13.50	13.28	13.67	13.32	12.93
adrenals	11.39	11.17	10.88	10.41	10.08	12.25	12.05	11.39	11.08	10.90
stomach	12.24	12.03	11.87	11.66	12.25	13.03	12.89	13.44	13.06	12.77
spleen	12.17	11.88	11.52	11.26	11.28	12.95	12.57	12.44	12.02	11.68
heart	12.53	12.35	12.10	11.88	12.72	13.26	12.95	13.81	13.50	13.25
pancreas	12.25	12.13	11.81	11.60	12.32	12.59	12.35	13.15	12.82	12.44
bladder	10.15	9.94	9.71	9.46	9.53	11.38	11.05	11.24	10.92	10.67
bladder contents	0.00	0.00	0.00	0.00	0.00	0.00	0.00	0.00	0.00	0.00
ascending large intestine	13.35	13.28	13.10	12.87	14.28	13.71	13.54	15.21	14.93	14.64
transcending large intestine	13.82	13.79	13.60	13.48	14.01	14.03	13.89	14.89	14.59	14.34
descending large intestine	11.09	10.87	10.69	10.46	12.36	12.20	11.95	13.70	13.35	13.09
sigmoid	11.51	11.39	11.19	11.05	11.18	12.33	12.16	12.36	12.02	11.81
rectum	10.84	10.49	10.17	9.67	8.72	11.60	11.18	10.31	9.87	9.48
small intestine	13.08	12.95	12.76	12.59	13.45	13.76	13.57	14.80	14.52	14.23
GI contents	12.23	12.10	11.87	11.69	12.66	12.92	12.73	13.71	13.39	13.12
prostate	0.00	0.00	0.00	0.00	0.00	9.72	9.30	9.29	9.29	8.77
testes	0.00	0.00	0.00	0.00	0.00	11.43	11.27	11.32	11.02	10.96
uterus	9.71	9.57	9.29	9.05	8.87	0.00	0.00	0.00	0.00	0.00
ovaries	10.47	10.16	9.94	9.47	9.71	0.00	0.00	0.00	0.00	0.00
skin	4.64	4.59	4.50	4.38	4.68	4.87	4.77	5.10	4.94	4.83
total brain	0.09	0.08	0.08	0.08	0.06	0.11	0.10	0.10	0.09	0.08
total colon	12.51	12.38	12.18	11.98	12.92	13.02	12.82	13.88	13.56	13.29
total breasts	12.09	11.91	11.78	11.57	11.36	0.00	0.00	0.00	0.00	0.00
total remainder tissues	6.55	6.43	6.29	6.12	6.42	6.82	6.65	7.00	6.77	6.59
Total ED (ICRP 103) in mSv	10.42	10.34	10.12	9.84	10.19	9.59	9.42	9.77	9.47	9.29
Average Torso Diameter (cm)	23.04	23.69	24.37	25.08	25.73	21.93	22.62	23.41	24.18	24.88
CAP Scan Length (cm)	60.10	61.60	63.40	64.90	66.40	59.50	61.30	63.40	65.20	67.00

Table B.8: 15-year-old phantom organ dose data in units of mGy for simulated Philips Brilliance 64 helical CT chest-abdomen-pelvis scans for 120 kVp, 100 mAs, pitch = 1, and 64 × 0.625 mm beam collimation.

	Females					Males				
Organ	15y 10th	15y 25th	15y 50th	15y 75th	15y 90th	15y 10th	15y 25th	15y 50th	15y 75th	15y 90th
body remainder	6.13	5.97	5.87	6.17	6.06	6.50	6.35	6.19	6.04	5.89
cerebrum	0.07	0.07	0.08	0.06	0.06	0.08	0.08	0.07	0.07	0.06
cerebellum	0.15	0.14	0.14	0.12	0.12	0.18	0.15	0.17	0.14	0.14
brain stem	0.11	0.10	0.10	0.10	0.08	0.14	0.12	0.13	0.10	0.10
spinal cord	8.01	7.77	7.60	7.02	6.90	7.85	7.60	7.37	7.12	6.93
salivary glands	0.58	0.50	0.49	0.53	0.50	0.67	0.70	0.65	0.63	0.61
esophagus	10.28	10.15	9.73	9.91	9.58	10.72	10.70	10.35	10.00	9.79
thyroid	11.26	9.96	8.07	11.08	8.94	10.46	12.58	11.14	11.34	11.56
thymus	11.23	11.14	10.86	11.51	11.23	12.02	11.86	11.67	11.47	11.20
eyes	0.13	0.12	0.12	0.10	0.10	0.12	0.11	0.12	0.11	0.11
eye lens	0.10	0.18	0.10	0.10	0.07	0.14	0.09	0.13	0.09	0.10
lungs	11.38	11.18	10.95	11.11	10.91	11.77	11.55	11.34	11.05	10.80
liver	12.07	11.88	11.62	12.38	12.10	12.92	12.62	12.27	11.95	11.64
gall bladder	12.24	12.04	11.93	13.05	12.80	13.70	13.40	13.15	12.97	12.67
kidneys	12.59	12.39	12.14	12.70	12.41	13.42	13.12	12.82	12.47	12.17
adrenals	11.19	10.88	10.47	10.15	9.97	11.08	10.97	10.82	10.26	10.00
stomach	11.98	11.87	11.76	12.34	12.00	13.16	12.93	12.63	12.29	12.09
spleen	11.86	11.52	11.32	11.38	11.06	12.13	11.85	11.56	11.25	10.97
heart	12.34	12.14	11.90	12.78	12.52	13.59	13.37	13.11	12.78	12.48
pancreas	12.09	11.87	11.61	12.34	12.08	12.94	12.64	12.29	11.90	11.66
bladder	9.92	9.72	9.54	9.57	9.37	10.94	10.68	10.46	10.16	9.97
bladder contents	0.00	0.00	0.00	0.00	0.00	0.00	0.00	0.00	0.00	0.00
ascending large intestine	13.19	13.11	12.96	14.37	14.08	15.04	14.73	14.43	14.22	13.99
transcending large intestine	13.69	13.57	13.45	14.04	13.89	14.78	14.47	14.25	14.03	13.71
descending large intestine	10.89	10.65	10.55	12.37	12.17	13.54	13.23	12.98	12.55	12.33
sigmoid	11.32	11.15	11.05	11.27	11.03	12.09	11.83	11.57	11.24	11.09
rectum	10.50	10.10	9.77	8.77	8.57	9.85	9.51	9.37	9.06	8.77
small intestine	12.93	12.79	12.61	13.50	13.25	14.66	14.37	14.13	13.84	13.58
GI contents	12.05	11.88	11.73	12.71	12.44	13.51	13.29	13.01	12.73	12.45
prostate	0.00	0.00	0.00	0.00	0.00	9.20	8.95	8.44	8.38	8.00
testes	0.00	0.00	0.00	0.00	0.00	11.04	11.04	10.86	10.78	10.18
uterus	9.52	9.44	9.19	8.82	8.62	0.00	0.00	0.00	0.00	0.00
ovaries	10.12	9.86	9.79	9.95	9.52	0.00	0.00	0.00	0.00	0.00
skin	4.57	4.48	4.40	4.71	4.63	5.00	4.91	4.80	4.68	4.57
total brain	0.08	0.08	0.08	0.06	0.06	0.09	0.08	0.08	0.07	0.07
total colon	12.33	12.16	12.02	12.98	12.76	13.69	13.39	13.13	12.83	12.59
total breasts	11.93	11.80	11.63	11.47	11.18	0.00	0.00	0.00	0.00	0.00
total remainder tissues	6.41	6.26	6.15	6.46	6.34	6.83	6.68	6.52	6.35	6.19
Total ED (ICRP 103) in mSv	10.39	10.17	9.93	10.33	10.01	9.55	9.46	9.20	8.99	8.78
Average Torso Diameter (cm)	23.67	24.27	24.91	25.56	26.15	23.75	24.37	25.07	25.77	26.38
CAP Scan Length (cm)	61.60	62.80	64.60	66.10	67.60	64.00	65.80	67.60	69.40	70.90

Table B.9: Newborn phantom bone dose data in units of mGy for simulated Philips Brilliance 64 helical CT chest-abdomen-pelvis scans for 120 kVp, 100 mAs, pitch = 1, and 64 × 0.625 mm beam collimation.

	Females					Males				
Bone	NB 10th	NB 25th	NB 50th	NB 75th	NB 90th	NB 10th	NB 25th	NB 50th	NB 75th	NB 90th
cartilage	4.97	5.00	5.15	5.16	5.06	5.01	5.24	5.18	4.98	5.20
skull	3.31	2.96	3.28	3.16	2.95	3.04	3.13	2.63	2.78	3.00
mandible	1.33	1.24	1.08	1.53	1.42	5.12	5.36	4.08	4.32	4.54
hyoid	24.51	22.20	23.44	20.67	18.43	25.73	24.59	17.96	19.68	23.92
sternum	41.75	43.98	43.31	42.10	41.25	42.45	42.92	42.14	42.73	43.50
cervical vertebrae	16.11	14.40	24.40	24.03	20.21	21.96	24.95	22.69	20.24	20.46
thoracic vertebrae	39.06	39.03	40.40	41.29	41.52	39.52	40.61	40.75	40.86	41.94
lumbar vertebrae	43.92	44.32	45.11	46.89	47.41	44.63	44.75	46.48	46.68	47.34
ribs	34.78	34.96	35.87	36.34	36.78	35.73	35.97	36.52	36.36	36.88
right scapula	31.02	30.63	32.06	32.76	32.98	30.78	31.98	32.98	32.33	32.94
right clavicle	32.09	31.31	35.12	33.68	33.99	33.98	35.51	33.62	33.16	35.01
right femur	19.36	18.96	20.02	20.16	18.93	20.24	19.73	19.87	21.06	20.85
right tibia	0.88	0.84	0.97	0.95	0.98	0.98	0.96	0.98	1.02	1.00
right fibula	0.44	0.42	0.42	0.48	0.41	0.61	0.62	0.64	0.64	0.57
right patella	1.99	2.01	2.12	1.88	1.89	2.66	2.73	2.45	2.32	2.19
right foot	0.21	0.28	0.24	0.22	0.22	0.26	0.28	0.30	0.27	0.25
left scapula	31.70	31.73	32.97	32.90	33.61	33.47	34.01	34.07	33.81	33.85
left clavicle	31.42	32.51	33.98	35.03	34.42	34.00	36.23	33.87	33.80	33.81
left femur	19.40	19.41	20.95	20.40	20.33	21.32	20.66	20.93	22.24	22.32
left tibia	0.85	0.87	1.01	0.86	1.02	1.02	1.02	1.03	1.12	1.02
left fibula	0.47	0.39	0.60	0.41	0.51	0.60	0.66	0.55	0.47	0.66
left patella	2.47	1.48	2.30	2.43	2.50	2.41	2.45	2.33	2.61	3.19
left foot	0.24	0.25	0.29	0.25	0.25	0.31	0.29	0.32	0.30	0.26
pelvis	41.91	42.67	44.07	44.53	45.30	43.26	43.69	44.91	45.35	45.29
sacrum	44.76	45.61	47.47	47.51	49.99	46.53	48.22	48.80	49.37	50.08
total bone	14.58	14.49	15.48	15.53	15.29	15.63	15.95	15.61	15.78	15.88

Table B.10: 1-year-old phantom bone dose data in units of mGy for simulated Philips Brilliance 64 helical CT chest-abdomen-pelvis scans for 120 kVp, 100 mAs, pitch = 1, and 64 × 0.625 mm beam collimation.

	Females					Males				
Bone	1y 10th	1y 25th	1y 50th	1y 75th	1y 90th	1y 10th	1y 25th	1y 50th	1y 75th	1y 90th
cartilage	13.41	13.41	13.35	13.40	13.46	13.11	13.25	13.37	13.22	13.22
skull	2.94	2.55	2.32	2.35	2.23	2.39	2.06	2.35	2.22	2.24
mandible	2.56	2.33	3.16	2.59	2.40	3.42	2.87	2.55	3.11	3.03
hyoid	30.16	28.57	26.18	24.29	22.32	28.46	23.57	25.24	22.79	25.11
sternum	50.64	51.17	50.79	51.24	51.68	50.47	50.83	51.08	51.50	51.63
cervical vertebrae	19.27	16.55	18.32	21.73	19.24	17.51	15.07	21.91	19.29	17.68
thoracic vertebrae	46.38	46.27	46.66	46.98	46.88	46.31	45.88	46.88	46.64	46.93
lumbar vertebrae	47.27	47.57	47.93	48.38	47.76	47.31	47.76	48.13	47.61	48.70
ribs	41.82	41.77	42.49	42.61	42.75	42.07	41.91	42.61	42.50	42.58
right scapula	39.25	40.41	41.88	42.48	41.95	41.09	41.27	42.50	41.60	41.59
right clavicle	41.82	39.47	40.23	41.60	40.28	40.08	38.74	40.73	39.67	40.33
right femur	18.92	18.50	18.67	18.56	18.26	18.68	17.99	18.14	17.86	18.35
right tibia	0.39	0.38	0.36	0.35	0.37	0.40	0.37	0.37	0.34	0.38
right fibula	0.27	0.29	0.22	0.32	0.27	0.30	0.29	0.28	0.28	0.25
right patella	1.39	1.30	1.31	1.20	1.31	1.36	1.37	1.40	1.22	1.27
right foot	0.24	0.26	0.24	0.27	0.27	0.28	0.26	0.25	0.25	0.25
left scapula	38.20	38.61	39.69	39.64	39.76	39.24	39.00	39.74	39.35	38.55
left clavicle	40.29	40.49	38.74	39.32	37.66	40.25	37.33	38.81	38.70	38.22
left femur	16.43	16.05	16.27	16.20	16.23	16.54	15.93	15.99	15.52	15.72
left tibia	0.39	0.40	0.41	0.35	0.34	0.42	0.39	0.37	0.35	0.36
left fibula	0.33	0.29	0.32	0.27	0.24	0.33	0.33	0.30	0.23	0.28
left patella	1.41	1.27	1.43	1.29	1.27	1.22	1.28	1.12	1.16	1.08
left foot	0.29	0.28	0.25	0.25	0.26	0.30	0.29	0.26	0.29	0.26
pelvis	45.45	45.78	46.05	45.89	46.16	45.67	45.89	45.58	45.40	45.92
sacrum	50.14	49.85	50.72	49.98	50.39	49.92	50.09	49.76	50.03	49.88
total bone	18.42	18.13	18.17	18.35	18.17	18.30	17.92	18.43	18.21	17.95

Table B.11: 3-year-old phantom bone dose data in units of mGy for simulated Philips Brilliance 64 helical CT chest-abdomen-pelvis scans for 120 kVp, 100 mAs, pitch = 1, and 64 × 0.625 mm beam collimation.

	Females					Males				
Bone	3y 10th	3y 25th	3y 50th	3y 75th	3y 90th	3y 10th	3y 25th	3y 50th	3y 75th	3y 90th
cartilage	14.29	14.56	14.59	14.19	14.00	14.22	14.62	14.44	14.01	14.08
skull	1.54	1.63	1.22	1.32	1.31	1.24	1.27	1.43	1.13	1.11
mandible	1.98	2.06	3.91	1.66	1.62	3.87	4.96	1.82	3.13	3.58
hyoid	16.71	21.37	19.11	13.81	15.87	15.27	20.92	17.78	14.04	18.76
sternum	48.64	49.51	49.94	49.08	49.48	48.92	48.94	49.40	49.76	49.25
cervical vertebrae	12.82	12.96	13.28	12.99	11.22	12.51	13.24	12.20	12.56	11.88
thoracic vertebrae	44.02	44.30	43.90	43.69	43.11	43.98	43.85	43.40	43.59	43.29
lumbar vertebrae	50.33	49.22	48.39	47.31	47.13	50.21	49.18	48.35	47.31	46.55
ribs	42.02	42.22	41.99	41.70	41.52	41.92	41.99	41.68	41.63	41.50
right scapula	28.75	29.49	28.37	29.49	28.57	29.21	28.78	27.32	29.19	28.59
right clavicle	33.79	36.09	35.77	35.81	33.66	34.01	36.13	34.63	34.56	33.66
right femur	15.28	15.01	15.14	14.57	14.85	15.09	15.34	14.75	14.96	14.57
right tibia	0.18	0.16	0.15	0.13	0.13	0.17	0.17	0.16	0.14	0.12
right fibula	0.13	0.11	0.11	0.11	0.09	0.15	0.15	0.12	0.11	0.08
right patella	0.29	0.26	0.26	0.17	0.22	0.29	0.30	0.22	0.24	0.23
right foot	0.12	0.12	0.12	0.13	0.11	0.14	0.12	0.11	0.12	0.11
left scapula	36.75	37.42	35.03	35.58	36.05	35.82	37.54	34.27	37.37	37.51
left clavicle	37.37	40.49	40.47	38.64	37.89	37.36	40.27	38.75	37.82	39.42
left femur	15.44	15.47	15.15	14.05	14.29	15.46	15.35	14.31	14.53	13.82
left tibia	0.19	0.17	0.16	0.13	0.14	0.19	0.18	0.15	0.14	0.13
left fibula	0.14	0.12	0.10	0.11	0.10	0.14	0.10	0.11	0.10	0.08
left patella	0.33	0.35	0.30	0.26	0.25	0.35	0.30	0.31	0.30	0.29
left foot	0.14	0.12	0.12	0.12	0.12	0.13	0.12	0.12	0.12	0.12
pelvis	48.32	47.99	47.31	46.56	46.35	48.32	47.66	46.95	46.60	45.84
sacrum	48.86	48.19	47.28	46.81	45.84	49.17	48.26	46.99	46.30	45.36
total bone	19.66	19.70	19.37	19.04	18.84	19.82	19.83	19.23	19.19	18.87

Table B.12: 5-year-old phantom bone dose data in units of mGy for simulated Philips Brilliance 64 helical CT chest-abdomen-pelvis scans for 120 kVp, 100 mAs, pitch = 1, and 64 × 0.625 mm beam collimation.

	Females					Males				
Bone	5y 10th	5y 25th	5y 50th	5y 75th	5y 90th	5y 10th	5y 25th	5y 50th	5y 75th	5y 90th
cartilage	14.04	14.20	13.81	13.56	13.85	14.15	13.83	13.41	13.81	13.76
skull	1.40	1.35	1.02	1.09	0.89	1.32	1.15	1.07	1.22	1.05
mandible	1.72	1.68	2.74	1.30	2.70	1.71	1.45	1.31	1.47	1.32
hyoid	19.47	19.47	13.07	13.89	14.00	18.55	13.67	11.99	17.02	13.93
sternum	50.76	51.44	52.83	52.38	53.34	51.28	52.14	51.77	53.25	53.61
cervical vertebrae	12.23	12.03	12.83	9.94	10.17	11.68	11.52	9.88	11.41	10.40
thoracic vertebrae	43.68	42.83	42.68	41.63	40.85	42.63	41.95	41.65	41.37	40.54
lumbar vertebrae	47.15	46.04	45.25	43.59	42.35	46.15	45.08	43.86	42.79	41.64
ribs	42.22	41.79	41.39	40.69	40.20	41.60	41.06	40.79	40.44	39.85
right scapula	29.32	27.45	28.98	27.47	26.04	27.45	27.69	28.15	27.25	26.05
right clavicle	33.90	35.26	35.49	32.63	34.66	35.08	34.44	32.96	35.04	34.38
right femur	14.45	13.88	13.59	13.17	12.65	14.07	13.61	13.25	12.92	12.41
right tibia	0.13	0.12	0.09	0.09	0.08	0.11	0.10	0.09	0.09	0.08
right fibula	0.09	0.10	0.08	0.08	0.08	0.09	0.09	0.08	0.08	0.07
right patella	0.21	0.21	0.19	0.19	0.17	0.23	0.22	0.18	0.20	0.18
right foot	0.12	0.11	0.10	0.10	0.10	0.09	0.10	0.11	0.10	0.10
left scapula	38.36	35.53	37.02	36.94	33.50	35.05	33.42	36.05	36.44	32.90
left clavicle	40.74	40.21	39.27	38.15	39.35	40.37	38.41	36.42	41.11	38.57
left femur	14.07	13.48	12.87	12.45	11.87	13.56	12.79	12.57	12.14	11.72
left tibia	0.13	0.12	0.10	0.08	0.08	0.12	0.11	0.10	0.09	0.08
left fibula	0.10	0.09	0.07	0.07	0.07	0.09	0.07	0.08	0.07	0.05
left patella	0.25	0.29	0.23	0.24	0.24	0.26	0.21	0.22	0.25	0.22
left foot	0.12	0.11	0.11	0.11	0.09	0.11	0.11	0.10	0.11	0.10
pelvis	46.55	45.79	44.99	44.11	43.10	45.69	44.87	44.18	43.40	42.68
sacrum	45.73	44.54	43.34	41.94	41.19	44.56	43.33	42.31	41.11	40.20
total bone	19.16	18.73	18.41	17.83	17.36	18.80	18.33	18.00	17.87	17.34

Table B.13: 8-year-old phantom bone dose data in units of mGy for simulated Philips Brilliance 64 helical CT chest-abdomen-pelvis scans for 120 kVp, 100 mAs, pitch = 1, and 64 × 0.625 mm beam collimation.

	Females					Males				
Bone	8y 10th	8y 25th	8y 50th	8y 75th	8y 90th	8y 10th	8y 25th	8y 50th	8y 75th	8y 90th
cartilage	13.90	13.72	13.82	13.41	13.05	13.95	13.52	13.82	13.25	13.14
skull	0.89	0.86	1.13	0.80	0.75	1.22	1.12	0.84	1.05	1.03
mandible	4.76	4.65	0.42	4.48	4.03	0.46	0.43	4.79	0.40	0.37
hyoid	22.36	22.07	23.59	21.23	17.17	23.42	18.29	24.58	18.96	19.42
sternum	54.98	53.75	53.64	53.34	52.56	54.38	53.33	53.20	52.51	52.13
cervical vertebrae	9.80	9.51	8.64	9.36	8.01	10.04	9.30	9.15	8.86	8.52
thoracic vertebrae	43.36	43.06	42.36	41.68	41.29	42.98	42.80	42.04	41.08	40.80
lumbar vertebrae	47.54	46.80	45.87	44.95	44.09	46.96	46.29	45.60	44.76	43.82
ribs	42.12	41.47	41.00	40.37	39.74	41.79	41.16	40.82	39.91	39.48
right scapula	32.20	32.17	32.07	30.93	30.81	32.05	32.04	31.74	30.79	30.72
right clavicle	38.82	38.60	37.07	37.91	36.28	38.82	37.74	37.21	37.47	36.75
right femur	10.50	10.33	9.97	9.67	9.35	10.50	10.23	9.93	9.90	9.56
right tibia	0.05	0.05	0.04	0.04	0.04	0.05	0.04	0.04	0.04	0.04
right fibula	0.04	0.04	0.04	0.04	0.04	0.04	0.03	0.03	0.03	0.03
right patella	0.18	0.14	0.13	0.13	0.14	0.14	0.13	0.14	0.12	0.14
right foot	0.08	0.07	0.07	0.08	0.08	0.08	0.08	0.08	0.07	0.07
left scapula	32.37	31.33	31.88	30.95	29.88	31.66	31.31	31.48	29.95	29.96
left clavicle	37.27	35.89	36.55	36.02	33.86	37.16	35.31	37.58	34.68	34.87
left femur	9.33	9.16	8.81	8.44	8.26	9.31	9.09	8.65	8.59	8.33
left tibia	0.05	0.05	0.04	0.04	0.04	0.05	0.05	0.04	0.04	0.04
left fibula	0.04	0.05	0.04	0.04	0.04	0.05	0.04	0.05	0.05	0.04
left patella	0.14	0.15	0.13	0.10	0.11	0.12	0.14	0.13	0.11	0.11
left foot	0.09	0.08	0.08	0.07	0.08	0.09	0.08	0.08	0.09	0.08
pelvis	42.94	42.60	41.89	40.98	40.40	42.47	41.73	41.21	40.51	39.75
sacrum	48.17	47.76	47.01	45.93	45.15	47.70	47.04	46.19	45.33	44.66
total bone	18.97	18.75	18.39	18.08	17.70	18.98	18.66	18.42	18.05	17.79

Table B.14: 10-year-old phantom bone dose data in units of mGy for simulated Philips Brilliance 64 helical CT chest-abdomen-pelvis scans for 120 kVp, 100 mAs, pitch = 1, and 64 × 0.625 mm beam collimation.

	Females					Males				
Bone	10y 10th	10y 25th	10y 50th	10y 75th	10y 90th	10y 10th	10y 25th	10y 50th	10y 75th	10y 90th
cartilage	13.35	13.04	12.90	12.47	12.56	13.52	13.07	13.08	12.66	12.35
skull	1.08	0.99	0.71	0.91	0.88	0.78	0.75	0.99	0.69	0.68
mandible	0.40	0.37	4.29	0.34	0.33	4.49	4.11	0.34	4.04	3.62
hyoid	20.56	16.46	19.64	16.29	18.55	20.32	18.35	20.62	18.14	16.68
sternum	52.79	52.11	51.60	51.19	50.62	52.66	51.90	51.96	51.62	50.44
cervical vertebrae	9.19	7.91	7.54	8.03	6.69	7.80	9.09	7.52	8.66	6.78
thoracic vertebrae	41.41	40.89	39.66	39.16	38.04	41.09	41.03	39.87	39.34	38.30
lumbar vertebrae	45.05	43.61	42.81	41.68	40.97	44.65	43.77	43.29	42.09	41.15
ribs	40.10	39.40	38.64	37.88	37.08	40.11	39.56	38.81	38.05	37.29
right scapula	30.71	30.63	29.70	29.30	28.56	30.63	30.55	29.96	29.16	28.68
right clavicle	37.52	36.10	36.41	35.59	33.96	36.68	36.86	35.50	36.43	34.61
right femur	9.82	9.41	9.24	8.96	8.65	9.66	9.31	9.25	8.84	8.57
right tibia	0.04	0.04	0.04	0.04	0.03	0.04	0.04	0.04	0.03	0.03
right fibula	0.03	0.03	0.03	0.03	0.03	0.04	0.04	0.04	0.03	0.03
right patella	0.15	0.14	0.11	0.11	0.09	0.14	0.13	0.12	0.11	0.09
right foot	0.08	0.07	0.07	0.07	0.06	0.07	0.07	0.06	0.07	0.07
left scapula	30.41	29.47	29.57	28.14	28.16	31.15	29.52	29.50	28.34	27.74
left clavicle	35.78	33.72	34.63	33.90	34.38	36.39	34.84	35.42	33.91	32.28
left femur	8.73	8.22	8.11	7.79	7.66	8.48	8.16	8.00	7.69	7.39
left tibia	0.04	0.04	0.04	0.04	0.03	0.04	0.04	0.04	0.03	0.03
left fibula	0.04	0.04	0.04	0.04	0.03	0.05	0.04	0.04	0.04	0.04
left patella	0.10	0.12	0.09	0.08	0.08	0.12	0.12	0.11	0.10	0.09
left foot	0.08	0.08	0.07	0.07	0.07	0.08	0.07	0.07	0.07	0.07
pelvis	40.70	39.90	39.05	38.30	37.42	40.46	39.72	39.05	38.12	37.27
sacrum	45.42	44.39	43.51	42.18	41.09	45.32	44.63	43.63	42.61	41.39
total bone	18.17	17.71	17.34	16.92	16.51	17.86	17.61	17.11	16.77	16.64

Table B.15: 13-year-old phantom bone dose data in units of mGy for simulated Philips Brilliance 64 helical CT chest-abdomen-pelvis scans for 120 kVp, 100 mAs, pitch = 1, and 64 × 0.625 mm beam collimation.

	Females					Males				
Bone	13y 10th	13y 25th	13y 50th	13y 75th	13y 90th	13y 10th	13y 25th	13y 50th	13y 75th	13y 90th
cartilage	11.69	11.87	11.45	11.27	11.50	12.80	12.78	12.69	12.46	12.18
skull	0.67	0.64	0.62	0.59	0.55	0.85	0.92	0.76	0.82	0.78
mandible	0.23	0.24	0.35	0.23	0.18	1.18	0.29	0.99	0.25	0.24
hyoid	5.10	5.75	5.07	4.75	4.95	6.97	7.21	6.44	6.53	6.09
sternum	47.51	46.92	46.13	45.22	46.83	52.76	51.41	49.83	48.62	47.72
cervical vertebrae	6.02	5.88	6.08	4.95	4.54	8.02	6.88	6.99	5.73	5.69
thoracic vertebrae	36.18	35.22	34.38	33.08	31.05	37.81	36.72	35.16	33.92	32.89
lumbar vertebrae	39.07	38.43	37.22	36.36	35.44	41.69	40.84	39.79	38.43	37.69
ribs	38.40	37.56	36.71	35.76	37.45	39.57	38.73	40.56	39.37	38.27
right scapula	31.35	30.61	29.86	29.18	28.09	30.04	28.71	29.00	26.73	26.91
right clavicle	33.11	32.31	32.44	31.18	33.12	32.53	31.49	34.99	31.77	32.61
right femur	8.89	8.77	8.47	8.23	9.38	8.94	8.70	10.07	9.70	9.24
right tibia	0.04	0.04	0.04	0.04	0.03	0.04	0.04	0.04	0.03	0.03
right fibula	0.04	0.04	0.04	0.04	0.03	0.04	0.04	0.03	0.03	0.03
right patella	0.15	0.14	0.14	0.13	0.13	0.12	0.10	0.10	0.09	0.09
right foot	0.08	0.08	0.08	0.09	0.07	0.07	0.08	0.07	0.07	0.07
left scapula	29.79	29.67	28.00	27.91	27.28	30.68	31.36	28.76	29.73	26.34
left clavicle	32.59	32.98	31.07	31.24	32.63	32.49	33.48	32.54	33.59	30.55
left femur	8.07	7.82	7.56	7.37	8.29	7.78	7.52	9.15	8.69	8.34
left tibia	0.05	0.04	0.04	0.04	0.03	0.04	0.04	0.04	0.04	0.03
left fibula	0.04	0.04	0.04	0.04	0.03	0.05	0.04	0.03	0.03	0.03
left patella	0.12	0.13	0.12	0.10	0.11	0.11	0.09	0.10	0.09	0.08
left foot	0.08	0.08	0.09	0.08	0.07	0.08	0.07	0.07	0.07	0.07
pelvis	34.62	33.86	33.06	32.16	33.91	37.57	36.63	38.03	36.76	35.71
sacrum	35.77	34.96	33.81	32.84	31.21	40.36	39.32	37.45	36.44	35.48
total bone	17.31	16.94	16.52	16.03	16.28	17.61	17.20	17.61	17.01	16.49

Table B.16: 15-year-old phantom bone dose data in units of mGy for simulated Philips Brilliance 64 helical CT chest-abdomen-pelvis scans for 120 kVp, 100 mAs, pitch = 1, and 64 × 0.625 mm beam collimation.

	Females					Males				
Bone	15y 10th	15y 25th	15y 50th	15y 75th	15y 90th	15y 10th	15y 25th	15y 50th	15y 75th	15y 90th
cartilage	11.87	11.44	11.18	11.56	11.18	12.30	12.56	11.92	11.82	11.45
skull	0.65	0.59	0.58	0.56	0.55	0.83	0.81	0.65	0.72	0.69
mandible	0.24	0.34	0.33	0.17	0.18	0.26	0.24	0.83	0.21	0.20
hyoid	6.00	4.99	4.55	5.26	4.55	5.65	6.97	5.76	6.27	5.83
sternum	46.61	46.23	45.42	46.92	45.91	48.40	47.76	46.39	45.59	45.00
cervical vertebrae	5.98	5.19	4.84	4.75	4.93	5.67	5.99	5.91	5.23	5.16
thoracic vertebrae	35.10	33.85	33.21	31.29	30.74	33.79	32.87	32.26	30.93	30.09
lumbar vertebrae	38.01	37.20	36.33	35.31	34.48	38.29	37.22	36.19	35.25	34.26
ribs	37.43	36.60	35.85	37.52	36.90	39.40	38.56	37.59	36.44	35.62
right scapula	30.55	29.65	29.11	28.14	28.44	27.50	25.63	26.22	24.16	24.50
right clavicle	32.28	31.93	30.78	32.54	33.18	33.00	31.23	31.97	29.53	29.99
right femur	8.74	8.43	8.26	9.42	9.14	9.51	9.25	8.84	8.62	8.14
right tibia	0.04	0.04	0.04	0.03	0.03	0.04	0.03	0.03	0.03	0.03
right fibula	0.04	0.04	0.04	0.03	0.03	0.04	0.03	0.03	0.03	0.03
right patella	0.13	0.15	0.15	0.16	0.13	0.10	0.09	0.09	0.07	0.07
right foot	0.08	0.09	0.08	0.07	0.07	0.07	0.07	0.06	0.06	0.06
left scapula	29.60	27.65	27.84	27.69	25.66	28.66	28.71	26.18	26.92	24.44
left clavicle	32.95	30.59	30.68	33.23	30.84	31.47	32.68	30.03	31.52	28.71
left femur	7.78	7.51	7.35	8.41	8.09	8.47	8.23	7.93	7.62	7.33
left tibia	0.04	0.04	0.04	0.03	0.03	0.04	0.03	0.03	0.03	0.03
left fibula	0.04	0.04	0.03	0.03	0.03	0.03	0.02	0.03	0.02	0.02
left patella	0.11	0.11	0.11	0.10	0.10	0.10	0.08	0.07	0.08	0.07
left foot	0.08	0.08	0.08	0.07	0.07	0.07	0.07	0.06	0.06	0.06
pelvis	33.63	32.98	32.29	33.96	33.05	36.26	35.38	34.43	33.45	32.51
sacrum	34.62	33.68	32.81	31.13	30.45	35.86	34.87	34.01	32.99	32.14
total bone	16.91	16.40	16.09	16.36	16.00	17.07	16.69	16.22	15.71	15.28

Table B.17: Newborn phantom marrow dose data in units of mGy for simulated Philips Brilliance 64 helical CT chest-abdomen-pelvis scans for 120 kVp, 100 mAs, pitch = 1, and 64 × 0.625 mm beam collimation.

	Females					Males				
Marrow Type	NB 10th	NB 25th	NB 50th	NB 75th	NB 90th	NB 10th	NB 25th	NB 50th	NB 75th	NB 90th
yellow marrow	—	—	—	—	—	—	—	—	—	—
sternum marrow	19.43	25.69	23.01	18.01	19.39	26.53	27.51	30.98	29.12	21.99
cervical vertebrae marrow	12.48	10.69	18.10	17.32	16.31	19.65	20.00	18.71	17.08	17.64
thoracic vertebrae marrow	26.15	25.82	26.77	26.59	26.28	29.40	28.06	29.76	29.18	28.85
lumbar vertebrae marrow	28.77	28.65	28.61	29.38	30.03	30.59	30.98	34.31	32.37	31.41
sacrum marrow	21.93	22.37	25.46	22.60	21.86	35.16	22.99	23.89	30.86	24.93
ribs marrow	19.88	18.92	20.88	20.07	22.25	22.29	24.30	24.14	21.58	25.13
right scapula marrow	11.44	11.04	13.15	12.94	11.68	13.44	13.18	13.62	14.18	13.54
right clavicle marrow	11.25	15.53	13.34	16.16	23.88	20.51	41.59	24.14	24.22	34.33
right femur marrow	17.20	14.68	17.30	14.89	16.33	21.97	20.73	21.30	19.85	20.88
right tibia marrow	0.83	0.63	0.68	0.73	0.71	0.70	0.83	0.90	0.83	0.69
right fibula marrow	0.18	0.09	0.16	0.14	0.09	0.15	0.12	0.08	0.15	0.12
right patella marrow	0.90	4.25	1.98	0.35	0.58	1.36	1.38	1.05	2.13	0.86
right foot marrow	0.08	0.08	0.05	0.06	0.10	0.06	0.08	0.07	0.08	0.10
left scapula marrow	11.88	12.87	12.10	13.29	11.31	14.60	13.85	12.61	14.05	12.91
left clavicle marrow	23.43	16.65	13.36	26.46	31.55	23.52	47.11	30.50	16.65	29.88
left femur marrow	18.50	15.07	18.87	14.14	17.90	23.00	22.34	22.66	20.72	20.63
left tibia marrow	0.59	0.74	0.61	0.68	0.63	0.76	0.92	0.99	0.83	0.66
left fibula marrow	0.14	0.16	0.12	0.08	0.11	0.20	0.14	0.16	0.18	0.20
left patella marrow	1.58	3.33	1.84	0.22	0.87	0.34	1.25	0.72	0.61	1.72
left foot marrow	0.06	0.07	0.11	0.09	0.08	0.14	0.13	0.11	0.07	0.09
pelvis marrow	15.02	15.43	15.85	15.84	17.04	18.64	17.70	19.02	17.16	18.70
skull marrow	0.88	0.78	0.69	0.66	0.62	0.87	0.77	0.69	0.84	1.04
total red marrow	9.14	8.74	9.46	9.02	9.51	10.81	10.35	10.83	10.43	10.85

Table B.18: 1-year-old phantom marrow dose data in units of mGy for simulated Philips Brilliance 64 helical CT chest-abdomen-pelvis scans for 120 kVp, 100 mAs, pitch = 1, and 64 × 0.625 mm beam collimation.

	Females					Males				
Marrow Type	1y 10th	1y 25th	1y 50th	1y 75th	1y 90th	1y 10th	1y 25th	1y 50th	1y 75th	1y 90th
yellow marrow	6.55	6.49	6.67	6.73	6.52	6.59	6.64	6.73	6.68	6.76
sternum marrow	13.21	13.62	13.22	13.51	13.52	13.39	13.22	13.29	13.28	13.47
cervical vertebrae marrow	12.49	10.54	11.38	14.17	12.03	11.07	9.38	14.18	12.03	10.78
thoracic vertebrae marrow	24.68	24.61	24.81	24.95	24.76	24.51	24.40	24.75	24.69	24.65
lumbar vertebrae marrow	24.62	24.79	24.72	25.12	24.87	24.62	24.55	24.89	24.55	25.15
sacrum marrow	12.72	12.77	12.91	12.72	12.71	12.70	12.82	12.78	12.62	12.60
ribs marrow	11.25	11.49	11.53	11.64	11.48	11.34	11.46	11.52	11.56	11.39
right scapula marrow	10.87	10.99	11.59	11.64	11.62	11.24	11.39	11.85	11.41	11.41
right clavicle marrow	12.40	12.16	11.11	10.77	11.32	11.89	10.58	11.59	11.08	11.91
right femur marrow	5.21	5.12	5.18	5.16	5.17	5.13	5.21	5.13	5.14	5.22
right tibia marrow	0.12	0.10	0.10	0.08	0.08	0.10	0.09	0.11	0.12	0.08
right fibula marrow	0.10	0.11	0.07	0.05	0.04	0.08	0.08	0.08	0.06	0.06
right patella marrow	0.34	0.37	0.46	0.31	0.30	0.21	0.22	0.30	0.17	0.42
right foot marrow	0.03	0.04	0.05	0.03	0.05	0.04	0.04	0.03	0.04	0.04
left scapula marrow	10.41	10.43	10.87	11.44	11.28	10.81	10.94	11.22	11.04	10.72
left clavicle marrow	11.13	10.42	10.38	11.33	11.30	11.41	10.87	11.44	11.43	11.27
left femur marrow	4.52	4.67	4.43	4.33	4.34	4.39	4.40	4.29	4.45	4.41
left tibia marrow	0.11	0.11	0.08	0.10	0.08	0.12	0.11	0.09	0.09	0.10
left fibula marrow	0.07	0.08	0.04	0.08	0.09	0.06	0.04	0.05	0.06	0.06
left patella marrow	0.28	0.17	0.17	0.29	0.24	0.22	0.24	0.24	0.27	0.23
left foot marrow	0.03	0.06	0.05	0.05	0.05	0.04	0.03	0.04	0.04	0.05
pelvis marrow	11.71	11.75	11.78	11.67	11.71	11.62	11.69	11.62	11.55	11.54
skull marrow	0.85	0.71	0.55	0.54	0.55	0.64	0.48	0.54	0.55	0.59
total red marrow	10.27	10.12	10.22	10.41	10.23	10.18	10.08	10.41	10.25	10.33

Table B.19: 3-year-old phantom marrow dose data in units of mGy for simulated Philips Brilliance 64 helical CT chest-abdomen-pelvis scans for 120 kVp, 100 mAs, pitch = 1, and 64 × 0.625 mm beam collimation.

	Females					Males				
Marrow Type	3y 10th	3y 25th	3y 50th	3y 75th	3y 90th	3y 10th	3y 25th	3y 50th	3y 75th	3y 90th
yellow marrow	6.44	6.39	6.32	6.20	6.10	6.25	6.31	6.12	6.13	5.99
sternum marrow	13.61	13.51	13.45	13.17	13.00	12.90	13.38	13.16	13.25	13.39
cervical vertebrae marrow	6.78	7.43	7.58	7.42	6.12	6.70	7.33	6.54	6.70	6.61
thoracic vertebrae marrow	22.93	22.78	22.74	22.64	22.32	22.69	22.98	22.42	22.53	22.26
lumbar vertebrae marrow	25.66	24.95	24.44	23.90	23.85	25.52	24.92	24.25	23.78	23.46
sacrum marrow	12.90	12.65	12.45	12.24	11.99	12.83	12.69	12.36	12.20	11.87
ribs marrow	11.60	11.56	11.56	11.41	11.35	11.56	11.54	11.46	11.36	11.37
right scapula marrow	8.19	8.52	8.09	8.42	7.99	8.30	8.18	7.90	8.14	8.06
right clavicle marrow	9.81	10.21	9.93	9.86	9.64	10.10	10.75	10.28	9.76	9.65
right femur marrow	5.49	5.54	5.42	5.13	5.04	5.59	5.51	5.31	5.23	4.97
right tibia marrow	0.05	0.04	0.04	0.03	0.03	0.05	0.05	0.04	0.03	0.03
right fibula marrow	0.02	0.04	0.02	0.02	0.02	0.03	0.04	0.01	0.03	0.02
right patella marrow	0.06	0.04	0.06	0.05	0.05	0.07	0.05	0.03	0.03	0.03
right foot marrow	0.02	0.01	0.02	0.01	0.02	0.02	0.01	0.02	0.03	0.01
left scapula marrow	10.53	11.02	10.27	10.22	10.45	10.06	10.90	10.13	10.63	10.66
left clavicle marrow	11.17	11.49	11.08	10.76	10.71	10.99	11.69	11.29	10.71	11.15
left femur marrow	5.44	4.99	5.14	4.93	4.95	5.33	5.25	5.12	4.91	4.74
left tibia marrow	0.05	0.05	0.03	0.03	0.03	0.05	0.05	0.03	0.04	0.03
left fibula marrow	0.02	0.05	0.02	0.04	0.02	0.02	0.04	0.03	0.04	0.03
left patella marrow	0.12	0.06	0.05	0.06	0.05	0.06	0.06	0.05	0.05	0.05
left foot marrow	0.02	0.02	0.02	0.02	0.02	0.03	0.02	0.01	0.02	0.02
pelvis marrow	12.72	12.57	12.42	12.23	12.05	12.66	12.61	12.34	12.22	11.93
skull marrow	0.48	0.56	0.43	0.33	0.37	0.45	0.57	0.41	0.36	0.43
total red marrow	10.32	10.28	10.13	9.94	9.78	10.21	10.25	9.96	9.86	9.74

Table B.20: 5-year-old phantom marrow dose data in units of mGy for simulated Philips Brilliance 64 helical CT chest-abdomen-pelvis scans for 120 kVp, 100 mAs, pitch = 1, and 64 × 0.625 mm beam collimation.

	Females					Males				
Marrow Type	5y 10th	5y 25th	5y 50th	5y 75th	5y 90th	5y 10th	5y 25th	5y 50th	5y 75th	5y 90th
yellow marrow	6.44	6.28	6.16	5.95	5.79	6.21	6.11	5.94	5.83	5.71
sternum marrow	13.22	12.99	13.68	13.43	14.14	13.14	13.49	13.46	13.76	14.24
cervical vertebrae marrow	6.38	6.19	6.75	5.19	5.40	6.15	5.98	5.08	6.06	5.42
thoracic vertebrae marrow	21.44	20.97	20.88	20.37	20.04	20.66	20.68	20.51	20.28	19.79
lumbar vertebrae marrow	22.71	21.88	21.42	20.67	20.09	21.99	21.47	20.80	20.39	19.80
sacrum marrow	11.47	11.27	10.75	10.38	10.11	11.23	10.88	10.52	10.21	9.90
ribs marrow	11.20	10.98	10.97	10.65	10.53	11.06	10.95	10.76	10.57	10.49
right scapula marrow	7.86	7.57	7.87	7.36	7.12	7.58	7.47	7.62	7.47	6.96
right clavicle marrow	9.32	9.71	9.86	8.64	9.16	9.88	9.52	8.99	9.66	9.72
right femur marrow	5.48	5.25	5.14	4.88	4.63	5.19	5.10	4.91	4.83	4.61
right tibia marrow	0.03	0.03	0.03	0.01	0.02	0.02	0.02	0.02	0.02	0.02
right fibula marrow	0.02	0.02	0.02	0.02	0.02	0.02	0.00	0.01	0.01	0.01
right patella marrow	0.05	0.02	0.04	0.05	0.03	0.04	0.03	0.05	0.03	0.06
right foot marrow	0.02	0.02	0.01	0.01	0.02	0.02	0.02	0.02	0.02	0.02
left scapula marrow	10.35	10.02	10.06	10.16	9.48	9.82	9.48	9.86	10.15	9.30
left clavicle marrow	11.16	11.09	11.13	10.16	10.51	10.57	10.81	10.05	11.01	10.40
left femur marrow	5.03	4.99	4.76	4.47	4.29	4.87	4.76	4.56	4.50	4.25
left tibia marrow	0.02	0.03	0.02	0.02	0.02	0.02	0.02	0.02	0.02	0.01
left fibula marrow	0.03	0.04	0.02	0.01	0.01	0.03	0.03	0.01	0.02	0.02
left patella marrow	0.04	0.05	0.04	0.06	0.05	0.05	0.04	0.04	0.04	0.03
left foot marrow	0.02	0.02	0.02	0.01	0.01	0.02	0.02	0.01	0.01	0.02
pelvis marrow	11.68	11.45	11.16	10.85	10.59	11.42	11.21	10.94	10.73	10.48
skull marrow	0.42	0.41	0.29	0.28	0.27	0.39	0.28	0.27	0.35	0.26
total red marrow	9.76	9.53	9.41	9.01	8.85	9.54	9.38	9.13	9.05	8.75

Table B.21: 8-year-old phantom marrow dose data in units of mGy for simulated Philips Brilliance 64 helical CT chest-abdomen-pelvis scans for 120 kVp, 100 mAs, pitch = 1, and 64 × 0.625 mm beam collimation.

	Females					Males				
Marrow Type	8y 10th	8y 25th	8y 50th	8y 75th	8y 90th	8y 10th	8y 25th	8y 50th	8y 75th	8y 90th
yellow marrow	3.14	3.09	3.07	2.99	2.93	3.03	2.97	2.93	2.87	2.83
sternum marrow	13.58	13.26	13.27	13.19	12.83	13.36	13.33	12.81	12.94	12.75
cervical vertebrae marrow	5.30	5.10	4.95	4.89	4.16	5.18	4.76	4.87	4.79	4.48
thoracic vertebrae marrow	19.62	19.64	19.34	19.19	19.00	19.54	19.43	19.24	18.91	18.76
lumbar vertebrae marrow	20.53	20.27	19.76	19.39	19.14	20.17	20.03	19.50	19.23	18.91
sacrum marrow	11.18	11.00	10.86	10.54	10.43	11.04	10.81	10.62	10.55	10.29
ribs marrow	10.52	10.37	10.13	9.91	9.73	10.40	10.23	10.15	9.85	9.68
right scapula marrow	7.84	7.67	7.67	7.43	7.27	8.07	7.80	7.65	7.31	7.26
right clavicle marrow	10.02	10.09	9.69	9.64	9.63	9.96	10.08	9.63	9.78	9.39
right femur marrow	4.39	4.28	4.23	4.09	3.98	4.43	4.32	4.20	4.15	4.01
right tibia marrow	0.01	0.01	0.01	0.01	0.01	0.01	0.01	0.01	0.01	0.01
right fibula marrow	0.00	0.00	0.00	0.01	0.01	0.01	0.02	0.00	0.01	0.01
right patella marrow	0.07	0.04	0.01	0.02	0.01	0.02	0.05	0.02	0.04	0.01
right foot marrow	0.01	0.01	0.01	0.00	0.01	0.01	0.01	0.01	0.01	0.01
left scapula marrow	8.25	8.03	7.62	7.67	7.18	8.38	7.83	7.72	7.54	7.26
left clavicle marrow	9.71	9.38	9.54	9.13	8.75	9.71	9.41	9.13	9.12	9.08
left femur marrow	3.85	3.84	3.65	3.62	3.49	3.86	3.80	3.73	3.57	3.56
left tibia marrow	0.01	0.01	0.01	0.01	0.01	0.01	0.01	0.01	0.01	0.01
left fibula marrow	0.02	0.01	0.01	0.01	0.01	0.01	0.01	0.00	0.01	0.01
left patella marrow	0.04	0.01	0.02	0.04	0.02	0.02	0.04	0.02	0.01	0.03
left foot marrow	0.01	0.01	0.01	0.01	0.01	0.01	0.01	0.01	0.01	0.01
pelvis marrow	9.76	9.60	9.46	9.24	9.10	9.62	9.49	9.32	9.17	8.97
skull marrow	0.19	0.19	0.18	0.17	0.15	0.18	0.17	0.18	0.17	0.17
total red marrow	8.23	8.16	8.02	7.86	7.70	8.08	7.98	7.86	7.68	7.56

Table B.22: 10-year-old phantom marrow dose data in units of mGy for simulated Philips Brilliance 64 helical CT chest-abdomen-pelvis scans for 120 kVp, 100 mAs, pitch = 1, and 64 × 0.625 mm beam collimation.

	Females					Males				
Marrow Type	10y 10th	10y 25th	10y 50th	10y 75th	10y 90th	10y 10th	10y 25th	10y 50th	10y 75th	10y 90th
yellow marrow	2.76	2.68	2.64	2.61	2.51	2.86	2.83	2.79	2.71	2.65
sternum marrow	13.00	12.71	12.56	12.37	12.30	12.78	12.73	12.82	12.68	12.19
cervical vertebrae marrow	5.21	4.09	4.11	4.15	3.68	4.05	4.73	4.03	4.63	3.61
thoracic vertebrae marrow	18.82	18.49	17.95	17.73	17.26	18.79	18.48	18.17	17.85	17.37
lumbar vertebrae marrow	19.00	18.83	18.31	17.76	17.55	18.94	18.69	18.33	18.03	17.43
sacrum marrow	10.34	10.32	9.95	9.77	9.48	10.51	10.27	9.99	9.77	9.50
ribs marrow	9.87	9.64	9.51	9.17	8.96	9.86	9.81	9.49	9.28	9.03
right scapula marrow	7.38	7.12	7.20	6.73	6.65	7.72	7.29	7.13	6.86	6.78
right clavicle marrow	9.54	9.27	9.21	8.76	8.48	9.53	9.27	8.77	9.16	8.86
right femur marrow	4.65	4.42	4.33	4.20	4.14	4.49	4.37	4.29	4.16	4.00
right tibia marrow	0.01	0.01	0.01	0.01	0.01	0.01	0.01	0.01	0.01	0.00
right fibula marrow	0.00	0.00	0.01	0.01	0.01	0.00	0.00	0.01	0.01	0.01
right patella marrow	0.02	0.01	0.02	0.02	0.01	0.04	0.02	0.04	0.01	0.01
right foot marrow	0.00	0.00	0.00	0.00	0.00	0.00	0.00	0.00	0.00	0.00
left scapula marrow	7.60	7.24	7.08	6.90	6.51	7.65	7.32	7.05	7.09	6.67
left clavicle marrow	9.40	8.35	8.80	8.37	8.47	9.09	8.72	8.78	8.93	8.22
left femur marrow	4.08	4.01	3.83	3.74	3.62	3.99	3.86	3.82	3.62	3.60
left tibia marrow	0.01	0.01	0.01	0.01	0.01	0.01	0.01	0.00	0.01	0.01
left fibula marrow	0.00	0.02	0.01	0.01	0.01	0.02	0.01	0.00	0.00	0.01
left patella marrow	0.03	0.02	0.01	0.01	0.02	0.01	0.01	0.01	0.03	0.00
left foot marrow	0.00	0.00	0.00	0.00	0.00	0.00	0.00	0.00	0.00	0.00
pelvis marrow	9.16	8.94	8.71	8.51	8.32	9.14	8.96	8.74	8.52	8.30
skull marrow	0.17	0.15	0.15	0.14	0.14	0.17	0.15	0.16	0.15	0.14
total red marrow	8.41	8.23	8.03	7.86	7.64	8.49	8.38	8.19	8.03	7.82

Table B.23: 13-year-old phantom marrow dose data in units of mGy for simulated Philips Brilliance 64 helical CT chest-abdomen-pelvis scans for 120 kVp, 100 mAs, pitch = 1, and 64 × 0.625 mm beam collimation.

	Females					Males				
Marrow Type	13y 10th	13y 25th	13y 50th	13y 75th	13y 90th	13y 10th	13y 25th	13y 50th	13y 75th	13y 90th
yellow marrow	2.11	2.06	1.99	1.93	1.96	2.21	2.15	2.17	2.09	2.02
sternum marrow	11.64	11.55	11.42	11.04	11.55	13.33	12.94	12.56	12.14	11.86
cervical vertebrae marrow	3.84	3.76	3.95	3.03	2.87	4.62	3.94	4.14	3.33	3.32
thoracic vertebrae marrow	18.66	18.15	17.64	16.87	15.66	19.51	19.01	17.93	17.28	16.72
lumbar vertebrae marrow	19.16	18.83	18.31	17.92	17.62	20.84	20.37	19.99	19.10	18.64
sacrum marrow	8.76	8.54	8.23	8.02	7.56	10.06	9.71	9.13	8.76	8.56
ribs marrow	9.60	9.36	9.18	8.84	9.26	10.02	9.80	10.17	9.77	9.52
right scapula marrow	7.99	7.89	7.72	7.28	7.08	7.61	7.10	7.19	6.47	6.78
right clavicle marrow	8.79	8.68	8.40	8.09	8.50	8.87	8.23	9.34	8.55	8.74
right femur marrow	4.77	4.62	4.49	4.39	5.07	4.97	4.85	5.52	5.32	5.11
right tibia marrow	0.01	0.01	0.01	0.01	0.01	0.01	0.01	0.01	0.01	0.01
right fibula marrow	0.00	0.00	0.00	0.00	0.00	0.00	0.00	0.00	0.00	0.00
right patella marrow	0.03	0.02	0.04	0.06	0.06	0.00	0.04	0.01	0.00	0.01
right foot marrow	0.00	0.00	0.00	0.00	0.00	0.00	0.00	0.00	0.00	0.00
left scapula marrow	7.69	7.54	7.21	7.05	6.82	7.68	7.74	7.18	7.26	6.56
left clavicle marrow	8.59	8.37	8.00	8.05	8.34	9.38	9.07	8.72	9.16	8.20
left femur marrow	4.20	4.09	4.01	3.92	4.51	4.38	4.20	5.10	4.88	4.66
left tibia marrow	0.01	0.02	0.01	0.01	0.01	0.01	0.01	0.01	0.01	0.01
left fibula marrow	0.01	0.00	0.05	0.01	0.01	0.02	0.00	0.02	0.00	0.01
left patella marrow	0.01	0.01	0.01	0.01	0.01	0.01	0.02	0.03	0.02	0.03
left foot marrow	0.00	0.00	0.00	0.00	0.00	0.00	0.00	0.00	0.00	0.00
pelvis marrow	8.26	8.04	7.85	7.63	7.95	9.06	8.90	9.18	8.82	8.56
skull marrow	0.11	0.12	0.11	0.10	0.10	0.17	0.17	0.15	0.15	0.13
total red marrow	9.24	9.02	8.80	8.52	8.52	10.00	9.81	9.72	9.33	9.05

Table B.24: 15-year-old phantom marrow dose data in units of mGy for simulated Philips Brilliance 64 helical CT chest-abdomen-pelvis scans for 120 kVp, 100 mAs, pitch = 1, and 64 × 0.625 mm beam collimation.

	Females					Males				
Marrow Type	15y 10th	15y 25th	15y 50th	15y 75th	15y 90th	15y 10th	15y 25th	15y 50th	15y 75th	15y 90th
yellow marrow	2.11	2.05	1.99	2.05	1.98	2.10	2.04	1.98	1.91	1.84
sternum marrow	11.47	11.47	10.93	11.48	11.33	12.21	11.93	11.62	11.22	11.12
cervical vertebrae marrow	3.82	3.24	2.91	3.03	3.20	3.31	3.47	3.29	3.00	3.07
thoracic vertebrae marrow	18.02	17.44	17.03	15.72	15.49	17.05	16.66	16.37	15.62	15.16
lumbar vertebrae marrow	18.57	18.37	17.93	17.59	17.04	19.19	18.56	17.84	17.48	17.03
sacrum marrow	8.54	8.21	7.99	7.51	7.35	8.78	8.45	8.33	8.00	7.79
ribs marrow	9.34	9.18	8.84	9.30	9.17	9.94	9.55	9.33	9.07	8.86
right scapula marrow	7.81	7.66	7.26	7.10	7.12	6.81	6.35	6.42	5.80	6.00
right clavicle marrow	8.45	8.50	8.21	8.43	8.70	9.04	8.49	8.50	7.80	8.06
right femur marrow	5.17	5.16	4.92	5.80	5.64	5.94	5.69	5.51	5.32	5.16
right tibia marrow	0.00	0.00	0.00	0.00	0.00	0.00	0.00	0.00	0.00	0.00
right fibula marrow	0.00	0.00	0.00	0.00	0.00	0.00	0.00	0.00	0.00	0.00
right patella marrow	0.00	0.00	0.00	0.00	0.00	0.00	0.00	0.00	0.00	0.00
right foot marrow	0.00	0.00	0.00	0.00	0.00	0.00	0.00	0.00	0.00	0.00
left scapula marrow	7.54	7.18	6.99	6.88	6.50	6.98	7.19	6.38	6.58	5.89
left clavicle marrow	8.41	7.99	7.77	8.76	7.99	8.88	8.98	8.41	8.13	7.83
left femur marrow	4.67	4.49	4.43	5.16	5.00	5.48	5.30	5.17	4.94	4.74
left tibia marrow	0.00	0.00	0.00	0.00	0.00	0.00	0.00	0.00	0.00	0.00
left fibula marrow	0.00	0.00	0.00	0.00	0.00	0.00	0.00	0.00	0.00	0.00
left patella marrow	0.00	0.00	0.00	0.00	0.00	0.00	0.00	0.00	0.00	0.00
left foot marrow	0.00	0.00	0.00	0.00	0.00	0.00	0.00	0.00	0.00	0.00
pelvis marrow	8.03	7.85	7.66	7.97	7.73	8.79	8.50	8.28	8.03	7.76
skull marrow	0.12	0.10	0.10	0.10	0.10	0.15	0.14	0.13	0.13	0.13
total red marrow	9.43	9.21	8.95	8.97	8.76	9.83	9.50	9.26	8.96	8.69

References

Agostinelli, S., Allison, J., Amako, K., Apostolakis, J., Araujo, H., Arce, P., Asai, M., Axen, D., Banerjee, S., Barrand, G., et al. (2003). Geant4—a simulation toolkit. *Nuclear Instruments and Methods in Physics Research Section A: Accelerators, Spectrometers, Detectors and Associated Equipment*, 506(3):250–303.

Allison, J., Amako, K., Apostolakis, J., Araujo, H., Arce Dubois, P., Asai, M., Barrand, G., Capra, R., Chauvie, S., Chytracek, R., et al. (2006). Geant4 developments and applications. *IEEE Transactions on Nuclear Science*, 53(1):270–278.

American Association of Physicists in Medicine et al. (2011). Size-specific dose estimates (SSDE) in pediatric and adult body CT examinations (Report # 204). *College Park, MD*.

Archambault, L., Beaulieu, L., Carrier, J., Castrovillari, F., Chauvie, S., Foppiano, F., Ghiso, G., Guatelli, S., Incerti, S., Lamanna, E., et al. (2003). Overview of geant4 applications in medical physics. In *Nuclear Science Symposium Conference Record, 2003 IEEE*, volume 3, pages 1743–1745. IEEE.

Axelsson, B., Khalil, C., Lidegran, M., Schuwert, P., and Mortensson, W. (1999). Estimating the effective dose to children undergoing heart investigations–a phantom study. *The British journal of radiology*, 72(856):378–383.

BEIR VII (2006). *Health risks from exposure to low levels of ionizing radiation*. The National Academies Press, Washington, DC.

Bergonié, J. and Tribondeau, L. (1906). De quelques résultats de la radiotherapie et essai de fixation d'une technique rationnelle. *Comptes-Rendus des Séances de l'Académie des Sciences*, 143:983–985.

Bierman, H. R. (1961). Homeostasis of the blood cell elements. In *Functions of the Blood*, page 357. Academic Press New York.

Bohr, H. and Lund, B. (1987). Bone mineral density of the proximal tibia following uncemented arthroplasty. *The Journal of arthroplasty*, 2(4):309–312.

Bohr, H. and Schaadt, O. (1985). Bone mineral content of the femoral neck and shaft: relation between cortical and trabecular bone. *Calcified tissue international*, 37(4):340–344.

Bohr, H. H. and Schaadt, O. (1987). Mineral content of upper tibia assessed by dual photon densitometry. *Acta Orthopaedica*, 58(5):557–559.

Bolch, W. E., Patton, P. W., Rajon, D. A., Shah, A. P., Jokisch, D. W., and Inglis, B. A. (2002). Considerations of marrow cellularity in 3-dimensional dosimetric models of the trabecular skeleton. *Journal of Nuclear Medicine*, 43(1):97–108.

Boone, J. M., Geraghty, E. M., Seibert, J. A., and Wootton-Gorges, S. L. (2003). Dose reduction in pediatric ct: A rational approach 1. *Radiology*, 228(2):352–360.

Boone, J. M. and Seibert, J. A. (1997). An accurate method for computer-generating tungsten anode x-ray spectra from 30 to 140 kv. *Medical physics*, 24:1661.

Brenner, D. J., Doll, R., Goodhead, D. T., Hall, E. J., Land, C. E., Little, J. B., Lu-

bin, J. H., Preston, D. L., Preston, R. J., Puskin, J. S., et al. (2003). Cancer risks attributable to low doses of ionizing radiation: assessing what we really know. *Proceedings of the National Academy of Sciences*, 100(24):13761–13766.

Brenner, D. J., Elliston, C. D., Hall, E. J., and Berdon, W. E. (2001). Estimated risks of radiation-induced fatal cancer from pediatric ct. *American journal of roentgenology*, 176(2):289–296.

Bushberg, J. T. and Boone, J. M. (2011). *The essential physics of medical imaging*. Lippincott Williams & Wilkins.

Carrier, J.-F., Archambault, L., Beaulieu, L., and Roy, R. (2004). Validation of geant4, an object-oriented monte carlo toolkit, for simulations in medical physics. *Medical physics*, 31(3):484–492.

Chao, T. and Xu, X. (2001). Specific absorbed fractions from the image-based vip-man body model and egs4-vlsi monte carlo code: internal electron emitters. *Physics in medicine and biology*, 46(4):901.

Chapple, C., Willis, S., and Frame, J. (2002). Effective dose in paediatric computed tomography. *Physics in medicine and biology*, 47(1):107.

Clark, L. D., Stabin, M. G., Fernald, M. J., and Brill, A. B. (2010). Changes in radiation dose with variations in human anatomy: moderately and severely obese adults. *Journal of Nuclear Medicine*, 51(6):929–932.

Clarke, R. (2004). *Control of low-level radiation exposure: time for a change? In: ICRP*

Supporting Guidance 4. Development of the Draft 2005 recommendations of the ICRP: a collection of papers, volume 34(Suppl):3–11. of *Ann ICRP*. Oxford: Elsevier.

Coursey, J., Schwab, D., Tsai, J., and Dragoset, R. (2010). Atomic weights and isotopic compositions (version 3.0). [online] available: http://physics.nist.gov/comp [2013 july 15]. *National Institute of Standards and Technology, Gaithersburg, MD.*

Cristy, M. (1980). Mathematical phantoms representing children of various ages for use in estimates of internal dose. Technical report, Oak Ridge National Lab., TN (USA).

Cristy, M. (1981). Active bone marrow distribution as a function of age in humans. *Physics in medicine and biology*, 26(3):389.

Cristy, M. and Eckerman, K. (1987). Specific absorbed fractions of energy at various ages from internal photon sources. vi. newborn. *ORNL/TM-8381*, 6.

DeMarco, J., Cagnon, C., Cody, D., Stevens, D., McCollough, C., O'Daniel, J., and McNitt-Gray, M. (2005). A monte carlo based method to estimate radiation dose from multidetector ct (mdct): cylindrical and anthropomorphic phantoms. *Physics in medicine and biology*, 50(17):3989.

DeMarco, J., Cagnon, C., Cody, D., Stevens, D., McCollough, C., Zankl, M., Angel, E., and McNitt-Gray, M. (2007). Estimating radiation doses from multidetector ct using monte carlo simulations: effects of different size voxelized patient models on magnitudes of organ and effective dose. *Physics in medicine and biology*, 52(9):2583.

Deus, S. and Poston, J. (1976). Development of a mathematical phantom representing a

10-year-old child for use in internal dosimetry calculations.[radiation dose calculations]. Technical report, Oak Ridge National Lab., Tenn. (USA).

Dixon, R. L. (2003). A new look at ct dose measurement: beyond ctdi. *Medical physics*, 30:1272.

Donnelly, L. F. (2005). Reducing radiation dose associated with pediatric ct by decreasing unnecessary examinations. *American Journal of Roentgenology*, 184(2):655–657.

Donnelly, L. F., Emery, K. H., Brody, A. S., Laor, T., Gylys-Morin, V. M., Anton, C. G., Thomas, S. R., and Frush, D. P. (2001). Minimizing radiation dose for pediatric body applications of single-detector helical ct strategies at a large children's hospital. *American Journal of Roentgenology*, 176(2):303–306.

Emery, J. and Follett, G. (1964). Regression of bone-marrow haemopoiesis from the terminal digits in the foetus and infant. *British journal of haematology*, 10(4):485–489.

Fawcett, D. and Bloom, W. (1986). A textbook of histology wb saunders co. *Philadelphia, pp556-558, p71.*

Feinendegen, L. E., Paretzke, H. G., and Neumann, R. D. (2007). Damage propagation in complex biological systems following exposure to low doses of ionising radiation. *Atoms for Peace: An International Journal*, 1(4):336–354.

Fisher, H. and Snyder, W. (1966). Variation of dose delivered by 137cs as a function of body size from infancy to adulthood. *ORNL*, 4007:221–228.

Fisher Jr, H. and Snyder, W. (1967). Distribution of dose in the body from a source of

gamma rays distributed uniformly in an organ. Technical report, Oak Ridge National Lab., Tenn.

Frost, H. M. and Straatsma, C. (1964). Bone remodelling dynamics. *Plastic and Reconstructive Surgery*, 33(2):196.

Geant4 Collaboration et al. (2007). Physics reference manual. *Version Geant4*, 9.

Gilbert, E. S. (2001). Invited commentary: Studies of workers exposed to low doses of radiation. *American journal of epidemiology*, 153(4):319–322.

Goske, M. J., Applegate, K. E., Boylan, J., Butler, P. F., Callahan, M. J., Coley, B. D., Farley, S., Frush, D. P., Hernanz-Schulman, M., Jaramillo, D., et al. (2008). The image gently campaign: increasing ct radiation dose awareness through a national education and awareness program. *Pediatric radiology*, 38(3):265–269.

Hall, E. J. and Giaccia, A. J. (2006). *Radiobiology for the Radiologist*. Lippincott Williams & Wilkins.

Hart, D. and Wall, B. (1994). Estimation of effective dose from dose–area product measurements for barium meals and barium enemas. *The British journal of radiology*, 67(797):485–489.

Hartsock, R., Smith, E., and Petty, C. S. (1965). Normal variations with aging of the amount of hematopoietic tissue in bone marrow from the anterior iliac crest. a study made from 177 cases of sudden death examined by necropsy. *American journal of clinical pathology*, 43:326.

Hubbell, J. and Seltzer, S. (2004). Tables of x-ray mass attenuation coefficients and mass energy-absorption coefficients (version 1.4). *National Institute of Standards and Technology, Gaithersburg, MD.*

Hwang, J., Shoup, R., and Poston, J. (1976a). Mathematical description of a newborn human for use in dosimetry calculations. Technical report, Oak Ridge National Lab., Tenn.(USA).

Hwang, J., Shoup, R., Warner, G., and Poston, J. (1976b). Mathematical descriptions of a one-and five-year old child for use in dosimetry calculations. Technical report, Oak Ridge National Lab., Tenn.(USA).

ICRP 102 (2007). Managing patient dose in multi-detector computed tomography (mdct). *ICRP Publication 102 (International Commission on Radiological Protection, Essen, Germany).*

ICRP 103 (2007). The 2007 recommendations of the international commission on radiological protection. *ICRP Publication 103 (International Commission on Radiological Protection, Essen, Germany*, 37.

ICRP 26 (1977). *Recommendations of the International Commission on Radiological Protection. ICRP Publication 26*, volume Ann ICRP 1(3). Oxford: Pergamon Press.

ICRP 60 (1991). *1990 recommendations of the International Commission on Radiological Protection.* ICRP Publication 60 New York: Pergamon Press.

ICRP 70 (1995). *Basic Anatomical and Physiological Data for Use in Radiological Protection: The Skeleton: A Report of a Task Group of Committee 2 of the International*

Commission on Radiological Protection Adopted by the Commission in July 1994. Pergamon Press.

ICRP 99 (2004). *International Commission on Radiological Protection. Low-dose extrapolation of radiation-related cancer risk. ICRP Publication 99*, volume 35 of *Annals of the ICRP*. Oxford: Elsevier.

International Electrotechnical Commission et al. (2002). Medical electrical equipment. part 2-44, particular requirements for the safety of x-ray equipment for computed tomography. *International Standard IEC*, pages 60601–2.

Jacobi, W. (1975). The concept of the effective dose a proposal for the combination of organ doses. *Radiation and environmental biophysics*, 12(2):101–109.

Jarry, G. (2002). *Monte Carlo dose verification of a commercial CT scanner with application for patient specific dosimetry*. UCLA.

Jarry, G., DeMarco, J., Beifuss, U., Cagnon, C., and McNitt-Gray, M. (2003). A monte carlo-based method to estimate radiation dose from spiral ct: from phantom testing to patient-specific models. *Physics in medicine and biology*, 48(16):2645.

Jiang, H. and Paganetti, H. (2004). Adaptation of geant4 to monte carlo dose calculations based on ct data. *Medical physics*, 31(10):2811–2818.

Johnson, L. (1964). Morphologic analysis in pathology: the kinetics of disease and general biology of bone. *Bone biodynamics*, 1:543–654.

Johnson, P. B., Whalen, S. R., Wayson, M., Juneja, B., Lee, C., and Bolch, W. E.

(2009). Hybrid patient-dependent phantoms covering statistical distributions of body morphometry in the us adult and pediatric population. *Proceedings of the IEEE*, 97(12):2060–2075.

Jones, D. and Wall, B. (1985). Organ doses from medical x-ray examinations calculated using monte carlo techniques. Technical report, National Radiological Protection Board, Harwell (United Kingdom).

Jones, R. M., Poston, J., Hwang, J., Jones, T., and Warner, G. (1976). Development and use of a fifteen year-old equivalent mathematical phantom for internal dose calculations.[radiation dose distributions from/sup 99m/tc-labeled compounds]. Technical report, Oak Ridge National Lab., Tenn.(USA).

Khursheed, A., Hillier, M., Shrimpton, P., and Wall, B. (2002). Influence of patient age on normalized effective doses calculated for ct examinations. *British journal of radiology*, 75(898):819–830.

Kost, S. D., Fraser, N. D., Carver, D. E., Pickens, D. R., Price, R. R., Hernanz-Schulman, M., and Stabin, M. G. (2015). Patient-specific dose calculations for pediatric CT of the chest, abdomen and pelvis. *Pediatric Radiology*, DOI:10.1007/s00247-015-3400-2.

Kramer, R. and Drexler, G. (1982). On the calculation of the effective dose equivalent. *Radiation Protection Dosimetry*, 3(1-2):13–24.

Kramer, R., Khoury, H., Vieira, J., Loureiro, E., Lima, V., Lima, F., and Hoff, G. (2004). All about fax: a female adult voxel phantom for monte carlo calculation in radiation protection dosimetry. *Physics in medicine and biology*, 49(23):5203.

Kramer, R., Vieira, J., Khoury, H., Lima, F., and Fuelle, D. (2003). All about max: a male adult voxel phantom for monte carlo calculations in radiation protection dosimetry. *Physics in medicine and biology*, 48(10):1239.

Kramer, R., Zankl, M., Williams, G., and Drexler, G. (1982). The calculation of dose from external photon exposures using reference human phantoms and monte carlo calculations: Part i: The male (adam) and female (eva) adult mathematical phantoms. *GSF-Report S-885*.

Kuczmarski, R. J., Ogden, C. L., Guo, S. S., Grummer-Strawn, L. M., Flegal, K. M., Mei, Z., Wei, R., Curtin, L. R., Roche, A. F., and Johnson, C. L. (2002). 2000 cdc growth charts for the united states: methods and development. *Vital and health statistics. Series 11, Data from the national health survey*, (246):1–190.

Landauer, Inc. (2006). Optically stimulated luminescence dosimetry for computed tomography—measurement of ctdi and dose profiles. *Landauer, Inc., 2 Science Road, Glenwood, Illinois 60425*.

Lavoie, L., Ghita, M., Brateman, L., and Arreola, M. (2011). Characterization of a commercially-available, optically-stimulated luminescent dosimetry system for use in computed tomography. *Health Physics*, 101(3):299–310.

Lee, C., Kim, K. P., Long, D. J., and Bolch, W. E. (2012). Organ doses for reference pediatric and adolescent patients undergoing computed tomography estimated by monte carlo simulation. *Medical physics*, 39(4):2129–2146.

Lee, C., Lee, C., Shah, A. P., and Bolch, W. E. (2006a). An assessment of bone marrow

and bone endosteum dosimetry methods for photon sources. *Physics in medicine and biology*, 51(21):5391.

Lee, C., Lee, C., Staton, R. J., Hintenlang, D. E., Arreola, M. M., Williams, J. L., and Bolch, W. E. (2007). Organ and effective doses in pediatric patients undergoing helical multislice computed tomography examination. *Medical physics*, 34:1858.

Lee, C., Lee, C., Williams, J. L., and Bolch, W. E. (2006b). Whole-body voxel phantoms of paediatric patients—uf series b. *Physics in medicine and biology*, 51(18):4649.

Lee, C., Lodwick, D., Williams, J. L., and Bolch, W. E. (2008). Hybrid computational phantoms of the 15-year male and female adolescent: applications to ct organ dosimetry for patients of variable morphometry. *Medical physics*, 35(6):2366–2382.

Lee, C., Williams, J. L., Lee, C., and Bolch, W. E. (2005). The uf series of tomographic computational phantoms of pediatric patients. *Medical physics*, 32(12):3537–3548.

Li, X., Samei, E., Segars, W. P., Sturgeon, G. M., Colsher, J. G., and Frush, D. P. (2008). Patient-specific dose estimation for pediatric chest ct. *Medical physics*, 35(12):5821–5828.

Li, X., Samei, E., Segars, W. P., Sturgeon, G. M., Colsher, J. G., and Frush, D. P. (2011a). Patient-specific radiation dose and cancer risk for pediatric chest ct. *Radiology*, 259(3):862–874.

Li, X., Samei, E., Segars, W. P., Sturgeon, G. M., Colsher, J. G., Toncheva, G., Yoshizumi, T. T., and Frush, D. P. (2011b). Patient-specific radiation dose and cancer risk esti-

mation in ct: Part i. development and validation of a monte carlo program. *Medical physics*, 38(1):397.

Li, X., Samei, E., Segars, W. P., Sturgeon, G. M., Colsher, J. G., Toncheva, G., Yoshizumi, T. T., and Frush, D. P. (2011c). Patient-specific radiation dose and cancer risk estimation in ct: Part ii. application to patients. *Medical physics*, 38(1):408.

Linton, O. W. and Mettler Jr, F. A. (2003). National conference on dose reduction in ct, with an emphasis on pediatric patients. *American Journal of Roentgenology*, 181(2):321–329.

Little, M. (1996). Evidence for curvilinearity in the cancer incidence dose-response in the japanese atomic bomb survivors. *International journal of radiation biology*, 70(1):83–94.

Little, M. and Muirhead, C. (1998). Curvature in the cancer mortality dose response in japanese atomic bomb survivors: absence of evidence of threshold. *International journal of radiation biology*, 74(4):471–480.

Little, M. and Muirhead, C. (2004). Absence of evidence for threshold departures from linear-quadratic curvature in the japanese a-bomb cancer incidence and mortality data. *International Journal of Low Radiation*, 1(2):242–255.

Little, M., Muirhead, C., and Charles, M. (1999). Describing time and age variations in the risk of radiation-induced solid tumour incidence in the japanese atomic bomb survivors using generalized relative and absolute risk models. *Statistics in medicine*, 18(1):17–33.

Little, M., Wakeford, R., Lubin, J., and Kendall, G. (2010). The statistical power of epidemiological studies analyzing the relationship between exposure to ionizing radiation and cancer, with special reference to childhood leukemia and natural background radiation. *Radiation research*, 174(3):387–402.

Marieb, E. N. and Hoehn, K. (2007). *Human anatomy & physiology*. Pearson Education.

Marine, P. M., Stabin, M. G., Fernald, M. J., and Brill, A. B. (2010). Changes in radiation dose with variations in human anatomy: larger and smaller normal-stature adults. *Journal of Nuclear Medicine*, 51(5):806–811.

Martin, C. (2014). Effective dose: how should it be applied to medical exposures?

MathWorks, Inc. (2012). Matlab 2012b.

McCollough, C., Cody, D., Edyvean, S., Geise, R., Gould, B., Keat, N., Huda, W., Judy, P., Kalender, W., McNitt-Gray, M., et al. (2008). The measurement, reporting, and management of radiation dose in CT. *Report of AAPM Task Group 23*.

McCollough, C. H., Leng, S., Yu, L., Cody, D. D., Boone, J. M., and McNitt-Gray, M. F. (2011). CT dose index and patient dose: they are not the same thing. *Radiology*, 259(2):311–316.

Meunier, P., Aaron, J., Edouard, C., and VlGNON, G. (1971). Osteoporosis and the replacement of cell populations of the marrow by adipose tissue: a quantitative study of 84 iliac bone biopsies. *Clinical orthopaedics and related research*, 80:147–154.

National Center for Health Statistics (US), Centers for Disease Control, et al. (2000). *2000*

CDC growth charts: United States. US Department of Health and Human Services, Centers for Disease Control and Prevention, National Center for Health Statistics.

National Center for Health Statistics (US) et al. (2002). *National health and nutrition examination survey*. National Center for Health Statistics (US).

Neuman, W. (1980). Bone material and calcification mechanisms. *Fundamental and clinical bone physiology*, pages 83–107.

Nickoloff, E. L., Dutta, A. K., and Lu, Z. F. (2003). Influence of phantom diameter, kvp and scan mode upon computed tomography dose index. *Medical physics*, 30:395.

Open Ergonomics (2008). Peoplesize 2008 visual anthropometry software. *URL: http://www. openerg. com/psz. htm (Accessed 17th August 2001)*.

Parfitt, A. (1988). The composition, structure and remodeling of bone: A basis for the interpretation of bone mineral measurements. *Bone mineral measurements by photon absorptiometry: methodological problems. Leuven University Press, Leuven*, pages 9–28.

Petoussi-Henss, N., Zankl, M., Fill, U., and Regulla, D. (2002). The gsf family of voxel phantoms. *Physics in medicine and biology*, 47(1):89.

Pierce, D. A. (2003). Mechanistic models for radiation carcinogenesis and the atomic bomb survivor data. *Radiation research*, 160(6):718–723.

Pierce, D. A. and Preston, D. L. (2000). Radiation-related cancer risks at low doses among atomic bomb survivors. *Radiation research*, 154(2):178–186.

Pierce, D. A., Shimizu, Y., Preston, D. L., Vaeth, M., and Mabuchi, K. (2012). Studies of the mortality of atomic bomb survivors. report 12, part i. cancer: 1950-1990. *Radiation research*, 178(2):AV61–AV87.

Preston, D., Pierce, D., Shimizu, Y., Ron, E., and Mabuchi, K. (2003a). Dose response and temporal patterns of radiation-associated solid cancer risks. *Health physics*, 85(1):43–46.

Preston, D., Ron, E., Tokuoka, S., Funamoto, S., Nishi, N., Soda, M., Mabuchi, K., and Kodama, K. (2007). Solid cancer incidence in atomic bomb survivors: 1958-1998. *Radiation research*, 168(1):1–64.

Preston, D. L., Pierce, D. A., Shimizu, Y., Cullings, H. M., Fujita, S., Funamoto, S., and Kodama, K. (2004). Effect of recent changes in atomic bomb survivor dosimetry on cancer mortality risk estimates. *Radiation research*, 162(4):377–389.

Preston, D. L., Shimizu, Y., Pierce, D. A., Suyama, A., and Mabuchi, K. (2003b). Studies of mortality of atomic bomb survivors. report 13: Solid cancer and noncancer disease mortality: 1950-1997. *Radiation research*, 160(4):381–407.

Preston, D. L., Shimizu, Y., Pierce, D. A., Suyama, A., and Mabuchi, K. (2012). Studies of mortality of atomic bomb survivors. report 13: solid cancer and noncancer disease mortality: 1950-1997. *Radiation research*, 178(2):AV146–AV172.

Pretorius, P. H., Xia, W., King, M. A., Tsui, B., Pan, T.-S., and Villegas, B. J. (1997). Evaluation of right and left ventricular volume and ejection fraction using a mathematical cardiac torso phantom. *Journal of nuclear medicine: official publication, Society of Nuclear Medicine*, 38(10):1528–1535.

Rosenstein, M. (1976). Handbook of selected organ doses for projections common in diagnostic radiology. Technical report, Bureau of Radiological Health, Rockville, Md.(USA).

Schauer, D. A. and Linton, O. W. (2009). NCRP report no. 160, ionizing radiation exposure of the population of the united states, medical exposure: are we doing less with more, and is there a role for health physicists? *Health physics*, 97(1):1–5.

Schlenker, R. and VonSeggen, W. (1976). The distribution of cortical and trabecular bone mass along the lengths of the radius and ulna and the implications forin vivo bone mass measurements. *Calcified tissue research*, 20(1):41–52.

Segars, W. (2001). *Development and application of the new dynamic NURBS-based cardiac-torso (NCAT) phantom*. PhD thesis, University of North Carolina, Chapel Hill.

Segars, W., Mahesh, M., Beck, T., Frey, E., and Tsui, B. (2008). Realistic CT simulation using the 4D XCAT phantom. *Medical physics*, 35(8):3800–3808.

Segars, W., Mori, S., Chen, G., and Tsui, B. (2007). Modeling respiratory motion variations in the 4D NCAT phantom. In *Nuclear Science Symposium Conference Record, 2007. NSS'07. IEEE*, volume 4, pages 2677–2679. IEEE.

Segars, W., Sturgeon, G., Mendonca, S., Grimes, J., and Tsui, B. M. (2010). 4d xcat phantom for multimodality imaging research. *Medical physics*, 37(9):4902–4915.

Segars, W. P., Lalush, D. S., and Tsui, B. (2000). Development of an interactive software application to model patient populations in the 4d nurbs-based cardiac torso phantom.

In *Nuclear Science Symposium Conference Record, 2000 IEEE*, volume 3, pages 20–51. IEEE.

Segars, W. P. and Tsui, B. M. (2002). Study of the efficacy of respiratory gating in myocardial SPECT using the new 4-D NCAT phantom. *Nuclear Science, IEEE Transactions on*, 49(3):675–679.

Segars, W. P. and Tsui, B. M. (2009). MCAT to XCAT: The evolution of 4-D computerized phantoms for imaging research. *Proceedings of the IEEE*, 97(12):1954–1968.

Segars, W. P., Tsui, B. M., Frey, E., and Fishman, E. (2003). Extension of the 4D NCAT phantom to dynamic x-ray CT simulation. In *Nuclear Science Symposium Conference Record, 2003 IEEE*, volume 5, pages 3195–3199. IEEE.

Shrimpton, P. and Wall, B. (2000). Reference doses for paediatric computed tomography. *Radiation Protection Dosimetry*, 90(1-2):249–252.

Siegel, J. A. and Stabin, M. G. (2012). Radar commentary: Use of linear no-threshold hypothesis in radiation protection regulation in the united states. *Health physics*, 102(1):90–99.

Siegel, J. A. and Welsh, J. S. (2015). Does Imaging Technology Cause Cancer? Debunking the Linear No-Threshold Model of Radiation Carcinogenesis. *Technology in cancer research & treatment*.

Siegel, M. J., Schmidt, B., Bradley, D., Suess, C., and Hildebolt, C. (2004). Radiation Dose and Image Quality in Pediatric CT: Effect of Technical Factors and Phantom Size and Shape. *Radiology*, 233(2):515–522.

Snyder, W., Ford, M., Warner, G., and Fisher Jr, H. (1978). Estimates of specific absorbed fractions for monoenergetic photon sources uniformly distributed in various organs of a heterogeneous phantom. *MIRD pamphlet*, 5.

Snyder, W. S., Cook, M., Nasset, E., Karhausen, L., Howells, G. P., and Tipton, I. (1975). *Report of the task group on reference man*, volume 23. Pergamon Oxford (England):.

Snyder, W. S., Ford, M. R., Warner, G. G., and Fisher Jr, H. (1969). Estimates of absorbed fractions for monoenergetic photon sources uniformly distributed in various organs of a heterogeneous phantom. Technical report, Oak Ridge National Lab., Tenn.

Spiers, F. (1969). Beta particle dosimetry in trabecular bone. *Delayed Effects of Bone-Seeking Radionuclides. Mays, Charles W. (ed.). Salt Lake City, University of Utah Press*, pages 95–108.

Spiers, F. and Beddoe, A. (1983). Sites of incidence of osteosarcoma in the long bones of man and the beagle. *Health physics*, 44:49–64.

Stabin, M., Eckerman, K., Bolch, W., Bouchet, L., and Patton, P. (2002). Evolution and status of bone and marrow dose models. *Cancer Biotherapy and Radiopharmaceuticals*, 17(4):427–433.

Stabin, M., Emmons, M. A., Segars, W. P., and Fernald, M. J. (2012). Realistic reference adult and paediatric phantom series for internal and external dosimetry. *Radiation Protection Dosimetry*, 149(1):49–55.

Stabin, M. and Xu, X. G. (2014). Basic principles in the radiation dosimetry of nuclear medicine. *Seminars in Nuclear Medicine*, 44(3):162–171.

Stabin, M. G. (2007). *Radiation protection and dosimetry: an introduction to health physics*. Springer Science & Business Media.

Staton, R. J., Lee, C., Lee, C., Williams, M. D., Hintenlang, D. E., Arreola, M. M., Williams, J. L., and Bolch, W. E. (2006). Organ and effective doses in newborn patients during helical multislice computed tomography examination. *Physics in medicine and biology*, 51(20):5151.

Strauss, K. J., Goske, M. J., Frush, D. P., Butler, P. F., and Morrison, G. (2009). Image gently vendor summit: working together for better estimates of pediatric radiation dose from ct. *American Journal of Roentgenology*, 192(5):1169–1175.

Tian, X., Li, X., Segars, W. P., Paulson, E. K., Frush, D. P., and Samei, E. (2014). Pediatric chest and abdominopelvic ct: organ dose estimation based on 42 patient models. *Radiology*, 270(2):535–547.

Triffitt, J. T. (1980). The organic matrix of bone tissue. In *Fundamental and clinical bone physiology*, pages 45–82. Lippincott Philadelphia, Pa.

Tsui, B., Zhao, X., Gregoriou, G., Lalush, D., Frey, E., Johnston, R., and McCartney, W. (1994). Quantitative cardiac spect reconstruction with reduced image degradation due to patient anatomy. *Nuclear Science, IEEE Transactions on*, 41(6):2838–2844.

Tsui, B. M., Terry, J. A., and Gullberg, G. T. (1993). Evaluation of cardiac cone-beam single photon emission computed tomography using observer performance experiments and receiver operating characteristic analysis. *Investigative radiology*, 28(12):1101–1112.

Turner, A. C., Zhang, D., Khatonabadi, M., Zankl, M., DeMarco, J. J., Cagnon, C. H., Cody, D. D., Stevens, D. M., McCollough, C. H., and McNitt-Gray, M. F. (2011). The feasibility of patient size-corrected, scanner-independent organ dose estimates for abdominal ct exams. *Medical physics*, 38(2):820–829.

Turner, A. C., Zhang, D., Kim, H. J., DeMarco, J. J., Cagnon, C. H., Angel, E., Cody, D. D., Stevens, D. M., Primak, A. N., McCollough, C. H., et al. (2009). A method to generate equivalent energy spectra and filtration models based on measurement for multidetector ct monte carlo dosimetry simulations. *Medical physics*, 36(6):2154.

UNSCEAR (2000). Effects of ionizing radiation. Technical report, United Nations Scientific Committee on the Effects of Atomic Radiation.

UNSCEAR (2013). Sources, effects and risks of ionizing radiation unscear 2013 report: Volume ii scientific annex b: Effects of radiation exposure of children. Technical report, United Nations Scientific Committee on the Effects of Atomic Radiation.

Valentin, J. (2002). Basic anatomical and physiological data for use in radiological protection: reference values: Icrp publication 89. *Annals of the ICRP*, 32(3):1–277.

Veit, R., Zankl, M., Petoussi, N., Mannweiler, E., Williams, G., and Drexler, G. (1989). Tomographic anthropomorphic models, part 1: Construction technique and description of models of an 8 week old baby and a 7 year old child. *GSF-Bericht*, 3:89.

Virtama, P. and Helelä, T. (1969). *Radiographic measurements of cortical bone: variations in a normal population between 1 and 90 years of age*. Acta Radiologica.

Vrieze, T. J., Sturchio, G. M., and McCollough, C. H. (2012). Technical note: Precision and accuracy of a commercially available ct optically stimulated luminescent dosimetry system for the measurement of ct dose index. *Med Phys.*, 39(11):6580–6584.

Wall, B., Kendall, G., Edwards, A., Bouffler, S., Muirhead, C., and Meara, J. (2014). What are the risks from medical x-rays and other low dose radiation?

Wessels, B. W., Bolch, W. E., Bouchet, L. G., Breitz, H. B., DeNardo, G. L., Meredith, R. F., Stabin, M. G., and Sgouros, G. (2004). Bone marrow dosimetry using blood-based models for radiolabeled antibody therapy: a multiinstitutional comparison. *Journal of Nuclear Medicine*, 45(10):1725–1733.

White, D. and Wilson, I. (1992). Photon, electron, proton and neutron interaction data for body tissues. *ICRU Report*, 46.

Wikipedia (2010). Human bone marrow.

Williams, G., Zankl, M., Abmayr, W., Veit, R., and Drexler, G. (1986). The calculation of dose from external photon exposures using reference and realistic human phantoms and monte carlo methods. *Physics in medicine and biology*, 31(4):449.

Xu, X., Chao, T., and Bozkurt, A. (2000). Vip-man: an image-based whole-body adult male model constructed from color photographs of the visible human project for multi-particle monte carlo calculations. *Health Physics*, 78(5):476–486.

Xu, X. G. and Eckerman, K. F. (2009). *Handbook of anatomical models for radiation dosimetry*. CRC Press.

Yushkevich, P. A., Piven, J., Hazlett, H. C., Smith, R. G., Ho, S., Gee, J. C., and Gerig, G. (2006). User-guided 3d active contour segmentation of anatomical structures: significantly improved efficiency and reliability. *Neuroimage*, 31(3):1116–1128.

Zankl, M., Veit, R., Williams, G., Schneider, K., Fendel, H., Petoussi, N., and Drexler, G. (1988). The construction of computer tomographic phantoms and their application in radiology and radiation protection. *Radiation and environmental biophysics*, 27(2):153–164.

Zankl, M. and Wittmann, A. (2001). The adult male voxel model golem segmented from whole-body ct patient data. *Radiation and environmental biophysics*, 40(2):153–162.

Zhang, G., Luo, Q., Zeng, S., and Liu, Q. (2008). The development and application of the visible chinese human model for monte carlo dose calculations. *Health physics*, 94(2):118–125.

Zubal, I. G., Harrell, C. R., Smith, E. O., Rattner, Z., Gindi, G., and Hoffer, P. B. (1994). Computerized three-dimensional segmented human anatomy. *Medical physics*, 21(2):299–302.